DYNAMIC CRUSTAL RECYCLING AND SURFACE PROCESSES AT THE SUTURE ZONE OF ARC-CONTINENT COLLISION: INSIGHTS FROM DEEP-TIME SEDIMENTARY STRATIGRAPHY AND MODERN LANDSCAPE OF THE COASTAL RANGE, EASTERN TAIWAN

by

LARRY SYU-HENG LAI

A DISSERTATION

Presented to the Department of Earth Sciences
and the Division of Graduate Studies of the University of Oregon
in partial fulfillment of the requirements
for the degree of
Doctor of Philosophy

December 2022

DISSERTATION APPROVAL PAGE

Student: Larry Syu-Heng Lai

Title: Dynamic Crustal Recycling and Surface Processes at the Suture Zone of Arc-Continent Collision: Insights from Deep-Time Sedimentary Stratigraphy and Modern Landscape of the Coastal Range, Eastern Taiwan

This dissertation has been accepted and approved in partial fulfillment of the requirements for the Doctor of Philosophy degree in the Department of Earth Sciences by:

Rebecca J. Dorsey	Chairperson/Advisor
Joshua J. Roering	Core Member
Diego Melgar	Core Member
Mark A. Fonstad	Institutional Representative

and

Krista M. Chronister	Vice Provost of Graduate Studies

Original approval signatures are on file with the University of Oregon Division of Graduate Studies.

Degree awarded December 2022

DISSERTATION ABSTRACT

Larry Syu-Heng Lai

Doctor of Philosophy

Department of Earth Sciences

December 2022

Title: Dynamic Crustal Recycling and Surface Processes at the Suture Zone of Arc-Continent Collision: Insights from Deep-Time Sedimentary Stratigraphy and Modern Landscape of the Coastal Range, Eastern Taiwan

The arc-continent collision system has been considered as a primary mechanism in the growth of continental crust, which involves development of both rising eroding mountains and subsiding syn-orogenic basins. However, the rates, timescales, and structural controls on these processes remain poorly understood. In this dissertation, I address these questions through stratigraphic and geomorphic studies in the Coastal Range of eastern Taiwan, an active arc-continent collisional orogen. The first portion of this work focuses on long-debated origin of the Lichi Mélange and associated basin evolution in the southern Coastal Range. Results of integrated stratigraphic and lithofacies analysis reveal a polygenetic origin (sedimentary deposit overprinted by structural shears) of the Lichi Mélange. This mélange unit is interbedded with orogen-derived turbidites that accumulated on accreting island-arc basement in a retrowedge foredeep basin from ca. 4.0 to 0.8 Ma. The next chapter investigates vertical crustal motions involved in creation of the modern Coastal Range. I applied high-resolution backstripping procedures to composite sections in southern and northern Coastal Range, using updated age constraints and foraminifera-based paleobathymetry. The results reveal abruptly oscillating vertical motions in the accreting arc crust, which can be interpreted by an eastward migrating flexural wave, followed by an extremely rapid uplift via transpressional deformation since 0.8-0.5 Ma. In the following chapter, I further conducted quantitative topographic analysis to evaluate the primary controls on the landscape patterns in the modern Coastal Range. The results show that, in this fast-eroding terrain, channel steepness and hillslope gradient are independent of uplift rate but systematically vary with bedload grain size and bedrock lithology. High flux of coarse sediment and ubiquitous mass-wasting hillslopes together dominate erosion processes and set the topographic limit of the Coastal Range. These three chapters collectively present a comprehensive investigation into the genesis of Taiwan's Coastal Range, from a subsiding deep-marine sedimentary basin millions of years ago to a rapidly emerging steep mountain belt today. The results provide novel perspectives in understanding how rock cycle, crustal deformation, and topographic evolution interact in an active mountain-building zone.

This dissertation includes previously published co-authored materials with electronic data spreadsheets in supplemental files.

CURRICULUM VITAE

NAME OF AUTHOR: Larry Syu-Heng Lai

GRADUATE AND UNDERGRADUATE SCHOOLS ATTENDED:

University of Oregon, Eugene, Oregon, United States of America
National Taiwan University, Taipei, Taiwan

DEGREES AWARDED:

Doctor of Philosophy, Earth Sciences, 2022, University of Oregon
Master of Science, Geosciences, 2015, National Taiwan University
Bachelor of Science, Geosciences, 2011, National Taiwan University

AREAS OF SPECIAL INTEREST:

Sedimentology, Stratigraphy, Basin Analysis
Tectonic Geomorphology
Active Tectonics

PROFESSIONAL EXPERIENCE:

Graduate Employee, Department of Earth Sciences, University of Oregon, 2017–2022

Research Assistant, Department of Science Education, National Taipei University of Education, 2016–2017

Substitute Military Service, Taroko National Park Headquarters, 2015–2016

Intern, Oil and Gas Exploration and Production Department, Formosa Petrochemical Corporation, 2013

Graduate Teaching Assistant, Department of Geosciences, National Taiwan University, 2011–2014

GRANTS, AWARDS, AND HONORS:

Research Excellence Award, Department of Earth Sciences, University of Oregon, 2021

Outstanding Teaching Assistant Award, Department of Earth Sciences, University of Oregon, 2020

General University Scholarship, University of Oregon, 2020

Government Scholarship for Study Abroad, Ministry of Education, Taiwan, 2019

Smith Scholarship, Department of Earth Sciences, University of Oregon, 2018

Graduate Student Research Grants, Geological Society of America, 2018

Johnston Scholarship, Department of Earth Sciences, University of Oregon, 2017

Dean's Award of College of Science (Master's Degree), National Taiwan University, 2015

Outstanding Student Paper Award, Joint Annual Meeting of Geological and Geophysical Society of Taiwan, 2015

Dean's Award of College of Science (Bachelor's Degree), National Taiwan University, 2011

Outstanding Student Paper Award, Joint Annual Meeting of Geological and Geophysical Society of Taiwan, 2011

PUBLICATIONS:

Lai, L.S.-H., Dorsey, R.J., Horng, C.-S., Chi, W.-R., Shea, K.-S., and Yen, J.-Y. (2022) Extremely rapid up-and-down motions of island arc crust during arc-continent collision. *Communications Earth & Environment*, 3(1), 100.

Lai, L.S.-H., Roering, J.J., Finnegan, N.J., Dorsey, R.J., and Yen, J.-Y. (2021) Coarse sediment supply sets the slope of bedrock channels in rapidly uplifting terrain: Field and topographic evidence from eastern Taiwan. *Earth Surface Processes and Landforms*, 46(13), 2671-2689.

Lai, L.S.-H., Dorsey, R.J., Horng, C.-S., Chi, W.-R., Shea, K.-S., and Yen, J.-Y. (2021) Polygenetic mélange in the retrowedge foredeep of an active arc-continent collision, Coastal Range of eastern Taiwan. *Sedimentary Geology*, 418, 105901.

Retallack, G.J., Broz, A.P., **Lai, L.S.H.**, and Gardner, K. (2021) Neoproterozoic marine chemostratigraphy, or eustatic sea level change? *Palaeogeography, Palaeoclimatology, Palaeoecology*, 562, 110155.

Lai, L.S.-H., Ng, T.-W., and Teng, L.S. (2018) Stratigraphic correlation of tuffaceous and psephitic strata in the Paliwan formation, southern Coastal Range of eastern Taiwan. *Bulletin of the Central Geological Survey, Ministry of Economic Affairs of Taiwan*, (31), 1-32.

Lai, L.S.-H., and Teng, L.S. (2016) Stratigraphy and structure of the Tai-Yuan basin, southern Coastal Range, eastern Taiwan. *Bulletin of the Central Geological Survey, Ministry of Economic Affairs of Taiwan*, (29), 45-76.

Lai, L.S.-H., and Teng, L.S. (2016) Geomorphologic and sedimentary features of the Chi-Shing-Tan gravel beach, Hualien, eastern Taiwan. *Journal of Geographical Research*, (64), 1-26.

Hsieh, M.-L., **Lai, L.S.-H.**, Lin, C.D.-J., and Shyu, J.B.H. (2012) Late Quaternary landscape evolution and genesis of the 2009 catastrophic landslide in the Hsiao-lin area, southwestern Taiwan. *Geomorphology*, 179, 225-239.

Hsieh, M.-L., **Lai, L.S.-H.**, Lin, C.D.-J., Hsu, C.-H., Chen, I.-W., Chen, H.-H., Kang, S.-J., Chou, C.-Y., and Shyu, J.B.H. (2012) Late Quaternary landscape evolution and genesis of the 2009 catastrophic landslide in the Hsiaolin area, southwestern Taiwan. *Western Pacific Earth Sciences*, 12(1), 129-146.

ACKNOWLEDGMENTS

It is a privilege to pursue my Ph.D. degree in such a collegial and conducive learning environment of the UO Earth Sciences department. This dissertation is resulted from collaborations within an international, multidisciplinary, cross-cultural team, and is impossible to be accomplished alone. I am grateful for this opportunity and tremendous support in all aspects from my advisor, mentors, collaborators, peers, and family.

This work would not possibly begin without my advisor, Becky Dorsey, who is literally the savior of my academic career. The journey began on May 30, 2015, when I just started fulfilling my military duty in Taiwan, and was about to make a life decision out of desperation – whether I should keep lingering in academia or drop it completely. A silver lining emerged when a glowing name caught my eyes on a poster abstract of the FACET workshop in Taipei, a name on papers about Taiwan's Coastal Range that I have read over numerous times. This summoned enormous courage from nowhere, and then I aggressively swooped in front of her to introduce myself during the workshop, using Chinglish that I can barely understand nowadays. I am still not sure how dare I did that, and why she somehow decided to take me as her student. Well, here we are now. Over the past 5 years, Becky acted as an ideal role model, and her patience, generosity, knowledge, diligence, and mentorship helped me to achieve my goals and become a better scientist. I appreciate her from my deep heart, and it is my honor to work with her.

My committee members, namely Josh Roering, Diego Melgar, and Mark Fonstad, have also been extremely helpful and provided much needed feedback during my Ph.D. development. I particularly want to thank Josh for introducing me to the field of process geomorphology and his guidance in my second comps project. This opened a whole new world and a new fantastic point of view that almost makes me sing Disney's Aladdin. It resulted one of the main chapters in this dissertation, inspired my long-term research idea, and led to my future post-doctoral position at UW.

In addition, I would like to express gratitude to my collaborators. Chreng-Shern Horng, Wen-Rong Chi, and Kai-Shuan Shea selflessly shared their knowledge and techniques out of their decades of experience in magneto-biostratigraphy studies of Taiwan, and offered hands-on training in rock paleomagnetism measurements, microfossil identifications, and data compilations. Noah Finnegan provided invaluable insights in fluvial geomorphology and support in academic writing. Jiun-Yee Yen's assistance in fieldworks, mental support, and building connections were beyond compare. Mae Marcaida and Lucas Mesalles are irreplaceable colleagues and friends, providing mutual support and real respect within I called "the Taiwan Coastal-Range trio."

I want to extend my appreciation to people who accompanied throughout this journey. It is always inspiring while talking science with brilliant minds in UO geomorphology group. The UO Earth Science office staffs, Marla Trox, Sandy Thoms, and Dave Stemple, helped significantly in my graduate progress. Having friendships with Kevin Gardner and Adrian Broz is simply priceless. Go Grand-Canyon survivors! My parents always made me feel supported and proud while pursuing my dream across the Pacific. Kristen Pinchun Yang, my life partner, keeps my body and soul together well.

This dissertation was supported by Government Scholarship for Study Abroad, Ministry of Education of Taiwan. I also appreciate other grants and funds offered by UO Earth Sciences, Geological Society of America, and National Science and Technology Council of Taiwan (erstwhile MOST) that made my research endeavors possible.

In dedication to whom I love and care about

TABLE OF CONTENTS

IV. COARSE SEDIMENT SUPPLY SETS THE SLOPE OF BEDROCK CHANNELS IN RAPIDLY UPLIFTING TERRAIN: FIELD AND TOPOGRAPHIC EVIDENCE FROM EASTERN TAIWAN 74

SUPPLEMENTAL FILES

ZIP FILE: CHAPTER II DATA SPREADSHEETS (Table S1–S5)

ZIP FILE: CHAPTER III DATA SPREADSHEETS (Supplementary Data 1–4)

ZIP FILE: CHAPTER IV DATA SPREADSHEETS (Table S1–S2)

LIST OF FIGURES

Figure Page

CHAPTER II

CHAPTER III

CHAPTER IV

LIST OF TABLES

Table Page

CHAPTER II

CHAPTER IV

CHAPTER I
INTRODUCTION

Sediments and topography form as net results of weathering, transport, and deposition. They have been jointly considered as carriers of natural information from eroding “sources” and depositional “sinks,” in response to temporal and spatial changes in tectonism, climate impacts, and biosphere activities. Scientists study source-to-sink systems to understand the driving mechanisms that control rock cycle and crustal evolution. However, to what degree we can decipher these signals from geologic and geomorphic records persists as a grand challenge. Significant uncertainties remain in our understanding of the magnitude, pace, and timescale required for different Earth’s processes, particularly in tectonically active regions, to influence our habitat and determine its evolution through time.

To seek breakthrough in this subject, I study sedimentary stratigraphy and landscape in the Coastal Range of eastern Taiwan – one of the most tectonically active mountain-building zones on Earth’s surface. The Taiwan orogen rises as a result of an ongoing arc-continent collision, where a volcanic island arc (Luzon Arc) is accreting to the Eurasian continental margin. This dissertation seeks to reconstruct the whole life of the Coastal Range, from a subsiding basin developed on top of island-arc crust that received sediments derived from early collisional mountain source, to a currently exhuming and eroding steep topography that has become a part of the growing mountain belt. This case study provides a rare opportunity to observe a complete cycle of crustal evolution from a “sink” to a “source”, and assess how surface processes respond to rock exhumation, erosion, deposition, and structural deformation at different time-space scales.

In chapter II, I studied deep-time syn-orogenic sedimentary stratigraphy in the southern Coastal Range, which allows me to explore the rates and mechanisms of crustal mixing and recycling, and associated basin development at this collisional plate suture. I first compile data from published and new field stratigraphic and sedimentologic measurements, rock paleomagnetism, and marine microfossils (planktic foraminifera and calcareous nanoplanktons) to establish a high-fidelity stratigraphic framework in this area. This framework provides robust stratal age constraints and permits reconstruction of basin geometry, depositional system, and sediment routing history. Combined evidence solves the long-debated genesis of the Lichi Mélange, a chaotic mixture of rocks from both colliding plates, and associated sedimentation in a retro-foredeep basin in response to episodes of accelerated source exhumation and tectonic reorganization.

In chapter III, I combined high-fidelity chronostratigraphic framework of southern Coastal Range established in chapter II with new data of field mapping and magneto-biostratigraphy in northern Coastal Range to detect dynamic vertical crustal motions that are required to produce accommodation space for sediment accumulation in the past and then invert the basement rock to modern surface. Foraminifera-based paleo water depth reconstruction and backstripping analysis are used to model the history of subsidence of island arc basement, detect the timing of transition to structural inversion, and estimate the rate of ongoing rapid uplift needed to exhume the basement rock to modern elevation of the Coastal Range.

In chapter IV, I focus on evolving landscape in the modern Coastal Range to investigate interactions between active tectonics and surface processes. I utilized theoretical tools in quantitative geomorphology with physical parameters constrained from digital elevation models and field observations (e.g., channel morphology, bedrock strength, characteristics of river sediments). Published data for independently measured uplift-rate field and climate forcing (e.g., annual precipitation) are compiled for a comprehensive assessment of the primary control(s) on patterns in fluvial landscape features such as hillslope gradient and channel slope. The results provide novel insights into how a mountainous landform reacts to rapid rock exhumation and transient surfaces processes related to sediment production and transport.

Chapters II and III of this dissertation are co-authored with Rebecca J. Dorsey, Chorng-Shern Horng, Wen-Rong Chi, Kai-Shaun Shea, and Jiun-Yee Yen, and were published in *Sedimentary Geology* and *Communications Earth & Environment*. Chapter IV is co-authored with Joshua J. Roering, Noah J. Finnegan, Rebecca J. Dorsey, and Jiun-Yee Yen, and was published in *Earth Surface Processes and Landforms*.

CHAPTER II

POLYGENETIC MÉLANGE IN THE RETROWEDGE FOREDEEP OF AN ACTIVE ARC-CONTINENT COLLISION, COASTAL RANGE OF EASTERN TAIWAN

This chapter has been published as Lai, L. S.-H., Dorsey, R. J., Horng, C.-S., Chi, W.-R., Shea, K.-S., and Yen, J.-Y. (2021) Polygenetic mélange in the retrowedge foredeep of an active arc-continent collision, Coastal Range of eastern Taiwan. *Sedimentary Geology*, 418, 105901. I, Rebecca. J. Dorsey, and Jiun-Yee Yen conducted field geological surveys and sedimentologic and stratigraphic measurements. Chorng-Shern Horng and I are responsible for sampling and experimental works for paleomagnetism study. Wen-Rong Chi, Kai-Shuan Shea, and I performed microfossil identifications and biostratigraphic analysis. I am the lead author on the paper, which involved data synthesis and analysis, preparation of figures and tables, and writing the entire manuscript. All other coauthors assisted with data interpretation and editorial feedback.

1. Introduction

“Mélange” in geology is a non-genetic lithological term defined as a mappable and chaotic rock unit consisting of extra-formational (exotic) blocks embedded in highly mixed and disrupted matrix (i.e., block-in-matrix fabrics) (Cowan, 1985; Greenly, 1919; Hsü, 1968). Mélanges form by large-scale stratal disruption via tectonic, diapiric, or sedimentary processes, or a combination of these processes (i.e., polygenetic) (Raymond, 1984, 2019). They provide insights into the kinematics of crustal deformation and rock mixing at active plate margins, and therefore are useful for reconstructing continental growth over deep time in tectonically active settings (Dilek et al., 2012). Processes of mélange formation at the continent-ocean interface of arc-continent collision zones are particularly controversial and poorly understood due to the relative paucity of well-preserved mélange records from ancient arc-continent collision zones globally (Festa et al., 2010), despite a few recent advances in a Neoarchean arc-continent collision system of the North China Craton (e.g., Kusky et al., 2020; Wang et al., 2019). The low preservation potential of mélanges at suture zones likely reflects the short lifetime (often

~5–15 Myr) of arc-continent collision systems and rapid crustal erosion that occurs after the forearc crust is accreted in the retrowedge of arc-continent collision suture zones (Draut & Clift, 2013).

To address these challenges, many studies have focused on active arc-continent collision orogens where young or active mélange generation can be directly observed (e.g., Harris & Audley-Charles, 1987; Huang et al., 2000). However, the genesis of these mélange units remains debated in part due to inconsistent definitions of "mélange" that lie at the center of controversies over tectonic models in many orogenic belts (Festa et al., 2012; Raymond, 2019). Growing evidence suggests that microscopic to outcrop-scale internal shears and block-in-matrix fabrics cannot be used as definitive criteria to distinguish mélange formation by faulting, diapirism, or gravitational processes (Ogata et al., 2012; Raymond, 1984; Wakabayashi, 2019), because mechanical styles of stratal disruption and brecciation depend on local physical properties (e.g., permeability, strength), which in turn depend on degree of consolidation, fluid content, pressure, temperature, and rate of structural loading and deposition (Festa et al., 2019; Michiguchi et al., 2011; Ogata et al., 2014). In addition, recycling and incorporation of juvenile crustal materials via episodic tectonic and/or sedimentary processes commonly overprint older features at the boundary between advancing orogenic fronts and adjacent sedimentary basins (Festa et al., 2016; Moore et al., 2019; Ogata, Festa, Pini, & Alonso, 2019). As such, interdisciplinary constraints from geologic mapping, stratigraphic analysis, kinematic study, etc. are required to advance our understanding of mélange formation in arc-continent collision zones.

The Lichi Mélange in the Coastal Range of eastern Taiwan (Figure 1) is widely considered a classic example of mélange formed in an arc-continent collision suture, but its origin is poorly understood and thus still a matter of debate (Figure 2). Prior studies have documented evidence in support of both sedimentologic (e.g., Liou et al., 1977; Page & Suppe, 1981) and tectonic (e.g., Chang et al., 2000; Chang et al., 2001; Chen, 1997b) processes of rock mixing, suggesting a possible polygenetic origin for the Lichi Mélange. However, the question of whether tectonic shearing or sedimentary

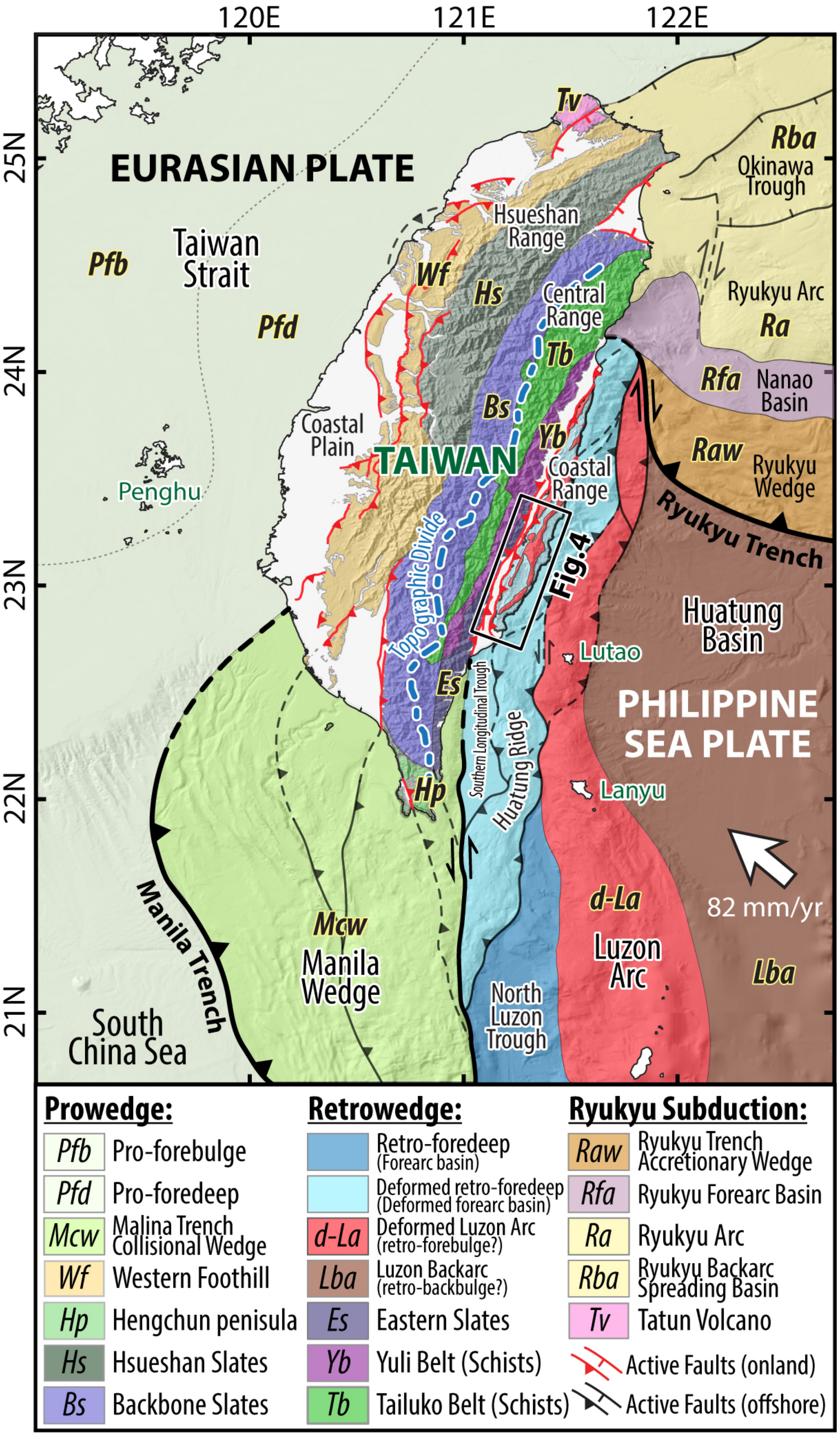

Figure 1. Geological setting. Plate configuration and tectonic domains at Taiwan arc-continent collision, synthesized and modified from previous studies (Chen et al., 2019; Huang et al., 2018; Lin et al., 2003; Malavieille et al., 2021).

(olistostromal) emplacement was the primary mode of shearing to form the Lichi Mélange remains unresolved. Such controversy is related to alternate models for basin evolution recorded by Plio-Pleistocene sedimentary rocks in the Coastal Range. According to the prevailing hypothesis (Figure 2A), the Coastal Range is underlain by relatively little-deformed volcanic islands and adjacent forearc, intra-arc, and backarc basins (e.g., Chen, 1997a; Huang et al., 1995; Song & Lo, 2002; Teng, 1987), and the Lichi Mélange formed by tectonic shearing in a mega-thrust belt during large-scale forearc shortening (e.g., Chang et al., 2001; Chen, 1997b; Huang et al., 2018; Huang et al., 2008). Other studies suggest an olistostromal origin for the Lichi Mélange and consider the main body of the mélange to be part of a genetically related sedimentary sequence (e.g., Barrier & Muller, 1984; Liou et al., 1977; Page & Suppe, 1981) that filled a syn-orogenic flysch basin and was later tectonically inverted (e.g., Dorsey, 1988; Lundberg & Dorsey, 1988) (Figure 2B). The second hypothesis postulates that the basin is deformed by large thrust faults due to strong crustal shortening, and the modern topography of the Coastal Range reflects the areal distribution of young structures and antiformal culminations rather than intact volcanic islands (Dorsey, 1992; Thomas et al., 2014).

The origin of the Lichi Mélange is likely also related to the formation of the late-Miocene Yuli Belt, an exhumed greenschist-blueschist facies metamorphosed mélange in the Central Range of Taiwan, located directly west of the Coastal Range (Figure 1). Recent studies of the Yuli Belt propose numerous tectonic models to explain mélange formation and rapid exhumation at the collisional plate suture (e.g., Chen, Chung, et al., 2017; Conand et al., 2020). Thus the Lichi Mélange sits at the center of ongoing debate over processes of mélange formation during accretion of oceanic arc crust, mechanisms of tectonic recycling in arc-continent collision suture zones, and processes that drive growth of continental lithosphere through time (Clift & Vannucchi, 2004). High-resolution age constraints, geologic mapping, process-based sedimentology, and stratigraphic studies are therefore needed to resolve long-standing uncertainty and debate over the origins of the Lichi Mélange.

For this study we conducted detailed geologic mapping, lithofacies analysis, measured sections, magneto-biostratigraphy, paleoslope and paleocurrent analyses to test hypotheses for sedimentary versus tectonic origins of the Lichi Mélange. The results are systematically compiled below and applied to interpret the basin-filling history, reconstruct basin geometry, and evaluate the role of the Lichi Mélange in the evolution of the Taiwan collisional orogen.

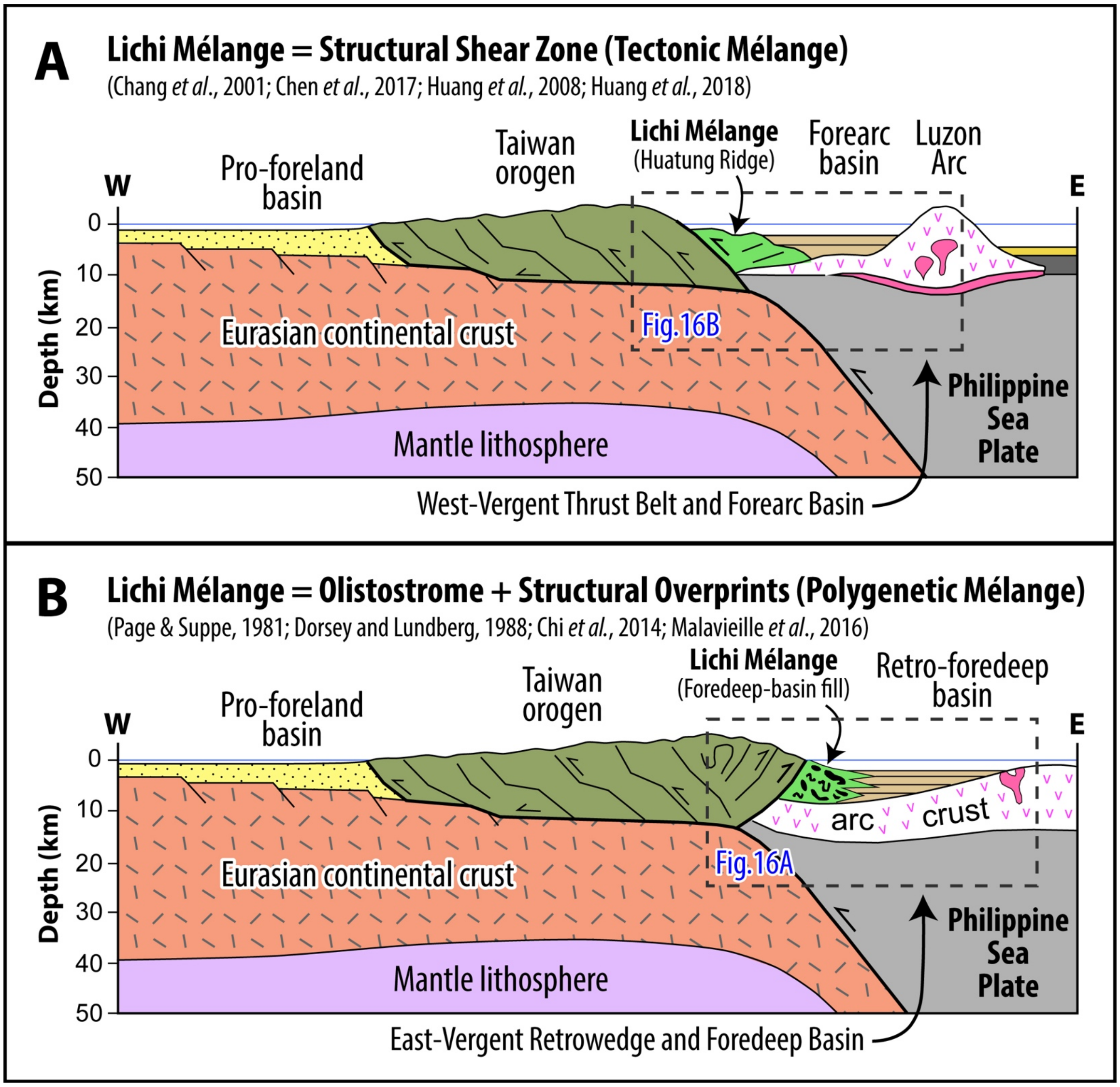

Figure 2. Comparison of published models for the origin and tectonic controls on formation of the Lichi Mélange. Figures are identical in the western half (central Taiwan orogen to pro-foreland basin); all differences are expressed in the eastern half, at the complex interface between Eurasian and Philippine Sea plates (dashed box). (A) Plate configuration and tectonic domains at Taiwan arc-continent collision, synthesized and modified from Huang et al. (2018). (B) Lichi Mélange originated as a sequence of marine mega-slumps (olistostromes) formed in a syn-orogenic foredeep basin at the east margin of the east-vergent retrowedge zone of the Taiwan orogen, modified from Malavieille et al. (2016).

2. Geological background

The island of Taiwan is an active arc-continent collisional orogen produced by oblique convergence between the Eurasian continental margin and Luzon Arc on the Philippine Sea plate (Figure 1) (Suppe, 1984; Yu et al., 1997). The orogen is characterized by a low gradient west-vergent prowedge thrust belt in the west and a steep east-vergent retrowedge in the east, separated by a high drainage divide that parallels the major structural fabrics (Fisher et al., 2007). The major morphotectonic units of Taiwan include: (1) Pliocene to modern pro-foreland basin and west-vergent thrust belt in the western Taiwan Strait, Coastal Plain, and Western Foothills; (2) deformed low-grade Eocene to Miocene meta-sandstone and argillite in the Hsueshan Range and western Central Range; (3) older metamorphic continental basement in the Tailuko Belt; (4) greenschist-blueschist facies mafic to ultramafic metamorphic rocks and associated meta-sediments in the eastern Central Range (Yuli Belt and Eastern Slates); and (5) accreted volcanic rocks of the Luzon Arc and overlying deformed sequence of unmetamorphosed flysch deposits in the Coastal Range (Chen, Chung, et al., 2017; Teng, 1990). Estimates for the age of onset of collisional mountain building in Taiwan vary from about 6.5 to 12.5 Ma based on stratigraphic evidence for flexural loading in the pro-foreland basin and earliest introduction of continental material into the trench (e.g., Chen et al., 2019; Lin et al., 2003; Tensi et al., 2006). Despite these differences, it is widely agreed that major orogenic uplift, crustal thickening and tectonic exhumation began at ca. 5 Ma. Pulses of accelerated exhumation occurred at ca. 1.5–2.0 Ma and 0.5 Ma as indicated by abrupt changes in sedimentation rate and sandstone petrography in syn-orogenic basins (Chen et al., 2019; Dorsey, 1988; Nagel et al., 2014; Teng, 1990), timing of pressure-temperature dependent metamorphism (Beyssac et al., 2008; Keyser et al., 2016; Sandmann et al., 2015), and bedrock cooling history based on thermochronologic studies (Hsu et al., 2016; Lee et al., 2015).

Previous studies of the Coastal Range have applied conflicting definitions of lithostratigraphic units (e.g., Chen, 2009; Horng & Shea, 1996; Huang et al., 2018; Lai, Ng, et al., 2018), regional structures (e.g., Chen, Huang, et al., 2015; Chen, 2009; Lai & Teng, 2016), and basin style and geometry (e.g., Chen et al., 2019; Huang et al., 1995; Lundberg & Dorsey, 1988; Teng, 1987). In addition, the term “mélange” has been defined differently in published analyses and geologic maps (e.g., Barrier & Muller, 1984; Chang et al., 2000; Chen, Huang, et al., 2017; Chen, 1997b; Hsu, 1956; Huang et al., 2018; Page & Suppe, 1981), resulting in ambiguous tectonic interpretations for eastern Taiwan. In the following sections, we present a standardized lithostratigraphic framework and rock classification scheme for coherent (non-mélange) strata in the Coastal Range based on a synthesis of classic and recent published studies. We then summarize existing knowledge of regional structures in the southern Coastal Range, current models for the Lichi Mélange and basin evolution, and provide standard definitions and stratigraphic nomenclature to be used in this paper.

2.1. Non-mélange strata and structures of the Coastal Range

Miocene rocks representing arc and forearc crust in the Coastal Range are unconformably overlain by a thick (4–7 km) section of PlioPleistocene synorogenic marine flysch and conglomerate (Figure 3). The Tuluanshan Formation is defined as all volcanic and volcaniclastic rocks beneath the unconformity, including the Chimei Igneous Complex (~15–9 Ma), Shihmen Volcanic Breccia, and older Shihtiping Tuff (~15–6 Ma) (Chen, 1997a; Lai et al., 2017; Song & Lo, 2002). A ~2 Myr time gap at the basal unconformity is characterized by an abrupt change in depositional age, cementation, clay mineralogy, and truncated normal faults that are restricted to the Tuluanshan Formation beneath the unconformity (Barrier & Angelier, 1986; Dorsey, 1992). Field and stratigraphic analysis for this study shows that the age gap is partly occupied by an eastward-younging thin discontinuous sequence comprised of the Biehchi Epiclastic Unit (~4 Ma), Kangkou Limestone (~5–3 Ma), and younger units of the Shihtiping Tuff (~4.2 Ma) (see details in Section 6.1).

The synorogenic Plio-Pleistocene succession of marine flysch and conglomerate in the Coastal Range records unroofing of metamorphic rocks in the Central Range orogen as documented with changes in abundance of metamorphic lithic fragments (e.g., Chen et al., 2019; Dorsey, 1985; Teng, 1979), illite crystallinity (Buchovecky & Lundberg, 1988; Dorsey et al., 1988; Yao et al., 1988), and reset detrital thermochronometers (Kirstein et al., 2014; Kirstein et al., 2010). Earlier stratigraphic studies named these deposits the Takangkou and Chimei formations (Hsu, 1956), or collectively the Takangkou Formation (e.g., Chang et al., 2000; Chen, Huang, et al., 2015; Huang et al., 2008; Page & Suppe, 1981). Definitional problems and inconsistencies led to a newer nomenclature that subdivides the section into the Fanshuliao and Paliwan formations (Chen, 2009; Teng, 1987). The Fanshuliao Formation contains thick slumped and chaotic horizons in mudstone and fine-grained turbidites, with sand composed of volcanic lithic fragments, plagioclase feldspar, quartz sand, and carbonate bioclasts (Teng, 1980; Teng et al., 2002). The Paliwan Formation consists of thin- to thick- bedded turbidites and submarine conglomerates with abundant low-grade metamorphic lithic fragments and only minor volcanic clasts (Chen, 1997a; Teng, 1982). The base of a widespread pebbly mudstone layer (Pm3) defines the contact between the Fanshuliao and Paliwan formations in the southern Coastal Range (Chen, 2009; Wang & Chen, 1993). Recent geologic mapping and stratigraphic analysis permits further subdivision based on recognition of multiple widespread marker beds of pebbly mudstone and tuffaceous turbidites (Figure 3) (Lai, Ng, et al., 2018; Lai & Teng, 2016).

The structure of the Coastal Range is dominated by large-displacement imbricate west-vergent thrust faults and associated regional-scale folds (Wang & Chen, 1993). Rapid uplift rates (e.g., Chen et al., 2020; Hsieh & Rau, 2009), kinematic analyses (Barrier & Angelier, 1986; Lin et al., 1999), and modern seismicity (Angelier et al., 2000; Lee et al., 2006) provide evidence for ongoing active deformation and crustal thickening in the Coastal Range. Of the total Philippine Sea – Eurasian plate convergence rate (~82–90 mm yr^{-1}), roughly 60 mm yr^{-1} shortening is absorbed by convergence in the Coastal Range and offshore structures to the east (~60 km) in the past ~1 Myr (Hsieh et al., 2020; Reed et al., 1992; Tsai et al., 2015).

In the southern Coastal Range, several west-vergent thrust faults and three large plunging folds control the distribution of map units (Figure 4) (Hsu, 1956; Lai & Teng, 2016; Wang & Chen, 1993). Among these structures, only the Longitudinal Valley fault is considered to be currently active (Angelier et al., 2000; Lee et al., 2006; Shyu et al., 2008). Most previous studies map the southern Tuluanshan fault along the drainage divide between the Taiyuan and Powhua regions (Chang et al., 2000; Chen, Huang, et al., 2017; Chen, 1997b; Wang & Chen, 1993), but dipping depositional contacts and continuous stratigraphy suggest the absence of a major fault in that area

(Barrier & Muller, 1984; Li, 1984; Lin et al., 2008). Field mapping for this study confirms the depositional nature of contacts where the southern Tuluanshan fault was originally proposed. West of there we have traced a ~100–300 m wide belt of 5–10 m wide fault zones with fault gouge and brittle shears aligned with the northern Tuluanshan fault, which we interpret as the southern Tuluanshan fault where it cuts the Chungye river (CYC) and the Mukeng river (MKC) sections (see details in Section 5).

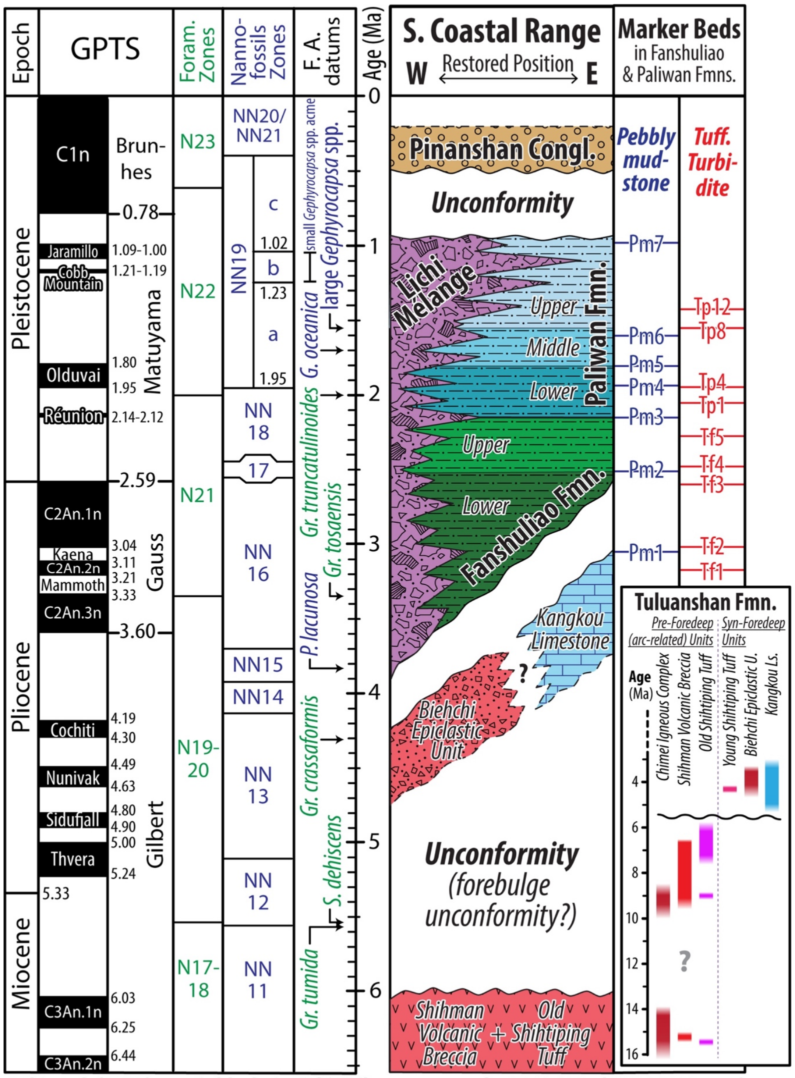

*Chi et al. (1981): exotic blocks in Lichi Mélange are aged ~18-5.6 Ma (NN3-NN11 zone)

Figure 3. Stratigraphic framework of southern Coastal Range, modified from Dorsey (1992); Lai, Ng, et al. (2018); Lai and Teng (2016). The geomagnetic polarity timescale (GPTS) and microfossils' first appearance (F.A.) datums of Indo-Pacific region are summarized (Anthonissen & Ogg, 2012; Backman et al., 2012; Chuang et al., 2018; Ogg, 2012). The lower right inset shows ages compiled for the entire Tuluanshan Formation (Chen, 2009; Dorsey, 1992; Huang & Yuan, 1994; Huang et al., 1988; Lai, Chu, et al., 2018).

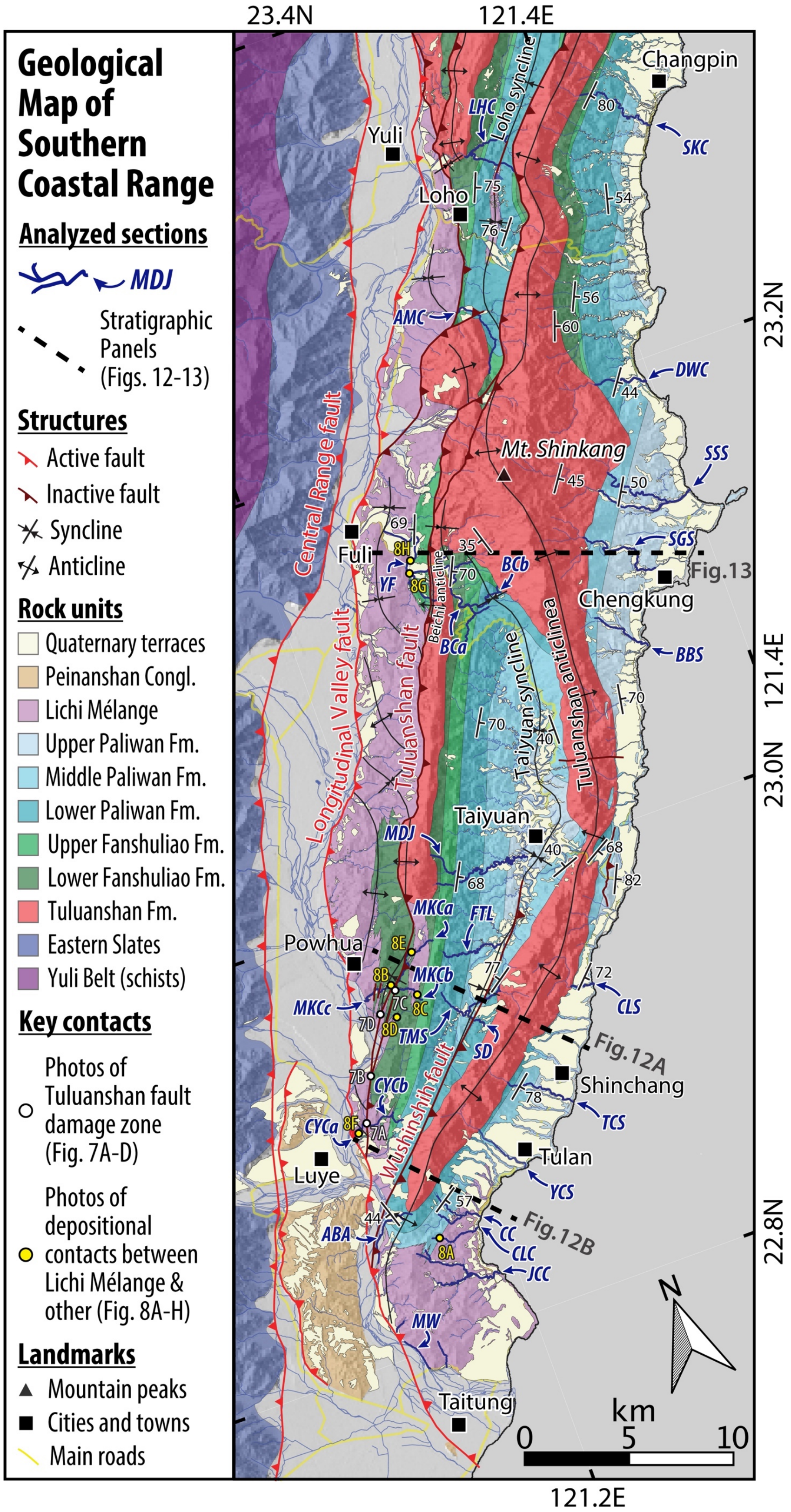

Figure 4. Geological map of southern Coastal Range, modified from Lai, Ng, et al. (2018); Lai and Teng (2016); Wang and Chen (1993). See detail maps in Figures S1-S9.

2.2. Lichi Mélange

The Lichi Mélange, originally named “Raikoka Formation” or “Lichi Formation” (Hsu, 1956; Ooe, 1939), *“consists mainly of poorly stratified mudstone in which some large or small rock fragments or blocks of hard greyish sandstone, gabbro, serpentin(ite), and a little slate are present”* (Hsu, 1956). The mélange contains pervasive shear fabrics in poorly consolidated scaly mudstone and block-in-matrix textures (Chang et al., 2000; Chen, Huang, et al., 2017; Chen, 1997b; Huang et al., 2018). Other block lithologies include andesite, volcaniclastic rock, limestone, ophiolite-bearing sedimentary rocks, amphibolite, low-grade meta-sandstone, and flysch blocks similar to the Fanshuliao and Paliwan formations (Liou et al., 1977; Page & Suppe, 1981; Sung, 1991). Clay minerals in the matrix are illite with relatively abundant kaolinite, in contrast to illite- and chlorite-rich Fanshuliao and Paliwan formations, suggesting different sediment source rocks, routing systems, weathering conditions, or mixing processes (Lin & Chen, 1986). Depositional contacts and shear zones linked to soft-sediment deformation and post-depositional thrusting suggest a complex mixture of tectonic and sedimentary rock-mixing products (e.g., Chang et al., 2000; Page & Suppe, 1981).

Despite previously published evidence for both tectonic and sedimentary origins for the Lichi Mélange, two alternate hypotheses describe the primary mode of rock mixing as either tectonic or sedimentologic (Chen, 1991; Huang et al., 2018; Teng, 1981) (Figure 2). The currently prevailing hypothesis postulates that the Lichi Mélange formed by shearing of older forearc-basin sediments in a post-depositional megathrust zone (Chang et al., 2000; Chang et al., 2001; Chen, Huang, et al., 2017; Huang et al., 2018; Huang et al., 2008; Huang et al., 2000), consistent with earlier models for deformation in a subduction-accretion complex (Figure 2A) (e.g., Biq, 1977; Chen, 1991, 1997b; Hsü, 1988; Teng, 1981). In this framework, zones with varying degree of stratal disruption and rock mixing α-δ scheme of Raymond (1984) are all mapped as Lichi Mélange (Chang et al., 2000; Chang et al., 2001; Chen, Huang, et al., 2017; Huang et al., 2008), and these mélange zones are defined as being bounded by discrete brittle thrust faults (Chen, 1997b; Wang & Chen, 1993). Thick segments of relatively coherent strata (α and β) are thus interpreted to be fault-bounded slivers of originally coherent sedimentary rocks, and exotic blocks (ophiolitic, volcanic, volcaniclastic rock types) are considered to be tectonically emplaced structural fault slices (Huang et al., 2018; Huang et al., 2008). Field observations reveal brittle scaly foliation and shear fabrics near the west-vergent Longitudinal Valley fault and Tuluanshan fault, particularly in the Powhua and Luye area (Chang et al., 2000; Chang et al., 2001; Chen, 1997b). Foraminifera biostratigraphic data are proposed to support a depositional age of ~3.35 to 8.5 Ma for structurally disturbed strata in the Lichi Mélange, generally older than nearby exposures of the Fanshuliao and Paliwan formations (~ 4–1 Ma) (Chen, Huang, et al., 2017; Huang et al., 2018; Huang et al., 2008). Unresolved challenges to this hypothesis include: (1) definition of mélange units that are based on genetic interpretations, making it difficult to assess the potential role of gravity-driven processes; (2) lack of consistent criteria for identifying tectonic faults; (3) contacts that were reported as depositional in original studies (Chang et al., 2000; Chang et al., 2001) or later work (Lin et al., 2008) remain unexplained; and (4) interpreted depositional ages of mélange matrix that are inconsistent with prior studies of calcareous nannoplankton biostratigraphy (see below).

A second group of studies interprets the Lichi Mélange as a complex of submarine-slide deposits derived from the steep fault-bounded western margin of the basin (e.g., Barrier & Muller, 1984; Ernst, 1977; Hsu, 1956; Page & Suppe, 1981; Wang, 1976). In this hypothesis, submarine slide blocks (olistoliths) are interbedded with and pass laterally into flysch facies of the Fanshuliao and Paliwan formations, and were later overprinted (tectonically reworked) by post-depositional brittle tectonic faults. This multi-stage hypothesis is supported by analogue modeling (e.g., Malavieille et al., 2021; Malavieille et al., 2016) and seismic reflection studies of offshore chaotic bodies in the North Luzon Trough that are proposed as a modern equivalent of the Lichi Mélange (e.g., Chi et al., 2014; Huang et al., 1997). Within this framework, the Lichi Mélange, or “Lichi Formation” (Hsu, 1956), was originally defined as chaotic disrupted broken formation and mixed block-in-matrix rocks (mélange) with locally interbedded coherent layers of conglomerate, pebbly mudstone, slump beds, mudstone, and flysch (Liou et al., 1977). Few undisputed depositional contacts have been reported between mélange and coherent strata associated with soft-sediment stretching, bending, folding, or fragmentation of blocks (Li, 1984; Page & Suppe, 1981). Early studies showed that calcareous nannoplankton assemblages in the Lichi Mélange matrix are similar to those of nearby

Plio-Pleistocene Fanshuliao and Paliwan formations (< ~4 Ma), and that exotic sedimentary blocks yield older fossils (~18 to 5.6 Ma) consistent with an olistostromal interpretation (Barrier & Muller, 1984; Chi et al., 1981; Li, 1984).

However, the sedimentary hypothesis also faces challenges: (1) coherent portions of the "Lichi Formation" are similar to the Fanshuliao and Paliwan formations, creating ambiguities in the definition of stratigraphic units and boundaries; (2) few depositional contacts have been reported in prior published studies; (3) distal olistostromal facies that are predicted by this hypothesis have not previously been identified in nearby Fanshuliao and Paliwan formations to the east (Chen, 1991; Teng, 1981); and (4) because Miocene sedimentary rocks were not recognized in the eastern part of the Central Range directly to the west, some workers argued there is no source area to supply Miocene-age sedimentary slide blocks and olistoliths (Huang et al., 2018).

Taken together, inconsistent stratigraphic definitions and age interpretations have led to major disagreements over the distribution, contact relationships, and origins of the Lichi Mélange. Recent studies of mélange-like marker beds (pebbly mudstone) in the Fanshuliao and Paliwan formations (Lai, Ng, et al., 2018; Lai & Teng, 2016), and a late Miocene depositional age for metasedimentary rocks in the eastern part of the Central Range (e.g., Chen, Chung, et al., 2017; Mesalles et al., 2020), have not yet been considered in this debate. These new findings reveal a need to re-evaluate critical field relationships in the Lichi Mélange, refine its definition, and reassess its stratigraphic context in the southern Coastal Range.

2.3. Nomenclature and definitions used in this paper

In this study, we adopt modern nongenetic terms of "mélange" and "broken formation" to describe mappable (at 1:25,000 or smaller scale) chaotic rocks that commonly have "pervasively deformed and fragmented matrix of finer-grained material", with and without inclusion of extra-formational blocks respectively (Hsü, 1968; Raymond, 1984; Silver & Beutner, 1980), which represent products of different forming mechanisms – rock-mixing plus stratal disruption versus only stratal disruption (Festa et al., 2012; Harris et al., 1998). The terms "olistostrome" and "olistolith", traditionally equivalent to "sedimentary mélange" and "slide blocks" following classic principles of stratigraphic superposition (Abbate et al., 1970), are applied to name sedimentary lithofacies in the Lichi Mélange (Table 1). The term "polygenetic mélange" is used for a mélange body formed through a multistage evolution that involves two or more styles of rock-mixing mechanisms (sedimentary, tectonic, or diapiric), and its primary fabrics have been overprinted (reworked) by later processes (Berkland et al., 1972; Festa et al., 2020; Ogata, Festa, Pini, Pogačnik, et al., 2019).

For the stratigraphic framework, this paper adopts an updated descriptive nomenclature and depositional ages for lithostratigraphic units in the Coastal Range, summarized in Figure 3. The Tuluanshan Formation (Chen, 1997a; Song & Lo, 2002) is capped by a regional unconformity (Dorsey, 1992) and is overlain by 4–7 km of marine flysch of the Fanshuliao and Paliwan formations (Chen, 2009; Lai, Ng, et al., 2018; Lai & Teng, 2016; Teng, 1987). Due to the difficulty of defining the contact between the Lichi Mélange and flysch units, we classify the products of sedimentary processes (i.e., lithofacies) independent of any existing lithostratigraphic classification scheme (Table 1, see details in Section 4). The Lichi Mélange in this study is defined narrowly as rocks (facies X3, olistostrome) characterized by poorly developed stratification that is broadly parallel to regional bedding (equivalent to the "colour bands" in Page and Suppe (1981)) and pervasively "sheared" matrix with extra-formational blocks (i.e., scaly block-in-matrix fabric). Chaotic sedimentary rocks without internal shear fabric or foliation that record soft-sediment deformation and sediment gravity flows (i.e., pebbly mudstones (facies X1), slump beds (facies X2), and other coherent strata (facies F1–F4, Vo)) are included in the Fanshuliao and Paliwan formations. For outsized (>10 m to a few km diameter) fractured blocks regardless of lithology that appear in all sedimentary units, we apply the neutral term "olistolith" (facies X4).

The term "exotic block" is reserved for blocks with lithologies whose source is not present in the surrounding sedimentary units (e.g., andesite, volcaniclastic sandstone and conglomerate, limestone), and which are different from any lithology found in country rocks of the Coastal Range (e.g., well-lithified quartz-rich sandstone without orogen-derived lithic fragments, ophiolitic rocks (gabbro, serpentinite, granodiorite, etc.), metasandstone) (Liou et al., 1977; Page & Suppe, 1981), in contrast to some blocks

Table 1. Lithofacies of sedimentary rocks in the southern Coastal Range. See photos in Figures 5 and 6.

Facies Name	Summary Description	Interpreted Processes	Strat. Unit	Mélange Fabric†
F1: Mudstone	Dark gray to black mudstone (clay-silt mixture) with rare very thin beds of siltstone to fine-grained sst. Internally structureless to weakly laminated, commonly includes slump zones ~ 0.5 to 5 m thick. Clay is orogen-derived.	Suspension settling	Fsl, Plw	α
F2: Turbidites	Sandstone and mudstone in laterally continuous beds. Sst beds ~ 0.01 to 0.5 m thick, normally graded with Bouma sequence, variable sand:mud ratio. Sandstone composition dominantly orogen-derived lithic fragments.	Low-density turbidity current	Fsl, Plw	α
F3: Thick-bedded sandstone and gritstone	Normally graded massive to laminated sandstone beds ~ 0.5 to 5 m thick. Granule conglomerate (grit) and pebbly sandstone in lower parts of thicker beds. Large flame and dish structures common near base. Sandstone and clast composition dominated by orogen-derived lithic fragments.	High-density turbidity current	Fsl, Plw	α
F4: Conglomerate	Clast-supported conglomerate with pebble to boulder sized clasts, indistinct normal or inverse to normal grading near base. Beds ~1 to 5 m thick. Bases of beds are planar to channelized. Clasts primarily well-rounded low-grade metasandstone and subangular to rounded andesite with trace amounts of mafic rocks (e.g., basalt, gabbro).	Non-cohesive debris flow (grain flow)	Fsl, Plw	α
X1: Pebbly mudstone	Matrix-supported, structureless pebbly mudstone in ~ 0.2 to > 300 m thick beds. Bimodal grain-size (mud and gravel), minor sand. Pebbleto boulder-size clasts are angular to subangular andesite & limestone, and subrounded to well-rounded metasandstone and mafic to ultramafic volcanic rocks, unoriented to locally imbricated. Clast-rich and clast-poor zones alternate within single beds. Large flame structures common at base of beds.	Cohesive debris flow or slurry flow	Fsl, Plw	α?
X2: Slump bed	Ductilely deformed, convoluted and distorted sedimentary intervals ~ 0.3 to 120 m thick. Local fragmented and dismembered sandstone present in locally sheared matrix (i.e., broken formation) with common structures like pinch-and-swell, ductile to quasi-brittle boudinage, and extensional fractures. Poorly-to-well developed S-C fabrics and scaly foliation observed in less competent fine-grained layers. Protolith is mainly turbidites (F2) with abundant soft-sediment deformation such as micro-faulting and asymmetrically inclined recumbent folds with open to s-shaped fold profile.	Submarine slope failure, slides, and slumps, with sedimentary (gravitational) shearing	Fsl, Plw	α, β, γ

Table 1 continued.

Facies Name	Summary Description	Interpreted Processes	Strat. Unit	Mélange Fabric†
X3: Olistostrome	Laterally extensive zones of chaotic, matrix-supported, unsorted to weakly bedded sedimentary mélange ~ 30 to >500 m thick. Dismembered sedimentary rocks (similar to facies F2) with extra-formational clasts in pervasively deformed fine-grained matrix. S-C fabrics, scaly foliation, and mildly developed slickensides commonly occur in ~1 to 10 meters thick (wide) sheared horizons near the basal contacts, with common structures like pinch-and-swell, ductile to quasi-brittle boudinage, and extensional fractures. Tabular to elongated clasts are aligned parallel to the scaly fabric. Bimodal grain-size (mud and gravel), minor sand. Matrix dominantly gray to moss green clays ("color bands"). Larger clasts display variable rounding. Locally brecciated matrix close to basal shear horizons and cross-cutting faults. Diverse clast compositions: andesite, volcaniclastic sandstone and conglomerate, well-lithified quartz-rich sandstone without orogen-derived lithic fragments, ophiolitic rocks (gabbro, serpentinite, granodiorite, etc.), limestone, metasandstone.	Blocky flow and cohesive debris flow with sedimentary brecciation, shearing, and rock-mixing	Lc	δ
X4: Olistolith	Decimeter- to km-scale single allochthonous block in slumped mudstone. Compositions include andesite, volcaniclastic sandstone and conglomerate, ophiolitic rocks (gabbro, serpentinite, granodiorite, etc.), limestone, and quartz-rich sandstone to low-grade metasandstone. Blocks commonly contain internal brittle shears and fractures with local diapiric mudstone intrusions.	Submarine rock slide or avalanche	Fsl, Plw, Lc	α?, δ?
Vo: Tuffaceous turbidites	White normally graded, planar to ripple-laminated tuffaceous sandstone, with Bouma sequence, in beds ~ 0.01 to 7 m thick. Grain size is silt to very-coarse sand with rare small pebbles near base. Grains are mostly fresh felspar with locally abundant dark minerals (biotite, pyroxene, hornblende) and volcanic lithic fragments. Minor glass shards at tops of some beds.	Syn-eruptive turbidity current	Fsl, Plw	α

†: We apply the 4-degree (α-δ) classification of stratal disruption (Raymond, 1984), also used in previous studies of the Lichi Mélange (e.g., Chang et al., 2000; Chang et al., 2001). Facies abbreviations: F = flysch; X = mélange; Vo = volcanic origin; sst = sandstone. Stratigraphic units: Fsl = Fanshuliao Formation; Plw = Paliwan Formation; Lc = Lichi Mélange.

originated from nearby intraformational sources such as turbidite facies F2 (so called "native blocks").

It should be noted that the definition of Lichi Mélange as a lithostratigraphic unit in this study is used in a manner of convenience for assessing the geologic map pattern and observed contact relationships, thus serving as the basis for additional analyses, which is different from the classic usage of the lithological term "mélange." Some chaotic facies in the Fanshuliao and Paliwan formations such as pebbly mudstone (X1) and part of slump bed (X2) can be also considered as "sedimentary mélange (olistostrome)" as conventionally defined (Ogata, Festa, Pini, Pogačnik, et al., 2019) or "small-scale mélanges and broken formations" if they are not mappable at 1:25,000 or smaller scale (e.g., Codegone et al., 2012).

3. Methods

Detailed geological mapping for this study targeted the Lichi Mélange and associated deposits exposed in road cuts and riverbanks of the southern Coastal Range (Figure 4). Lithostratigraphic descriptions were executed in selected river sections along three geological transects: (1) Powhua-Shinchang; (2) Luye-Tulan; and (3) FuliChengkung transects (Figures S1-S14). Among these sections, we compiled existing data for microfossil biostratigraphy and magnetostratigraphy from previous studies (Barrier & Muller, 1984; Chang, 1967, 1969; Chen, Huang, et al., 2015; Chen, Huang, et al., 2017; Chen, 1988b; Horng & Shea, 1996; Huang & Yuan, 1994) and manually georeferenced their sample localities on maps in order to project them to our measured sections (Figures S3–S9). We also include digitized unpublished calcareous nannoplankton fossil data from Chi et al. (1981) in our analysis (Figure 3 and Table S3). We also collected fresh mud rock samples for new microfossil analysis in the Lichi Mélange matrix and surrounding sedimentary units from all studied river sections (Figures S3–S9), with a focus on calcareous nannoplankton data that were relatively limited in previous studies and three additional samples for planktonic foraminifera identifications (the Yungfong (YF) section) (Tables S3-S4). Additional paleomagnetic drill core samples were collected from strata in coherent continuous sections (Fanshuliao and Paliwan formations), and processed through stepwise thermal demagnetization, alternating-field demagnetization, or a combination of both methods to obtain reliable measurements of primary remanent component of the paleomagnetic declination and inclination at each site (Figure S17). A "double-tilt correction" was later applied to progressively remove tilting by regional fold plunge and then bedding tilt (Fisher, 1953; Ramsay, 1961) (Table S5). After compiling these magneto-biostratigraphy datasets, we interpreted the depositional ages based primarily on paleomagnetic polarity reversals and the first appearance datum (FAD) for index fossils due to potential fossil reworking (Chen, 1988b, 2009; Chi et al., 1981), whose ages follow recent compilations for the Indo-Pacific region (Anthonissen & Ogg, 2012; Backman et al., 2012; Chuang et al., 2018; Ogg, 2012) (Figure 3).

To understand paleo-basin geometry and facies architecture, we constructed three stratigraphic panels by correlating stratigraphic sections along W-E transects (Powhua-Shinchang, Luye-Tulan, Fuli-Chengkung) and hanging the youngest widespread chronostratigraphic horizons, or datums, such as the first appearance datum (FAD) of microfossils, paleomagnetic reversals, and event marker beds like pebbly mudstone (X1) and tuffaceous turbidites (Vo). The approximate unfolded horizontal distance was calculated using standard geometrical methods (e.g., Ragan, 2009) and mean bedding dip along the transects (Figure 4).

To reconstruct sediment routing pathways and sediment sources, we measured sedimentary structures for paleocurrent (e.g., flute casts, ripple cross-lamination, imbricated gravel clasts) and paleoslope (e.g., axial planes of asymmetric slump folds) directions in each studied section and the Loho and Changpin areas, including data for tuffaceous turbidites (Lai, Ng, et al., 2018). All directional data were restored to paleo-horizontal using a "double-tilt correction." More comprehensive descriptions of our methodologies are included in the supplementary materials.

4. Lithofacies and facies associations

Nine lithofacies are identified in Plio-Pleistocene sedimentary rocks of the southern Coastal Range based on their distinctive characteristics and corresponding interpreted sedimentary processes (Table 1). We employ the classification scheme of Raymond (1984), in which categories α to δ are used to indicate degree of stratal disruption. This scheme was widely applied in previous studies of the Lichi Mélange (e.g., Chang et al., 2001; Chen, Huang, et al., 2017). Lithofacies are then grouped into three facies associations according to their stratigraphic context, sedimentological affiliations, and contact relationships, and these are used to interpret depositional processes, paleoenvironments, and other rock-forming mechanisms (Table 2).

Facies Association 1 (FA1) consists of submarine flysch deposits spanning a wide range of grain size and sedimentary features comprising most of the Fanshuliao and Paliwan formations. The major facies in this group are mudstone (facies F1), turbidites (F2), thick-bedded sandstone and gritstone (F3), and conglomerate (F4) (Figure 5A, B, C). Finer-grained facies in this association are the depositional products of cohesionless sediment gravity flows including sand-rich low- to high-density turbidity currents and gravel-rich grain flows (Table 1). Clasts in this facies association are primarily composed of orogen-derived lithic fragments (e.g., slate, low-grade metasandstone), followed by minor andesite and mafic rocks (e.g., basalt, gabbro). They are interpreted as the deposits of proximal to outer submarine fans with supra-fan lobes and channels that formed on a deep basin plain (Chen, 1988a; Dorsey & Lundberg, 1988). The deep-sea fan deposits likely were derived from submarine canyons that funneled sediment downslope from onshore river sources (Stow & Mayall, 2000).

Facies Association 2 (FA2) includes sedimentary deposits that display a wide range of chaotic textures and internal structures formed by stratal disruption, slumping, sliding, and/or rock-mixing (Table 2). Extraformational clasts (pebble size and larger) in these facies include meta-sandstone, slate, volcanic andesite, volcaniclastic rocks, ophiolitic rocks (gabbro, serpentinite, granodiorite), limestone, and well-sorted quartz-rich sandstone (Chen et al., 2008; Lai, Ng, et al., 2018; Liou et al., 1977; Page & Suppe, 1981). Pebbly mudstone (X1) and slump beds (X2) represent plastically deformed and disrupted sediments in the Fanshuliao and Paliwan formations (Figure 5E, F). These facies locally include outsized, decimeter- to kilometer-scale olistoliths (X4) (Figure 6A, B) that commonly display small-scale internal brittle fractures and local diapiric mudstone intrusions (Figure 6C) indicating rapid emplacement in unconsolidated sediment that created local fluid overpressure (Ogata, Festa, Pini, & Alonso, 2019). Olistoliths are composed of various extraformational lithologies such as andesite,

Table 2. Facies associations of sedimentary rocks in the southern Coastal Range.

Facies Association	Occurrence and Lithofacies Contacts	Depositional Setting	Rock Unit†
FA1: Cohesionless sediment gravity flows	Submarine flysch facies F1 to F4 (Figure 5A-C). F1 = distal basin plain and slope. Base of beds in all facies are typically sharp (erosive). Facies F3 and F4 locally display channelized bases with ~ 2 to 230 m deep and 10's to 100's m wide erosional channels incised into facies F1 and F2.	Proximal to distal submarine fan with supra-fan channels, and distal basin plain.	Fsl, Plw
FA2: Submarine mass wasting and cohesive debris flows	Interbedding, soft-sediment deformation, and lateral transitions among pebbly mudstone (X1), slump bed (X2), and/or olistostrome (X3) (Figures 5E-F, 6D-E), with randomly distributed lithic blocks (X4) (Figure 6A-C). Observed Basal Contact Styles: (1) Base of facies X1, X3, and X4, where resting on FA1, is sharp and erosive (Figure 8A, 8G), locally with sheared horizons (Figure 8F-G). Facies X3 locally onlap or downlap onto incised channel margins (Figure 8E). (2) Base of facies X1 and X3 transitional from X2 (Figure 5E). (3) Base of facies X1 transitional from thick-bedded sandstone and gritstone (F3). (4) Diapiric intrusions of mixed underlying strata at the margins of X4 (Figure 6A-C). Observed Upper Contact Styles: (1) Upper contact of facies X1, X2, X3, and X4 where overlain by facies association FA1 is sharp (Figure 8B-D). (2) Upper and lateral margins of facies X4 commonly surrounded by facies X1, X2, and X3 (Figures 6A-E, 10A-B). (3) Upper contact of facies X1 gradually transitional to thick-bedded sandstone and gritstone (F3). (4) Upper contact of facies X3 transitional to X2.	Muddy sediment-rich, mass-transport complex derived from steep slope and deposited at base of slope to proximal basin floor. Local brittle and plastic deformation zones record shearing on discrete basal surfaces of large mass movements. Variable degrees of sediment liquefication and lubrication that facilitated mass transport.	Lc, Fsl, Plw
FA3: Volcaniclastic deposition	Fresh tuffaceous sandstone beds (Vo) with sharp erosive bases. Primarily interbedded with turbidites (F2), uncommonly preserved where facies other than F2 are dominant (Figure 5D).	Distal syn-eruptive turbidity currents.	Fsl, Plw

†: Abbreviations of stratigraphic units follow Table 1.

volcaniclastic sandstone and conglomerate, ophiolitic rocks (gabbro, serpentinite, granodiorite, etc.), limestone, and quartz-rich sandstone (Figures 6A-E, S15–S16). Olistostrome facies (X3) are characterized by very thick massive beds of disturbed mudstone with indistinct bedding and relatively weak shear fabrics (Figure 6D, E). Intensive rock dismemberment including characteristic boudinage structures occurs locally within the basal zone of slump beds facies (X2) (Figure 6F), fitting the definition of "broken formation." Well-developed scaly foliations with connective tightly spaced slickensides, schistosity-cisaillement (S-C) fabrics, and reoriented clasts with extensional structures commonly occur along sheared horizons near the base of the olistostrome (X3) (Figures 6G, S15C). These basal deformation features in chaotic sedimentary rocks may be the result of gravitational-related shearing during mass movements (Ogata et al., 2014; Tripsanas et al., 2008). Detailed field observations reveal depositional successions of chaotic facies (FA2) interpreted as products of submarine mass wasting and flow transformations from slides and slumps to cohesive debris flows that initiated on mud-rich unstable submarine slopes and accumulated at base-of-slope to proximal basin plain environments (Festa et al., 2016; Ogata et al., 2012) (Table 2).

Lastly, FA3 consists of tuffaceous turbidites (Vo) (Figure 5D) that represent distal syn-eruptive volcaniclastic deposits associated with syn-collision volcanism of the Luzon Arc (Lai, Ng, et al., 2018; Yang et al., 1995).

This classification scheme permits interpretation of processes using a modern evidence-based approach that provides an unambiguous basis for defining lithostratigraphic units (Tables 1, 2). The Lichi Mélange in this scheme is restricted to facies that display pervasive shear fabrics: olistostrome (X3) (Figure 6D, E). In contrast, coherent facies (F1-F4), and mixed facies produced by sediment gravity flows and slumping (X1, X2) are assigned to the Fanshuliao and Paliwan formations (Figure 5). Olistoliths (X4) are included in the lithostratigraphic unit of its surrounding facies (Figure 6A, B, C).

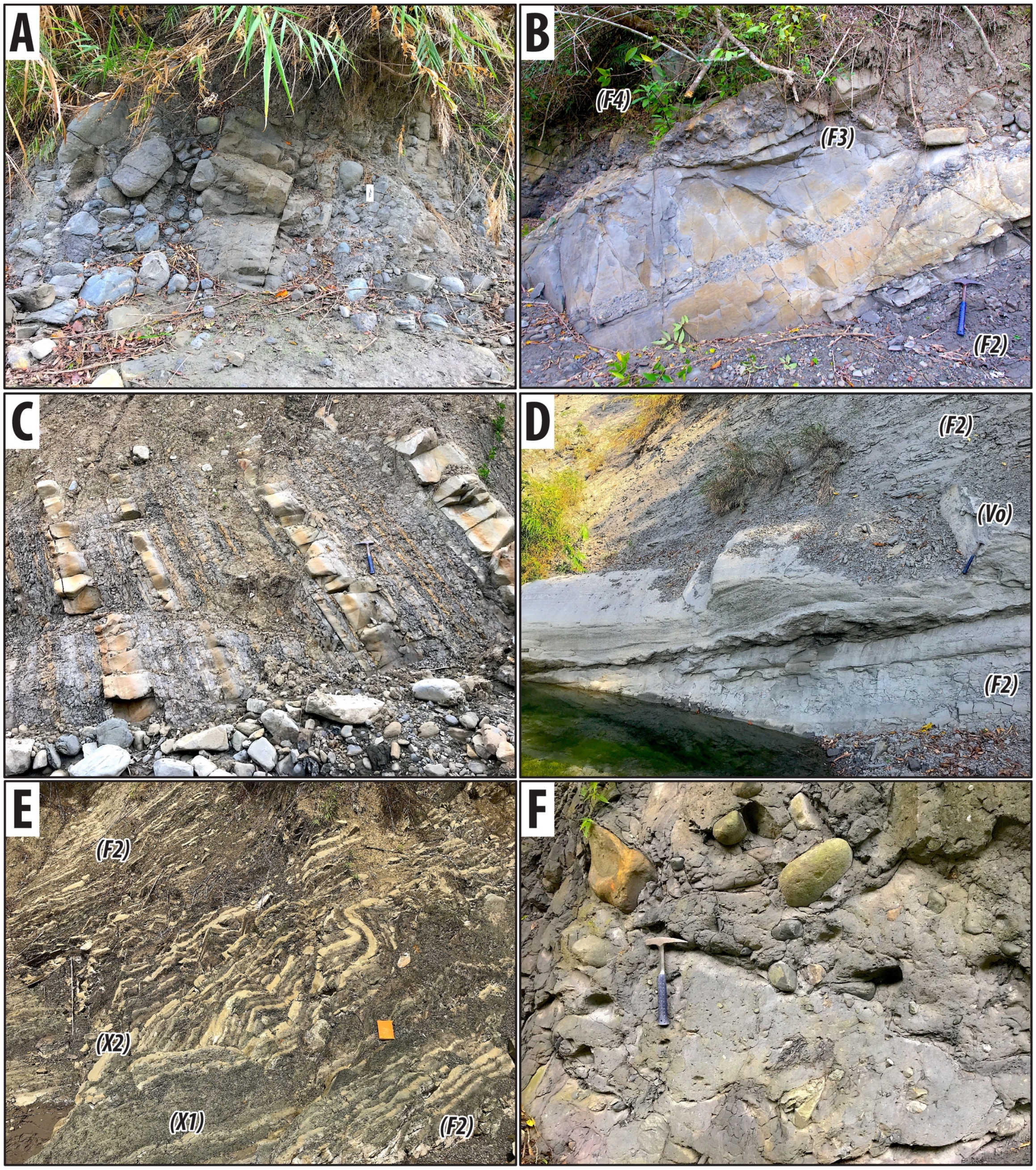

Figure 5. Lithofacies photos – I: products of sediment gravity flows. (A) Conglomerate (F4) in Mukeng river – C (MKCc) section. Notes the bedding is overturned; (B) Thick-bedded sandstone and gritstone (F3) in MKCc section, associated with conglomerate (F4) and turbidite (F2); (C) Turbidite (F2) and interbedded mudstone (F1) in Mukeng river – B (MKCb) section; (D) Tuffaceous turbidite Tp12 (Vo), interbeds with orogen-derived turbidites (F2) in Madagida river (MDJ) section; (E) Slump bed (X2) associated with pebbly mudstone Pm1 (X1) and turbidites (F2) in MKCc section; (F) Pebbly mudstone Pm3 (X1) in MDJ section.

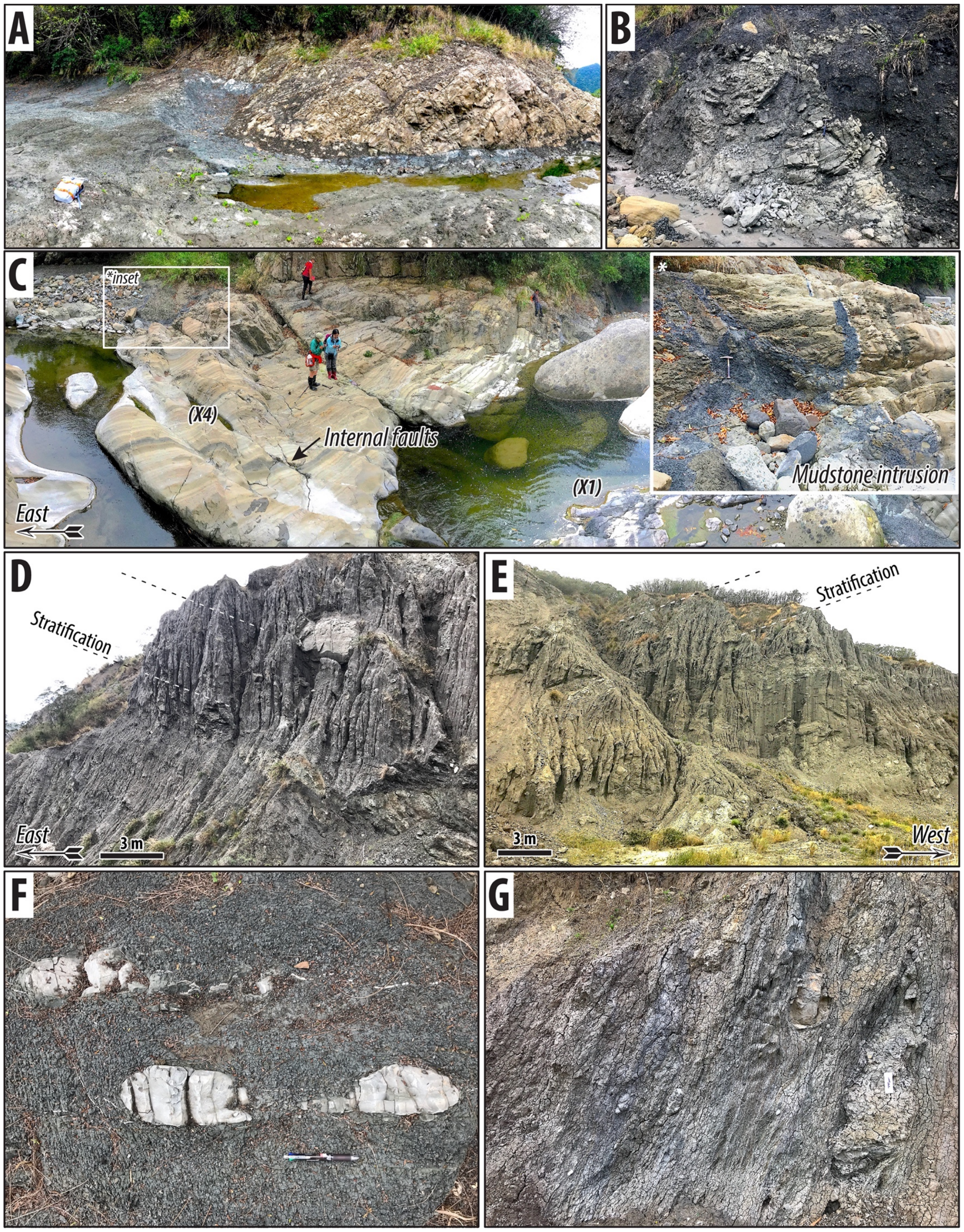

Figure 6. Lithofacies photos – II: products of mass wasting. (A) Volcaniclastic (andesitic) sandstone olistoliths (X4) embedded in slump bed (X2) with soft-sediment deformation at Yungfong (YF) section; (B) Sandstone olistoliths (X4) with soft-sediment deformation in olistostrome (X3) at Mukeng river – A (MKCa) section; (C) Volcaniclastic (andesitic) sandstone olistoliths (X4) with muddy injectites (inset) in Bieh river – A (BCa) section, associated with pebbly mudstone Pm2 (X1) and slump bed (X2). Note internal faults truncated at the margins of the block; (D) olistostrome (X3) in Juchiang river (JCC) section with south-dipping stratifications; (E) olistostrome (X3) in Moon World (MW) section with east-dipping stratifications; (F) Sedimentary boudinages in slump bed (X2) at Mukeng river – C (MKCc) section (i.e., broken formation); (G) Scaly foliation and sigmoidal-shaped blocks formed by non-coaxial shear and extensional fracturing (block-in-matrix fabrics) in a sheared horizon near a basal contact of olistostrome (X3) facies at MKCc section.

5. Contact and map relationships

In our field survey, we identified the fault zone rocks (i.e., uncompacted cataclasite, fragmented mudstone with pencil cleavage, and fault gouge) of the Tuluanshan fault (Figure 7), which cuts all lithological units including Lichi Mélange in the southern Coastal Range (Figures 4, S1-S2). These fault zone rocks display brittle shear fabrics with well-polished slickensides that overprint primary sedimentary fabrics and structures of rocks on both sides of the main fault. This observation confirms that brittle shear fabrics are not diagnostic for differentiating chaotic rocks generated by different mechanisms (cf. Chang et al., 2000; Chen, 1997b), and the "structurally ordered block-in-matrix fabrics" subject to tectonic overprints are restricted to narrow fault-damage zones.

In contrast to identified brittle fault contacts, most contacts between Lichi Mélange and other sedimentary units are depositional. Eight of the best exposed depositional contacts are documented in Figure 8, including the classic outcrops reported by Page and Suppe (1981) (their Locality J) (Figure 8A) and Li (1984) (their site L12) (Figure 8C). According to stratigraphic younging direction indicated by sharp bases and normally graded Bouma sequences in turbidites (facies F2), the Lichi Mélange is both underlain and overlain by deposits of the Fanshuliao and Paliwan formations, in exposures that reveal clear interbedding relationships. Depositional contacts in Chungye river – A (CYCa) and Yungfong (YF) sections exhibit gradational transitions from deposits of non-cohesive sediment gravity flows (facies association FA1) to submarine mass-wasting products (FA2), thus displaying clear conformable lithological transitions that reflect straightforward depositional contact relationships (Figures 10, S15-S16).

The degree of shearing at depositional contacts varies from none (e.g., Figure 8A, B, D, H) to high (e.g., Figure 8F). None of the sheared contacts coincides with post-diagenetic brittle fault gauge, cataclasite, or pencil cleavage, making them easily distinguished from brittle fault zones of the Tuluanshan fault (Figure 7) and Wushinshih fault (Lai & Teng, 2016). There is no evidence of shearing at the depositional contacts between Lichi Mélange and Fanshuliao Formation near the headwaters of Mukeng river (MKC) section (Figures 4, 8C, D, S2), which previous workers speculated is the southern extent of the Tuluanshan fault (cf. Chang et al., 2000; Chen, 1997b; Huang et al., 2018).

Similarly, the well exposed depositional contact at Chunchie river (CC), Chiaolai river (CLC), and Juchiang river (JCC) sections around Fukang area (Lin et al., 2008; Page & Suppe, 1981) clearly refute a previously hypothesized east-vergent thrust at that locality (cf. Chang et al., 2001; Chen, Huang, et al., 2017; Huang et al., 2018) (Figure 8A).

Some studies map a “Yungfong fault” at the contact between Lichi Mélange and Fanshuliao Formation in the Yungfong (YF) section (Figures 4, S2), with variously proposed vergence directions (west-vergent or east-vergent) (Chang et al., 2000; Chen, 1997b; Lo et al., 1993). Soft-sediment extension features (boudinage) are commonly observed in the Lichi Mélange (i.e., olistostrome (X3)). Scaly foliation near the basal sheared contact has an attitude identical to regional bedding dipping toward west (Figure 8G), and it correlates laterally to another exposure 0.6 km to the north where an unambiguous depositional contact is reported (Barrier & Muller, 1984; Hsu, 1956) (Figures 8H, S16). The sense of shear measured along this localized sheared horizon seems to be consistent with the orientation of regional tectonic stress field (Chang et al., 2000; Chen, 1997b), but is also consistent with reconstructed paleoslope directions after bedding corrections, suggesting an alternative explanation of gravity-driven sliding and basal shear (see Section 7.1). These relations suggest that localized shear fabrics near the southern contact represent localized shears produced by mass movement at the base of thick olistostrome beds. The YF section appears to be a continuous succession, an interpretation supported by internal consistency among index microfossils (see Section 6.1).

Based on careful assessment of contact relationships, our geological map reveals common pinch-out of the Lichi Mélange with lateral and vertical facies transitions to pebbly mudstone beds (X1) of the Fanshuliao and Paliwan formations (Figures 4, S1–S2), thus confirming their interbedding relationship. The Lichi Mélange is primarily preserved in the western part of the Coastal Range, except in the Fukang area where thick Lichi Mélange extends to the east and southeast where it is exposed along the modern coastline (Figure 4). The internal stratification and shear fabrics of the Lichi Mélange broadly coincide with regional bedding trends (Page & Suppe, 1981). We also observe random fabric orientation, particularly around Fukang area, and locally preserved onlap onto channel margins (Figure 8E), revealing a map pattern typical of large-scale sedimentary mélange (Festa et al., 2019). Lichi Mélange and other units in this area were reworked together by post-depositional tectonic deformation (cross-cutting thrust faults and folds) (Figures 4, 7), and therefore the Lichi Mélange can be considered as a "polygenetic mélange."

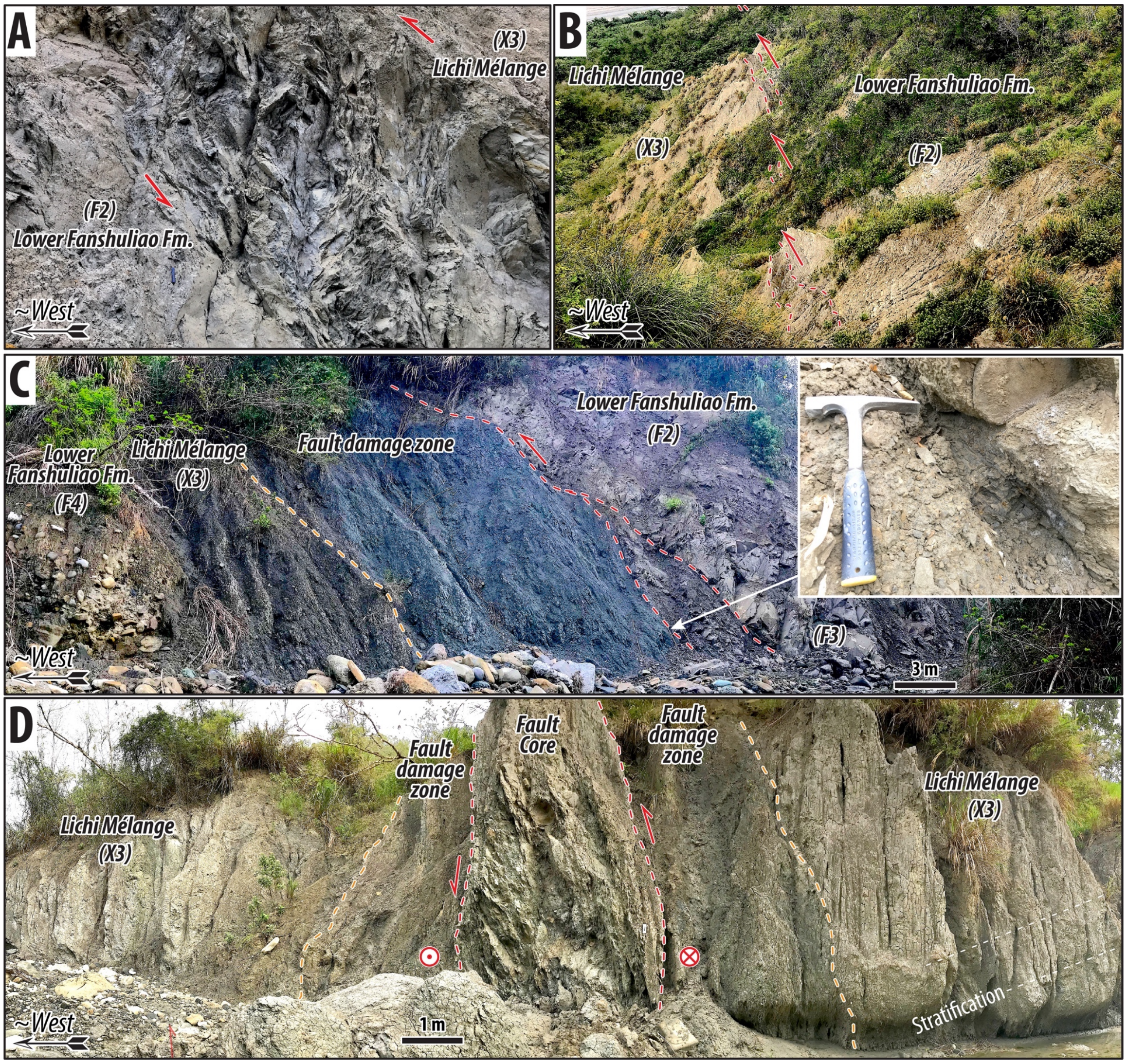

Figure 7. Field photos for Tulaunshan fault damage zone and core (uncompacted cataclasite and/or gouge zone). (A) Tuluanshan fault cataclasite in Chungye river (CYC) section; (B) Gouge zone (bounded by red dash lines) of the Tuluanshan fault along Road no.192; (C) Tuluanshan fault zone in at the base of Mukeng river – B (MKCb) section. The inset shows exposed fault gouge. Pencil cleavage exists in footwall damage zone; (D) Tuluanshan fault zone along Mukengnan river, equivalent to site #19 in Chang et al. (2000). See locations in Figure 4. (For interpretation of the references to colour in this figure legend, the reader is referred to the web version of this article.)

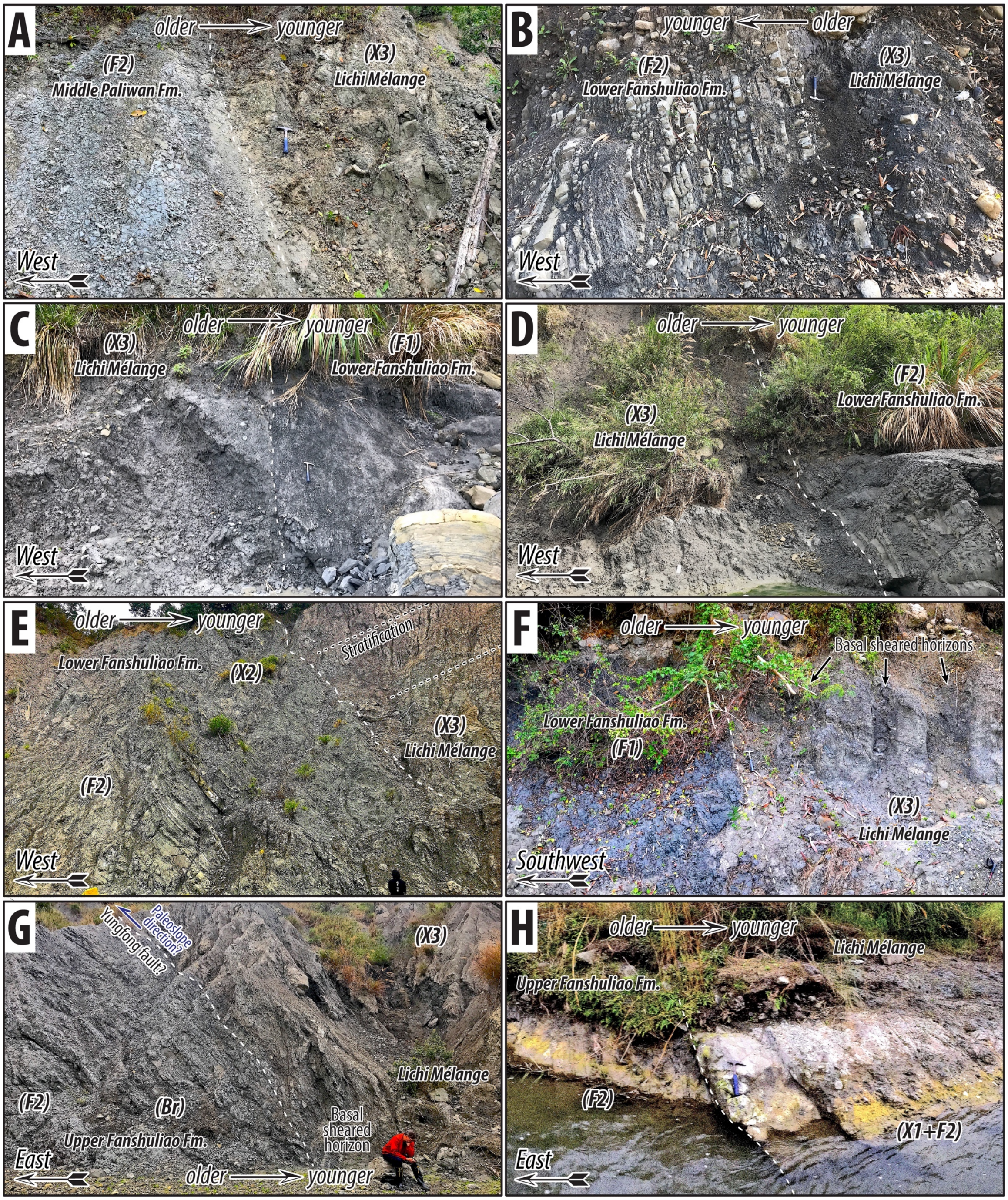

Figure 8. Field photos for depositional contacts (white dash lines) between Lichi Mélange & other units. (A) Chiaolai river (CLC) section, same place as 'Locality J' in Page and Suppe (1981); (B) Mukeng river – C (MKCc) section. Notes the bedding is overturned; (C) Mukeng river – B (MKCb) section; (D) Mukengnan river section upstream; (E) MKCa section downstream. The stratifications (black dash lines) of olistostrome (X3) appears to onlap on an erosive contact (white dash lines) locally truncating on lower Fanshuliao formation; (F) Chungye river – A (CYCa) section; (G-H) southern and northern contacts of Yungfong (YF) section respectively, which was previously inferred to the "Yungfong fault" (Chang et al., 2000; Chen, 1997b). See locations in Figure 4.

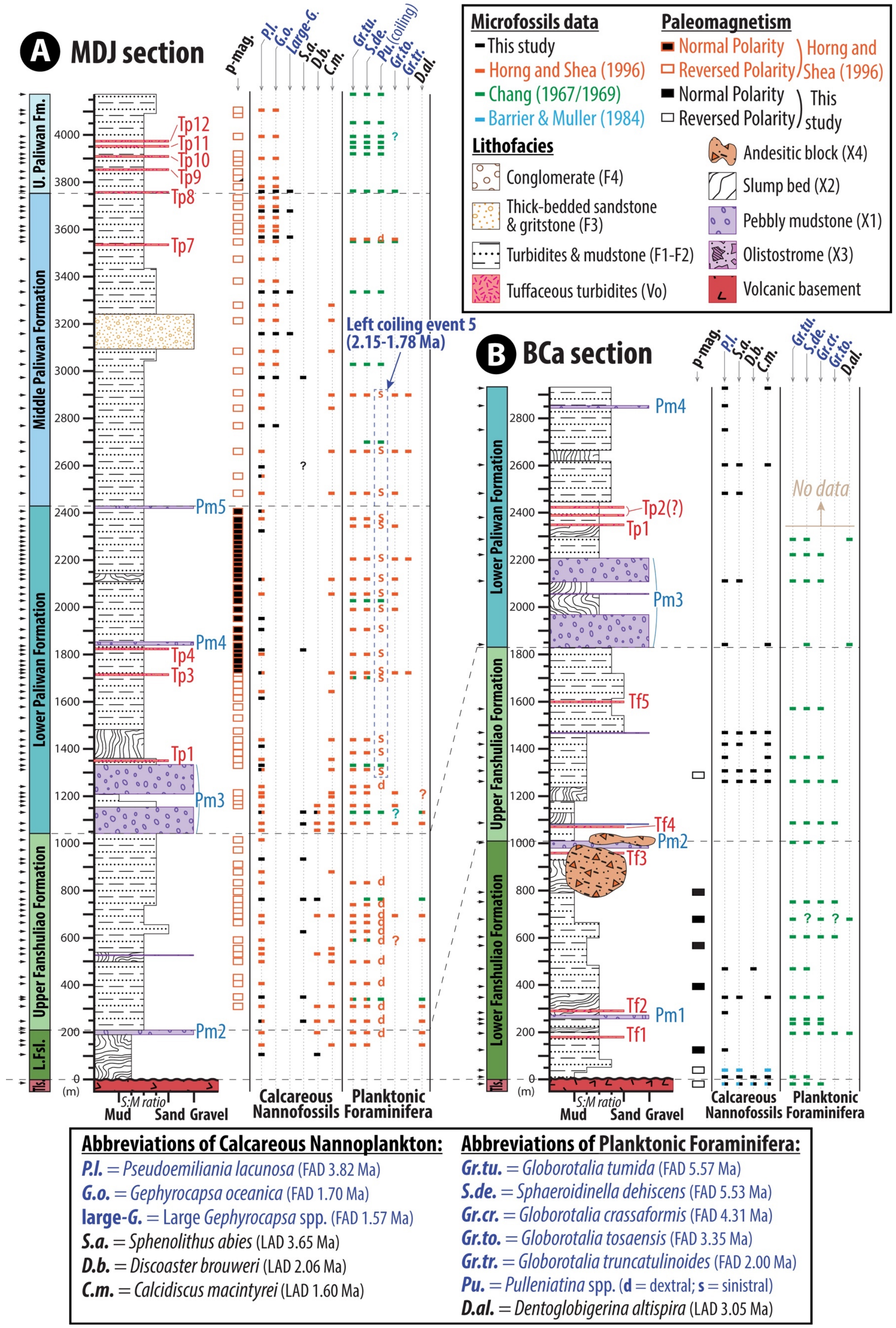

Figure 9. Type sections for Fanshuliao and Paliwan formations in the southern Coastal Range. (A) Madagida river (MDJ) section; (B) Bieh river – A (BCa) section. Black arrow heads on the left mark the stratigraphic heights of magneto-biostratigraphic constraints. See detail sample numbers in Figures S1, S5, S8, S11 and data in Tables S3, S5.

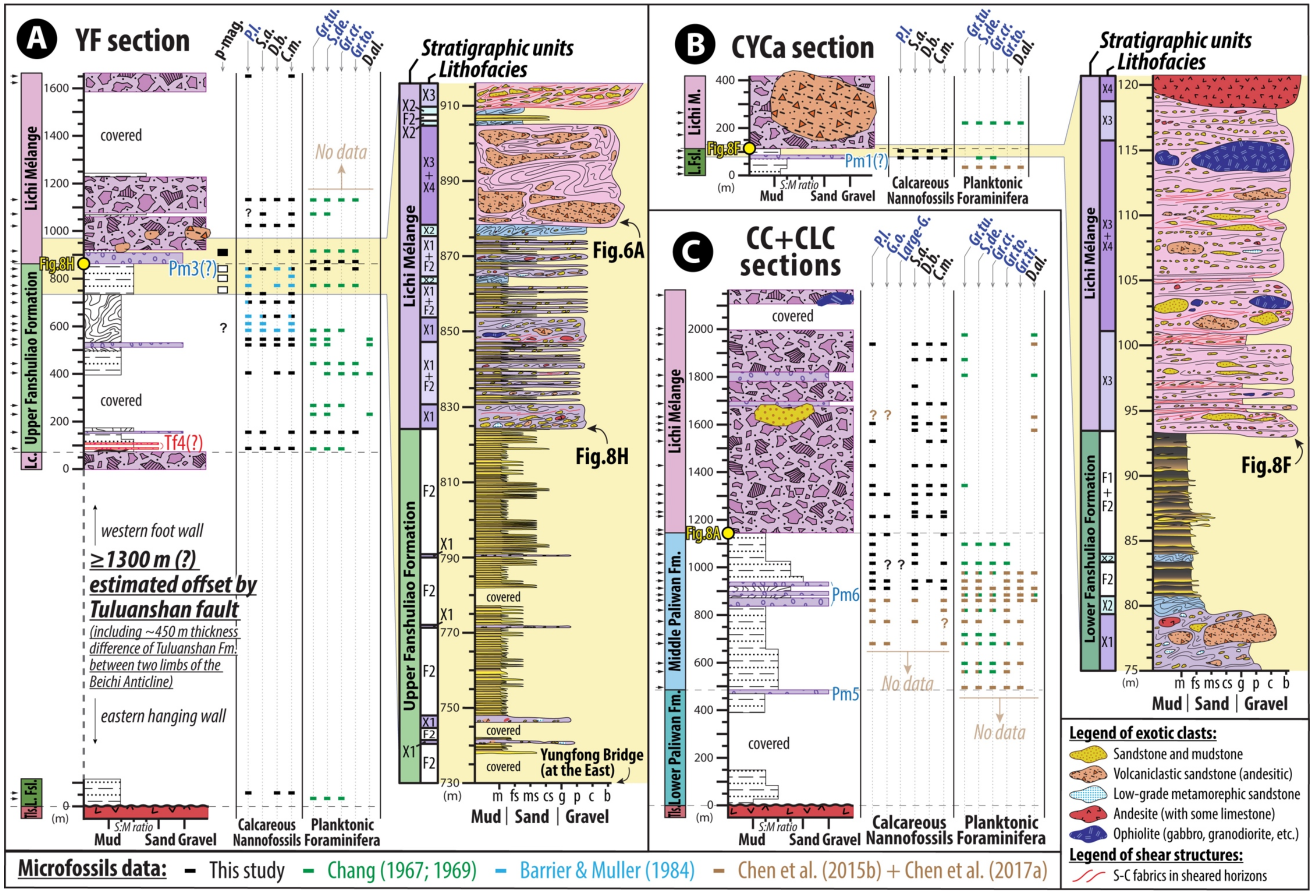

Figure 10. Selective sections showing stratigraphic columns and lithofacies changes in the depositional transitions between Lichi Mélange and other sedimentary units. (A) Yungfong (YF) section and measured depositional contact zone; (B) Chungye river A (CYCa) section and measured depositional contact zone; (C) synthesis of the Chunchie river (CC) and Chiaolai river (CLC) sections. Lithological legends and abbreviation of magneto-biostratigraphy follow Figure 9. Yellow circles mark the depositional contact zones shown in Figure 8. Black arrow heads on the left mark the stratigraphic heights where magneto-biostratigraphic constraints exist. See details of sample numbers, microfossils data, and measured contact zone photos in Figures S12, S13, S15, S16, and Tables S3, S4. (For interpretation of the references to colour in this figure legend, the reader is referred to the web version of this article.)

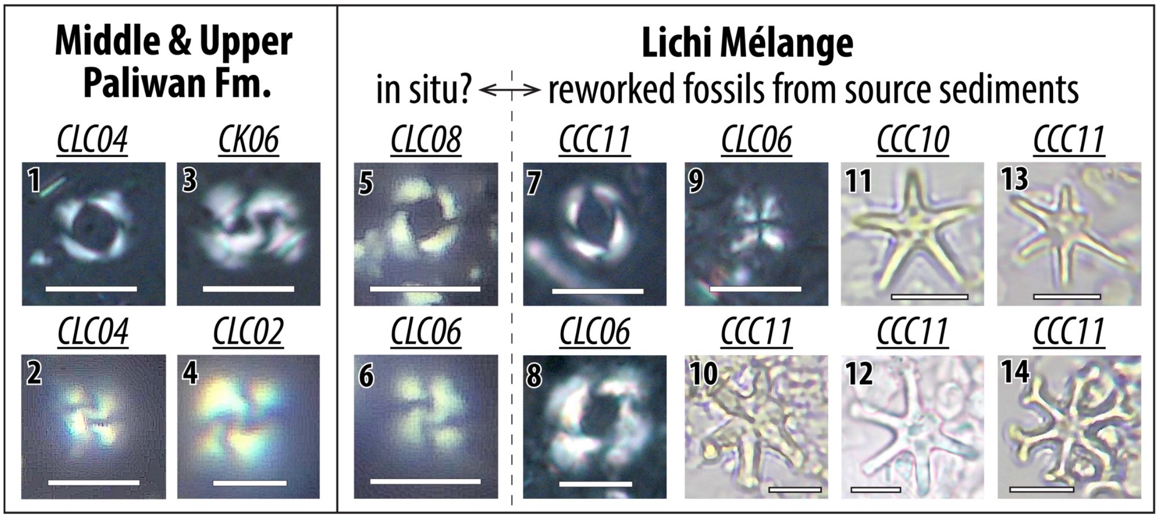

Figure 11. Polarizing micrographs of index calcareous nannofossils, recovered from Paliwan Formation, and overlying Lichi Mélange, with scale bars of 5 µm. Photo numbers 1 and 5 are *Pseudoemiliania lacunosa*. Numbers 2 and 6 are *Gephyrocapsa oceanica*. Numbers 3 and 4 are large *Gephyrocapsa* sp. Numbers 7 and 8 are medium and large forms of *Reticulofenestra pseudoumbilicus* respectively. Number 9 is *Sphenolithus abies*. Number 10 is *Discoaster druggii* (?). Number 11 is *Discoaster quinqueramus*. Number 12 is *Discoaster surculus*. Number 13 is *Discoaster brouweri*. Number 14 is *Discoaster variabilis*. See sample locations in Figures S5, S7 and Table S3.

6. Basin-fill stratigraphy of the southern Coastal Range

6.1. Age of sedimentary units and unconformities in the southern Coastal Range

The sedimentary fill of the southern Coastal Range basin is dominated by Plio-Pleistocene deep-marine orogen-derived deposits that formed by gravity-driven processes (Lichi Mélange, Fanshuliao and Paliwan formations). These deposits overlie a regional unconformity on top of Miocene Shihmen Volcanic Breccia and older Shihtiping Tuff of the Tuluanshan Formation (Figure 3).

Our compilation of age data shows that the same group of youngest index microfossils are present in the matrix of Lichi Mélange and interbedded Fanshuliao and Paliwan formations (Figures 9, 10, S3–S14). Microfossils whose last-appearance ages are older than the first appearance datum (FAD) of younger ones repeatedly appear in both Lichi Mélange and interbedded units, indicating persistent fossil reworking that limits the reliability of the Last Appearance Datum (LAD) for interpretations of depositional age. Planktonic foraminifera *Globorotalia crassaformis* (FAD 4.31 Ma), *Globorotalia tosaensis* (FAD 3.35 Ma) and calcareous nannoplankton *Pseudoemiliania lacunosa* (FAD 3.82 Ma) are present in the oldest strata which are exposed in the west, including Mukeng river (MKC), Chungye river (CYC), and Yungfong (YF) sections (Chang, 1967; Barrier and Muller, 1984; Chen et al., 2017b) (Figures 10, S3–S7, S11–S13). At the southeast end of the Coastal Range (Fukang area) (Figures 4, S1), calcareous nannoplankton *P. lacunosa* (FAD 3.82 Ma) and trace *Gephyrocapsa oceanica* (FAD 1.70 Ma) are present in the Lichi Mélange matrix in the Chunchie (CC), Chiaolai river (CLC), and Moon World (MW) sections (Chen, Huang, et al., 2017; Chi et al., 1981). Large *Gephyrocapsa* spp. (FAD 1.57 Ma) appears near the top of the underlying Paliwan Formation (Figures 10C, 11, S5-S6, S12). Although older (Miocene) calcareous nannoplanktons *Reticulofenestra pseudoumbilicus* (medium and large), *Sphenolithus abies*, and *Discoaster* spp. are abundant in the matrix of the Lichi Mélange in this area, the clear evidence for an unsheared depositional contact with stratigraphic superposition (Figure 8A) and common olistostromal features (Figure 6D) indicate that the Miocene fossils are reworked from older sediments (Figure 11). Thus, the whole sedimentary sequence in the southern Coastal Range was deposited between ca. 4 and 1 Ma, and the depositional age of the Lichi Mélange is similar to that of interbedded Fanshuliao and Paliwan formations.

The Kangkou Limestone is only preserved at the base of the Sanshian river (SSS), Shingang river (SGS), and Babian river (BBS) sections (Figures 4, S8, S9). In this area, it contains planktonic foraminifera *Gr. crassaformis* (FAD 4.31 Ma) at the base and abundant *Gr. tosaensis* (FAD 3.35 Ma) and *Dentoglobigerina altispira* (LAD 3.05 Ma) near the top (Figure S14), suggestive of a depositional age range between 4.31 and 3.05 Ma (Huang & Yuan, 1994). Huang and Yuan (1994) interpreted that the top of the Kangkou Limestone may be younger based on a single, uncertainly identified specimen of *Globorotalia truncatulinoides* (FAD 2.00 Ma) (Sample #26 in their Table 4). This tentative age assignment is not considered in our compilation because it could not be verified. The Biehchi Epiclastic Unit is exposed at the base of the Bieh river (BC) section and was deposited at ca. 4.2–3.8 Ma based on the presence of planktonic foraminifera *Gr. crassaformis* (FAD 4.31 Ma) (Chang, 1969), calcareous nannoplankton *P. lacunosa* (FAD 3.82 Ma) (Barrier & Muller, 1984), and the youngest peak U–Pb age (~4.2Ma) of detrital zircon (Chen, Chung, et al., 2015). The age distribution of these two intermittent units partially overlaps that of the Lichi Mélange and lower Fanshuliao Formation, and appears to be a discontinuous record of the ~2 Myr transition from the youngest stages of arc volcanism to sedimentary basin formation during collisional orogenesis (Dorsey, 1992).

6.2. Type sections and marker beds of the Fanshuliao and Paliwan formations

The Madagida river (MDJ) and Bieh river – A (BCa) sections are widely accepted as stratotypes for the Fanshuliao and Paliwan formations in the southern Coastal Range (Chen, 2009; Huang et al., 2018) (Figure 9). Widespread layers of pebbly mudstone (facies X1, named Pm1 to Pm7) and tuffaceous turbidites (facies Vo, named Tp1 to Tp14 in the Paliwan Formation) provide useful marker beds that allow us to map and correlate these deposits (Lai, Ng, et al., 2018; Lai & Teng, 2016). In this study, we discovered five more tuffaceous turbidites (named Tf1 to Tf5) in the Fanshuliao Formation (Figure 3). The Paliwan Formation in the MDJ section was previously dated between ca. 2.15 to 1.5 Ma (Horng & Shea, 1996). In this study we refine the age interpretation with revised placement of the first occurrences of *G. oceanica* (FAD 1.70 Ma) and large *Gephyrocapsa* spp. (FAD 1.57 Ma) in this section (Figure 9A). The proposed age of the Fanshuliao Formation in the southern Coastal Range varies from ~4.94–3.35 Ma (Chen, 2009; Lee & Chi, 1990) to ~3.35–2.15 Ma (Horng & Shea, 1996; Lai & Teng, 2016). Based on compilation of previous and new data with lithostratigraphic correlations, the lower Fanshuliao Formation is reassigned here to the upper Gauss Chron, ranging in age from the top of the Keana reverse polarity event (C2An.1r; 3.04 Ma) to the Gauss-Matuyama boundary at 2.59 Ma. The upper Fanshuliao Formation corresponds to the lower Matuyama Chron (C2r.2r, 2.59–2.14 Ma) (Figure 9B). This revised age interpretation is supported by the presence of planktonic foraminifera *Gr. tosaensis* (FAD 3.35 Ma) near the bottom of the section (site 222 in Chang (1969)) (Figures S7, S13B).

Pebbly mudstone and tuffaceous turbidite marker beds have unique sedimentary textures and clast compositions that permit regional correlation. These marker beds are interpreted to record distinct geological events such as seismicity-triggered submarine debris flows and volcanic eruptions (Chen et al., 2008; Lai, Ng, et al., 2018). This allows us to tune their ages using our updated high-resolution magneto-biostratigraphy, and we use the marker beds as age anchors for other sections based on detailed geologic mapping and lithostratigraphic correlation. For example, pebbly mudstone beds Pm2, Pm3, and

Pm5 were deposited near the Gauss-Matuyama boundary (2.59 Ma), the onset of *Pulleniatina* spp. left coiling event 5 (2.15 Ma), and the top of the Olduvai normal polarity event (C2n, 1.80 Ma), respectively. Tuffaceous turbidites Tp7-Tp14 formed between the FAD of large *Gephyrocapsa* spp. (1.57 Ma) and onset of small *Gephyrocapsa* spp. acme zone (1.23 Ma), consistent with ages determined by apatite fission tracks (1.5 ± 0.1 Ma) and U–Pb zircon dating (1.6 ± 0.1 Ma) on equivalent beds (Chen, Chung, et al., 2015; Yang et al., 1995). The tuffaceous turbidites Tp3-Tp4 and pebbly mudstone Pm4 formed around the base of the Olduvai event (~1.95 Ma), and the tuffaceous turbidites Tf1-Tf2 and pebbly mudstone Pm1 form near the base of C2An.1n event in Gauss Chron (~3.04 Ma).

6.3. Stratal architecture of the southern Coastal Range

Using correlations summarized above and restored distances between stratigraphic sections, we constructed 2D west-east facies panels that reveal the original paleo-basin geometry along three studied stratigraphic transects (Figures 12, 13). The panels show that sedimentary strata of the Fanshuliao and Paliwan formations and Lichi Mélange onlap onto a basin-wide basal unconformity on top of the Tuluanshan Formation (arc volcanic basement). The basal unconformity has a restored gentle west dip (≤ 6–7°) and defines an asymmetric basin low that corresponds to maximum stratigraphic thicknesses near the orogenic front (Chen, 2009; Dorsey, 1992). All units of the Fanshuliao Formation, and lower and middle parts of the Paliwan Formation, thin and pinch out to the east due to eastward onlap onto the basal unconformity.

The reconstructed stratigraphic architecture of eastward thinning and onlap in Plio-Pleistocene orogen-derived deposits of the southern Coastal Range is unlike the arc-ward thickening stratal pattern that is typically observed in forearc basins (Noda, 2016, 2018). The observations of paleo-basin geometry and evidence for considerable basal erosion are inconsistent with previous interpretations that the Coastal Range deposits represent the sedimentary fill of an inherited, uneroded forearc basin (cf. Chang et al., 2000; Teng et al., 1988). There is no evidence for a large local bathymetric low to support a backarc basin interpretation (cf. Chen, 1988b; Chen, 1997a; Song & Lo, 2002) or pull-apart intra-arc basin (cf. Chen, Huang, et al., 2015; Huang et al., 1995; Huang et al., 2006). Instead, the stratal pattern is best explained as the basin fill of a flexural foredeep basin where deposits thicken toward the orogen that supplied sediment to the basin (DeCelles & Giles, 1996; Sinclair, 2012). This interpretation is consistent with the predictions of a syn-collisional retrowedge basin model proposed in other studies (e.g., Chen et al., 2019; Dorsey & Lundberg, 1988; Lundberg & Dorsey, 1988; Malavieille et al., 2016) (See details in Section 8.2).

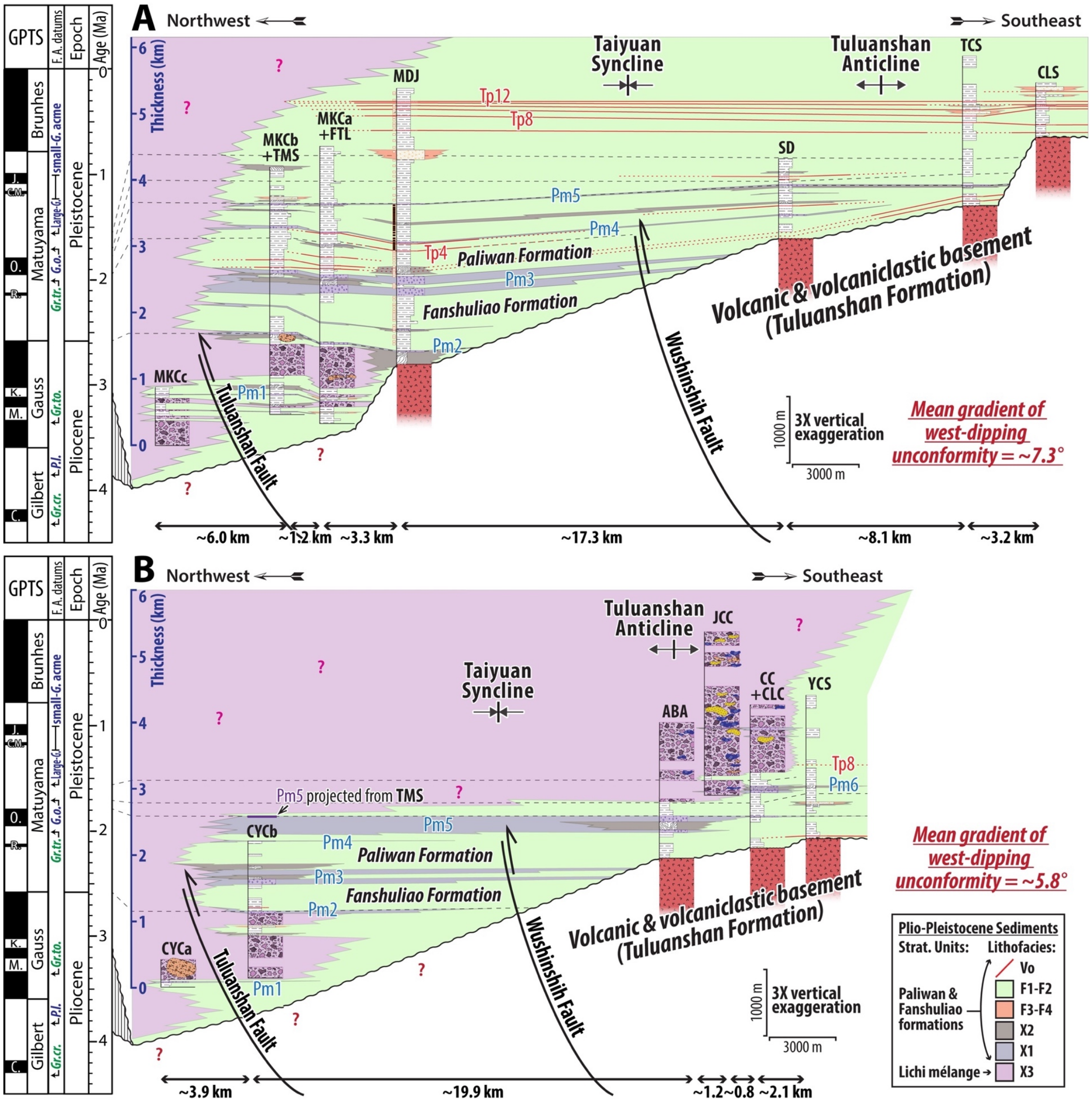

Figure 12. Stratigraphic panels of southern Taiyuan area, with restored distances between stratigraphic sections. (A) Powhua-Shinchang transect; (B) Luye-Tulan transect. Black and white rectangles with red outlines along the Madagida river (MDJ) section show paleomagnetic polarities. See locations of transects in Figure 4. See details of litho-bio-magnetostratigraphic information in Figures S10-S12. (For interpretation of the references to colour in this figure legend, the reader is referred to the web version of this article.)

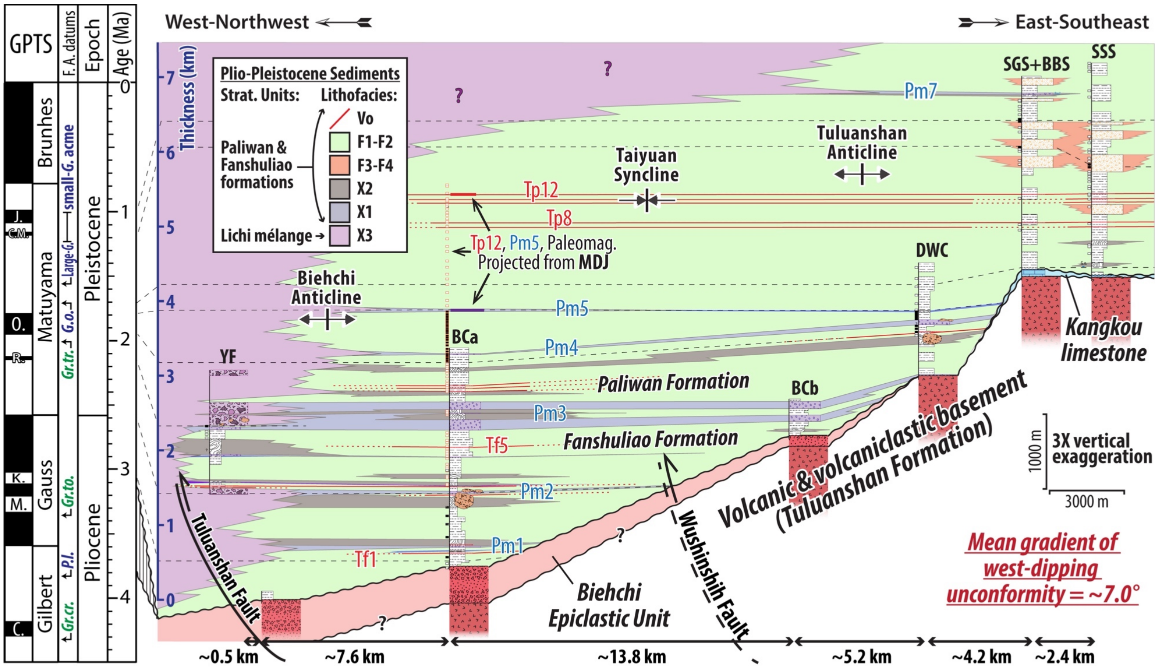

Figure 13. Stratigraphic panel of Fuli-Chengkung area, with restored distances between stratigraphic sections. Black and white rectangles with red outlines show paleomagnetic polarities of Bieh river – A (BCa), Duwei river (DWC), Shingang river (SGS), Babian river (BBS), and Sanshian river (SSS) sections, with data projected from the Madagida river (MDJ) section. See location of the transect in Figure 4. See details of litho-bio-magnetostratigraphic information in Figures S12-S14. (For interpretation of the references to colour in this figure legend, the reader is referred to the web version of this article.)

7. Paleoslope and paleocurrent data

7.1. Paleoslope orientations

Paleoslopes determined from vergence direction of asymmetric slump folds (facies X2) show prevailing east to southeast slump directions in modern coordinates (Figure 14A). Our results are consistent with previously published data in the Luye region (Page & Suppe, 1981) that indicate a regional east to southeast-dipping paleoslope in the southern Coastal Range. Structural and bedding-corrected striae measured at the basal depositional contact of Lichi Mélange in YF section (site #5–6 in Figure 7 of Chang et al. (2000)) (Figure 8G) and base of a thick exotic sandstone block in JCC section (site #1–2 in Figure 8 of Chang et al. (2001)) (Figures S5, S12B) indicate shear directions consistent with local paleoslope indicators, suggesting that they formed by the similar mass-wasting processes (Figure 14A). After correcting for 30° ± 10° clockwise block rotation based on paleomagnetic fabrics (Lee et al., 1990), our results imply a northstriking, east-dipping steep slope at the tectonically controlled western basin margin. This slope was the site of common submarine mass wasting events that generated the Lichi Mélange and associated submarine debris flows (Lundberg & Dorsey, 1988; Page & Suppe, 1981). Minor westward paleoslope directions near the base of the BCa section are interpreted to represent local structural complexities, and do not record a regional-scale west-dipping slope on the western flank of a volcanic arc massif (cf. Chen, 1997a; Huang et al., 1995; Song et al., 2002).

7.2. Paleocurrent directions

Paleocurrent directions exhibit temporal and spatial variations among different lithofacies (Figure 14B). In orogen-derived turbidites and other cohesionless sediment gravity flow facies (F2–F4), paleotransport is dominantly toward the south in modern coordinates, with increasing indicators of southeastward transport in the southern region. We observe an up-section increase of southeast transport directions in the younger Paliwan Formation, which is mainly preserved in the eastern part of the basin. Pebbly mudstone (facies X1) shows transport dominantly to the southeast (in modern coordinates), consistent with paleoslope directions measured in slump beds (facies X2) nearby (Figure 14A). In contrast, tuffaceous turbidites (facies Vo) have diverse paleocurrent directions with a relatively stronger components of westward to southwestward paleoflow directions (Figure 14 B).

After correcting for 30° ± 10° clockwise block rotation in the Coastal Range rocks (Lee et al., 1990), we use paleoslope and paleo transport indicators to interpret the location of source areas and sediment-routing pathways for each facies association. The main source of facies association FA1 (facies F2–F4), which formed in a submarine fan system (Table 2), was located west of the basin (Chen, 1997a; Teng, 1982). The up-section increase in east-directed paleocurrents implies increased input from the west, which we interpret as a response to eastward migration and basinward advance of the Taiwan collisional orogenic front. Consistent east- to southeast-directed directions of paleocurrent in FA1 and paleoslope in pebbly mudstone (X1) and slump beds (X2) reveal a north-trending, east-dipping submarine slope at the steep unstable western basin margin. This shows that the eastern retrowedge of the Taiwan orogen was the main source of mass-transport deposits in facies association FA2. Syn-eruptive tuffaceous turbidites (FA4) display spatially variable paleocurrent directions with a dominant mode to the west and southwest (Figure 14B). These turbidites were derived from an active volcanic source east of the basin, not the volcanic island of Lutao located southeast of the modern Coastal Range (cf. Horng & Shea, 1996; Yang et al., 1995) (Figure 1). Our interpretation of an eastern source is supported by a westward decrease in thickness of the tuffaceous turbidites (Lai, Ng, et al., 2018).

8. Discussion

8.1. Paleogeography and depositional setting

Stratigraphic panels in the southern Coastal Range reveal an important pattern of lateral facies change in which western sections contain abundant olistostromal facies (association FA2), and age-equivalent sections in the east are dominated by flysch facies (association FA1) (Figures 12, 13). Proximal facies including slump beds (X2), olistostromes (X3), and olistoliths (X4) are more abundant in the west and pass laterally into distal facies with pebbly mudstone beds (X1) in the east. This facies architecture records downslope disintegration of mass flows during transformation from slides, slumps, and blocky flows to cohesive debris flows to high-density turbidity currents (Festa et al., 2016; Nemec, 1990; Ogata et al., 2012) (Figure 15B), consistent with measured dominant eastward paleoslope directions (Figure 14A). These facies associations formed by submarine slumping and deposition by sediment gravity flows in deep-water slope to submarine fan and basin plain environments (Figure 15A). The depositional setting was subject to frequent deliveries of orogen-derived sediment that was routed into the basin by a combination of widespread slope failures and gravity-driven transport funneled through submarine canyons (Stow & Mayall, 2000).

Minor syn-eruptive tuffaceous turbidites (facies Vo, association FA4) represent a distal record of arc volcanism during ~4–1 Ma deposition of the orogen-derived sedimentary sequence (Lai, Chu, et al., 2018; Song & Tang, 2019) (Figures 12, 13, 15A). The tuffaceous turbidites were derived from volcanoes located east to northeast of the basin (Lai, Ng, et al., 2018) (Figure 14B), and thus are distinct and different than the magmatic events (>16–14 Ma and ~10–6 Ma) recorded in the underlying Tuluanshan

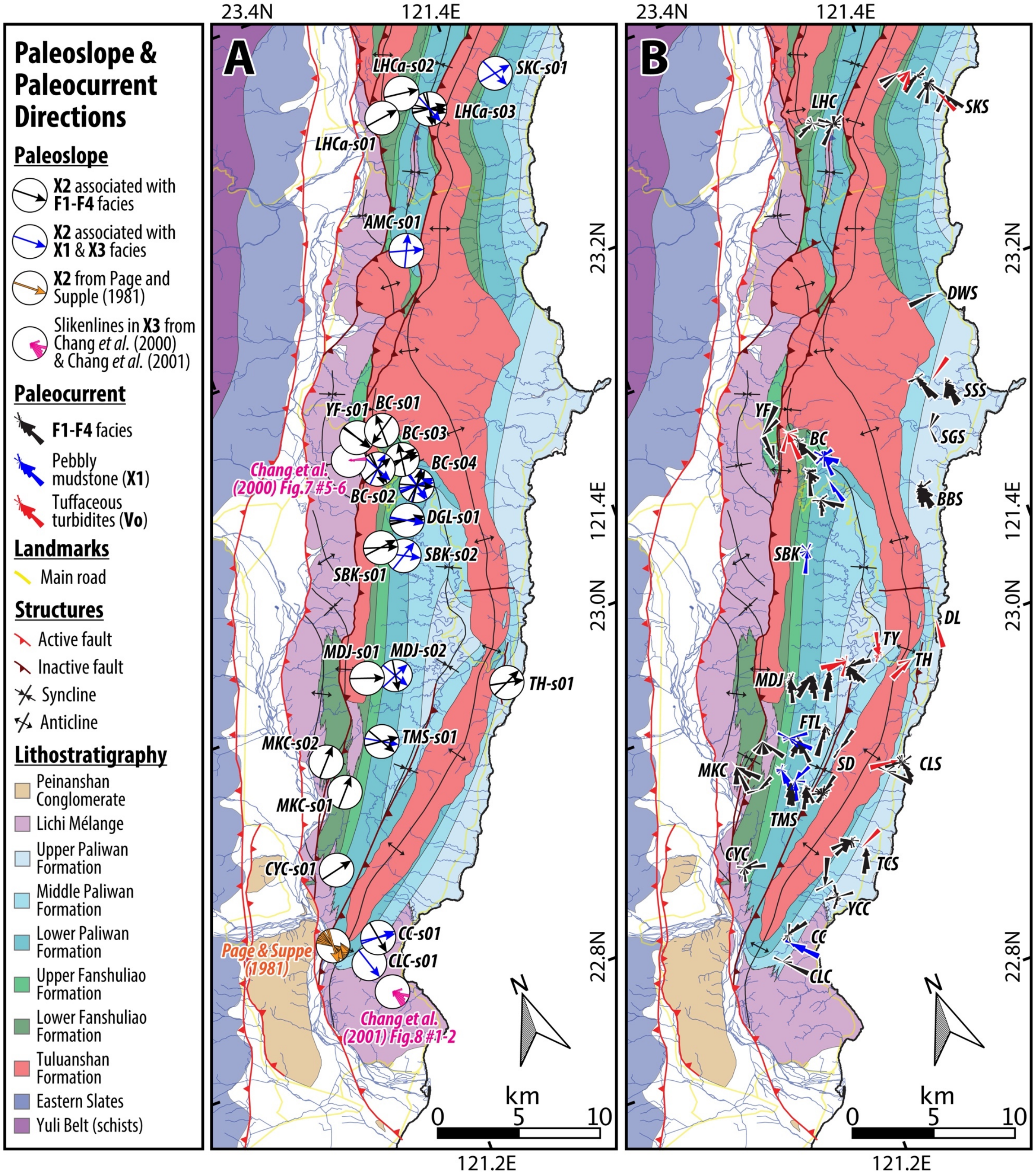

Figure 14. Paleoslope and paleocurrent directions. (A) Inferred paleoslope direction from vergence direction of slump folds (facies X2), including results from Page and Suppe (1981), and bedding corrected east-vergent slikenline shearing sense in basal shear horizons of olistostrome (facie X3) (Chang et al., 2000; Chang et al., 2001); (B) Inferred paleocurrent direction from imbrication, cross-lamination, and flute cast. See method details in text. See raw data, locations, and used structural restorations in the Tables S1, S2.

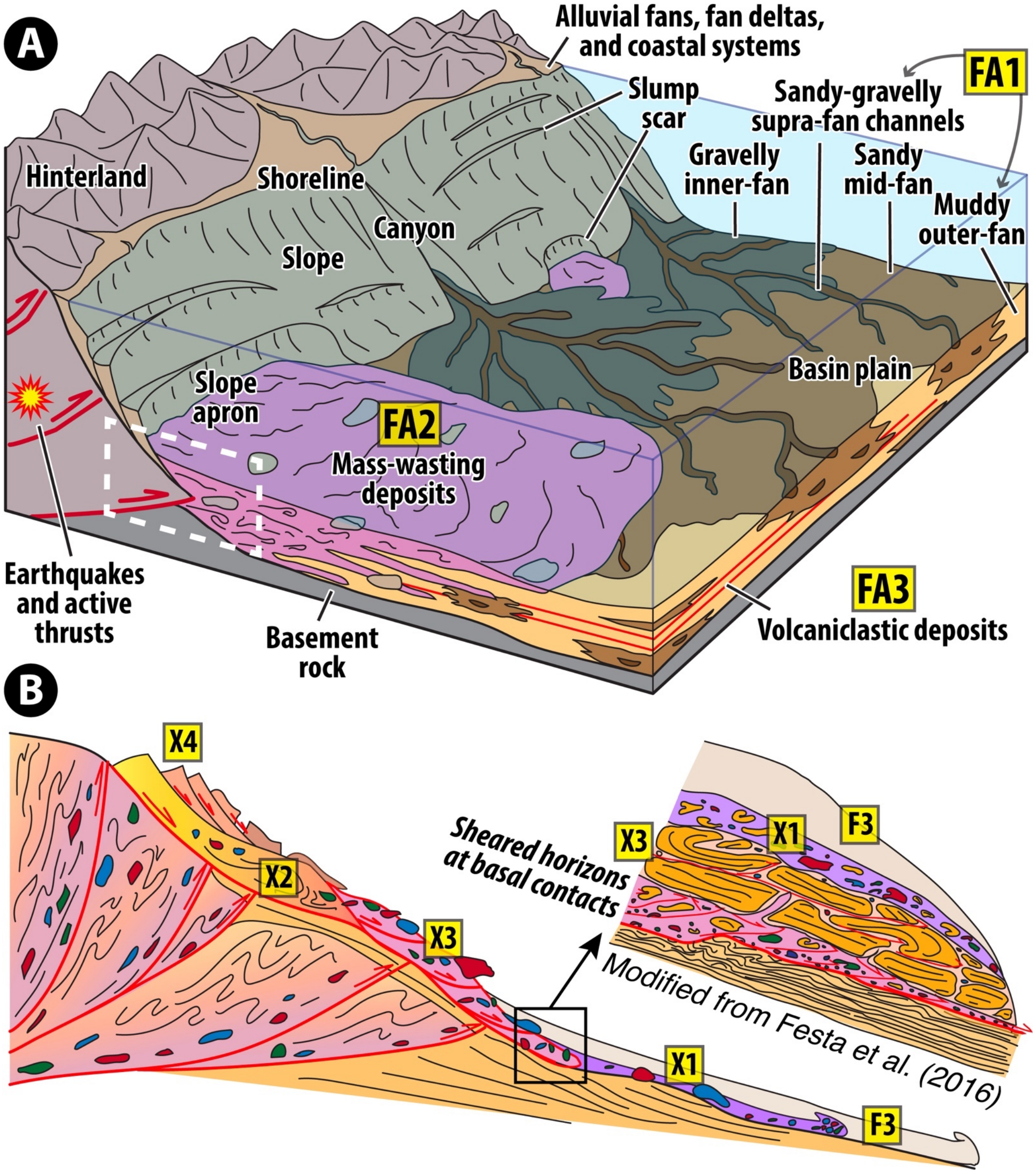

Figure 15. Lithofacies classification scheme. (A) Depositional environment model (modified from Stow and Mayall (2000)) and facies associations (FA1–3) of the Coastal Range sedimentary rocks. White dash box marks the place where mélange-forming processes are portrayed in B; (B) Facies model (modified from Festa et al. (2016); Ogata et al. (2012)) for mass-wasting deposits (facies association FA2) and structurally orientated shears (facies association FA3). See detail descriptions of lithofacies and facies associations in Tables 1, 2.

Formation below the basal unconformity (Figure 3). These results are consistent with the presence of north-trending volcanic arc main body identified in the offshore directly east of Taiwan based on well-defined magnetic (Hsieh et al., 2014; Shyu et al., 1996) and gravity anomalies (Doo et al., 2018). We infer that the offshore volcanoes have subsequently subsided below sea level and are now being deformed in an active offshore imbricate thrust belt (Hsieh et al., 2020).

Based on facies interpretations above, we conclude that strata of the southern Coastal Range accumulated in a syn-orogenic, syn-collisional marine foredeep basin directly east of a steep orogenic front that formed the tectonically active western margin of the basin (Figure 15). Active volcanoes east of the basin delivered distal tuffaceous turbidites during this time (~4–1 Ma), suggesting the eruptive centers shifted to the east during development of the basal unconformity and retro-foredeep system (see Section 8.2). The implied Plio-Pleistocene volcanoes are distinctly younger than the ~15–6 Ma volcanic arc and forearc environments recorded in the underlying Tuluanshan Formation, and may be related to a "double island arc" interpretation proposed by Yang et al. (1996).

8.2. Retro-foredeep basinal system in the Luzon forearc

Results of our geologic mapping and basin reconstruction reveal that the modern topography of the Coastal Range is controlled by tightly folded and faulted rocks of a marine foredeep basin that formed on the eastern retrowedge flank of the Taiwan orogen, and later was deformed into the present configuration of regional thrust faults and related anticlinal culminations (Figures 2B, 16A) (e.g., Chen et al., 2019; Dorsey, 1988; Lundberg & Dorsey, 1988). This conclusion is a departure from previous interpretations that high topographic ridges in the Coastal Range represent an inherited configuration of relatively undeformed volcanic islands and surrounding forearc, intra-arc, and backarc basins (Figures 2A, 16B) (e.g., Chen, 1988a; Huang et al., 1995; Teng et al., 1988).

Data presented above provide evidence for east-dipping paleoslopes and olistostromal facies in the west, which pass laterally eastward into an eastward-thinning marine flysch succession that onlaps onto a gently west-dipping regional unconformity (Figures 12, 13). While the observed basin geometry differs from the filling style of typical forearc basins (Noda, 2016, 2018), it is similar to the architecture of the modern

North Luzon Trough as seen in offshore seismic reflection studies south of Taiwan (e.g., Chi et al., 2014; Hirtzel et al., 2009; Lundberg et al., 1997). This similarity suggests that the eastward-onlapping pattern of Plio-Pleistocene orogen-derived deposits in the Coastal Range may reflect inherited, pre-collisional forearc basin bathymetry. It is also not certain that the east-dipping paleoslope at the west margin of the 4–1 Ma Coastal Range basin was controlled by east-vergent thrusts, as proposed by previous workers (e.g., Lundberg & Dorsey, 1990; Page & Suppe, 1981; Suppe & Liou, 1979) and this study (Figures 15A, 16), considering that the west margin of the modern North Luzon Trough does not show consistent east-vergent thrust structures (Figure 1).

Despite these ambiguities, several observations suggest that the modern setting is not an exact analog for the past. First, the entire Coastal Range basin subsided rapidly below sea level until ~1 Ma, as indicated by the youngest depositional age of thick marine deposits in the north-central Coastal Range (Huang et al., 2018; Lee, 1992). This requires a major tectonic reorganization that abruptly ended subsidence and initiated uplift, precluding gradual southward propagation of the collision (see also Hsu et al. (2016); Lee et al. (2015)). Second, it appears the kinematic style at the east margin of the Taiwan collisional orogen may have become more transpressional in the past ca. 1 Myr during tectonic reorganization (see Section 8.4). Third, the traditional forearc basin model cannot explain the observed sudden change in depositional age and benthic foraminiferal assemblages at the basal contact of SSS, SGS, and BBS sections (Figures 13, S14A-B). In these sections the basal erosional unconformity records an age gap of ~6–4 Myr and is capped by the shallow marine Kangkou Limestone which is directly overlain by deep-water flysch (facies F1 and F2) (Huang & Yuan, 1994). These stratigraphic relations imply a dynamic history of vertical crustal motions comprising regional slow uplift and erosion of forearc volcanic basement (Tuluanshan Formation), deposition of shallow-water limestone on the eroded basement, then rapid subsidence to deep water during initiation of the collisional basin (Dorsey, 1992). The vertical crustal motions have previously been interpreted as a localized intra-arc pull-part mechanism (Huang et al., 1995), but there is no field evidence for large-scale normal faults that postdate deposition of the Kangkou Limestone and predate the Paliwan Formation in the Coastal Range (Barrier & Angelier, 1986; Lin et al., 1999).

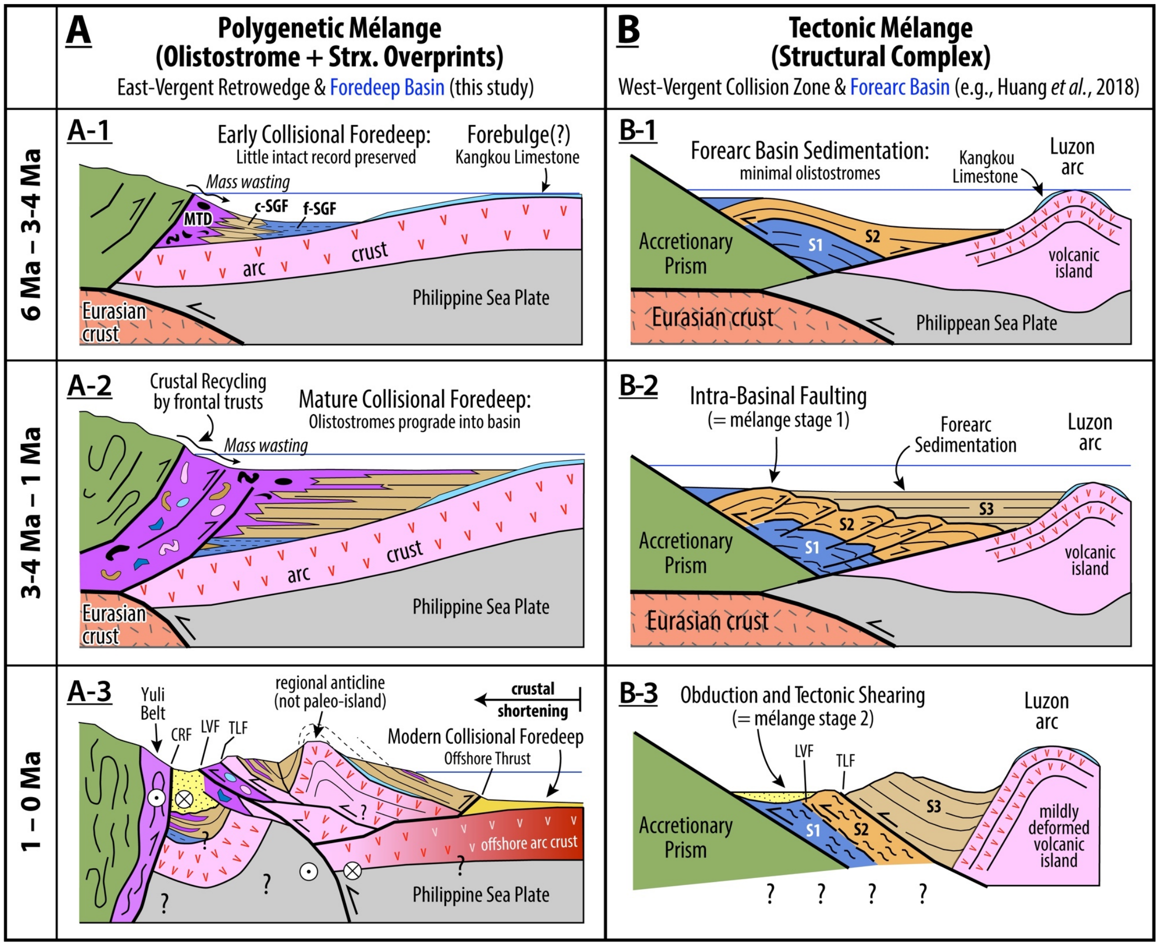

Figure. 16. Synthetic comparison of the two end-member models interpreting the role, age, and evolution of the Lichi Mélange. (A) Olistostromal origin model. Details are synthesized from several publications (Chi et al., 2014; Dorsey & Lundberg, 1988; Malavieille et al., 2016; Page & Suppe, 1981) and this study. MTD is mass-transport deposits (facies association FA2). Coarseand fine-grained facies of cohesionless sediment gravity flows (facies association FA1) are marked as c-SGF and f-SGF respectively. CRF is the Central Range Fault (Shyu et al., 2016). LVF is the Longitudinal Valley fault. TLF is the Tuluanshan fault; (B) Tectonic origin model, modified from Huang et al. (2018) which summarized various versions to date and proposed the presence of chronostratigraphic sequence 1–3 (S1 to S3).

We therefore postulate that the asymmetric westward-deepening basin geometry represents a deflection profile produced by lithospheric flexure in response to tectonic loading in the Taiwan collisional orogen to the west (Figure 16A). This is consistent with rapid sediment accumulation rates in the Coastal Range (≥ 1–7 mm yr−1) that record rapid subsidence east of the growing Taiwan collisional orogen in response to rapid thrust-loading in the orogenic thrust belt during deposition (Lundberg & Dorsey, 1988). Within this framework, the basal unconformity between the Tuluanshan Formation and overlying orogen-derived sediments is interpreted as a result of regional uplift and erosion on a broad flexural forebulge (Dorsey, 1992) (Figure 3). The Kangkou Limestone and Biehchi Epiclastic Unit formed during development of the unconformity (~6–4 Ma), and they represent local thin discontinuous deposits that accumulated intermittently on the flexural forebulge. These relationships suggest rapid subsidence in response to an eastward migrating wave of flexural depression that is a common aspect of foreland basin evolution (DeCelles, 2012; DeCelles & Giles, 1996).

This hypothesis is consistent with the observed eastward progradation of coarse-sediment facies including mass-wasting deposits (X1 and X3) and channelized gravelly sediment gravity-flow deposits (F3 and F4), which are best explained as the result of basinward migration of the depocenter in response to an eastward advancing submarine slope at the retrowedge orogenic front, likely caused by a series of east-vergent thrusts (Figures 15A, 16A). This pattern represents a marine analog to migrating coarse-sediment facies that are commonly interpreted as a response to a migrating flexural wave in terrestrial foreland basins (Dubille & Lavé, 2015; Heller et al., 1988; Sinclair, 2012). Lithofacies of the Tuluanshan Formation beneath the basal unconformity (Figure 3) make up a sequence of volcanic and volcaniclastic rocks that record underwater to subaerial eruptions within and on the flanks of late Miocene (~15–6 Ma) subduction-related arc volcanoes (Chen, 1997a; Lai & Song, 2013; Song & Lo, 2002). This suggests that the Plio-Pleistocene retro-foredeep basin of the Coastal Range formed on top of older, deeply subsided crust of an inactive Luzon Arc, similar to the modern retro-foredeep in the North Luzon Trough offshore of southeastern Taiwan (Figure 1). In the modern southeast offshore region, a unique collisional foredeep basin is forming where the forearc is closing due to the transition from intra-oceanic subduction to a mature arc-continent collision (e.g., Hirtzel et al., 2009; Lundberg et al., 1997).

8.3. Genesis and distribution of the Lichi Mélange

All published studies agree that the modern expression and distribution of the Lichi Mélange are influenced by tectonic shearing related to faults in the western Coastal Range that have been active in the past ca. 1 Myr (e.g., Chang et al., 2000; Page & Suppe, 1981). However, there is a considerable debate over the question of whether sedimentary processes (e.g., sliding and slumping) were involved in formation of this mélange (Chen, 1997b; Huang et al., 2018; Teng, 1981). This study confirms the ubiquitous presence of depositional contacts and interbedding between Lichi Mélange and Plio-Pleistocene orogen-derived flysch facies of the Fanshuliao and Paliwan formations (Figures 8, 10). Young (~4–1 Ma) microfossils coexist among these sedimentary units in the southern Coastal Range (Figure 11), providing an important new constraint on this question. Our data show that the Lichi Mélange was generated by olistostromal and mass-wasting processes (Figure 15). We also observe evidence of overprinting tectonic shear fabrics and fault-zone breccias produced by post-depositional, cross-cutting, west-vergent thrust faults including the Tuluanshan fault (Figures 4, 7). This late-stage structural disturbance is currently active along the strands of the Longitudinal Valley fault (Angelier et al., 2000; Lee et al., 2006). The structural fabrics related to young deformation are mainly restricted to brittle damage zones within and adjacent to the faults, and they are volumetrically minor compared to widespread sedimentary features and depositional contacts that are commonly observed in the Lichi Mélange (Barrier & Muller, 1984; Page & Suppe, 1981).

Based on evidence presented above, we propose a polygenetic model for evolution of the Lichi Mélange in eastern Taiwan (Figure 16A). During the growth of orogenic topography between ~6 and 1 Ma, eastward propagating thrust faults drove basinward migration of a steep submarine slope at the advancing retrowedge front of the collisional orogen (e.g., Malavieille et al., 2021) (Figure 16A-1, A-2). Thrustcontrolled slope oversteepening resulted in slope failures, slides, and slumps that produced olistostrome deposits at the western margin of a syn-orogenic marine foredeep basin formed on older inactive arc and forearc crust (Figure 15A). During the advance of the orogenic thrust front, older olistostromes and associated sediments may be reworked into the frontal slope to produce new olistostromes, thus forming an "olistostromal carpet" (see Festa et al. (2010) and references therein). Later, the olistostrome deposits were overprinted by post-depositional tectonic fault zones associated with the Tuluanshan and Longitudinal Valley faults (Figure 16A-3). The young, post-1 Ma stage of active deformation and rapid uplift inverted the foredeep basin along west-vergent thrusts in the Coastal Range (Lundberg & Dorsey, 1990), rapidly constructed steep rugged topography of the modern Coastal Range, and overprinted the Lichi Mélange to form a polygenetic mélange.

Our interpretation for the Lichi Mélange contrasts with a popular model proposed in prior studies, in which the Lichi Mélange solely formed by tectonic shearing of older sedimentary rocks in an east-vergent then west-vergent mega-thrust zone as a result of large-scale tectonic shortening in the forearc region (e.g., Chang et al., 2001; Chen, 1997b; Huang et al., 2018) (Figure 16B). New constraints on the age, contacts, map relations, interbedding, and sedimentary facies associations (this study) contradict the "tectonic-only" mélange model, and clearly require emplacement by submarine mass wasting. Some workers suggest that preservation of the Lichi Mélange in the western belt of the southern Coastal Range indicates that it formed as a tectonic mélange produced entirely by fault zone deformation (Chen, 1991; Huang et al., 2018; Teng, 1981). However, the affinity of mélange to fault zones only suggests the likelihood of structural overprints, and does not provide evidence for its origin (Festa et al., 2019; Raymond, 2019; Wakabayashi, 2019). In fact, abundant olistostromal facies such as slump beds (X2), pebbly mudstone (X1), and olistoliths (X4) are also reported close to mapped patches of Lichi Mélange in the northern Coastal Range (e.g., Lundberg & Dorsey, 1988; Song et al., 1994; Teng et al., 2002), suggesting that deposits associated with the sedimentary mélange are common in the northern Coastal Range as well.

The extent to which tectonic deformation has been absorbed in the present form of the Lichi Mélange remains unclear. It is plausible that post-depositional structures (both pre-1 Ma east-vergent thrusts and post-1 Ma west-vergent thrusts) influenced some of the shear surfaces formed by preceding olistostromal processes (Figure 16A-2, A-3). Further meso-scale and microscopic studies of shear fabrics in the mélange matrix are needed to address this question.

8.4. Crustal shortening and tectonic recycling at the suture of an arc-continent collision

Because the Lichi Mélange formed primarily by sedimentary mass-wasting processes, the belt of rocks mapped as this mélange should not be considered as a "mega-thrust" zone that absorbs most of the crustal shortening associated with accretion of the Luzon Arc (e.g., Chang et al., 2001; Chen, 1997b; Huang et al., 2008; Teng, 1987).

Tectonic horizontal shortening within the Coastal Range is primarily taken up by structures of the west-vergent fold-and-thrust belt that initiated ca. 1 Ma and postdate deposition in the Coastal Range foredeep basin (Chi et al., 1981; Dorsey, 1992). In addition, paired shortening on the oblique west-vergent Longitudinal Valley fault and east-vergent thrust belt offshore of eastern Taiwan (e.g., Hsieh et al., 2020; Huang et al., 2010) suggests that the Coastal Range is an active doubly-vergent transpressional wedge within the active collisional suture between the Eurasian and Philippine Sea plates (e.g., Malavieille et al., 2016; Thomas et al., 2014) (Figure 16A). Similar doubly-vergent wedge structures have been reported in the northern Coastal Range (e.g., Yen et al., 2018), directly offshore to the east (e.g., Hsieh et al., 2020), and the Huatung Ridge in southern offshore (e.g., Chi et al., 2014; Hirtzel et al., 2009; Huang et al., 2000) (Figure 1).

Our data confirm that exotic blocks in olistostromes of the Lichi Mélange, and variably rounded clasts of associated debris flow deposits, contain a diverse set of lithologies including arc-related andesite, andesitic volcaniclastic sandstone, limestone, ophiolitic rocks (gabbro, serpentinite, granodiorite), low-grade metasandstones, slate fragments, and Miocene quartz-rich sandstones that represent fragments of the Eurasian and Philippine Sea plates. This observation, combined with widespread evidence for east- and southeast-dipping paleoslopes, indicates that all of these rock types were exposed and deformed in thrust sheets in the eastern retro-wedge of the Taiwan collisional orogen (Figure 16A). We propose that many of these rock lithologies represent shallow-crustal equivalents of high-P greenschist to blueschist grade metamorphic rocks in the Yuli Belt, which occupies the easternmost belt of the metamorphic Central Range belt directly west of the Coastal Range (Figures 1, 16A). The Yuli Belt was recently recognized as a metamorphosed late-Miocene (~ 6–9 Ma) mélange (Chen, Chung, et al., 2017; Mesalles et al., 2020) that contains Miocene mafic and ultramafic fragments of the South China Sea as well as arc-affinity metavolcanic rocks (Jahn & Liou, 1977; Sun et al., 1998). Unmetamorphosed equivalents of similar aged low-grade meta-sediments (i.e., Eastern Slates) adjacent to the Yuli Belt (Figure 1), interpreted as a former forearc basin sequence (Mesalles, 2014; Stanley et al., 1981), represent the likely source of exotic Miocene sedimentary blocks in the Lichi Mélange (Chi et al., 1981). This idea is supported by the distinctive quartz-rich petrography of exotic sandstone blocks, which closely resembles that of sedimentary rocks now exposed at the south end of the Eastern Slate belt on the Hengchun peninsula (Sung, 1991).

These results suggest that volcanic arc and forearc crustal fragments of the oceanic Philippine Sea plate were tectonically recycled into the eastern retrowedge of the collisional orogen, likely by accretion and/or underplating within a subduction zone or subduction channel complex. This took place during deposition of the Lichi Mélange, prior to final closure of the retro-foredeep basin (Malavieille et al., 2016; Page & Suppe, 1981; Suppe & Liou, 1979). A modern analog may be seen in the Timor arc-continent collision system, where a retro-foredeep basin is currently active in the Banda forearc region and fragments of the Banda Arc crust have already been emplaced in the Bobonaro Mélange in the retrowedge sector of the active Timor collisional orogen (e.g., Harris et al., 1998; Tate et al., 2015). Another comparable example of tectonically reworked olistostromes that formed in the retrowedge of a collisional orogen is well-documented in the late Cretaceous – Eocene northern Apennine belt in Italy (e.g., Barbero et al., 2020; Malavieille et al., 2016).

During the past ca. 1 Myr, the Lichi Mélange and retro-foredeep strata of the Coastal Range have been rapidly uplifted, imbricated, and incorporated along with underlying volcanic arc crust into the leading edge of the modern collisional orogen (Figure 16A). These rocks are now part of a new, rapidly uplifting emergent mountain range (Coastal Range) that represents a potential source for a new generation of mélange formation (either tectonic or sedimentary). This large-scale mechanism of arc crustal shortening and tectonic recycling at the ocean-continent interface of a doubly-vergent collisional orogen may be a general process in the formation of polygenetic mélange in arc-continent collision systems, which play a critical role in the growth of continental lithosphere through time (Clift et al., 2008; Draut & Clift, 2012).

9. Conclusions

Our multidisciplinary study confirms a sedimentary origin for the ca. 4–1 Ma Lichi Mélange in the southern Coastal Range of eastern Taiwan. This unit formed by submarine slope failures, slides, slumps, and debris flows that interfinger laterally with a coeval thick (ca. 4–7 km) succession of turbidite-dominated flysch deposits that filled a syn-orogenic marine retro-foredeep basin. The entire syn-collisional succession overlies and onlaps eastward onto a regional unconformity that formed by erosion of older, late Miocene volcanic-arc and forearc-basin deposits. Major arc volcanism recorded in the Miocene Tuluanshan Formation ceased prior to the onset of eastward migrating subsidence, which we infer took place in front of the east-vergent retrowedge of the collisional orogen. Minor tuffaceous turbidites in the post-Miocene flysch sequence record input from a different, younger volcanic source that was located offshore to the east during Plio-Pleistocene basin development. Diverse rock types in Lichi Mélange blocks and clasts of associated debris flow deposits indicate that arc and forearc crustal fragments of the oceanic Philippine Sea plate were tectonically recycled into the eastern retrowedge belt of the collisional orogen during the 4–1 Ma formation of the Lichi Mélange and associated flysch deposits near the tectonically controlled western margin of the basin.

During the past ca. 1 Myr, the Lichi Mélange and retro-foredeep strata of the Coastal Range have been rapidly uplifted, deformed, and incorporated into the ocean-facing margin of the modern collisional orogen along with underlying Miocene volcanic arc crust. The present-day expression of the Lichi Mélange is modified by structural overprints and fault-zone fabrics, but the mélange itself did not form solely by fault-zone processes. It is a complex association of olistostromes emplaced by large submarine slides and slumps derived from the eastern retrowedge of the Taiwan collisional orogen. These results reveal a dynamic and complicated history of mélange-forming processes in respond to frequent rock mixing and reworking at the oceanic interface of an active arc-continent collision. Similarity between our findings in eastern Taiwan and other polygenetic mélanges associated with retrowedge basins suggests that tectonic recycling linked to crustal shortening may be a common process in retrowedge foredeep basins of active collisional orogens, particularity in (but not limited to) arc-continent collision systems.

10. Bridge

Chapter II investigates long-debated genesis of the Lichi Mélange and associated of retrowedge foredeep basin developed on top of the Luzon Arc crust during Taiwan's orogenesis. The results show how crustal materials got progressively mixed and recycled at an arc-continent collisional suture zone via both structural burial, mixing, exhumation, and sedimentary redistribution. Debates and conflicts in nomenclatures and regional geological observations are systematically reviewed. Combined microfossil biostratigraphy, magnetostratigraphy, and lithofacies analysis offers new insights to the syn-orogenic evolution history of the southern Coastal Range basin and its depositional environment. This accomplishment serves as an important basis of regional geology and stratigraphic framework for the subsequent chapters in this dissertation. In Chapter III, I present results of back-stripping analysis using data from Chapter II and new data in northern Coastal Range. The study in Chapter III aims to detect the style, magnitude, and rate of vertical motions of the accreting Luzon Arc crust involved in creation of the modern Coastal Range.

CHAPTER III

EXTREMELY RAPID UP-AND-DOWN MOTIONS OF ISLAND ARC CRUST DURING ARC-CONTINENT COLLISION

This chapter has been published as Lai, L. S.-H., Dorsey, R. J., Horng, C.-S., Chi, W.-R., Shea, K.-S., and Yen, J.-Y. (2022) Extremely rapid up-and-down motions of island arc crust during arc-continent collision. *Communications Earth & Environment*, 3(1), 100. I, Rebecca. J. Dorsey, and Jiun-Yee Yen conducted field geological surveys and sedimentologic and stratigraphic measurements. Chorng-Shern Horng and I are responsible for sampling and experimental works for paleomagnetism study. Wen-Rong Chi, Kai-Shuan Shea, and I performed microfossil identifications and biostratigraphic analysis. I am the lead author on the paper, which involved data synthesis and analysis, programming for basin subsidence modeling works, preparation of figures and tables, and writing the entire manuscript. All other coauthors assisted with data interpretation and editorial feedback.

1. Introduction

Vertical crustal motions are fundamental to the creation of topography, development of sedimentary basins, and the rock cycle (Champagnac et al., 2012; Turner & Williams, 2004). Rapid vertical displacement rates (mm yr^{-1}) are often driven by tectonic processes such as crustal thickening in Tibet (Taylor et al., 2021) and Taiwan (Lundberg & Dorsey, 1988, 1990; Sandmann et al., 2015), strike-slip deformation along the San Andreas fault (Dorsey et al., 2011; Spotila et al., 2001), lithospheric thinning in Central Anatolia (Öğretmen et al., 2018) and D'Entrecasteaux island of Papua New Guinea (Baldwin et al., 2004), and deflections due to changes in surface or subsurface mass loads in Hawaii (Watts & Cochran, 1974) and Antarctica (Barletta et al., 2018). Mass redistribution by erosion and sedimentation amplifies vertical crustal motions (Willett, 1999) and is important for understanding interactions between tectonic and surface processes involved in mountain building and continental growth (Lister & Forster, 2009). Among these settings, extreme rates (>10 mm yr^{-1}) of long-term (>10^5–10^7 years) rock uplift are seldom detected (Gingerich, 2021). Many studies rely on thermochronology (Reiners & Brandon, 2006) and petrology-geochemistry (Brown, 2014) to assess long-term vertical movements of crustal materials, but these methods are limited by the requirement of suitable minerals, geothermal gradient, temperature, and duration needed to thermally reset thermochronometers. Assumptions of ancient topography and thermal structure are often essential for use of thermochronologic methods to estimate long-term rock uplift (Braun et al., 2006), but it is difficult to constrain these quantities in rapidly growing orogens constructed of unmetamorphosed rocks. Thus, the rates, timescales, and structural controls on vertical motions of shallow crust in active mountain belts remain poorly understood.

Stratigraphic study of inverted syn-orogenic sedimentary basins provides a powerful tool with which to document rapid subsidence and uplift of unmetamorphosed near-surface rocks in zones of mountain building at tectonically active plate margins (Turner & Williams, 2004). Integrated paleomagnetic and biostratigraphic analysis can yield extremely high resolution [e.g., ± 5–20 thousand years (kyr)] for dating stratigraphic intervals (Dorsey et al., 2011), and thus, remarkably high-fidelity estimates for rates of vertical crustal motions and tectonic processes. We applied this technique to investigate stratigraphic records of the Coastal Range in eastern Taiwan, which reveal a history of extremely rapid vertical crustal oscillations during accretion of volcanic-arc crust to a continent.

The island of Taiwan has emerged since late Miocene time through active collision between the Luzon island arc on the Philippine Sea plate and the Chinese continental margin of the Eurasian plate (Byrne et al., 2011) (Figure 1). Rapid (~82 mm yr^{-1}) oblique convergence (Yu et al., 1997) between the two plates induces rapid exhumation and denudation (Dadson et al., 2003), and some studies infer that collision has propagated southward through time (Huang et al., 2006; Suppe, 1981; Teng, 1990). Other studies of the metamorphic core (Central Range) and western foreland basin suggest that collision was geologically simultaneous from north to south, with pulses of accelerated exhumation from ~0.1 to 2–4 mm yr^{-1} at 2.0–1.5 million years ago (Ma) and then to 4–8 mm yr^{-1} at ~0.5 Ma (Hsu et al., 2016; Lee et al., 2015). These accelerations correspond to tectonic reorganizations of the overriding Philippine Sea plate (Sibuet et al., 2021; Wu et al., 2016) that drive exhumation of high-pressure metamorphosed

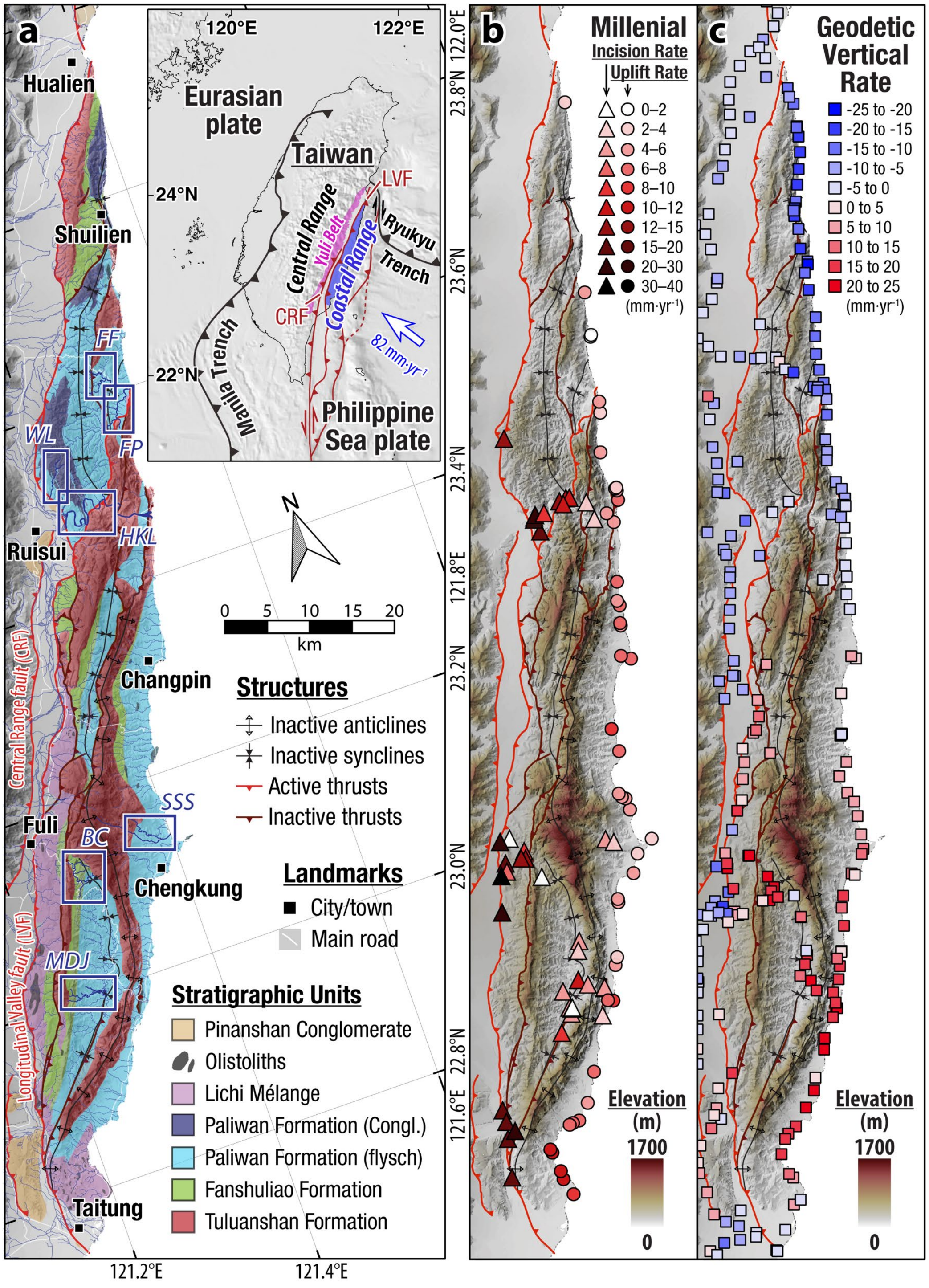

Figure 1. **The Coastal Range of eastern Taiwan.** (a) Regional tectonic configuration (Sandmann et al., 2015; Sibuet et al., 2021) (inset), simplified geological map of the Coastal Range (Lai, Dorsey, et al., 2021) and analyzed stratigraphic sections (blue boxes), including Hsiukuluan river (HKL), Wulou river (WL), Fungfu (FF), and Fungpin (FP) sections in the north, and Bieh river (BC), Madagida river (MDJ), and Sanshian river (SSS) sections in the south. (b) Millennial rates of marine terrace uplift and river incision, compiled by Lai, Roering, et al. (2021) **(c)** Geodetic rates of vertical deformation measured during 2000-2008 (Ching et al., 2011). Negative values mean subsidence.

Miocene arc crust-bearing mélange (Yuli Belt) from >35 km crustal depth (Chen, Chung, et al., 2017; Lo et al., 2020; Mesalles et al., 2020; Sandmann et al., 2015; Yui et al., 2014) and rapid Quaternary emergence of the unmetamorphosed arc crust in the Coastal Range (Lundberg & Dorsey, 1990).

The Coastal Range contains a thick succession of Plio-Pleistocene orogen-derived marine flysch, conglomerate (Fanshuliao and Paliwan formations), and olistostromes (Lichi Mélange) that rest unconformably on Miocene volcanic arc basement (Tuluanshan Formation, ca. 15–6 Ma) (Figure 2) (Dorsey, 1992; Lai, Dorsey, et al., 2021). The basal unconformity (ca. 6–4 Ma) is a broad erosive surface discontinuously capped by thin shallow-marine limestone (Kangkou Limestone, 5.6–3.5 Ma) and limestone clast-bearing epiclastic deposits (Biehchi Epiclastic Unit, 5–3.5 Ma) that are directly overlain by uncemented deep-water flysch (Huang & Yuan, 1994; Lai, Dorsey, et al., 2021). These relations record slow uplift, erosion, and intermittent sedimentation on arc basement near sea level, followed by rapid subsidence that created accommodation space for thick basin-filling sediment (Dorsey, 1992; Lundberg & Dorsey, 1988). Basin inversion and uplift must have occurred in the last roughly 1 million years based on observation of the tilted youngest marine flysch and creation of modern Coastal Range topography (Lundberg & Dorsey, 1990). Yet, the timing and rates of these processes remain unclear. Thermochronology and petrological methods are not suitable for solving this problem because of the short duration of burial and very low paleo-geothermal gradient revealed by clay mineralogy (~14 °C km^{-1}) (Dorsey et al., 1988) and no post-depositional resetting of fission-track detrital thermochronometers (Kirstein et al., 2014). Early studies used calcareous nannoplankton data (Chang & Chi, 1983; Chi et al., 1981) and simplified lithostratigraphic columns to derive a range of subsidence rates (0.8–5 mm yr^{-1}) and minimum uplift rate (5.9–7.5 mm yr^{-1}) with unknown spatial variability (Lundberg & Dorsey, 1988, 1990). Many of these studies are now outdated and pre-date recent advances in paleomagnetism and microfossil studies (Chen, Huang, et al., 2015; Horng & Shea, 1996; Lai, Dorsey, et al., 2021; Lee, 1989, 1992).

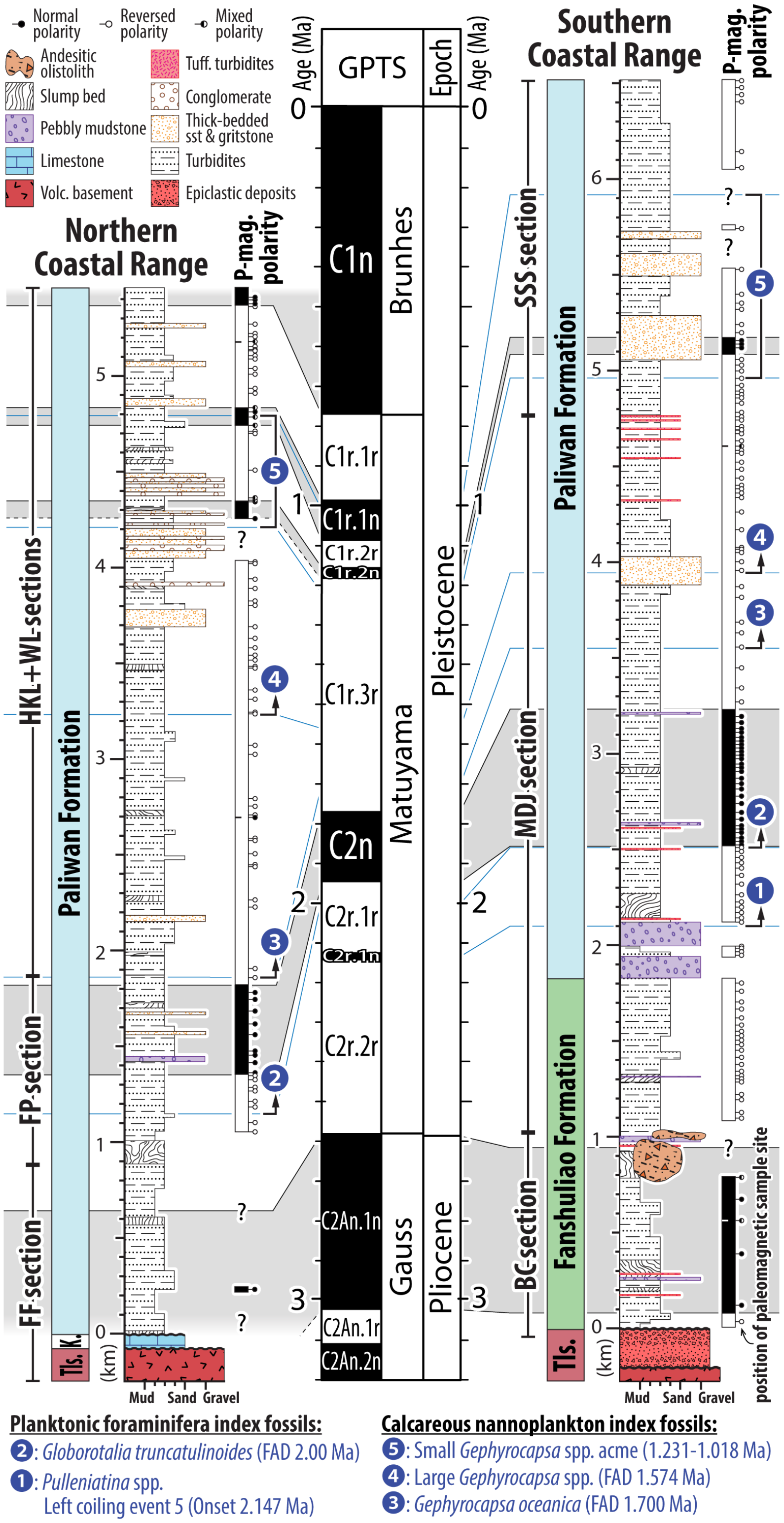

Figure 2. Stratigraphy of the Coastal Range. Locations of studied sections are shown in Figure 1. GPTS = Geomagnetic polarity timescale. FAD = First appearance datums of index microfossils. Tls. = Tuluanshan Formation; k. = Kangkou Limestone. See details of stratigraphic correlation in Supplementary Figures 1–2.

To document the timing, magnitude, and rates of vertical crustal motions in the Coastal Range of eastern Taiwan, we compiled geologic and magneto-biostratigraphic data to date and accurately reconstruct two composite stratigraphic columns in the northern and southern Coastal Range (Figures 1–2). This includes our published data from the southern Coastal Range (Lai, Dorsey, et al., 2021) (Supplementary Figure 1) and new detailed geologic mapping, paleomagnetic measurements, and microfossil identifications of planktonic foraminifera and calcareous nannoplankton in the northern Coastal Range (Supplementary Figures 2–6; Supplementary Data 1–2). The foraminifera data provide improved paleobathymetry estimates (Supplementary Figure 7, Supplementary Data 3), and compiled magneto-biostratigraphy constrains depositional age (Figure 3a). Dense sampling of microfossils and paleomagnetic sites yields high temporal resolution (~1–15 kyr) and high accuracy (2–43 kyr) of age controls that surpass other geologic dating methods (Supplementary Data 4). Because the youngest inverted sediment is consolidated and lithified, we have to account for deposits that accumulated above the top of our measured sections and subsequently were removed by erosion. Porosity-effective stress of sandstone and vitrinite reflectance data indicate that ca. 0.45–1.95 km of strata was eroded off the youngest deposits preserved in our measured sections (Hong, 2020). Due to uncertain variability of compaction history and geothermal structure, we used a conservative thickness of 0.5–1.0 km for eroded sediments to reconstruct the deepest subsidence prior to onset of structural inversion (Figure 3a).

Using high-fidelity constraints on stratigraphy and paleobathymetry, updated eustatic sea level curve (Supplementary Figure 7), and porosity-depth functions for relevant sediment types (Supplementary Figure 8), we conducted a modern 1-D backstripping analysis (Allen & Allen, 2013) to progressively remove decompacted sediment and correct paleo-water depth along two composite sections. This allowed us to reconstruct the history of subsidence and uplift of arc basement in the north and south (Figure 3b–c). See details in the Methods section.

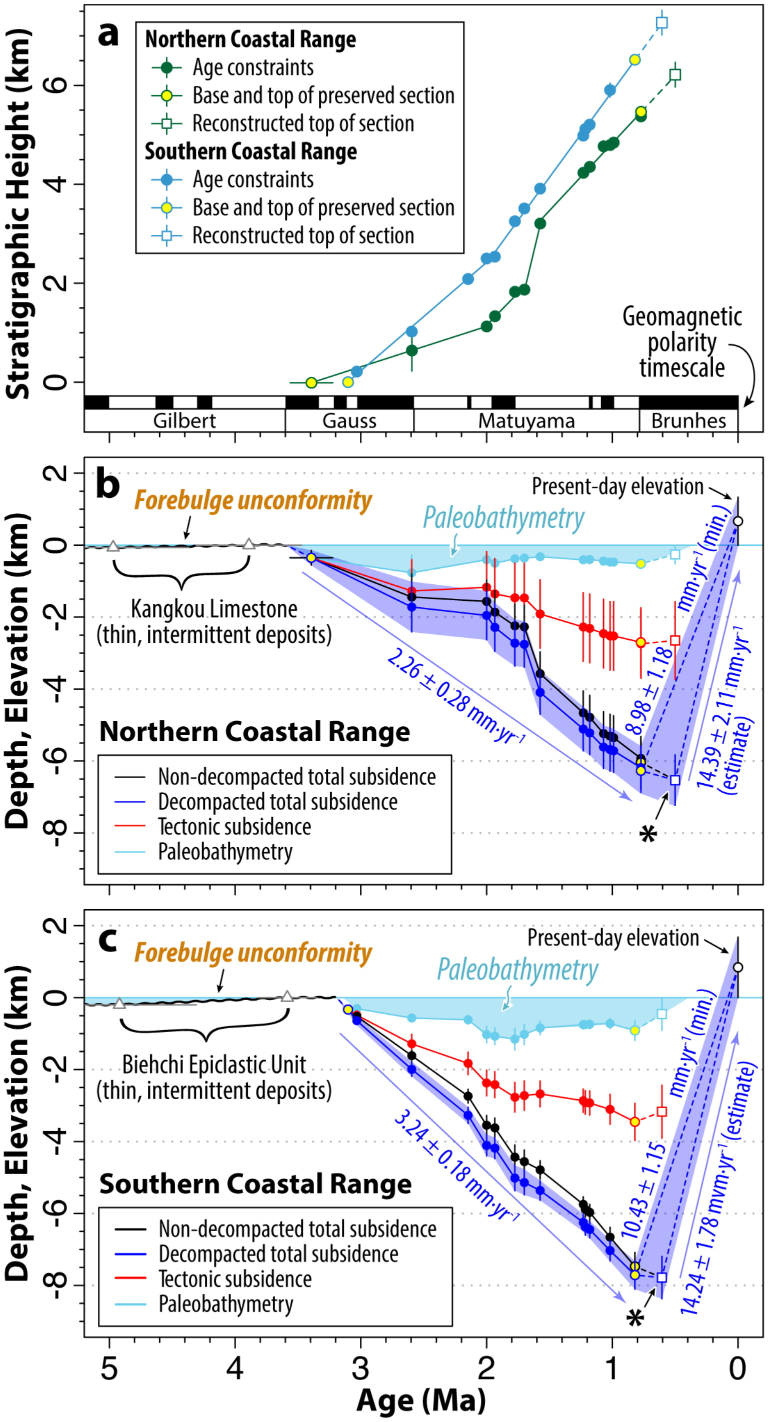

Figure 3. Sediment accumulation rates and subsidence-uplift histories of the Coastal Range. (a) Stratigraphic age models for the Coastal Range. (b-c) Geohistory curves of the northern and southern Coastal Range. Symbols and color-fill style follow Figure 3a. Asterisk in each curve is the reconstructed depth using youngest sediment eroded from top of section. See details of data and calculation results in Supplementary Data 4.

2. Results and Discussion

2.1. Subsidence-uplift histories of the Taiwan Coastal Range

Our results reveal that >5.48–6.51 km of preserved orogen-derived sediment accumulated between ~3.39 and 0.77 Ma, with a minor increase in sedimentation rate at ~2.0 Ma (Figure 3a). Volcanic-arc basement subsided to depths of 6.53–7.78 km below modern sea level at rates of 2.26 mm yr^{-1} in the north and 3.24 mm yr^{-1} in the south, with tectonic forces and sediment loads making subequal contributions to the total subsidence (Figure 3b–c). The age of youngest, now-eroded sediment is estimated to be ~0.61–0.50 Ma, providing a reasonable age estimate for the end of subsidence and onset of structural inversion (Figure 3a). Since the folded basal unconformity and underlying volcanic basement rocks are exposed well above sea level, the difference between present-day heights of antiformal peaks and the reconstructed depth of arc basement at the end of deposition (0.82–0.77 Ma for the youngest preserved sediment; 0.61–0.50 Ma at the top of eroded sediment) provide a conservative estimate for the amount of vertical displacement during basin inversion. To exhume the volcanic-arc basement to present elevations of the Coastal Range (0–1.33 km in the north, 0–1.68 km in the south) requires extremely rapid rock uplift rates of at least 8.89–14.39 mm yr^{-1} in the north and 10.43–14.24 mm yr^{-1} in the south (Figure 3b–c; Supplementary Data 4).

The minor increase in sedimentation rate at ~2.0 Ma and onset of basin inversion at ~0.8–0.5 Ma are coeval with proposed episodes of accelerated rock exhumation in the metamorphic Central Range to the west (Hsu et al., 2016) (Figures 3a and 4a). Post-0.5 Ma uplift rates of ca. 9–14 mm yr^{-1} represent the lower bound of long-term average exhumation rates in the Coastal Range. These rates are intermediate between spatially variable millennial uplift rates measured in coastal marine terraces (2.3–11.8 mm yr^{-1}) (Chen et al., 2020; Hsieh & Rau, 2009) and fluvial incision rates (15.1–27.3 mm yr^{-1}) measured near the western major oblique thrust fault (Longitudinal Valley fault) (Shyu et al., 2006) (Figure 1b). Notably, millennial uplift rates in the northern Coastal Range (2.3–4.7 mm yr^{-1}) (Chen et al., 2020; Hsieh & Rau, 2009) are considerably slower than our calculated long-term exhumation rates (~9–14 mm yr^{-1}), and geodetic data (Ching et al., 2011) reveal subsidence at rates locally up to ~23.5 mm yr^{-1} in the north (Figure 1b–c).

This implies that the northern part of inverted arc crust may have entered a new subsidence stage very recently.

Taken together, the stratigraphic record in the Coastal Range reveals two short cycles of up-and-down crustal motions (Figure 3b–c). Coeval histories of uplift and subsidence in the north and south support an interpretation of simultaneous crustal dynamics along the collisional suture (Hsu et al., 2016; Lee et al., 2015; Sibuet et al., 2021), in contrast to southward-propagating growth of the Taiwan orogen inferred in some models (Huang et al., 2006; Suppe, 1981; Teng, 1990). These findings indicate the need for a revised tectonic interpretation to explain the observed rapid vertical oscillations of arc crust in this active arc-continent suture zone.

2.2. Drivers of rapid crustal oscillations during oceanic arc accretion

We infer that the first cycle of uplift (~6–3.4 Ma) and subsidence (~3.4–0.5 Ma) of volcanic basement was driven by early flexure and loading of accreting Luzon arc crust. This interpretation is supported by recent results showing that Plio-Pleistocene sediments (Lichi Mélange, Fanshuliao and Paliwan formations) formed on – and were derived from – an east-dipping submarine paleoslope at the steep western margin of the basin (Lai, Dorsey, et al., 2021; Page & Suppe, 1981). These sediments onlap the westward-inclined basal unconformity on top of Miocene arc basement (Tuluanshan Formation) and display lateral facies changes that record eastward progradation of coarse deposits into the basin (Lai, Dorsey, et al., 2021). These observations are best explained by basinward migration of the depocenter in response to eastward migration of a thrust-bounded submarine slope at the retrowedge orogenic front (Figure 4a). Thus, the first stage of vertical crustal oscillation in the Coastal Range (slow uplift) is interpreted as a signal of forebulge uplift. This stage was followed by subsidence in an evolving retrowedge foredeep basin driven by eastward migration of a flexural wave (Dorsey, 1992; Lundberg & Dorsey, 1988). These processes took place during development of the prowedge foreland basin in western Taiwan starting ~6.5–5 Ma (Lee et al., 2015; Lin & Watts, 2002).

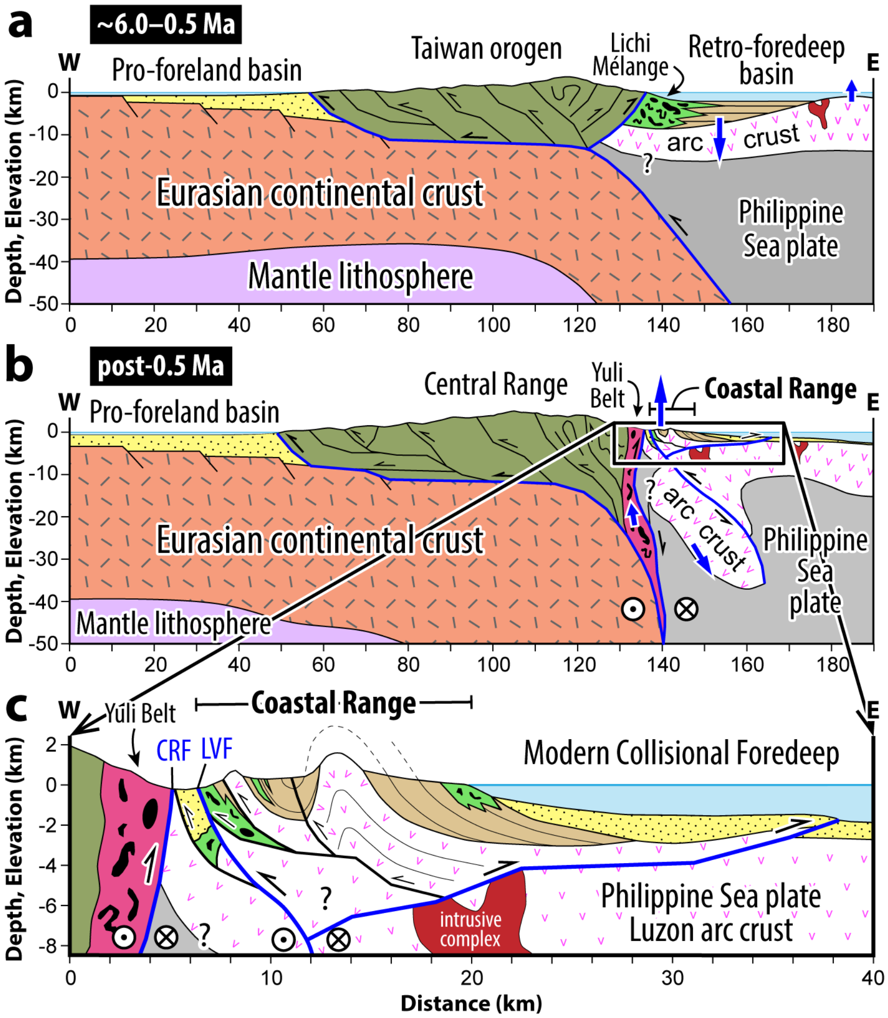

Figure. 4. Conceptual model for the history of vertical motions (blue arrows) of the Philippine Sea plate arc crust in the past ~6 Ma. (a) Forebulge uplift and foredeep subsidence occur on the Luzon arc crust during 6–0.5 Ma, in response to eastward migrating orogenic load (Dorsey, 1992; Lai, Dorsey, et al., 2021). (b) Post-0.5 Ma rapid uplift due to transpressional deformation and isostatic rebound of the overriding plate (Lundberg & Dorsey, 1990; Sandmann et al., 2015; Shyu et al., 2011). (c) Representative structural cross-section in the modern Coastal Range (Hsieh et al., 2020; Lai, Dorsey, et al., 2021). Blue lines mark major boundary faults. LVF = Longitudinal Valley fault; CRF = Central Range fault.

The absence of transgressive deposits at the basal unconformity between shallow-marine limestone (5.6–3.5 Ma) and overlying deep-marine flysch (~3.4–3.1 Ma) requires a sudden increase in water depth at ~3.5 Ma (Figure 3b–c). This abrupt subsidence likely resulted from local extensional faulting (Barrier & Angelier, 1986; Huang et al., 1995) in the upper dilating crust of a migrating flexural forebulge (Di Martire et al., 2015), and may be in part related to an increase in orogenic load on the Philippine Sea plate due to accelerated topographic growth in the retrowedge at 3.2 ± 0.6 Ma (Mesalles et al., 2014). Lithospheric bending of the Philippine Sea plate induced by northward subduction at the Ryukyu trench (Wang & Lee, 2011) may have also influenced vertical displacements in the accreting arc crust. However, this hypothesis predicts southward migration (relative to the Coastal Range) of vertical-displacement signals, but the observed cycles of uplift and subsidence occurred simultaneously in northern and southern Coastal Range transects (Figure 3b–c). Therefore, we suggest that northward subduction at the Ryukyu-trench exerted little or no influence on vertical crustal motions during ~6–0.5 Ma basin evolution.

Post-0.5 Ma extremely rapid uplift and basin inversion created the modern topography of the Coastal Range in a small doubly-vergent structural wedge during an abrupt change to wrench-style transpressional deformation (Hsieh et al., 2020; Lai, Dorsey, et al., 2021) (Figure 4b–c). While rapid vertical displacements are observed in other oblique-convergent settings (Dorsey et al., 2011; Spotila et al., 2001), it is unusual to document large-scale exhumation at rates >10 mm yr^{-1} driven solely by upper-crustal deformation. Isostatic adjustments to changes in lithospheric structure provide a mechanism that can explain this behavior (Watts, 2001). A tectonic load on the Philippine Sea plate may have been suddenly released when forearc lithosphere was broken and subducted at the collisional suture zone (Chemenda et al., 2001; Malavieille et al., 2002; Shyu et al., 2011). Downward extraction of lithospheric fragments may have caused rapid exhumation of the overriding plate crust near the suture (Froitzheim et al., 2006; Majka et al., 2014), which may be partially responsible for the post-0.5 Ma uplift of metamorphosed (Yuli Belt) and unmetamorphosed (Coastal Range) arc crust in eastern Taiwan (Figure 4b–c) (Lai, Dorsey, et al., 2021; Sandmann et al., 2015; Zhang et al., 2020). Isostatic compensation by erosional unloading may also have contributed to the creation of topography (Abbott et al., 1997; Molnar, 2012), but its role remains unclear. It is possible that we have underestimated post-0.5 Ma long-term uplift rates in the northern Coastal Range, because present-day topography in the north may currently be influenced by the modern subsidence stage. This youngest and ongoing subsidence likely is driven by northward convergence and reversed subduction polarity of the Philippine Sea plate at the Ryukyu trench (Teng et al., 2000; Yen et al., 2018) (Figure 1).

This study reveals a history of extremely rapid vertical oscillations (up-and-down cycles) of near-surface rocks in only ~3 Myr during active accretion of island arc crust to a growing continental margin (Figure 3). Our results highlight the short-lived episodic nature of arc-continent collision (Draut & Clift, 2013) and challenge ideas about long timescales that are often invoked for the rise and fall of mountainous topography by coupled tectonic and surface processes (10^6–10^7 years) (Allen, 2008). We find that growth of topography to form an eroding steep mountain range directly on the footprint of a formerly subsiding marine basin can be accomplished in only ~500–800 kyr. This study shows that the change of direction in vertical motion, and transformation of a subsiding basin to an eroding mountainous source, can occur very quickly to drive extremely rapid rock cycling and mixing at this and other collisional plate boundaries (Lai, Dorsey, et al., 2021). Because arc collision and accretion are recognized as a fundamental process in the growth of continental crust (Albarède, 1998), our results suggest that extremely rapid vertical crustal motions may be characteristic of deformation in arc-continent suture zones through geologic time (Clift et al., 2003).

Existing methods of thermochronology, petrology, and geochemistry provide a useful record of crustal burial and exhumation in these settings, but they cannot detect such short rapid vertical trajectories in shallow unmetamorphosed crust. Integrated magneto-biostratigraphy and basin subsidence analysis thus offers an important tool for documenting high-resolution histories of vertical crustal motions in tectonically active systems. This approach spans a crucial time gap that needs to be bridged to better understand dynamic feedbacks among long-term geologic (tectonic) processes and shorter timescale impacts such as climate change and landscape response (Allen, 2008; Champagnac et al., 2012; Romans et al., 2016).

3. Methods

3.1. Geological mapping and lithostratigraphy

Detailed geological mapping for this study targeted excellent exposures in road cuts and riverbanks of the Coastal Range (Figure 1). Marker beds (pebbly mudstone and tuffaceous turbidite) and fault zones were carefully mapped across the study area (Supplementary Figures 3–4). We also compiled information from previously published geological maps (Chen & Wang, 1997; Hsu et al., 2017; Hsu, 1956; Huang & Yuan, 1994; Lai, Ng, et al., 2018; Lai & Teng, 2016; Teng et al., 2016; Wang & Chen, 1993; Yi et al., 2012). Lithostratigraphic descriptions in type sections of the southern Coastal Range [Bieh river (BC), Madagida river (MDJ), and Sanshian river (SSS) sections] are from Lai, Dorsey, et al. (2021) (Supplementary Figure 1). New results in the northern Coastal Range [Hsiukuluan river (HKL), Wulou river (WL), Fungfu (FF), and Fungpin (FP) sections] are compiled in Supplementary Figure 2. We produced composite columns for the northern and southern Coastal Range (Figure 2) through correlations based on marker beds and the first appearance datums (FAD) of index fossils (Supplementary Figures 1–2) and aided by construction of a balanced geological cross section (Supplementary Figure 5). This approach assumes that the thickness (i.e., rock volume) of each unit does not change substantially across the local structures (faults and folds).

3.2. Magnetostratigraphy

In the southern Coastal Range, we adapted results and interpretations of paleomagnetic chrons from previous published studies (Horng & Shea, 1996; Lai, Dorsey, et al., 2021; Lai, Ng, et al., 2018; Lai & Teng, 2016) (Supplementary Figure 1). In the northern Coastal Range, we compiled published paleomagnetism data (Lee, 1989, 1992) along with new data from samples collected in coherent strata from continuous sections (Paliwan Formation) for Hsiukuluan river (HKL), Wulou river (WL), and Fungpin (FP) sections, avoiding chaotic mass-transport deposits (slump beds, olistoliths) (Supplementary Figures 2–4). Paleomagnetic samples were collected using a standard (22 mm diameter) drill core from fresh mudstone exposures, and remanent magnetization was measured with a 2G three-axis cryogenic magnetometer. To remove viscous remanent component of overprinting magnetic signals, we applied stepwise thermal demagnetization (THD, from room temperature up to 800°C) or alternating-field demagnetization (AFD, from 0 up to 80 mT) to most samples. We applied a combination of THD and AFD (e.g., THD to 360°C followed by AFD procedure) in cases of some specimens that became thermally unstable at higher temperatures. Through these procedures, we obtained reliable measurements of primary remanent component of the paleomagnetic declination and inclination from Zijderveld-type diagrams at each site

(Supplementary Figure 6). We derived mean paleomagnetic directions by restoring the perturbations of regional folds (bedding dip) (Supplementary Data 1). The age values and their uncertainty ranges of magnetic reversals follow the most recent global geomagnetic polarity timescale (Channell et al., 2020; Ogg, 2020).

3.3. Calcareous nanoplanktons and planktonic foraminifera biostratigraphy

In the southern Coastal Range, we adapted results and age interpretations from previous published studies (Horng & Shea, 1996; Lai, Dorsey, et al., 2021; Lai, Ng, et al., 2018; Lai & Teng, 2016) (Supplementary Figure 1). In the northern Coastal Range, we digitized and manually georeferenced unpublished calcareous nannoplankton fossil charts (Supplementary Data 2) and sample localities (Supplementary Figures 3–4) from original notes and field maps of previous works by W.-R. Chi (Chi et al., 1980; Chi et al., 1981) (Supplementary Figure 2). For planktonic foraminifera biostratigraphy, we compiled published data of index fossils (Chang, 1967, 1968, 1969; Chang & Chen, 1970) and collected five new samples in Fungfu (FF) and Fungpin (FP) sections (Supplementary Figures 2 and 4; Supplementary Data 2). Samples were collected from fresh intact exposures of mudstone, and we used 63 μm sieve to extract proper size foraminifera for identification.

Interpretation of depositional ages is based primarily on the first appearance datum (FAD) for index fossils due to the potential of fossil reworking, which is commonly reported in turbidite-dominated deposits of the Coastal Range (Chen, 2009; Chi et al., 1981; Lai, Dorsey, et al., 2021) and confirmed by our work. Age values and uncertainties are based on recent compilations for the Indo-Pacific region (Chuang et al., 2018; Raffi et al., 2020) (Figure 2).

3.4. Paleobathymetry

When abundance data of both benthic and planktic foraminifera are available, one can empirically estimate the paleobathymetry (W) of the marine sediment through a regression relating planktic percentage ($\%P_s$) to modern water depth(Hayward & Triggs, 2016; van Hinsbergen et al., 2005). The planktic percentage ($\%P_s$) is defined as:

$$\%P_s = 100 \cdot \frac{P}{P + B - S - O} \tag{1}$$

, where P is the number of in situ planktic specimens; B is the number of benthic specimens; S is the number of stress-marker benthic specimens that are more sensitive to other environmental factors (e.g., oxygen level) rather than water depth (in the genera *Bolivina, Bulimina, Chilostomella, Fursenkoina, Globobulimina, Uvigerina* s.s.); O is the number of organically cemented benthic specimens and reworked fossils. Once ($\%P_s$) is calculated, the paleobathymetry (W) can be estimated through this logistic function:

$$W = \exp\left[\alpha + \frac{1}{\beta}\ln\left(\frac{\%P_s}{100 - \%P_s}\right)\right] - 0.1 \tag{2}$$

, where α and β are empirical constants from modern settings. Despite the lack of modern offshore constraints near Taiwan, we adapted $\alpha = 1.45 \pm 0.080$ and $\beta = 5.23 \pm 0.042$ (means ± standard errors) regressed from modern analogue of 0–4500 m water depth in subtropical Pacific near New Zealand by Hayward and Triggs (2016).

We converted qualitative (in ordinal scale) abundance data of from Chang (1967, 1968, 1969) (V: >50 specimens; A: 21-50 specimens; C: 11-20 specimens; F: 6-10 specimens; R: <6 specimens; ?: unsurely identified; D: reworked fossils) into quantitative (ratio) scale with ranges of uncertainty (V = 75 ± 25; A = 35 ± 15; C = 15 ± 5; F = 7 ± 3; R = 3 ± 2; ? = 1 ± 1; excluding reworked fossils) to constrain parameters P, B, and S. Parameter O is assumed to be zero because we have excluded reworked fossils. We then used equation (2) to calculate the paleobathymetry (W) and its uncertainty (standard error) through Gaussian error propagation at each sample site of Chang (1967, 1968, 1969) along studied sections [Fungfu (FF), Fungpin (FP), Bieh river (BC), Madagida river (MDJ), and Sanshian river (SSS) sections] (Supplementary Data 3).

Fossil abundance data are sometimes absent [e.g., data of Hsiukuluan river (HKL) and Wulou river (WL) sections from Chang and Chen (1970)] or paleobathymetry cannot be calculated using the planktic-percentage method (e.g., $\%P_s = 0$ or 100). In these cases, we used an alternative method from Hohenegger (2005), which relies solely on the presence/absence of the benthic species and their modern water depth distributions. The basic function of this method can be written as:

$$W = \sum_{n=1}^{m} l_n {d_n}^{-1} \Big/ \sum_{n=1}^{m} {d_n}^{-1} \tag{3}$$

, where l_n and d_n are the location parameter (i.e., mean water depth) and its dispersion (water depth range) of the *n*th benthic species, respectively; *m* is the total amount of benthic species that are considered. This method is based on the idea that species with narrower present-day depth distribution could yield more information about the paleobathymetry of the sediment than species adapted to live in a wide range of water depth. We collected constraints of the minimum and maximum distributed water depths of different benthic species or genera (ω_{min} and ω_{max} respectively) from publications to date (see cited data in Supplementary Data 3). We then derived the geometric mean ($l_n = \sqrt{\omega_{max} \cdot \omega_{min}}$) and range ($d_n = \omega_{max} - \omega_{min}$) of water depth for each species or genus, and calculated the paleobathymetry (*W*) through equation (3). The uncertainty of paleobathymetry (σ_w) can be estimated as below:

$$\sigma_w = \sqrt{\sum_{n=1}^{m} (l_n - W)^2 {d_n}^{-1} \Big/ \sum_{n=1}^{m} {d_n}^{-1}} \tag{4}$$

Lastly, we projected these sample locations along the composite stratigraphic columns to determine changes in paleobathymetry through time (Supplementary Figures 1, 2, and 7).

3.5. Age models and quality of age measurements

Age constraints (paleomagnetic reversals and first appearance datums of index fossils) and their measured present-day stratigraphic heights (before correcting effects of compaction) on the composite sections (Figure 2) are used to conducted linear regressions between thickness and age (Supplementary Data 4). We visually determine data trends and group data to be fitted in different regression lines (Figure 3a). These linear models are then used to predict (using extrapolation and interpolation) depositional ages of the section boundaries (base of section, top of preserved section, top of reconstructed section) and paleobathymetry samples (Supplementary Data 3–4).

The resolution of our dating with these integrated magneto-biostratigraphy methods is expected to be as good as the precision [~1–15 thousand years (kyr)] of each astronomically-calibrated age of paleomagnetic reversal (Channell et al., 2020) and first appearance datum (FAD) for index fossils (Chuang et al., 2018), once they are accurately placed in the stratigraphic sections. The stratigraphic position of each age-control datum was determined using the two sample sites that define a magnetic polarity reversal or the first appearance of an index fossil. The stratigraphic thickness between two bounding paleomagnetic sample sites mostly lies between 8 to 288 m, except a poor constraint (828 m) at reversal between polarity chrons C2An1.n and C1r.2r (Gauss-Matuyama boundary) near the base of Fungfu (FF) section in the northern Coastal Range (Figures 2; Supplementary Figures 1–2). Using the mean sediment-accumulation rates calculated from height-age linear regressions, the uncertainty (accuracy) for most of our age measurements is estimated to be ± 2–43 kyr (0.1%–2%) from targeted age values [± ~507 kyr (~10%) for the Gauss-Matuyama boundary in the FF section] (Supplementary Data 4). This demonstrates remarkably high-resolution and high-fidelity controls on depositional ages and associated vertical subsidence and uplift rates.

3.6. Subsidence analysis: decompaction and backstripping

We used established numerical methods of basin geohistory analysis (Allen & Allen, 2013) that correct for loss of pore space during progressive burial and compaction of sediment through time to reconstruct of subsidence history of the sedimentary basin. Stratigraphic thickness, corrected for the effects of compaction and sea level, is therefore used to track the depth of the basement top through time (Lee et al., 2019). This approach assumes that the pore spaces are interconnected (i.e., no overpressure), and the sediment porosity [$\emptyset(\mathrm{z})$] varies as an exponential function of depth (z):

$$\emptyset(z) = \emptyset(0) \cdot e^{-z/C} \tag{5}$$

, where C is a decay constant that varies with lithology. We calculated global average porosity-depth functions from previous publications (Kominz et al., 2011; Lee et al., 2019) to estimate initial porosity [$\emptyset(0)$], decay constant (C), and uncertainties (standard errors) for sandy, muddy, and mean marine sediments (Supplementary Figure 8; Supplementary Data 4). We assumed that basement rocks below the basal unconformity (i.e., Kangkou Limestone, Tuluanshan Formation) have not compacted. This assumption is supported by the presence of calcite-cemented Miocene volcaniclastic sandstones beneath the unconformity that are directly overlain by uncemented mudstones and sandstones above the contact (Dorsey, 1992; Lai, Dorsey, et al., 2021), showing that rocks beneath the unconformity were cemented prior to deep post-Miocene basin subsidence. Rocks beneath the unconformity may be subject to minor, inconsiderable amounts of compaction that do not affect the results of our subsidence analysis.

For *N* stratigraphic units, the present-day thickness (T_0) of each unit was buried at a depth of D_0 when the youngest sediment deposited prior to structural tilting and erosion. There are 14 preserved units ($N = 14$) in both northern and southern Coastal Range. Stratigraphic positions of all age boundaries are presented in Supplementary Data 4. Uncertainties of T_0 of preserved units (unit 1 to 14) are limited by the stratal thickness between the two bounding samples that confine the magnetic reversals or the first appearance datums (FAD) of index fossils (Supplementary Figures 1–2; Supplementary Data 4). The uppermost preserved sediment at the top of unit 1 is consolidated and lithified, which means that there must have been a considerable thickness of strata (called unit 0 in this study) above preserved unit 1 that was subsequently removed by erosion during post-0.5 Ma uplift. Porosity-effective stress of the sandstone (Hong, 2020) and compiled vitrinite reflectance (Chim et al., 2018) data yield an estimated range of eroded thickness of ca. 2.2–3.7 km above marker bed tuff Tp12 near the top of the Madagida river (MDJ) section (Supplementary Figure 1). This implies ca. 0.45–1.95 km sediment that was deposited above unit 1 and has since been removed. For simplicity, we assumed a conservative thickness range of 0.75 ± 0.25 km for the unpreserved unit 0 in both the north and south composite sections, and we used it to reconstruct the top of section prior to structural inversion (Figure 3; Supplementary Data 4).

To calculate the thickness of each unit at some earlier time (i.e., decompacted thickness, T_i), when the unit was buried only to a depth of D_i, we can use the mass-balance equation:

$$\int_{D_i}^{D_i+T_i} [1 - \emptyset_i(z)]dz = \int_{D_0}^{D_0+T_0} [1 - \emptyset_i(z)]dz \tag{6}$$

, where the $\emptyset_i(z)$ is the porosity of unit *i* ($i = 0, 1, 2, ..., N$) at depth *z*. This approach assumes the volume of sediment grains within the unit does not change. The quantity

$[1 - \emptyset_i(z)]$ represents the volume of sediment grains (per unit volume of the strata) at any level within the unit. After integrating equation (5), equation (6) is rearranged to iteratively solve T_i:

$$\Rightarrow T_i = \sum_{k=1}^{M} F_i^k \cdot \left[\varphi_1 \cdot e^{-T_i/C_i^k} + \varphi_2\right] \tag{7}$$

$$, with \begin{cases} \varphi_1 = -C_i^k \cdot \emptyset_i^k(0) \cdot e^{-D_i/C_i^k} \\ \varphi_2 = -\varphi_1 + T_0 + C_i^k \cdot \emptyset_i^k(0) \cdot e^{-D_0/C_i^k} \cdot \left[e^{-D_0/C_i^k} - 1\right] \end{cases}$$

, where F_i^k is the fraction of lithology *k* (*k* = 1, 2, ..., *M*) in unit *i*. There are three types of lithology (*M* = 3) determined in this study. The fraction of sand (*k* = 1), mud (*k* = 2), and pebbly mudstone (*k* = 3) was measured in all sections (Supplementary Figures 1–2; Supplementary Data 4). We assumed that unit 0 contains subequal fractions of sand and mud ($F_0^1 = 0.5$; $F_0^2 = 0.5$; $F_0^3 = 0$). The initial porosity [$\emptyset_i^k(0)$] and decay constant (C_i^k) for sandy, muddy, and mean marine sediments were applied respectively (Supplementary Figure 8). After repeating equations (6) and (7) for each unit from top to the base of section, we computed the sum of decompacted unit thickness (ϵ_i) at the time when unit *i* finished deposition:

$$\epsilon_i = \sum_{i=0}^{N} T_i \tag{8}$$

These procedures [equations (6) to (8)] account for the effects of removing incrementally older units from the top and allow the section to expand as underlying units are unloaded.

To evaluate the amounts of total subsidence (i.e., the true depth of the basement, σ_i) at the end of unit *i* deposition, we need to correct the magnitude of paleo water depth by assuming the basin was filled with water to sea level:

$$\sigma_i = \epsilon_i + W_i - \Delta_i \tag{9}$$

, where W_i and Δ_i are the paleobathymetry and sea level relative to modern datum at the time of unit *i* finishing deposition. We combined means and standard errors of available paleobathymetry estimates (Supplementary Data 3) with reconstructed global sea level from Miller et al. (2020) using age constraints in each section (within the range of age uncertainty with extra ± 0.2 Myr and ± 0.01 Myr for paleobathymetry and relative sea level respectively) as the values of W_i and Δ_i at each unit boundary (Supplementary

Figure 7; Supplementary Data 4). Paleobathymetry constraint was not available for the reconstructed unit 0 above the preserved strata. In this case, we assumed the paleobathymetry of reconstructed basin top (at the end of unit 0 deposition, W_0) and its uncertainty range as a half of the W_1 value at the top of preserved strata [$W_0 = W_1/2 \pm W_1/2$] because basin inversion in the Coastal Range possibly began between the ends of unit 1 and unit 0 (Figures 3; Supplementary Figure 7).

Since the folded basal unconformity and underlying volcanic basement rocks are exposed well above sea level (Figure 4c), we can calculate the minimum and the best-estimated long-term rock exhumation rates using the decompacted depth of basement at depositional ends of unit 1 and unit 0 (σ_1 and σ_0) to the present-day elevations of the antiformal peaks in northern and southern Coastal Range (0–1.33 km and 0–1.68 km, respectively) (Figure 3).

We further estimated the amount of subsidence that was contributed by tectonic forces (so-called "tectonic subsidence," ζ_i) at the end of unit *i* deposition by removing effects of paleo water depth and local (Airy) isostatic response to applied sediment loads:

$$\zeta_i = \epsilon_i \frac{\left(\rho_a - \bar{\rho_s}^i\right)}{(\rho_a - \rho_w)} + W_i - \Delta_i \frac{\rho_a}{(\rho_a - \rho_w)} \tag{10}$$

, where ρ_w is the density of marine water ($\rho_w = 1025$ kg m^{-3}); ρ_a is the density of asthenospheric mantle ($\rho_a = 3300$ kg m^{-3}). $\bar{\rho_s}^i$ is the average (integral) density ($\bar{\rho_s}^i$) of the unit *i* with various lithologies *k* at each time frame of sedimentation:

$$\bar{\rho_s}^i = \left(\sum_{i=0}^{N} \sum_{k=1}^{M} F_i^k \cdot \Omega_i^k\right) \Big/ \epsilon_i \tag{11}$$

Ω_i^k represents the average (integral) 1-D mass of unit *i* for given lithology *k* at some earlier time, assuming the pore spaces were filled by marine water,

$$\begin{aligned} \Omega_i^k &= \int_{D_i}^{D_i+T_i} \left\{ \emptyset_i^k(z) \cdot \rho_w + \left[1 - \emptyset_i^k(z)\right] \cdot (\rho_g)_k \right\} dz \\ &= (\rho_g)_k \cdot T_i + \left[\rho_w - (\rho_g)_k\right] \cdot C_i^k \cdot \emptyset_i^k(0) \cdot e^{-D_i/C_i^k} \cdot \left[1 - e^{-T_i/C_i^k}\right] \end{aligned} \tag{12}$$

, where $(\rho_g)_k$ represents the averaged density of sediment grain for each lithology *k* in unit *i*. We applied the means and standard errors of the grain densities for sandy, muddy, and mean marine sediments (for pebbly mudstone) respectively from previously published data (Lee et al., 2019) (Supplementary Figure 8; Supplementary Data 4).

Uncertainties of all input parameters were considered in the analysis. Thus, we were able to estimate the uncertainties of calculated tectonic subsidence (ζ_i) and decompacted total subsidence (σ_i) through Gaussian error propagation or delta method (Supplementary Data 4). Throughout the analysis, we found that the primary source of error is the present-day (non-decompacted) thickness of each unit (T_0), followed by uncertainties in paleobathymetry estimates (W_i).

Lastly, we plotted the subsidence history (i.e., geohistory) diagrams for northern and southern composite sections, which show changes in depth of basement [i.e., decompacted total subsidence (σ_i)] and calculated corresponding amount of tectonic subsidence (ζ_i) through time (Figure 3b–c). The amount of total subsidence prior to decompaction correction was also plotted as a standard convention. The position of basement top at the beginning of subsidence for each composite section was reconstructed by projecting along the oldest segment of subsidence curve to the sea level (0 km). This indicates the end of formation of the basal unconformity (Dorsey, 1992; Lundberg & Dorsey, 1988), which is characterized by a broad erosive surface that formed near sea level and is capped by discontinuous thin (ca. 50–200 m) deposits of shallow-marine limestone (Kangkou Limestone, from 5.57–4.37 Ma to 4.31–3.47 Ma) and limestone-clast bearing epiclastic rocks (Biehchi Epiclastic Unit, from 5.53–4.31 Ma to 3.82–3.35 Ma) (Huang & Yuan, 1994; Lai, Dorsey, et al., 2021) (Supplementary Figures 1–2).

4. Data availability

Data presented in this paper are provided in Supplementary Data 1–4 (Microsoft Excel spreadsheets) and permanently stored at https://doi.org/10.6084/m9.figshare.19350530.

5. Code availability

Analyses and production of figures were conducted using R version 4.0.3. All scripts and data in required formats are freely available at https://doi.org/10.5281/zenodo.5823613.

6. Bridge

Chapter III highlights dynamic up-and-down crustal motions that took place during accretion of the Luzon Arc crust at the suture zone of Taiwan's arc-continent collision. The results reveal rapid basin subsidence and succeeding exhumation of unmetamorphosed rocks at extreme vertical rates ever documented. Owing to unprecedently high-resolution controls of depositional age by magneto-biostratigraphy, this study provides new constraints about the timing of tectonic reorganizations, and the maximum age of modern Coastal Range topography. This case study also confines the possible shortest timescale (<500 thousand years) required to create a steep mountain range by structural inversion of a deep-water sedimentary basin. This Coastal Range is now subject to rapid erosion in response to rapid rock uplift and generating massive amounts of sediments in the progress of a new stage of crustal recycling. The topographic gradient of this mountain fundamentally set the style and efficiency of erosion processes and sediment production, but the controls of current landscape patterns in the Coastal Range was poorly studied. In the following Chapter IV, I present results of geomorphic analysis in order to explore how surface processes shape this rapidly uplifting terrain.

CHAPTER IV

COARSE SEDIMENT SUPPLY SETS THE SLOPE OF BEDROCK CHANNELS IN RAPIDLY UPLIFTING TERRAIN: FIELD AND TOPOGRAPHIC EVIDENCE FROM EASTERN TAIWAN

This chapter has been published as Lai, L. S.-H., Roering, J. J., Finnegan, N. J., Dorsey, R. J., and Yen, J.-Y. (2021) Coarse sediment supply sets the slope of bedrock channels in rapidly uplifting terrain: Field and topographic evidence from eastern Taiwan. *Earth Surface Processes and Landforms*, 46(13), 2671-2689. I and Jiun-Yee Yen conducted field geomorphic surveys, measurements, and data acquisition. I am the lead author on the paper, which involved data synthesis, programming for topographic analysis, theoretical analysis, preparation of figures and tables, and writing the entire manuscript. Joshua J. Roering, Noah J. Finnegan, and Rebecca J. Dorsey assisted with conceptualizing the research, developing theoretical framework, data interpretation, and editorial feedback.

1. Introduction

River incision is a major driver of landscape evolution, controlling the relief and shape of mountainous topography on the Earth's surface (Hilley et al., 2019; Whipple et al., 2013). The rate of incision in bedrock river channels is widely assumed to scale with basal flow shear stress or the rate of potential energy dissipation (i.e., stream power) (Howard & Kerby, 1983; Lague, 2014; Whipple & Tucker, 1999). In this framework, the channel steepness of graded bedrock rivers (i.e., rivers with smoothly concave-up profiles following Flint (1974)) is often used as a topographic proxy for erosion rate that is used to detect spatial patterns of tectonic uplift rate, climate forcing, and bedrock erodibility (Kirby & Whipple, 2012; Whipple, 2004; Wobus et al., 2006). However, theoretical studies, experiments, and field evidence demonstrate that coarse sediment supply governs incision processes and sets channel slopes (Chatanantavet & Parker, 2008; Cowie et al., 2008; Finnegan et al., 2017; Johnson et al., 2009; Sklar & Dietrich, 1998). Coarse sediment can act as a primary driver for bedload abrasion and debris-flow scour (i.e., the so called "tools effect"), which causes bedrock erosion (Sklar & Dietrich, 2001).

Sediment also can limit exposure of the bed to wear and weathering (i.e., the cover effect), thus reducing incision (Shobe et al., 2016; Whipple & Tucker, 2002). The production of gravel-size (diameter >2 mm) sediment from hillslope sediments has also been highlighted as a critical factor in controlling downstream bedload transport, and it may be related to source rock lithology, weathering type, and hillslope gradient (Attal et al., 2015; Marshall & Sklar, 2012; Roda-Boluda et al., 2018; Sklar et al., 2017).

Despite their well-known importance, sediment effects are seldom incorporated into stream-power based analyses of fluvial landscapes, particularly in rapidly uplifting or eroding mountains where high coarse-sediment fluxes are well-documented in channels (e.g., DiBiase et al., 2018; Whittaker et al., 2010) and adjacent sedimentary basins (e.g., Allen et al., 2013; Dubille & Lavé, 2015). As a result, two questions persist in tectonic geomorphology: (1) what is the relative importance of sediment supply effects in setting channel slope? and (2) can the effects of sediment supply and caliber set channel slopes in steep, rapidly eroding landscapes, rather than the commonly invoked factors of uplift rate, flow discharge, and rock resistance to erosion?

Previous observations in fast-eroding, landslide-dominated landscapes across a range of climate and tectonic settings reveal the potential insensitivity of channel steepness to high (>0.6-1 $\mathrm{mm \cdot yr^{-1}}$) rates of uplift or erosion (Adams et al., 2020; DiBiase et al., 2010; Fellin et al., 2017; Hilley et al., 2019; Ouimet et al., 2009; Yanites et al., 2018). Yet the mechanisms underlying these observations remain poorly understood. Most of these studies were conducted in regions with relatively uniform bedrock and analyzed with stream-power based incision models. In fact, sediment effects, especially coverage effects, are still overlooked in the derivation of the stream-power model (Venditti et al., 2020). Several studies have begun to address how sediment may influence channel slope by empirically correlating the nonlinear relationship between channel steepness and fast erosion rates to adjustments in numerical constants, and/or by embedding sediment-flux dependent variables into the stream-power model (Adams et al., 2020; Gasparini et al., 2006; Hilley et al., 2019; Ouimet et al., 2009; Whipple & Tucker, 2002). These modifications are indirectly supported by observations of channel widening in sediment-rich channels (Finnegan et al., 2007; Lavé & Avouac, 2001; Yanites & Tucker, 2010) and variability of water discharge associated with the threshold of sediment entrainment (DiBiase & Whipple, 2011; Lague et al., 2005). However, the extent to which these amendments honor the basic assumptions behind stream-power models (e.g., incision rate scales with basal shear stress of the mean flow discharge) makes it difficult to constrain incision mechanisms due to ambiguities in model parameterization (Duvall et al., 2004; Tomkin et al., 2003; van der Beek & Bishop, 2003).

In a few cases, mechanistic incision models that consider both tools and cover effects have successfully predicted the threshold for influence of sediment entrainment and coarse sediment flux on channel slope (Chatanantavet & Parker, 2009; Sklar & Dietrich, 2004). Despite the physical basis for this sediment-driven approach, it is difficult to constrain or approximate the relevant parameters in natural settings, and therefore sediment-driven models are infrequently applied to explain orogen-scale fluvial landscape (Sweeney & Roering, 2017; Venditti et al., 2020). Thus, considerable uncertainty remains regarding the extent to which channel steepness is set by coarse-sediment load, and hence whether channel steepness encodes local tectonic processes in rapidly uplifting regions (Finnegan et al., 2017).

In this study, we develop a field-based application of a mechanistic incision model – the saltation-abrasion model (Sklar & Dietrich, 2004, 2006) – to quantitatively assess the influence of sediment effects on fluvial bedrock channel slope in Taiwan, one of the fastest uplifting terrains on Earth. We investigate channels with varying substrate lithology and sediment source rock in the Coastal Range of eastern Taiwan, and compare analytical outcomes to independently constrained bedrock strength, uplift rate, and precipitation. The results suggest that channel steepness is insensitive to uplift rate and river discharge, and indicate the prevalence of sediment-controlled incision processes. We conclude that, in this setting, bedrock lithology exerts the main control on channel slope by modulating the supply and caliber of coarse sediment supply from landslide-dominated hillslopes.

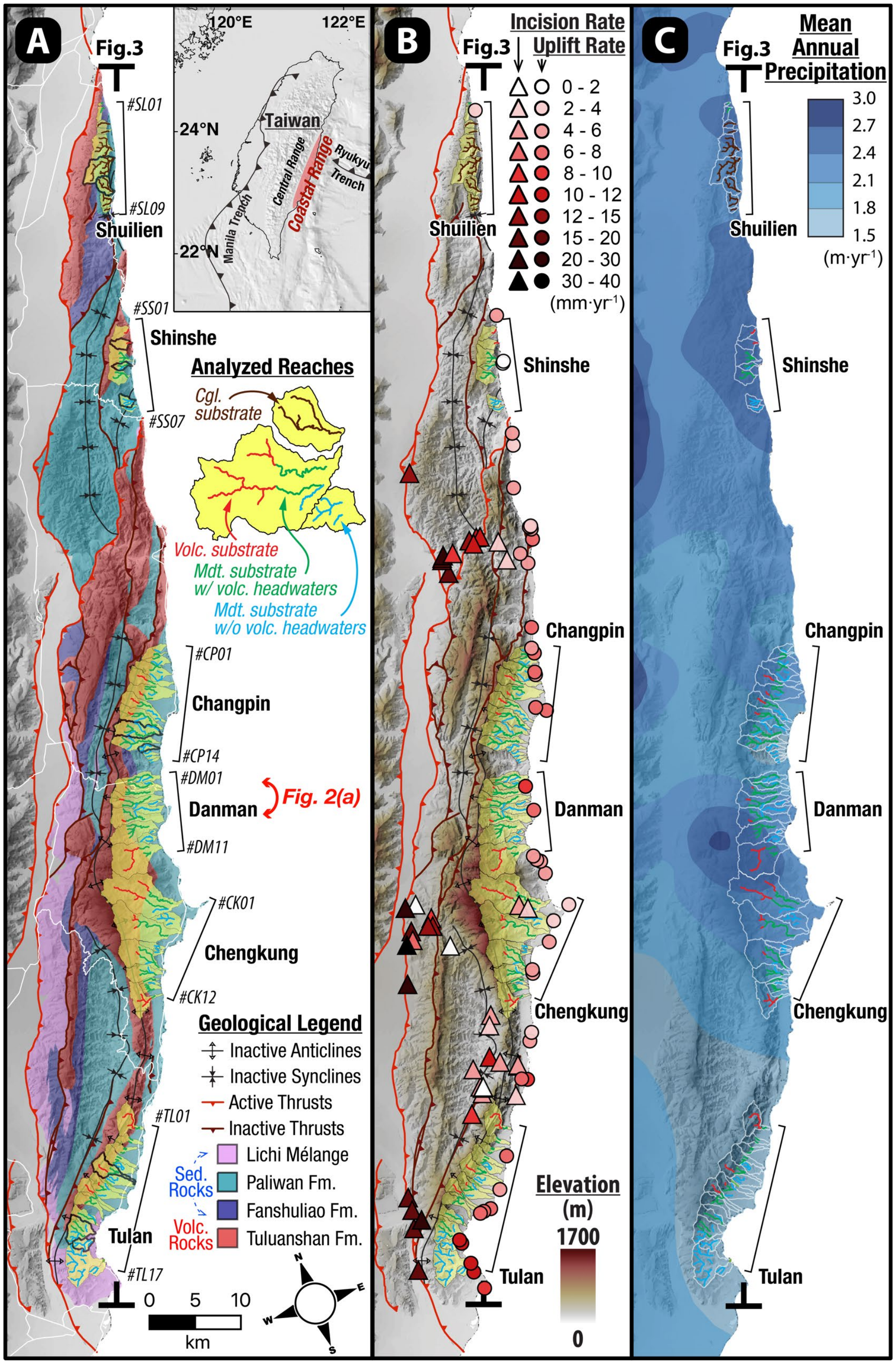

Figure 1. Study area. (a) Simplified geological map, modified from Hsu (1956); Lai, Dorsey, et al. (2021); Wang and Chen (1993), and analyzed catchments in the Taiwan Coastal Range. Inset shows location of the mountain range. White lines are major roads. Black outlines are catchments with field measurements. Abbreviations of lithologies: Volc = volcanic rocks; Sed = sedimentary rocks; Cgl = conglomerate; Mdt = mudstone and flysch. (b) Rates of uplift and incision (see cited data in Table S1). (c) 1949-2018 mean annual precipitation (Water Resources Agency, 2019).

2. Geological setting

2.1. Taiwan Coastal Range

The Coastal Range of eastern Taiwan (Figure 1(a)) is composed of deformed oceanic forearc crust of the Philippine Sea plate that has accreted to metamorphic continental crust in the Central Range during the past ca. 1 Myr as a result of active arc-continent collision (Lai, Dorsey, et al., 2021; Lundberg & Dorsey, 1990). River catchments in the Coastal Range are formed on steeply dipping (up to ~90° or overturned) strata with large contrasts in bedrock strength between Plio-Pleistocene marine foredeep basin deposits (Lichi Mélange, Paliwan and Fanshuliao Formations; mudstone, flysch, and locally abundant conglomerate) and underlying Miocene volcanic basement (Tuluanshan Formation; volcanic and volcaniclastic rocks with minor limestone) (Figure 2(a)) (Dorsey, 1992; Wang & Chen, 1993). Hillslopes are characterized by ubiquitous landslide scarps. Local low-relief transient surfaces at the top of some major drainage divides (Hsieh et al., 2017) are superposed on geological structures (fold axes and thrusts). These observations indicate that the landscape of the Coastal Range mainly reflects a pattern of differentially eroded bedrock lithologies and structures (Hsieh et al., 2020; Lai, Dorsey, et al., 2021), and does not preserve a topographic signal inherited from older (Miocene) volcanic islands (cf. Hsieh et al., 2017; Hsieh et al., 2011; Lai & Song, 2013).

Holocene rates of rock uplift along the coast are constrained by 10^3-10^4 year-scale marine terraces, and generally increase from ca. 1.8 $\mathrm{mm \cdot yr^{-1}}$ in the north to ca. 11.8 $\mathrm{mm \cdot yr^{-1}}$ in the south (Figures 1(b), 3(a)) (Chen et al., 2020; Hsieh & Rau, 2009). Tectonic uplift initiated ca. 1 Ma, as indicated by the age of the youngest marine sedimentary rocks in the whole Coastal Range (Huang et al., 2018; Lai, Dorsey, et al., 2021). Using the highest elevation of Miocene volcanic basement rock on the range crest (~1.6 km), thickness (~4-6 km) and paleo-depositional water depth (up to ~1.5-2 km) of Plio-Pleistocene marine sedimentary rocks (Ingle, 1975), the geologically averaged uplift rate is roughly 5.6-9.6 $\mathrm{mm \cdot yr^{-1}}$ over the past ca. 1 Myr (Lundberg & Dorsey, 1990), consistent with rates derived from marine terraces in the central Coastal Range (Changpin-Danman area; Figure 1(b)). Incision rates calculated over 10^3-10^4 yr timescales based on incised river terraces increase from east to west across the Coastal

Range (Figure 1(b)) (Hsieh et al., 2017; Shyu et al., 2006), and display high variability that may reflect stochastic downcutting over millennial timescales (Finnegan et al., 2014). Catchment-averaged erosion rates are unavailable in the study area due to absence of quartz-rich sediment suitable for cosmogenic nuclide analysis. Nonetheless, several locations in the coastal area exhibit similar independently-measured incision and uplift rates (Figure 3(a)), suggesting a quasi-equilibrium in which downstream graded channels are adjusted to the modern base-level (e.g., Duvall et al., 2004; Kirby & Whipple, 2012).

In contrast to the strong spatial variability of rock uplift and incision, the Coastal Range experiences relatively similar precipitation along the range (ca. 1.5 to 2.7 m/yr), with a slight decrease toward the south (Figures 1(c), 3(b)) (Water Resources Agency, 2019) and no detectable long-term change in annual precipitation over a half-century record (Yu et al., 2006). Under the tropical-subtropical monsoon climate system, about 79% of precipitation falls between May and October and mostly accumulates during short events like monsoon storms and typhoons (on average 3.6 per year) (Chen & Chen, 2003), indicating the influence of episodic large floods.

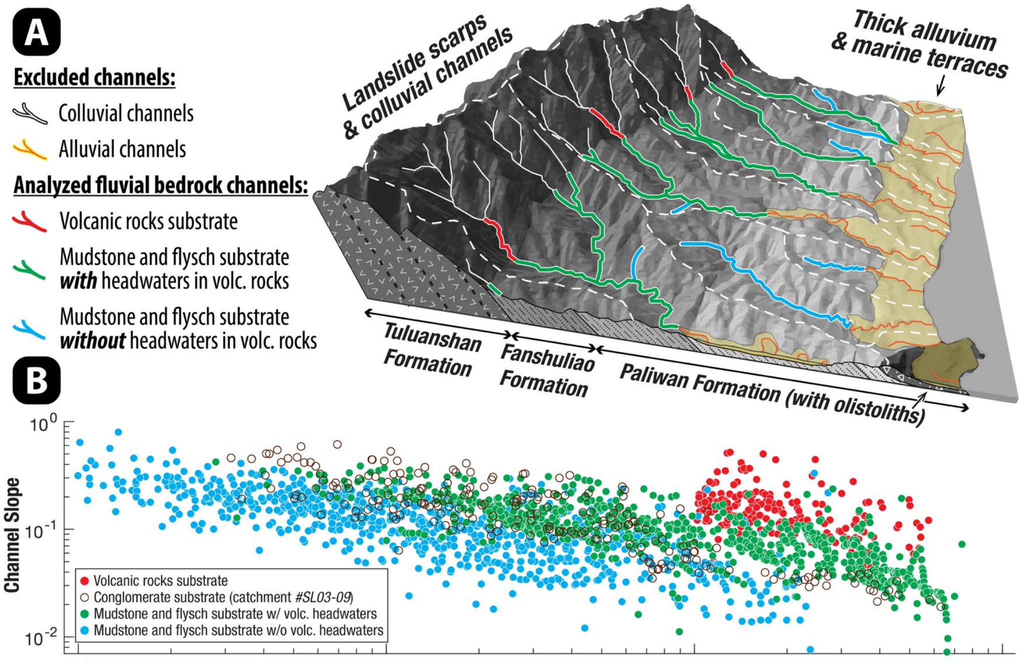

Figure 2. Channel analysis. (a) Example of channel selection from Danman area (catchment #DM02-06). (b) Compiled slope-area data from all analyzed fluvial bedrock channels (Figure 1a), showing strong dependence of channel steepness on lithologies of bed substrate and upstream sediment source.

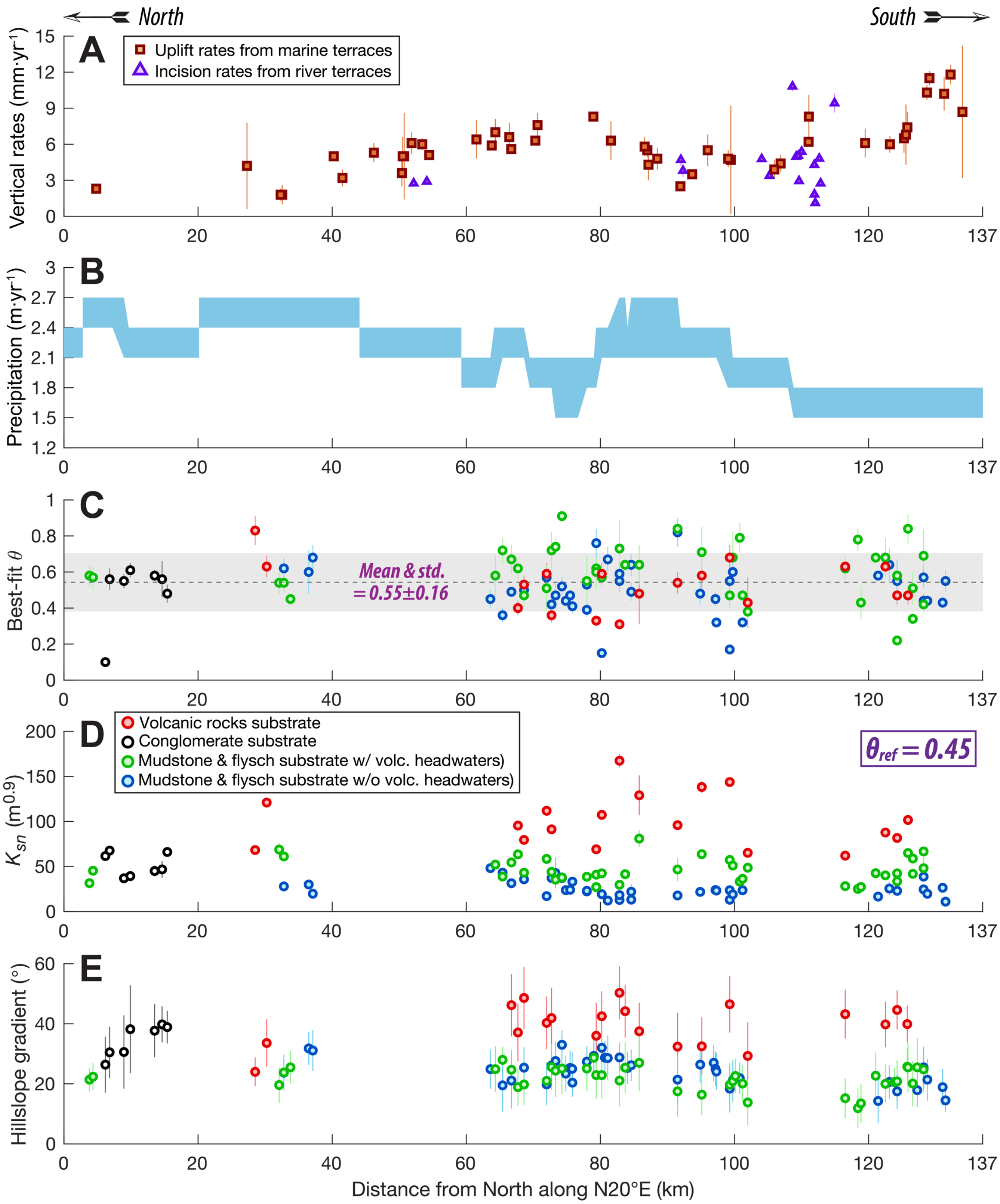

Figure 3. Geomorphic measures and natural forces in the coastal catchments of the Taiwan Coastal Range, plotted along N20°E orientation from the North. (a) Inferred coastal uplift rates from marine terraces and fluvial incision rates from river terraces (Figure 1c). (b) Span of mean annual precipitation in coastal catchments, projected from Figure 1(c). (c) Best-fit channel concavity (θ) for analyzed channels and the mean concavity for all data and its deviation. (d) Channel steepness index (K_{sn}) and its standard error based on reference concavity (θ_{ref}) 0.45 for analyzed channels. (e) Mean hillslope gradient along analyzed reaches. Uncertainties are the standard errors of the data or means. See data in Table S1 and measured area of hillslope gradient in Figure S1.

2.2. Study catchments

In this study we focused on east-coast river catchments where uplift and precipitation are best constrained (Figure 1(a)). Six areas were selected, covering the full range of uplift rate and precipitation with similar distributions of bedrock lithologies (volcanic basement along the ridge crest and sedimentary rock at lower elevations) (Hsu, 1956; Lai & Teng, 2016; Wang & Chen, 1993). Studied channels are generally perpendicular to the regional bedding strike (Figure 2(a)). We avoided catchments crossing geological structures (both active and inactive) to minimize areas of pervasive rock fracture (DiBiase et al., 2018; Neely et al., 2019) and potential local base-level set by downstream hard rocks (Forte et al., 2016). We classified reaches into groups with different substrate lithology: (1) reaches with volcanic rock substrate; (2) reaches with conglomerate substrate (only in the Shuilien area); and (3) reaches with mudstone and flysch substrate. Channels that cross the dipping depositional boundary between volcanic rocks and overlying sedimentary rocks often exhibit pronounced slope breaks. For this scenario, we separated channel segments into different groups with corresponding substrate rock type and analyzed them separately. In addition, we further subdivided reaches with mudstone and flysch substrate into groups with or without connection to headwaters developed in volcanic rocks to evaluate the influence of sediment supply on downstream reaches with similar substrate. This allows us to independently assess the relative role of channel-slope controlling factors (rock uplift, precipitation, substrate type, and sediment supply).

Although catchments involving known active structures are excluded, the presence of ancient thrusts and antiformal axes near the western headwaters in analyzed catchments may imply a higher uplift rate over longer timescales (10^5-10^6 yr) (Shyu et al., 2006) (Figure 1). Along-profile (west-east) variation of uplift rate and associated orographic precipitation could affect channel profiles over geological timescales (Kirby & Whipple, 2001). Therefore, we restricted our analyses to channels downstream of the lowest identified knickpoints (Table S1), which likely have reached an approximate balance between erosion and rock uplift (Kirby & Whipple, 2012). Additionally, uplift rates within individual catchments are relatively uniform compared to the strong north-south changes (Figures 1(b, c), 3(a, b)). The small cross-strike length of studied catchments (<8 km) compared to the large along-range (north-south) distance over which uplift rates were measured (ca. 137 km) also reduces the likelihood of significant uplift gradients within the studied channel profiles (Figure 1). Thus, our analysis assumes that published millennial rates of uplift measured along the coast are representative of catchment-average rates, and the effect of orographic precipitation is minimal.

3. Theoretical background

3.1. Flint's Law and channel slope

The slope of fluvial bedrock channel profiles (S_T) tends to have a power-law relation with upstream drainage area (A) (Flint, 1974),

$$S_T = K_s\, A^{-\theta} \tag{1}$$

where K_s and θ are indices of channel steepness and concavity. Because the value of concavity index usually falls in a relatively restricted range, one can apply a constant reference concavity (θ_{ref}) in a particular setting and modify Equation (1) to derive normalized steepness index (K_{sn}) that allows effective comparison of the steepness of channel profiles over various geological conditions (Wobus et al., 2006),

$$K_{sn} = S_T\, A^{\theta_{ref}} \tag{2}$$

As a presupposition of the stream-power model, the normalized steepness index (K_{sn}) is expected to vary with rock uplift rate (relative to base level), lithology, and climate (Kirby & Whipple, 2012; Whipple et al., 2013). Therefore, K_{sn} has been extensively used as a topographic metric or proxy to interpret tectonic forcing (e.g., DiBiase et al., 2010; Duvall et al., 2004; Ouimet et al., 2009).

To avoid uncertainties of DEM data noise in K_{sn} calculation and better identify knickpoints, an alternative method is the integral transformation (χ transformation) of the downstream coordinate that removes the effect of drainage area in Equation (2) (Perron & Royden, 2013),

$$z(x) = z(x_b) + \frac{K_{sn}}{{A_0}^{\theta_{ref}}}\,\chi \quad \text{with} \quad \chi = \int_{x_b}^{x} \left(\frac{A_0}{A}\right)^{\theta_{ref}} dx \tag{3}$$

where $z(x_b)$ is the base level elevation at outlets x_b, $z(x)$ is the elevation at the distance x from outlets, and A_0 is an arbitrary reference drainage area. In this framework, ($dz/d\chi$)

linearly scales with K_{sn}. Abrupt changes in $dz/d\chi$ along the linearized profile therefore define the presence of knickpoints.

3.2. Slope component analysis using a mechanistic model

To address the dominant physics in formulating channel slope, Sklar and Dietrich (2004, 2006) developed a mechanistic model for bedrock incision by assuming that bed erosion only occurs when bedrock at the channel bed is exposed to bedload impacts and abrasion during floods (high flows). The model casts the slope of bedrock channels (S_T) as the sum of three components, where,

$$S_{\mathrm{T}} = S_{D_s} + \Delta S_{Q_s} + \Delta S_E \tag{4}$$

S_{D_s} is the slope required for floods to exceed the threshold of sediment motion. Because flow basal shear stress increases linearly with channel slope for given hydraulic radius (Finnegan et al., 2017), the S_{D_s} term can be derived from the critical Shields stress (${\tau_c}^*$), a non-dimensionalization of threshold flow basal shear stress necessary for sediment entrainment for a given submerged grain weight,

$$S_{D_s} = \frac{{\tau_c}^* R_b D_s}{R_h} \tag{5}$$

where ${\tau_c}^*$ can be estimated through an empirical function with channel slope [${\tau_c}^* \cong 0.15 \cdot {S_T}^{0.25}$] (Lamb et al., 2008); R_b is the non-dimensional buoyant density [$R_b = (\rho_s - \rho_w)/\rho_w$], which is calculated from flow density (ρ_w) and sediment density (ρ_s); D_s is the particle diameter; R_h is high-flow hydraulic radius, which can be calculated by assuming a rectangular channel cross-section [$R_h = H_f W/(2H_f + W)$] with high-flow channel width (W) and depth (H_f).

ΔS_{Q_s} describes the excess slope (above S_{D_s}) needed to generate flood sediment discharge that accommodates the upstream sediment flux and initiate incision on exposed bedrock, where,

$$\Delta S_{Q_s} = (\tau^* - {\tau_c}^*)\frac{R_b D_s}{R_h}\left(\frac{Q_s}{Q_c}\right)^{2/3} \tag{6}$$

τ^* represents the high-flow Shields stress [$\tau^* = R_h S_T / R_b D_s$]; Q_s and Q_c are the flux of upstream sediment and the sediment transport capacity by floods, respectively. The relative transport capacity by floods can be empirically approximated by the fraction of bedrock exposure (F_e) on channel bed [$Q_s/Q_c = 1 - F_e$], assuming that the extent of observed bedrock exposure is representative of the average state of the bed, and the long-term averaged periodicity and intensity of floods do not vary significantly (Chatanantavet & Parker, 2008).

$\varDelta S_E$ represents the additional slope necessary for incision to match rock uplift and convolves the percentage of bed exposure and the energy delivered to the bed per unit bedload impact. Once S_T, S_{D_s}, and $\varDelta S_{Q_s}$ are constrained first, $\varDelta S_E$ can be derived through Equation (4).

In order to explore the patterns of these slope components independent of drainage area, we can apply Equation (2) to calculate the normalized steepness index for all terms in Equation (4),

$$K_{sn} = \left(S_{D_s} + \varDelta S_{Q_s} + \varDelta S_E\right) A^{\theta_{ref}} = K_{sn}^{D_s} + K_{sn}^{Q_s} + K_{sn}^{E} \tag{7}$$

This approach provides a direct way to quantify the relative importance of sediment effects on setting the channel steepness by partitioning it into transport-limited terms ($K_{sn}^{D_s}$ and $K_{sn}^{Q_s}$) and a detachment-limited term K_{sn}^{E}. In coarse-sediment starved channels, $K_{sn}^{D_s}$ and $K_{sn}^{Q_s}$ may be negligible such that channel steepness is governed by K_{sn}^{E}. In these settings, the model predicts strong correlation among channel steepness (K_{sn}), bedrock strength, and rock uplift (erosion) rate, in agreement with the traditional stream-power model (Wobus et al., 2006). By contrast, $K_{sn}^{D_s}$ and $K_{sn}^{Q_s}$ play dominant roles in coarse-sediment rich channels (Johnson et al., 2009). Under these conditions, the model predicts that channel steepness should vary primarily with bedload flux and grain size rather than uplift (erosion) rate and bedrock strength.

3.3. Channel width

Channel width (W), a crucial factor controlling basal shear stress and incision, typically exhibits a power-law relationship with upstream drainage area (A) due to its dependence on water discharge (Montgomery & Gran, 2001),

$$W = K_w A^b \tag{8}$$

where K_w is a scaling coefficient representing the channel wideness, and b is an empirical exponent. Once a regional reference b value is constained (b_{ref}), normalized wideness

(K_{wn}) can be derived as channel width proxy independent of drainage area or flow discharge (Yanites & Tucker, 2010),

$$K_{wn} = W\ A^{-b_{\text{ref}}} \tag{9}$$

4. Methods

4.1. Digital elevation model analysis

To constrain topographic measures necessary for analyses, we used the MATLAB codes from the TopoToolbox 2 (Schwanghart & Scherler, 2014) and the Topographic Analysis Kit (Forte & Whipple, 2019) to extract channel slope (S_T) and upstream drainage area (A) along channel profiles from 5-m resolution Digital Elevation Model (DEM) in analyzed catchments and conduct further calculations. We restricted our analysis to fluvial reaches where channel slope progressively decreases with drainage area (Duvall et al., 2004), avoided steep upland colluvial channels by setting a threshold drainage area for each substrate rock type (e.g., 10^6 m^2 for volcanic reaches and 10^4 m^2 for sedimentary reaches), and manually excluded downstream segments subject to thick alluvium or uncertainties of wide terraces where channels are narrower than a single grid cell (5 m) of DEM data (Figure 2(b)). Small patches of high-elevation, low-relief transient surfaces can be observed in few study catchments (SL04-05, SS01-03, CK12) (Figure S2) (Hsieh et al., 2017), but these areas only exist in the excluded colluvial regime of volcanic watersheds [$A < 10^6$ (m^2)] that do not affect our analysis.

We apply the "χ-disorder method" to find the best-fit concavity index (θ) for each analyzed reach that minimized the variability of elevation ($z(x)$) for given similar χ values in Equations (3) (Hergarten et al., 2016). Steep reaches with extremely low concavity index (e.g., θ <0.1) near headwaters, indicating debris-flow dominated channels, are further excluded (Penserini et al., 2017). In calculating normalized channel steepness (K_{sn}, $K_{sn}^{D_s}$, $K_{sn}^{Q_s}$, and K_{sn}^{E} in Equations (4) and (7)), the reference concavity (θ_{ref}) is set to the global average 0.45 as the matter of convenience for readers to compare their results to this paper (Kirby & Whipple, 2012). This value is within the uncertainty (one standard deviation) of the mean concavity in the Coastal Range (θ = 0.55±0.16, see details in *Results*) (Figure 3(c)). By setting the arbitrary reference drainage area (A_0) in Equation (3) as 1 m^2 and the base level as sea level [$z(x_b)$ = 0 (m)], the slope of linearized river profile ($dz/d\chi$) is equivalent to K_{sn} and is used to identify knickpoints (Perron & Royden, 2013). K_{sn} values on the basis of regional average concavity (θ_{ref} = 0.55) are also calculated (Figure S1). For the purpose of this study, we focus on K_{sn} calculated from profiles downstream of all identified knickpoints (not including the slope break between volcanic substrate and sedimentary substrate) (Figures S2, S3) and calculate their mean value in each catchment for further comparison against uplift rate, precipitation, bedrock strength, and sediment size (Table S1).

Mean hillslope gradient adjacent (125 m) to each population of analyzed reaches was also extracted to examine whether the source areas have attained sufficiently steep slopes suggestive of landslide-dominated sediment production (Figure S2) (Montgomery & Brandon, 2002). Instead of calculating mean gradient for the whole catchment, our method enables us to obtain relevant hillslope data by eliminating uncertainties generated from upland transient surfaces, wide marine terraces, and alluvial fans (Hsieh et al., 2017; Hsieh et al., 2011).

4.2. Field constraints on physical parameters

We conducted channel surveys at 31 sites across the mountain range during non-flood days, spanning regions with different uplift rate, mean annual precipitation, and all combinations of reaches with varying rock types of substrate and sediment source (Figures 1(a), S1). To address sediment transport capacity and river hydraulics (e.g., high-flow hydraulic radius (R_h) in Equations (5) and (6)), we measured high-flow channel width (W) and depth (H_f) at each site on markers of seasonal floods such as stranded debris, vegetation, and scoured channel wall (Figure 4(a)). The values of measured W along with DEM extracted drainage area (A) are also used to calibrate the best-fit reference exponent (b_{ref}) in Equation (9) for calculating normalized channel wideness (K_{wn}). For grain size analysis, we used the Wolman pebble count procedure (Wolman, 1954) for ~100 channel bed grains to record intermediate grain diameter and clast lithology, and we apply the 50th and 84th percentiles of grain diameter (D_{50} and D_{84}) as representatives of D_s in Equations (5) and (6)). We simultaneously estimated the bed exposure percentage (F_e) by the fraction of steps on the channel bed with thin sandy sediment or exposed bedrock, which is an empirical proxy of relative transport capacity

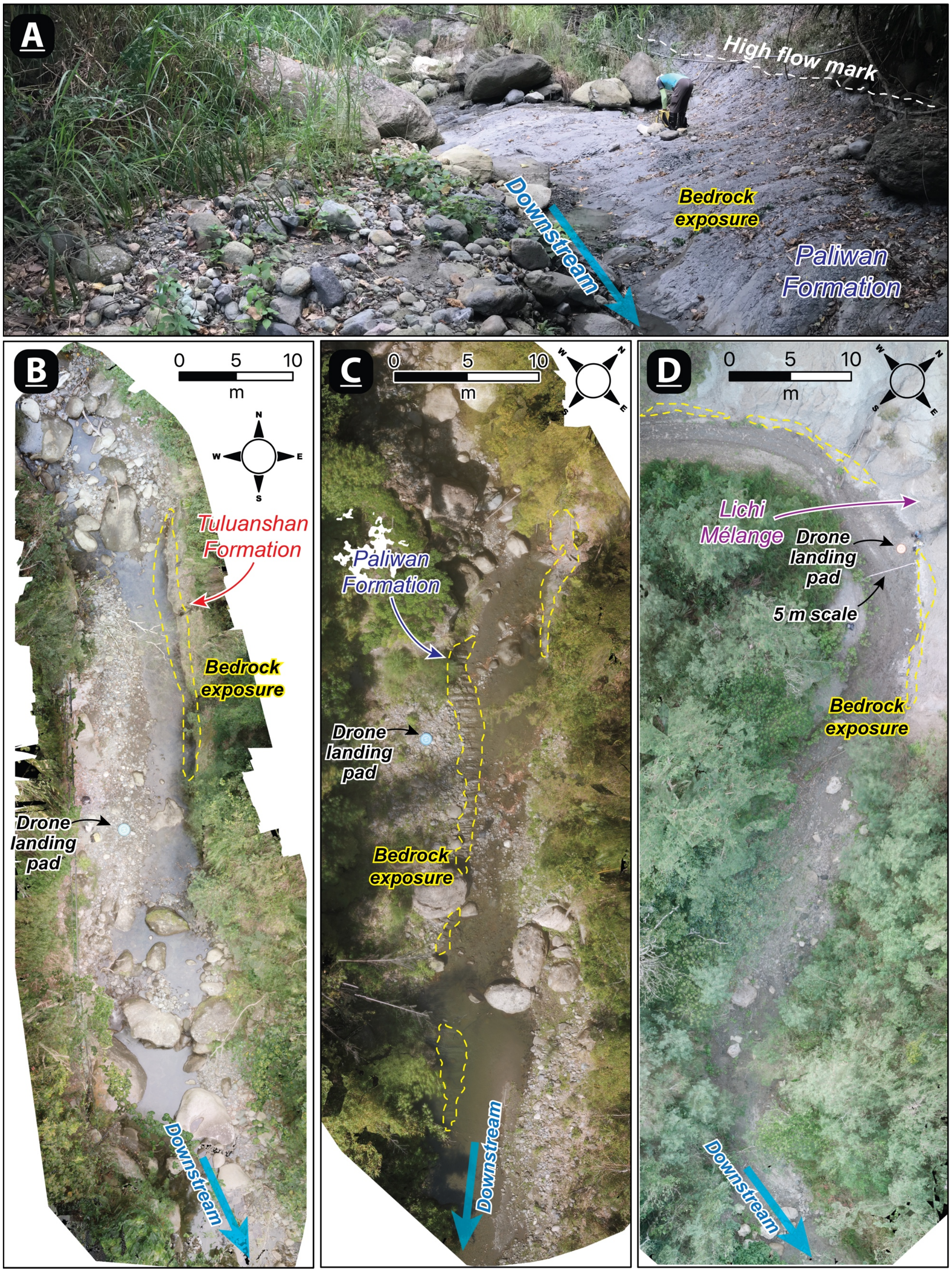

Figure 4. Representative field photos. (a) Field photo of at site CC-2. (b) Aerial image of at site TCC-1. (c) Aerial image of at site TCC-4. (d) Aerial image of at site CLS-2. See locations in Tables 1, S2, and Figure S1.

by floods for Equation (6) (Chatanantavet & Parker, 2008). Bed exposure is also independently measured through point counts with drone aerial imagery at sites with limited vegetation cover (Figure 4(b, c, d)). To represent the relative strength of different channel substrate, we apply Schmidt rebound hammer tests on fresh bedrock exposed at the base of channel bank (Shobe et al., 2017) and convert the reading to uniaxial compressional strength values. Lastly, we constrained the non-dimensional buoyant density (R_b) in Equations (5) and (6) with assumed flow density [$\rho_w = 1000$ kg/m^3] and published mean bedrock density as sediment density [$\rho_s = \sim 2432$ kg/m^3] (Sinotech Engineering Consultants Inc., 2006).

5. Results

Results from topographic analysis reveal that the best-fit concavity index (θ) for analyzed channels varies mainly between 0.4 to 0.7, with a mean and standard deviation of 0.55±0.16 (Figures 3(c)). The mean θ and its variation do not change significantly among different substrate lithology, with 0.53±0.13 in volcanic rocks regions, 0.55±0.15 in mudstone and flysch regions, and 0.49±0.18 in conglomerate regions (Table S1). For reaches with mudstone and flysch substrate, the θ value is higher when connected to headwaters in volcanic rocks (0.60±0.15) compared to those only linked to mudstone and flysch hillslopes (0.50±0.14) (Figures 3(c)).

When applying the global average θ as the reference concavity index ($\theta_{\text{ref}} = 0.45$) (Kirby & Whipple, 2012), the normalized channel steepness K_{sn} (downstream of all identified knickpoints) in the Coastal Range has no statistically significant relationship with rock uplift rate and mean annual precipitation (Figures 3(d), 5(a, b)). Instead, K_{sn} has a strong dependence on the lithology of the channel substrate and sediment source rock (Figure 2(b)). Channels in volcanic rocks are consistently steeper than conglomerate regions, followed by mudstone and flysch areas. For mudstone and flysch reaches, K_{sn} is systematically higher (~2 times) when connected to volcanic headwaters. These of K_{sn} patterns remain identical while applying different θ_{ref} such as the regional mean (0.55) (Figure S1).

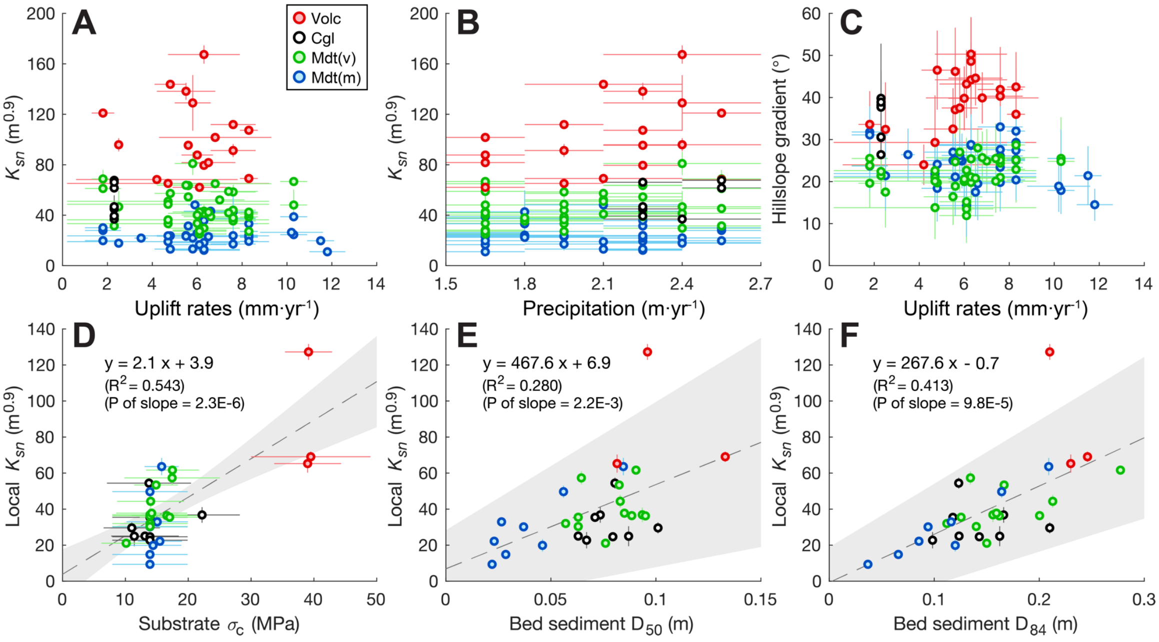

Figure 5. **Functions of channel slope and hillslope gradient.** (a-b) Normalized channel steepness (K_{sn}, based on $\theta_{\text{ref}} = 0.45$) plotted against local uplift rates and mean annual precipitation. (c) Mean hillslope gradient along analyzed reaches plotted against local uplift rates. (d-f) Local K_{sn} at each field site plotted against bed substrate uniaxial compressive strength (σ_c) and bed sediment grain size (D_{50} and D_{84}). Uncertainties are the standard errors of the data or means. Dash lines and shades show linear regressions and 95% confidence intervals. Abbreviations of channel categories: Volc = reaches in volcanic rocks; Cgl = reaches in conglomerate; Mdt(v) = reaches in mudstone and flysch with volcanic headwaters; Mdt(m) = reaches in mudstone and flysch without volcanic headwaters. See data in Tables 2 and S1.

During analysis, sporadic knickpoints were identified within our analyzed fluvial reaches (Figure S2). These localized knickpoints occur at a wide range of elevations (Figure S3) and align with regional bedding strike, suggesting their affinity to substrate variability, likely (1) exotic blocks (i.e., olistoliths) embedded in sedimentary units (e.g., CP09,11; DM10; TL14,16,17) (Lai, Dorsey, et al., 2021; Page & Suppe, 1981; Song et al., 1994); (2) interbedded muddy turbidities within conglomerate units (e.g., SL05) (Wang & Chen, 1993); (3) remnants of thick Quaternary mass-flow fans (e.g.,CP03; CK08; TL12,14,15) (Hsieh et al., 2011); (4) interbedded lava flows or sills (e.g., CK03) (Lai & Song, 2013), rather than tectonic-driven processes (Wobus et al., 2006). Because channels above identified knickpoints have been initially excluded from our analysis, these lithology controlled knickpoints should not influence our findings.

Hillslope gradient shows a similar relationship to bedrock lithology and uplift rate (Figures 3(d), 5(c)). Catchments in volcanic rocks and conglomerate tend to have steeper hillslope gradient (30-50°) than those in mudstone and flysch (10°-30°). Given relatively invariant hillslope gradient values across a wide range of uplift rate and the presence of ubiquitous landslide scarps near drainage divides (Hsieh et al., 2017), hillslopes in our study area have likely attained threshold values for each rock type. As a result, the sum of mass-wasting products should approximate the amount of erosion (or uplift) (Montgomery & Brandon, 2002).

Our field data reveal that local K_{sn} at each field site correlates with substrate strength and river sediment grain size (Figure 5(d, e, f), Table 1). In general, bed sediment size (D_{50} and D_{84}) exponentially decays downstream (Sternberg, 1875) and is about twice as a coarse in reaches connected to conglomerate and volcanic watersheds (Figures 5(a, d), 6(a, b)). This is confirmed by the composition of channel bed gravels in which larger clasts are more associated with resistant lithology (e.g., andesite and limestone eroded from volcanic; clasts of meta-sandstone and ophiolitic rocks recycled from conglomerate) (Figure 6 (c, d)).

To evaluate potential signals of channel width adjustments to increases of sediment coverage, normalized channel wideness (K_{wn}) is calculated for each field site through Equation (9) based on a reference exponent 0.34 (b_{ref}) obtained from power-law regression between measured high-flow channel width and upstream drainage area [$W = 0.062\ A^{0.34}$] (Figure 7(a)). Our data shows that the K_{wn} is independent of K_{sn}, uplift rate, and annual precipitation but is generally higher in mudstone and flysch reaches connected to volcanic rock sources (Figure 7(d, e, f), Table 2). Notably, wider channels (i.e., greater K_{wn}) appear more frequently in areas experiencing faster uplift rate, where higher sediment flux is expected under a steady-state assumption (erosion ≈ uplift). Thus, dynamic width adjustment in response to varying sediment flux may act as an ancillary mechanism on setting channel slope (i.e., modulating hydraulic radius (R_h) in Equations (5) and (6)) (Finnegan et al., 2005; Yanites et al., 2018).

Results from our slope component analysis reveal the sums of $K_{sn}^{D_s}$ and $K_{sn}^{Q_s}$ approximate the observed steepness (local K_{sn}), and K_{sn}^{E} values tend to be small (up to ~12% of the local K_{sn}) due to limited (<19%) bedrock exposure but with large

Table 1. Parameters constrained from DEM and field measurements (with standard errors of the means) for analyses. See raw data and field site coordinates in Table S2.

Catch. number	Channel category†	Field sites	σ_c(MPa)	F_e	W (m)	H_f (m)	D_{50} (m)	D_{84} (m)	A (m^2)	Local S_T	Hillslope (°)
TL06	Volc	TCC-1	39.0±5.3	0.068±0.068§	8.00±0.36	2.50±0.14	0.082	0.230	2685925	0.0835±0.0064	39.8±7.6
TL06	Mdt(v)	TCC-2	17.5±4.2	0.019±0.012§	15.30±1.50	2.40±0.14	0.091	0.277	2712275	0.0785±0.0021	20.0±6.4
TL06	Mdt(v)	TCC-3	16.6±5.6	0.060±0.006	18.10±0.10	2.60±0.40	0.089	0.200	3419250	0.0418±0.0009	20.0±6.4
TL06	Mdt(v)	TCC-4	17.0±4.8	0.127±0.087§	18.45±3.05	2.50±0.30	0.063	0.126	4490700	0.0360±0.0014	20.0±6.4
TL15	Mdt(m)	CLS-1	14.4±4.5	0.031±0.003	4.30±0.36	2.60±0.14	0.046	0.120	170125	0.0880±0.0152	21.4±7.0
TL15	Mdt(m)	CLS-2	13.9±6.0‡	0.190±0.025§	9.00±1.00	1.55±0.15	0.022	0.037	1088200	0.0180±0.0019	21.4±7.0
TL14	Mdt(m)	CC-1	13.9±6.0‡	0.045±0.045§	4.50±0.50	1.60±0.40	0.037	0.094	506400	0.0818±0.0038	25.5±6.9
TL14	Mdt(v)	CC-2	14.9±3.5	0.115±0.115§	13.30±2.50	2.10±0.10	0.083	0.167	1511825	0.0885±0.0016	24.8±7.5
TL14	Mdt(v)	CC-3	10.1±3.9	0.015±0.015§	8.50±0.50	1.65±0.05	0.076	0.150	2859275	0.0262±0.0008	24.8±7.5
CP09	Mdt(v)	DD-1	13.9±6.0‡	0.041±0.041§	9.00±0.70	2.25±0.05	0.094	0.156	1339175	0.0645±0.0069	24.4±8.8
CP09	Mdt(v)	DD-2	13.9±6.0‡	0.020±0.020§	12.65±0.55	1.75±0.05	0.057	0.112	3715800	0.0354±0.0005	24.4±8.8
CP09	Mdt(v)	DD-3	13.9±6.0‡	0.150±0.140§	11.70±0.40	1.85±0.15	0.095	0.162	4034550	0.0386±0.0008	24.4±8.8
CP09	Mdt(v)	DD-4	13.9±6.0‡	0.020±0.002	11.70±0.50	1.75±0.05	0.063	0.140	4268700	0.0315±0.0003	24.4±8.8
CP09	Mdt(m)	DD-5	13.9±6.0‡	0.000±0.000§	5.80±0.83	1.64±0.14	0.056	0.164	912325	0.1033±0.0070	27.6±6.5
CP11	Mdt(m)	NSB-1	13.9±6.0‡	0.030±0.003	4.20±0.40	1.50±0.10	0.029	0.066	1167800	0.0276±0.0032	23.4±6.0
SS06	Mdt(m)	WTS-1	15.8±2.7	0.040±0.001§	4.60±0.60	1.45±0.15	0.085	0.209	468650	0.1785±0.0134	31.8±5.5
SS06	Mdt(m)	WTS-2	15.5±3.5	0.150±0.015	3.55±0.65	1.80±0.20	0.023	0.085	1546350	0.0364±0.0016	31.8±5.5
SS06	Mdt(m)	WTS-3	15.1±4.9	0.120±0.012	5.25±1.45	1.55±0.05	0.027	0.116	1656675	0.0524±0.0023	31.8±5.5
SS02	Volc	BG-1	39.5±9.5	0.000±0.000	3.10±0.10	1.10±0.20	0.133	0.245	500450	0.1882±0.0078	33.6±7.9
SS02	Volc	BG-2	39.1±3.7	0.005±0.005§	7.20±1.10	1.65±0.05	0.096	0.210	1760200	0.1969±0.0068	33.6±7.9
SS04	Mdt(v)	SS-1	14.0±5.3	0.029±0.003	7.95±0.25	1.50±0.10	0.083	0.213	677900	0.1054±0.0083	23.8±4.6
SS04	Mdt(v)	SS-2	14.2±5.6	0.021±0.009§	7.45±1.15	1.80±0.10	0.085	0.159	857925	0.0807±0.0045	23.8±4.6
SS04	Mdt(v)	SS-3	17.4±7.6	0.040±0.004	7.80±0.60	1.75±0.05	0.065	0.134	984650	0.1152±0.0073	23.8±4.6
SL07	Cgl	SRB-1	11.0±4.5	0.040±0.004	2.46±0.20	3.04±0.09	0.098	0.207	997975	0.0591±0.0061	37.7±8.8
SL07	Cgl	SRB-2	22.2±6.0	0.040±0.004	6.00±0.30	1.79±0.26	0.072	0.164	1186400	0.0680±0.0080	37.7±8.8
SL07	Cgl	SRB-3	13.1±5.4	0.020±0.002	10.93±0.69	1.52±0.16	0.063	0.123	2276175	0.0345±0.0027	37.7±8.8
SL07	Cgl	SRB-4	11.4±2.2	0.049±0.005	10.18±0.91	1.55±0.05	0.086	0.162	2610425	0.0323±0.0072	37.7±8.8
SL06	Cgl	GTS-1	13.8±6.7	0.010±0.001	3.40±0.90	2.04±0.07	0.080	0.122	3683775	0.0604±0.0034	34.4±12.4
SL06	Cgl	GTS-2	13.9±6.0‡	0.010±0.001	8.65±0.45	2.10±0.10	0.075	0.138	4155300	0.0259±0.0012	34.4±12.4
SL06	Cgl	GTS-3	13.9±6.0‡	0.030±0.003	8.50±0.90	2.40±0.10	0.071	0.112	5770675	0.0321±0.0013	34.4±12.4
SL06	Cgl	GTS-4	13.9±6.0‡	0.010±0.001	7.80±0.60	1.93±0.18	0.067	0.096	5842950	0.0205±0.0041	34.4±12.4

†: Abbreviations of channel categories follow **Figure 5**.

‡: The mean of uniaxial compressional strength measured in mudstone and flysch (Lichi Mélange, Paliwan and Fanshuliao formations).

§: Averaged bed exposure percentage from estimates of drone aerial images and Wolman counts. Others are only estimated through Wolman counts.

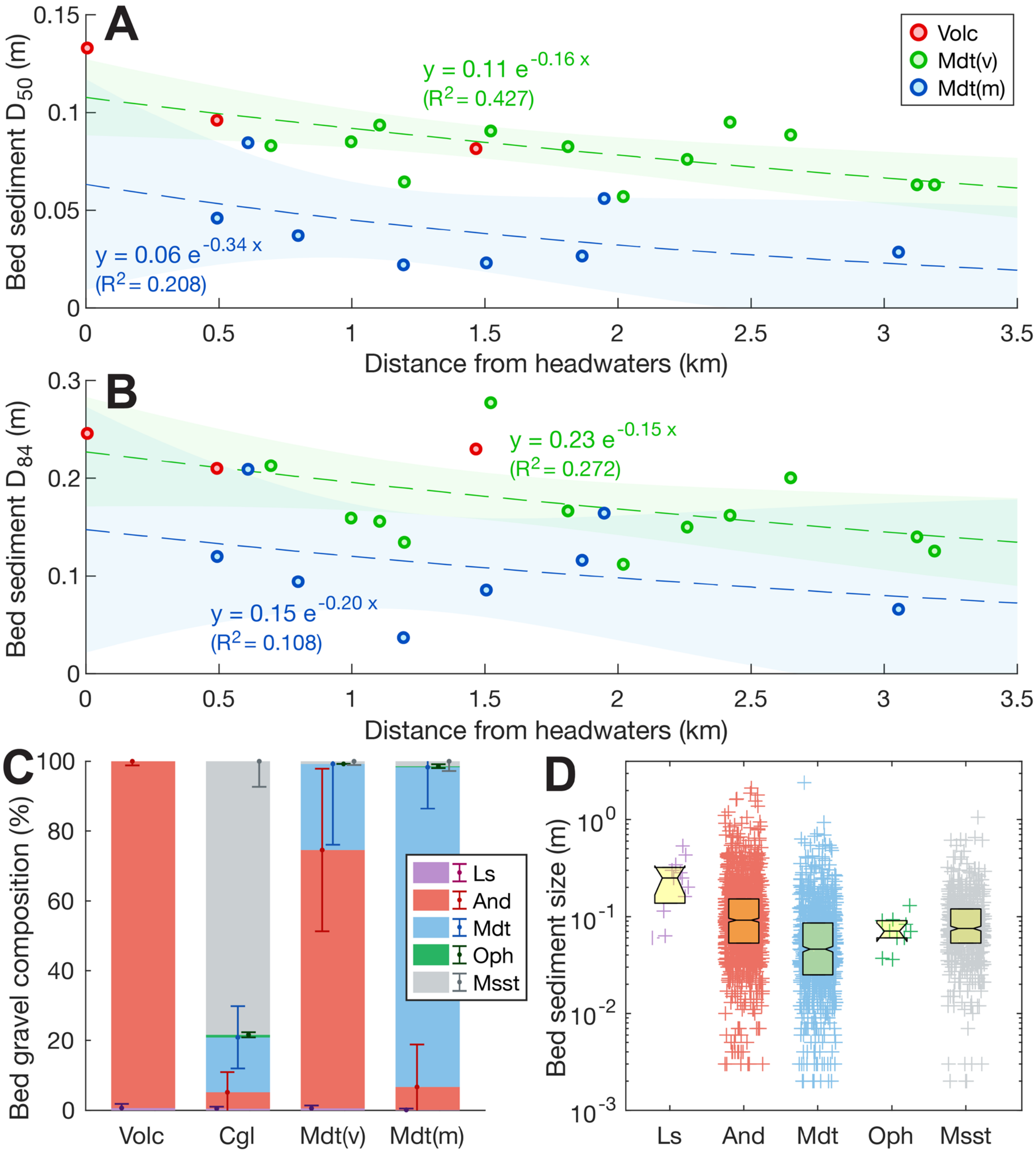

Figure 6. Size and constitution of channel bed sediments. (a-b) Bed sediment grain size (D_{50} and D_{84}) plotted against the distance from headwaters for reaches with (red and green) and without (blue) volcanic rock source, with best-fit exponential decay function (Sternberg, 1875). **(c)** Mean percentage of bed gravel lithology (with the standard deviation) in four classes of analyzed reaches. **(d)** Dependence of bed gravel size on lithology. Yellow boxes show the interquartile range and the median (with notched 95% confidence interval) of the data. Abbreviations of channel categories follow Figure 5. Lithological abbreviations: Ls = limestone; And = andesite; Mdt = mudstone and flysch; Oph = ophiolitic rocks; Msst = meta-sandstone. See raw data in Table S2.

uncertainties (Figures 8(a, b), S4). Values of $K_{sn}^{D_s}$ account for up ~20% or ~40% of the local K_{sn}, based on D_{50} or D_{84} as representative bedload size, respectively. We also find that $K_{sn}^{D_s}$ roughly correlates to mean hillslope gradient (Figure 8(c, d)).

Taken together, these observations quantitatively confirm that channel slopes in the Coastal Range are set primarily by the size and supply of hillslope coarse-sediment supply (controlled by bedrock lithology) rather than uplift rate and flow discharge (See details in *Discussion*).

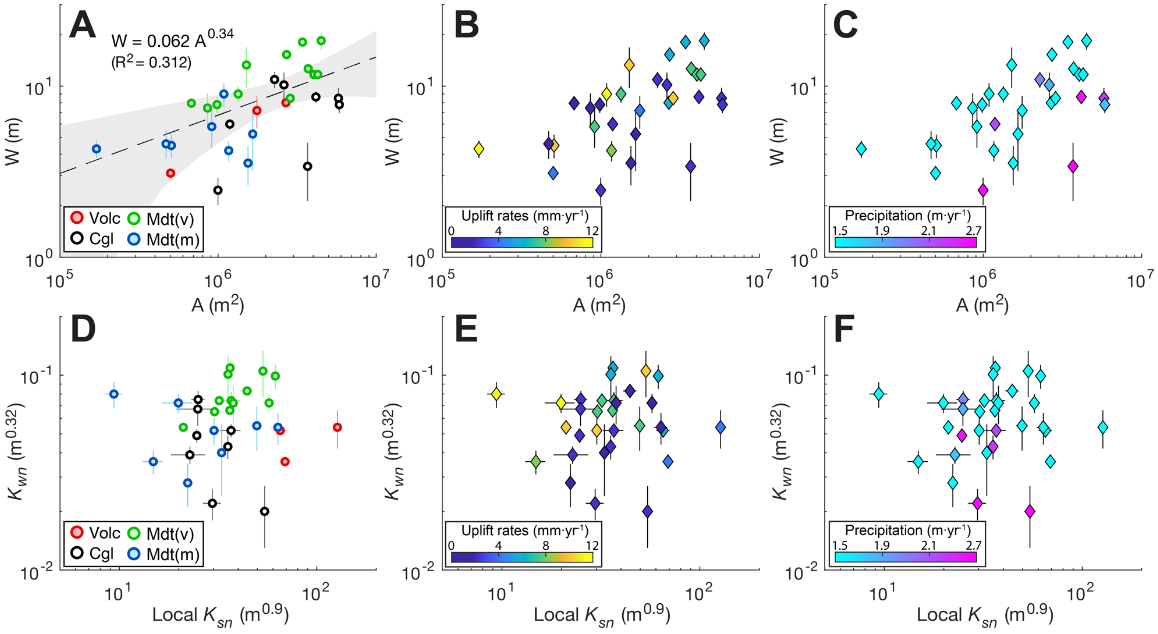

Figure 7. Functions of channel width. (a-c) High-flow width (*W*) plotted against upstream drainage area (*A*), colored in fourth channel categories (abbreviations follow Figure 5), regional uplift rate, and precipitation. Broken line and shade show the shows the best-fit power-law regression with 95% confidence intervals. (d-f) Normalized channel wideness (K_{wn}) plotted against local normalized channel steepness (K_{sn}, based on $\theta_{\text{ref}} = 0.45$), colored in fourth channel categories, regional uplift rate, and precipitation. Uncertainties are standard errors of the data. The results show that K_{sn} is more sensitive to variabilities of substrate strength and sediment supply (i.e., bedload size) than channel width. See data in Tables 1, 2, and S1.

Table 2. Analytic results of channel wideness and steepness components. Percentages of K_{sn} components at each site are plotted in Figure 8.

Catchment Number	Field sites	K_{wn}	Based on bed sediment D_{50}			Local K_{sn}	Based on bed sediment D_{84}		
			$K_{sn}^{D_s}$	$K_{sn}^{Q_s}$	K_{sn}^{E}		$K_{sn}^{D_s}$	$K_{sn}^{Q_s}$	K_{sn}^{E}
TL06	TCC-1	0.052±0.003	4.8±0.6	57.7±9.9	2.8±11.1	65.3±5.0	13.5±1.7	49.4±9.2	2.4±10.6
TL06	TCC-2	0.099±0.014	4.4±0.9	56.5±12.7	0.7±12.9	61.7±1.6	13.6±2.8	47.5±11.1	0.6±11.5
TL06	TCC-3	0.109±0.009	3.7±1.0	31.4±11.2	1.3±11.3	36.4±0.8	8.4±2.2	26.9±10.4	1.1±10.6
TL06	TCC-4	0.101±0.024	3.0±1.1	29.7±12.2	2.8±12.3	35.5±1.4	5.9±2.1	27.0±11.3	2.6±11.6
TL15	CLS-1	0.072±0.008	1.0±0.2	18.5±4.8	0.4±5.9	19.9±3.4	2.7±0.5	16.8±4.6	0.4±5.8
TL15	CLS-2	0.080±0.012	0.8±0.2	7.5±2.4	1.1±2.6	9.4±1.0	1.3±0.3	7.0±2.3	1.1±2.5
TL14	CC-1	0.052±0.008	1.7±0.8	27.6±16.3	0.9±16.4	30.2±1.4	4.3±1.9	25.1±15.5	0.8±15.7
TL14	CC-2	0.105±0.028	3.7±1.3	45.8±16.4	3.9±16.5	53.4±1.0	7.4±2.6	42.4±15.3	3.6±15.5
TL14	CC-3	0.054±0.002	4.4±0.3	16.5±1.6	0.2±1.8	21.1±0.7	8.8±0.6	12.2±1.4	0.1±1.7
CP09	DD-1	0.074±0.008	3.9±0.6	32.1±6.1	0.9±7.3	36.8±3.9	6.4±0.9	29.6±5.8	0.8±7.1
CP09	DD-2	0.074±0.005	3.5±0.3	28.1±5.4	0.4±5.5	32.0±0.6	6.9±0.6	24.8±2.7	0.3±2.8
CP09	DD-3	0.066±0.003	6.0±0.8	27.1±5.4	3.1±5.5	36.3±0.7	10.3±1.4	23.3±5.0	2.7±5.3
CP09	DD-4	0.065±0.004	4.1±0.4	25.9±2.7	0.3±2.7	30.4±0.3	9.1±0.8	21.0±2.3	0.3±2.5
CP09	DD-5	0.055±0.014	3.1±1.1	46.6±17.2	0.0±17.5	49.7±3.4	9.2±3.1	40.5±15.3	0.0±16.0
CP11	NSB-1	0.036±0.005	1.5±0.3	13.0±3.4	0.3±3.9	14.9±1.7	3.5±0.7	11.1±3.1	0.2±3.6
SS06	WTS-1	0.054±0.010	4.7±1.4	57.3±19.5	1.6±20.1	63.6±4.8	11.7±3.4	50.5±17.9	1.4±18.8
SS06	WTS-2	0.028±0.007	1.5±0.5	18.6±7.6	2.1±7.7	22.2±1.0	5.5±2.0	15.0±6.4	1.7±6.8
SS06	WTS-3	0.040±0.016	1.8±0.8	28.6±13.7	2.5±13.8	33.0±1.5	7.7±3.6	23.2±11.1	2.1±11.8
SS02	BG-1	0.036±0.002	10.7±3.1	58.3±24.8	0.0±0.0	69.1±2.9	19.8±5.8	49.2±23.1	0.0±0.0
SS02	BG-2	0.054±0.012	7.8±2.2	119.0±33.3	0.4±33.7	127.2±4.4	17.2±4.7	109.7±30.9	0.4±31.5
SS04	SS-1	0.083±0.004	3.9±0.5	39.6±7.1	0.8±8.0	44.3±3.5	10.1±1.2	33.6±6.7	0.7±7.6
SS04	SS-2	0.072±0.016	3.8±1.1	33.5±10.4	0.5±10.6	37.8±2.1	7.0±2.0	30.3±9.5	0.4±9.9
SS04	SS-3	0.072±0.008	3.3±0.5	52.6±8.7	1.4±9.5	57.3±3.6	6.9±1.0	49.0±8.3	1.4±9.1
SL07	SRB-1	0.022±0.004	6.1±1.3	22.9±5.6	0.6±6.5	29.6±3.0	12.7±2.6	16.4±4.6	0.4±6.1
SL07	SRB-2	0.052±0.004	3.9±1.0	32.0±11.6	0.9±12.4	36.8±4.3	8.8±2.2	27.2±10.8	0.8±11.9
SL07	SRB-3	0.075±0.008	3.6±0.9	21.2±7.3	0.3±7.6	25.1±1.9	7.0±1.7	17.8±6.7	0.2±7.2
SL07	SRB-4	0.067±0.012	5.1±1.3	19.6±7.3	0.3±9.2	25.0±5.5	9.6±2.3	15.2±6.7	0.2±9.0
SL06	GTS-1	0.020±0.007	8.3±3.5	45.8±19.9	0.3±20.4	54.4±3.0	12.8±5.4	41.4±18.0	0.3±19.1
SL06	GTS-2	0.049±0.004	4.6±0.6	19.9±3.2	0.1±3.4	24.7±1.1	8.3±1.0	16.3±2.8	0.1±3.2
SL06	GTS-3	0.043±0.006	4.6±0.9	30.2±6.5	0.6±6.7	35.4±1.4	7.7±1.5	27.2±5.9	0.6±6.3
SL06	GTS-4	0.039±0.004	4.7±1.0	18.0±6.5	0.1±8.0	22.8±4.5	6.9±1.4	15.8±6.2	0.1±7.8

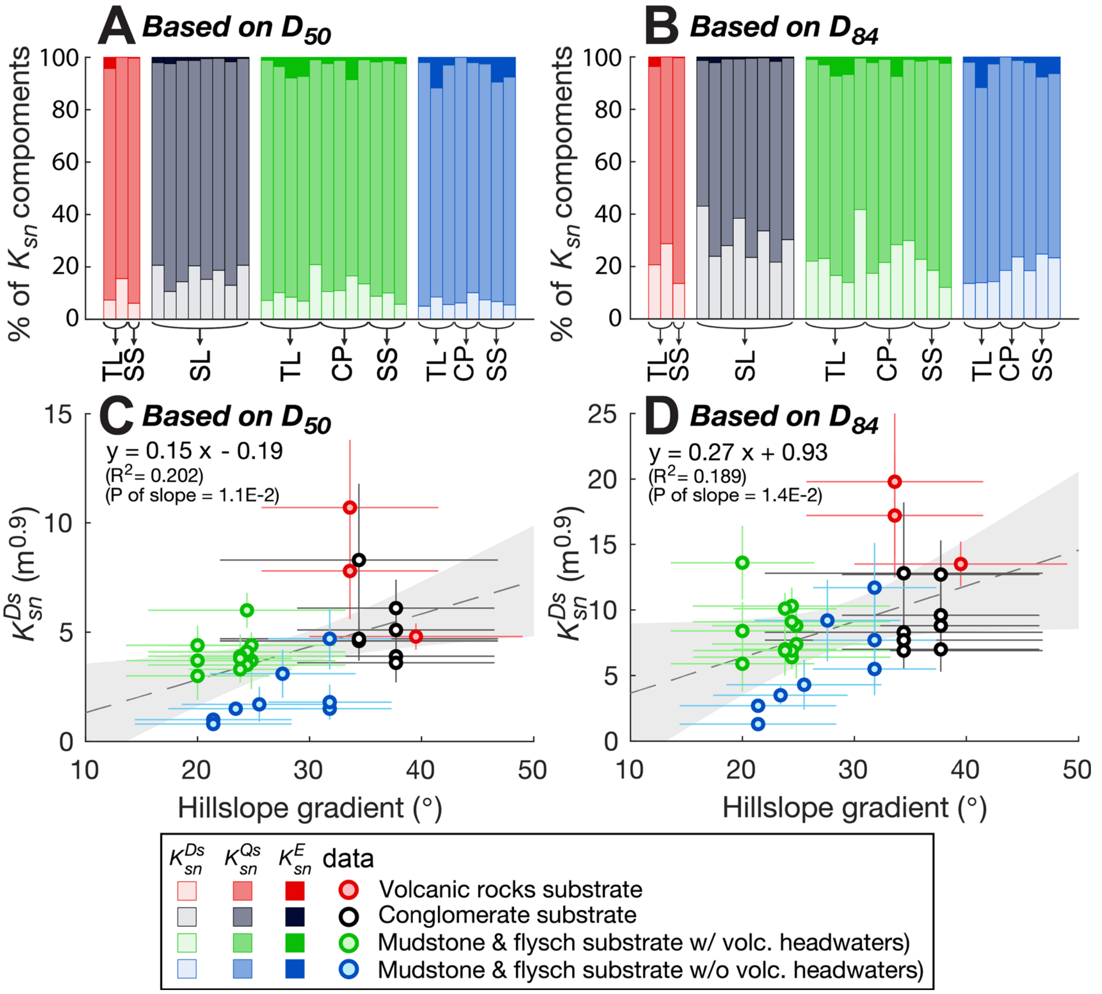

Figure 8. **Channel steepness partitions.** (a-b) Percentage of K_{sn} components in Equation (7) based on D_{50} and D_{84} respectively. Abbreviations of study regions: TL: Tulan; SS: Shinshe; CP: Changpin; SL: Shuilien. (c-d) $K_{sn}^{D_s}$ plotted against mean hillslope gradient (with standard error), based on D_{50} and D_{84} respectively. Broken lines and shade zones show linear regressions and 95% confidence intervals. Abbreviations in legends follow Figure 1(a). See data in Tables 1 and 2 and functions of other K_{sn} components in Figure S4.

6. Discussion

6.1. Sediment effects on channel concavity

One important prediction of the saltation-abrasion model is the dependency of channel concavity on the size of hillslope sediment supply (Sklar & Dietrich, 2008). In transport-limited systems where channel slope primarily depends on river sediment size and supply (S_{D_s} and ΔS_{Q_s} in Equation (4)), Sklar and Dietrich (2008) predicted that channel profiles have higher concavity when connected to coarser sediment supply because of stronger long-profile gradient of sediment size (i.e., downstream fining) after long-distance abrasion. Other studies have also documented a covariance of the size and the mass fraction of gravel-size (diameter > 2 mm) hillslope debris that will eventually become bedload, indicating that stronger bedrock may produce not only larger but also more bedload-sized sediments, plausibly modulating downstream channel profiles (Marshall & Sklar, 2012; Sklar et al., 2017).

The data and results of this study appear to support this hypothesis by demonstrating a generally higher mean concavity (θ) in mudrock reaches connected to volcanic bedrock (~0.60) compared to reaches with limited inputs of resistant clasts (~0.50) (Figure 3(c)). Yet it should be noted that the data of best-fit θ are noisy and the difference of the means is statistically insignificant (the range of standard deviation overlaps). This may reflect the short length of our analyzed reaches, in which downstream fining by abrasion is difficult to untangle among reaches with different substrate lithology and sediment source rock (Figure 6(a, b)). Our field site therefore provides an advantage in that the values of channel steepness (K_{sn}) derived from short channel profiles in this study are less likely to be influenced by systematic bias of sediment-size governing concavity variation.

6.2. Channel steepness set by hillslope sediment supply

The results of our slope component analysis (Equations (7)) reveal that channel steepness (K_{sn}) in the Coastal Range is set primarily by sediment flux ($K_{sn}^{Q_s}$), followed by a secondary contribution of sediment size ($K_{sn}^{D_s}$) (Figures 8(a, b)). These observations agree with model predictions for sediment-rich channels (Sklar & Dietrich, 2006). In addition, although K_{sn}^{E} is thought to record bedrock erodibility, observed values of K_{sn}^{E} are too small to generate the apparent correlation between local K_{sn} and substrate strength (Figure 5(d)), which implies that the bedrock resistance signal may be reflected in $K_{sn}^{D_s}$ and/or $K_{sn}^{Q_s}$ (Figure S4). Because $K_{sn}^{D_s}$ inherently scales with bed sediment size (Equations (5) and (7)), the correlation between $K_{sn}^{D_s}$ and mean hillslope gradient implies that the generation of coarse sediments can be attributed to steeper hillslopes and frequent delivery of landslide debris (Figure 8(c, d)). This inference is supported by the lithological dependency of sediment size, in which gravels derived from volcanic and conglomerate hillslopes exhibit greater size and durability than erodible debris from mudstone and flysch watersheds (Figure 6(d)). Based on these observations, we hypothesize that bedrock lithology can modulate $K_{sn}^{D_s}$ and $K_{sn}^{Q_s}$ terms in Equation (7) through mass-wasting sediment production on threshold hillslopes, which leads to steepening in channels connected to strong rocks (see also Attal et al., 2015; DiBiase et al., 2018; Finnegan et al., 2017; Roda-Boluda et al., 2018; Shobe et al., 2016; Shobe et al., 2021).

It is possible that both of our measured bedload D_{50} and D_{84} may not represent the actual sediment size in calculations, which could lead to overestimation or underestimation of the $K_{sn}^{D_s}$ and $K_{sn}^{Q_s}$ terms. It is also worth noting that the sediment size, high-flow channel geometry, and bedrock coverage we measured may only represent a "snapshot" of channel appearance at each site whereby the fractions of $K_{sn}^{D_s}$ and $K_{sn}^{Q_s}$ terms might change over relatively short timescales. That said, bedload D_{50} and D_{84} of gravel-rich bedrock channels scale systematically with other grain-size percentiles (Rickenmann & Recking, 2011), which justify the representativeness of our grain size data. Widening of channel morphology in response to increased supply of sediment supply has also been shown to provide possible concomitant restriction on K_{sn} (Figure 7(b, e)) (Lavé & Avouac, 2001; Yanites et al., 2018). The variability of flow discharge through time, which is proposed to be a critical factor in control of the frequency of alluvium removal and bed incision (DiBiase & Whipple, 2011; Lague, 2010; Lague et al., 2005), is difficult to characterize, however. Considering which most precipitation in the Coastal Range is accumulated during storms and typhoon events (Chen & Chen, 2003), runoff exceeding the threshold to move coarse sediment likely happens during floods. Thus, the bed exposure percentage, that we used to approximate relative transport capacity by floods (Equation (6)), may sufficiently reflect the net effect of discharge variability over time (Chatanantavet & Parker, 2008). Given these uncertainties mentioned above, we highlight the dominance of $K_{sn}^{D_s}$ and $K_{sn}^{Q_s}$ terms from slope component analysis (Figure 8(a, b)) as direct evidence that incision processes governed by coarse sediment can limit the tectonic steepening of channels over an order of magnitude variation in uplift rates (1.8 to 11.8 mm·yr^{-1}) and relatively constant precipitation (1.5 to 2.7 m·yr^{-1}) (Figures 5(a, b, c), 9(b)).

6.3. Natural restriction on channel steepening

Our analysis highlights the invariance of K_{sn} across a wide range of fast uplift rates for a given bedrock setting (Figures 3, 5(a)). A similar uncorrelated relationship between K_{sn} and rock uplift (erosion) rate has been observed in other bedrock rivers undergoing rapid tectonic uplift (generally >0.6-1 mm·yr^{-1}) (e.g., Adams et al., 2020; DiBiase et al., 2010; Fellin et al., 2017; Hilley et al., 2019; Ouimet et al., 2009), where omnipresent landslide or abundant coarse bedload sediment are reported. In one exception, Duvall et al. (2004) found steeper channels in high uplift (5 mm·yr^{-1}) zones compared to slow uplift (0.75-2 mm·yr^{-1}) zones in a system with limited coarse-sediment load, similar to channels in a detachment-limited system typically observed in soil-mantled landscapes (i.e., erosion rate <0.3-0.6 mm·yr^{-1}) (Figure 9(a)). The combined evidence above reveals the first-order role of coarse-sediment load in modulation of fluvial bedrock channel slope, indicating that channel steepness does not necessarily scale with rock uplift rate, bedrock strength, or mean water discharge due to the sediment effects predicted by mechanistic incision models (Sklar & Dietrich, 2004, 2006), especially in fast-uplifting (i.e., fast-eroding), landslide-prone landscapes (Figure 9(b)). Our field-based analysis supports this perspective by demonstrating a clear connection between channel steepness and coarse-sediment size and availability (Figure 5(d, e, f)).

Moreover, if channel steepness does not vary with rock uplift rate in quasi-equilibrium channel profiles, the faster rates of long-term incision in areas with higher uplift rates must depend on mechanisms other than the steepening of channel slope (Snyder et al., 2003). It is plausible that the influence of erosion on channel slope is essentially zero in this landscape as reflected in very low percentage of the K_{sn}^{E} term (Figure 8(a, b)). Further, the large uncertainty in K_{sn}^{E} may indicate that erosion is accomplished rapidly during random and episodic bedrock exposure created by fluctuations in sediment supply and transport during floods (Figure S4) (Montgomery et al., 1996; Stock & Dietrich, 2003). However, under the steady state assumption, the flux of coarse sediment supply should be influenced by erosion rate, which predicts an unverified proportionality between the $K_{sn}^{Q_s}$

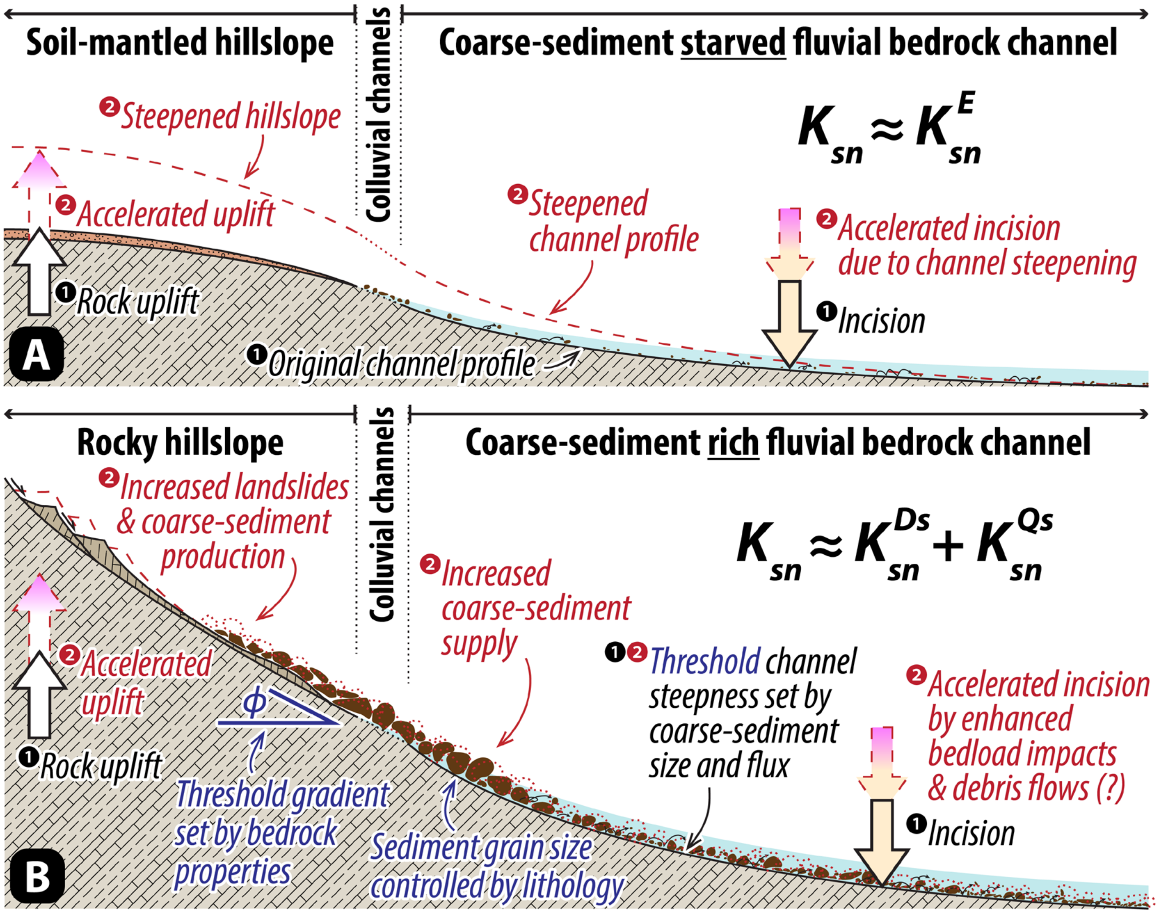

Figure 9. Mechanistic-model based hypothesis of channel steepening coupled with hillslope processes in response to an increase of uplift rate under steady-state assumption. (a) Soil-mantled hillslope and coarse-sediment starved fluvial channels in slow-eroding (i.e., slow-uplifting) landscape. In this system, channel steepness is dominated by K_{sn}^{E} term in Equation (7) and can scale with rock uplift rate, following prediction of the stream-power model. **(b)** Rocky hillslope and coarse-sediment rich fluvial channels in fast-eroding (i.e., fast-uplifting) landscape. In this system, channel steepness is dominated by $K_{sn}^{D_s}$ and $K_{sn}^{Q_s}$ terms in Equation (7) and can become insensitive to variability of rock uplift rate. A proposed threshold channel steepness is set by bedload sediment size and supply for given bedrock and hydraulic conditions. Accelerated incision may be accomplished by processes other than channel steepening such as enhanced bedload impacts and perhaps additional debris-flow scour.

term (ultimately the K_{sn} in Equation (7)) and uplift rate. Thus, there must be another unidentified variable that accounts for confining the observed "threshold" of channel steepness in the Coastal Range over a 10-fold variation of uplift (erosion) rate (Figures 3(d), 5(a, b)).

One possibility is that the fraction of the hillslope bedload-size sediment supply may vary with uplift rate and bedrock properties (Sklar & Dietrich, 2008; Sklar et al., 2017). For maintaining a relatively constant K_{sn}, the fraction of bedload supply should decrease in places with faster erosion (uplift) rate (restricting the $K_{sn}^{Q_s}$ term) under this hypothesis. This is unlikely in our study area because the frequency of mass-wasting events, and their contribution of bedload sediments, are expected to increase with erosion (uplift) rate (Montgomery & Brandon, 2002; Roering, 2012). A second possibility is that the decoupling of channel steepness from uplift rate can be accomplished entirely through channel widening (i.e., enhanced bank erosion) which limit downcutting by flow basal shear stress (Lavé & Avouac, 2001; Yanites et al., 2018). Although there is a slight tendency to find wider channels in areas with faster uplift rate (i.e., higher sediment outflux), our data shows weak or no correlation between normalized channel wideness (K_{wn}) and uplift rate (Figure 7(b, e)). Similar findings in previous studies also show no detectable change in channel width of quasi-equilibrium channels over a wide range of uplift rate (~0.1-4 mm·yr^{-1}) (DiBiase et al., 2010; Snyder et al., 2003), challenging the generality of the width-adjustment hypothesis.

Thus, we propose a third possibility that there is a need to consider the mechanics of enhanced downcutting processes in order to balance uplift rate in landscapes with confined channel steepness and coarse sediment supply (Figure 9(b)). The abundant presence of rounded and imbricated (transported) volcanic rock large boulders (e.g., diameter >1 m) in channels several kilometers away from its source supports the partial role of debris-flow processes in shaping the fluvial channel profiles (Figure 4(a, c)), which require unrealistically large high-flow hydraulic radius (R_h) to exceed the threshold of sediment entrainment of these boulders by fluvial bedload processes (Equation (5)). This scenario is plausible because the efficiency of channel bed erosion scales with coarse-sediment flux per unit channel width (Sklar & Dietrich, 2001; Vázquez-Tarrío et al., 2020) and the frequency of episodic debris flows (Stock &

Dietrich, 2003; Stock et al., 2005), which increase with uplift rate and the occurrence of landslides on steep hillslopes (Attal et al., 2015; Larsen & Montgomery, 2012).

6.4. Mountain relief limited by bedrock

While sediment size and supply clearly exert a strong influence on channel slopes in the Coastal Range, our data also implies that bedrock lithology plays a vital role in formation of fast-uplifting fluvial landscapes. It has been well-documented that the mass strength of rock controls the occurrence of threshold hillslopes (i.e., angle of repose), and the insensitivity of gradient to uplift rate when mass wasting outpaces soil production (Figure 9) (Montgomery & Brandon, 2002; Ouimet et al., 2009; Roering, 2012). In addition to rock resistance, rock textures, degree of diagenesis, durability against weathering, and overprinting properties (e.g., fractures) have been reported to provide complicated controls on rock mass strength that sets the threshold gradient for hillslope and the size of sediment production (Marshall & Sklar, 2012; Migoń, 2020; Neely et al., 2019; Sklar et al., 2017).

Growing evidence shows that increases in coarse sediment supply corresponding to steeper threshold hillslopes can cause steepening of downstream bedrock channels by retarding incision through channel coverage (Attal et al., 2015; Finnegan et al., 2017; Neely & DiBiase, 2020; Roda-Boluda et al., 2018; Shobe et al., 2016; Shobe et al., 2021). Our observations in the Coastal Range strongly support this idea (Figure 5(e-f)) by demonstrating the lithological control on sediment particle size (Figure 6(d)) and the discrepancy in steepness among reaches in mudstone and flysch substrate purely caused by the difference in coarse sediment input from volcanic rocks (Figures 2(b), 3(d), 5(a, b, d, f)). Results from slope component analysis further reveal that bedrock can modulate channel steepness by not only providing strength against incision on the channel bed as popularly considered (i.e., controlling K_{sn}^{E} term in Equation (7)), but also by transmitting their lithological signals into sediment size and then setting slope by modulating the $K_{sn}^{D_s}$ and $K_{sn}^{Q_s}$ terms. Taken together, the dominance of $K_{sn}^{D_s}$ and $K_{sn}^{Q_s}$ in governing channel steepness (Figure 8(a, b)) and the invariance of K_{sn} against varying uplift and climatic forces in the Coastal Range (Figure 5(a, b)) suggest that sediment size and supply appears to define a “threshold” of channel steepness in fast-uplifting, landslide-dominated terrains

(Figure 9(b)) (DiBiase et al., 2018; Hilley et al., 2019). Since the properties of exhumed bedrock may fundamentally set the landscape-scale erodibility and the threshold of both hillslope gradient and channel steepness, it raises the possibility that coupled hillslope-channel processes of mass-wasting and sediment-governed incision ultimately limit the shape and relief of orogenic landscape (Egholm et al., 2013; Roering, 2012; Schmidt & Montgomery, 1995).

6.5. Applicability of incision models

Our results suggest that stream power based incision models might be too simplistic to describe, explain, and simulate the bedrock fluvial landscape in rapidly uplifting (eroding), mass-wasting terrains (Tomkin et al., 2003; van der Beek & Bishop, 2003). At the very least, these models fail to provide a satisfying explanation for the observed pattern of channel steepness in the Taiwan Coastal Range, particularly the insensitivity of uplift rates and precipitation, and the strong correlation with bed lithology and sediment source rocks (Figure 5). Rather, a physics-based incision model (e.g., saltation-abrasion model) that invokes the contributions of sediment entrainment and relative transport capacity on channel slope, can account for our observations (Figure 8).

The steepness partitioning method (Equation (7)) adopted here provides a field-based explanation for sediment effects on setting channel steepness. Most generally, we suggest that stream power assumptions may be reasonably applied in slowly uplifting (or eroding) landscapes with soil-mantled hillslopes and coarse-sediment starved channels, where K_{sn} may be dominated by the residue term K_{sn}^{E} in Equation (7) (Figure 9(a)). Conversely, when the $K_{sn}^{D_s}$ and $K_{sn}^{Q_s}$ terms govern K_{sn}, particularly in fast uplifting landscapes with rocky hillslopes and coarse-sediment rich channels, incision models that do not consider sediment effects may be unable to capture key mechanistic controls on channel slope (Figure 9(b)) (Venditti et al., 2020; Whipple et al., 2013).

7. Conclusions

Our field observations and application of a saltation-abrasion model quantify the relative importance of coarse sediment effects on fluvial bedrock channel slope in the Coastal Range of eastern Taiwan, a rapidly uplifting and eroding landslide-dominated landscape. We find that a dynamic interplay between mass-wasting on hillslopes and coarse-sediment governed incision may act to limit steepening of channel profiles in this and other active orogenic belts. Furthermore, our data reveal that bedrock lithology controls the gradient of threshold hillslopes and could further set the steepness of downstream channels through the production of coarse sediment. For a given combination of bedrock strength and climate forcing, we suggest that coarse sediment from steep hillslopes exerts a primary control on bedrock channel gradient, which leads to decoupling of channel steepness from uplift rate in areas of rapid tectonic uplift. Channel steepness, commonly used as a proxy for mapping regional patterns of tectonic uplift, may instead reflect coarse sediment size and sediment supply in bedrock channels of fast-eroding (>1 $mm \cdot yr^{-1}$) landscapes. This influence is closely associated with and genetically linked to frequent landsliding, in addition to adjustments of channel width to variations in sediment coverage.

CHAPTER V
DISSERTATION SUMMARY

This dissertation has examined the sedimentary stratigraphy and modern topography of Taiwan’s Coastal Range with important implications for syn-orogenic crustal recycling, sedimentary basin development, and landscape evolution at the interface of two converging plates in an active arc-continent collision system.

In chapter II, I established a high-fidelity stratigraphic framework for sedimentary strata in the southern Coastal Range of eastern Taiwan, using integrated field surveys, sedimentology, paleomagnetism, and microfossil studies, which provide robust constraints on the origins of the Lichi Mélange. The genesis of this polygenetic mélange unit is closely associated with sedimentation in a retrowedge foredeep basin, which developed in response to episodes of accelerated exhumation and tectonic mixing in the source regions of the Taiwan arc-continent collision zone.

In chapter III, I combined high-resolution chronostratigraphy, paleo water depth reconstruction, and backstripping models of crustal subsidence history to document an extremely rapid emergence of the Coastal Range of eastern Taiwan from deep marine to modern elevation (up to 1.3-1.6 km) along the plate suture zone over the past ~500 thousand years, at world-class rates of rock uplift of ~9–14 mm/yr.

In chapter IV, I combined theoretical tools in quantitative geomorphology with physical parameters constrained from digital elevation models and field observations to investigate the primary surface processes that control the shape of modern landscape in Taiwan’s Coastal Range. I found the presence of threshold channel steepness and limited relief in a tectonically active mountain topography, which is insensitive to spatial variabilities in tectonic uplift or climate. Such landscape is governed by sediment-controlled fluvial incision, sediment production on hillslopes (i.e., soil production and landslides), and associated bedrock properties.

Combined works in this dissertation outline the future for sedimentological and geomorphic research to understand the interactions and feedbacks among surface and tectonic processes, and to detect their temporal-spatial scales. This study emphasizes the critical role of sediment in crustal recycling and landscape evolution in a rapidly evolving collision suture zone. The results provide new insights into how sediments are generated, transported, deposited, buried, lithified, exhumed, and recycled during collisional orogenesis. Integrated methods of stratigraphic and topographic analyses applied in this dissertation are at the cutting edge of our ability to constraint spatial patterns of Earth's surface processes across different timescales. To seek breakthrough, future works should address the physical and chemical controls on sediment generation and redistribution, and their dependence on tectonics, climate forcing, landform, and bedrock lithology. New approaches, theories, and techniques (particularly in dating sediments and processes) are needed to find the link between transient Earth surface activities and deep-time sedimentary records, and disentangle complex signals from them. Many workers are putting efforts on this or related topics (e.g., Romans et al., 2016; Shobe et al., 2022; Straub et al., 2020), and I intend to continue my endeavor in this exciting field. I am hopeful that sediment-focused research will unlock more potentials to extract valuable information from geologic and geomorphic archives. This will allow us to better reconstruct the past and thus improve our ability to predict the future of the surface environment on our mother Earth and extraterrestrial planets.

APPENDIX A
CHAPTER II SUPPORTING INFORMATION

***Tables S1–S5 are included in supplemental files of this dissertation**

Detail methodologies

Geological mapping and lithostratigraphy

Detailed geological mapping for this study targeted he Lichi Mélange and associated deposits exposed in road cuts and riverbanks of the southern Coastal Range (Figure 4). Marker beds (pebbly mudstone and tuffaceous turbidite) and fault zones were carefully mapped across the study area (Figures S1-S2). We also compiled information from previously published geological maps (Doo & Shyu, 1966; Hsu, 1956; Lai, Ng, et al., 2018; Lai & Teng, 2016; Lin et al., 2008; Lo et al., 1993; Wang & Chen, 1993). Lithostratigraphic descriptions were executed in type sections of the Fanshuliao and Paliwan formations in the MDJ and BCa sections (Figure 9), and other selected river sections along three geological transects: (1) Powhua-Shinchang; (2) Luye-Tulan; and (3) Fuli-Chengkung transects. We described in detail lithologic transitions at well exposed depositional contacts between the Lichi Mélange and Fanshuliao Formation in the CYCa and YF sections. The concept of lithofacies description and analysis is applied for unit classifications.

Calcareous nanoplanktons and planktonic foraminifera biostratigraphy

We compiled existing data from studies with complete information of sample localities and identified fossils per site (Barrier & Muller, 1984; Chang, 1967, 1969; Chen, Huang, et al., 2015; Chen, Huang, et al., 2017; Chen, 1988a; Horng & Shea, 1996; Huang & Yuan, 1994). Sample localities were manually georeferenced from published maps into geographic information system (GIS) software in order to project them to stratigraphic height in measured sections (Figures S3-S9). We also digitized unpublished calcareous nannoplankton fossil charts using georeferenced sample coordinates from Chi et al. (1981) and include them in our data repository (Table S3). Data of Chi et al. (1981) for sedimentary blocks in the Lichi Mélange are lost and immemorable, yet their interpreted range of fossil zones (NN3-NN11) and depositional age (~18-5.6 Ma) are compiled in this study (Figure 3).

We also collected samples for new microfossil analysis in the Lichi Mélange from all major river sections (Figures S3-S7), with a focus on calcareous nannoplankton data that were relatively limited in previous studies. In mélange, we collected fine-grained matrix to constrain its maximum forming age by the presence of the youngest index fossils. For localities that were reported to have potential surface contamination (Site J17 in Chen, Huang, et al. (2017)), we revisited and resampled the sites and nearby exposures (Figure S5). Three samples for planktonic foraminifera identifications were collected in YF section (Figure S7). Samples were collected from fresh intact exposures of fine-grained mudstone. Samples were crushed prior to further dispersion of samples in deionized water aided by ultrasonic vibration. Because calcareous microfossils are often limited in the mélange, we centrifuged the suspended particles in dispersed mud to extract concentrated fossils of calcareous nannoplankton. Microfossils were placed on thin sections for observation using an optical microscope. For preparing planktonic foraminifera samples, we omitted ultrasonic vibration and used 63 μm sieve to extract proper size fossils for identification.

Interpretation of depositional age from microfossil assemblages is challenging due to the potential for reworking of older fossils, which is commonly reported in turbidite-dominated deposits of the Coastal Range (Chen, 1988b, 2009; Chi et al., 1981) and confirmed by our work. Therefore, depositional ages are based primarily on the first appearance datum (FAD) for index fossils, whose ages are based on recent compilations for the Indo-Pacific region (Anthonissen & Ogg, 2012; Backman et al., 2012; Chuang et al., 2018) (Figure 3).

Magnetostratigraphy

We conducted paleomagnetic measurements for strata in coherent continuous sections (Fanshuliao and Paliwan formations), avoiding slump beds and chaotic mass-transport deposits. Paleomagnetic samples were collected using a standard (22 mm diameter) drill core from fresh mudstone exposures, and remanent magnetization was measured with a 2G three-axis cryogenic magnetometer. As reported in Horng and Shea

(1996), the primary carrier of remanent magnetization here is pseudo-single-domain magnetite. To remove viscous remanent component of overprinting magnetic signals, progressive thermal demagnetization (THD) was applied to most of the samples with ten or more increments from room temperature to 600°C. The results from some specimens with relatively low intensities of natural remanent magnetization became thermally unstable at higher temperatures (usually >360°C). In these cases, we applied stepwise alternating-field demagnetization (AFD) from 0 up to 80 mT or a combination of THD and AFD (e.g., THD to 360°C followed by AFD procedure). Using these methods, we obtained reliable measurements of primary remanent component of the paleomagnetic declination and inclination from Zijderveld diagrams at each site (Figure S17). We derived mean paleomagnetic directions by applying a double-tilt correction in which we first removed perturbations by restoring regional fold plunge and then bedding tilt (Fisher, 1953; Ramsay, 1961). This correction procedure is also applied to compiled original data from Horng and Shea (1996) of the MDJ section (see applied structural corrections in Table S5). FAD of microfossils were used to interpret polarity chrons, and the age of magnetic reversals follows the global geomagnetic polarity timescale (Ogg, 2012).

Basin restoration

To reconstruct paleo-basin geometry we constructed three stratigraphic panels by correlating stratigraphic sections along W-E transects (Powhua-Shinchang, Luye-Tulan, and Fuli-Chengkung). Stratigraphic columns were projected into the closest transect and placed at structurally restored horizontal positions (Figures 4, S1-S2). Panels were hung from the youngest widespread chronostratigraphic horizons, or datums, such as FAD of microfossils, paleomagnetic reversals, and event marker beds. We assume kink-folds to be the dominant style of regional folding (Chi et al., 1981), and approximate the unfolded horizontal length using standard geometrical methods (e.g., Ragan, 2009) and mean bedding dip along the transects. The results provide a reasonable reconstruction of original relative positions of stratigraphic sections and facies architecture in the southern Coastal Range.

Sediment-transport directions

To reconstruct sediment routing pathways and sediment sources, we measured paleocurrent and paleoslope directions in each studied section and the Loho and Changpin areas (i.e., AMC, LHC, SKC sections) (Figures 4, 14), including data for tuffaceous turbidites (Lai, Ng, et al., 2018). Paleocurrent directions were measured from flute casts, ripple cross-lamination, and imbricated gravel clasts. For ripple cross-lamination, we only measured foreset laminae that show ≥ 10° angle from the bedding plane to reduce uncertainty (Bradley, 1987; Bradley & Hanson, 2002). Paleoslopes were determined by measuring axial planes of asymmetric slump folds (Bradley & Hanson, 1998; Strachan & Alsop, 2006). All directional data were restored to paleo-horizontal using a double-tilt correction (same as for paleomagnetic directions).

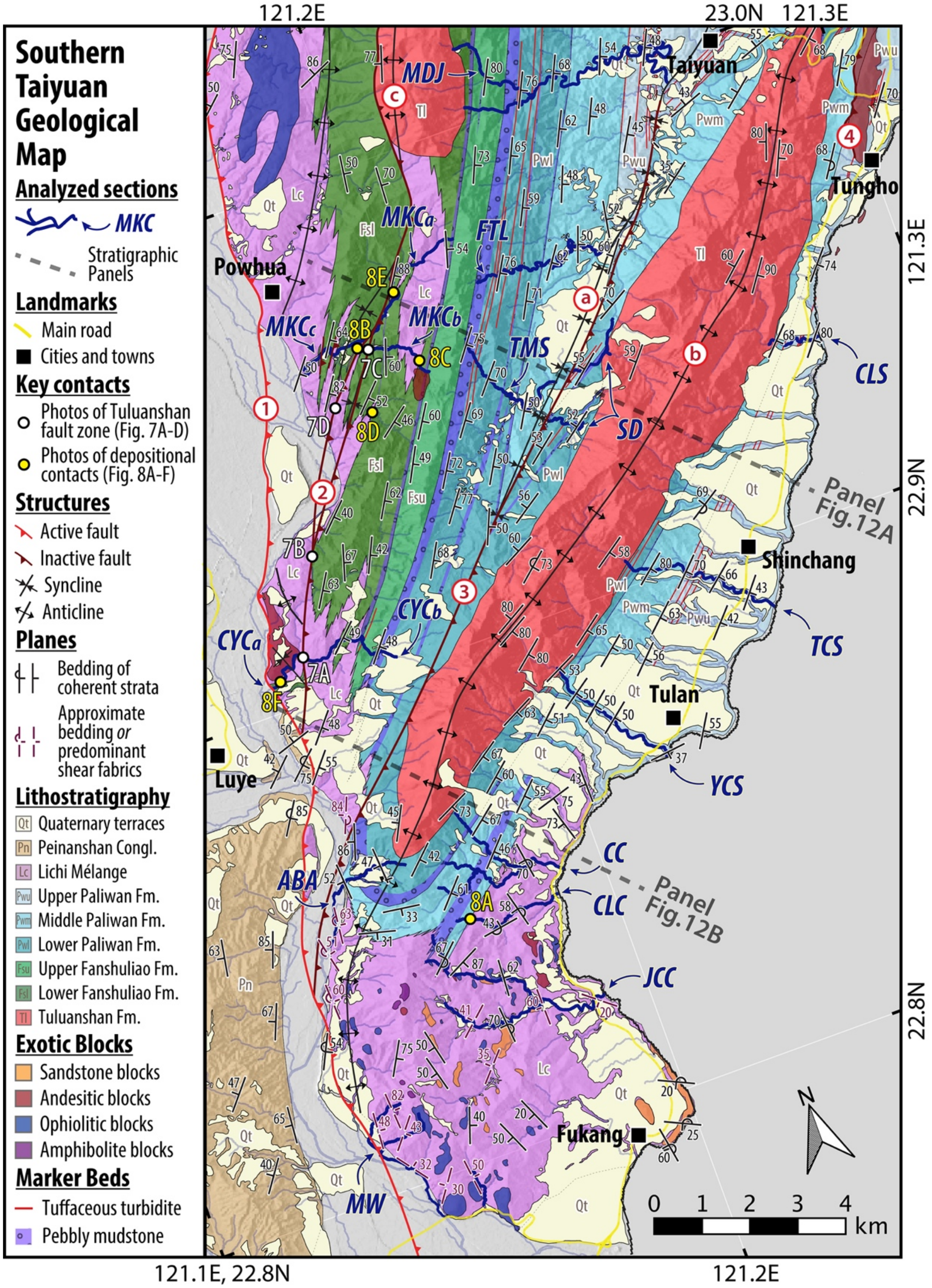

Figure S1. **Geological map of southern Taiyuan, modified from Doo and Shyu (1966); Lai, Ng, et al. (2018); Lai and Teng (2016); Lin et al. (2008); Page and Suppe (1981).** Labels in red circles mark major structures: 1 = Longitudinal Valley fault; 2 = Tuluanshan fault; 3 = Wushinshih fault; 4 = Tama fault; a = Taiyuan syncline; b = Tuluanshan anticline; c = Biehchi anticline.

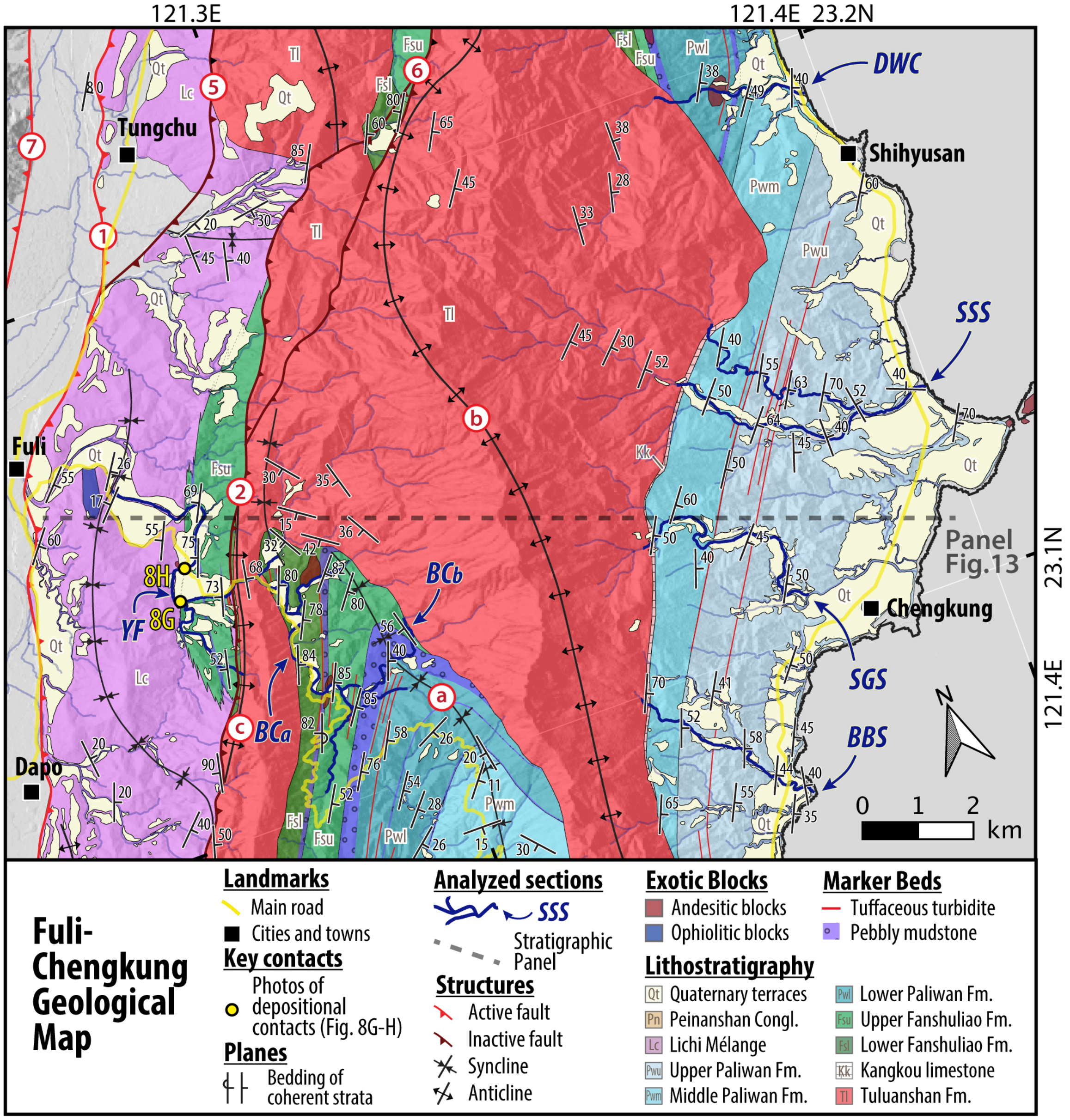

Figure S2. **Geological map of Fuli-Chengkung area, modified from Barrier and Muller (1984); Hsu (1956); Lai, Ng, et al. (2018); Lai and Teng (2016); Wang and Chen (1993).** Labels in red circles mark major structures: 1 = Longitudinal Valley fault; 2 = Tuluanshan fault; 5 = Kuanyinshan fault; 6 = Huatungshan fault; 7 = Central Range fault; a = Taiyuan syncline; b = Tuluanshan anticline; c = Biehchi anticline.

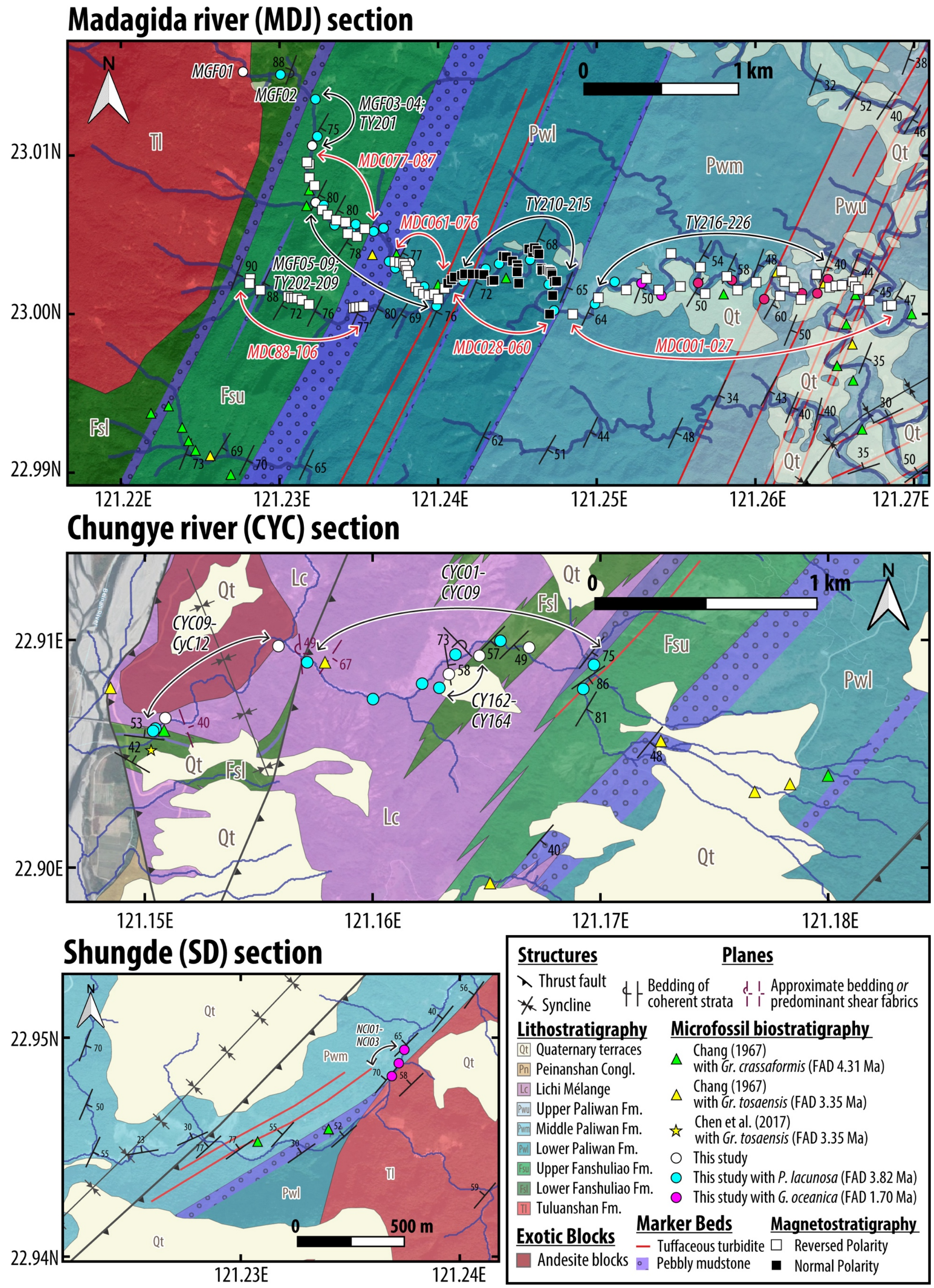
Madagida river (MDJ) section

Chungye river (CYC) section

Shungde (SD) section

Figure S3. **Paleomagnetism (red labels, from Horng and Shea (1996)) and microfossil samples (black labels) locations for MDJ, CYC, and SD sections**. See stratigraphic columns in Figures S10, S12 and new raw data in Tables S3, S5.

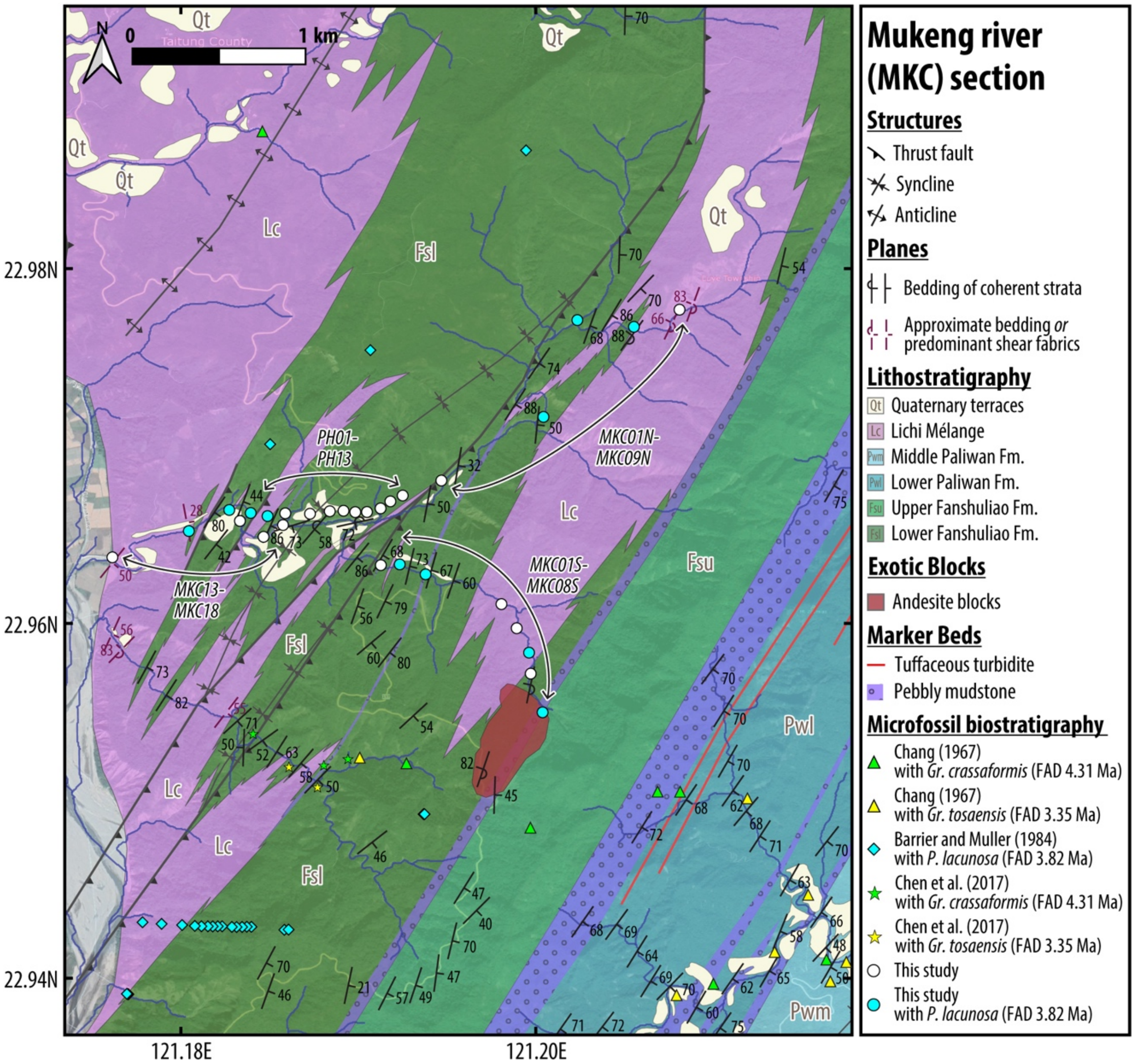

Figure S4. Microfossil sample locations for MKC section. See stratigraphic columns in Figure S11 and new raw data in Table S3.

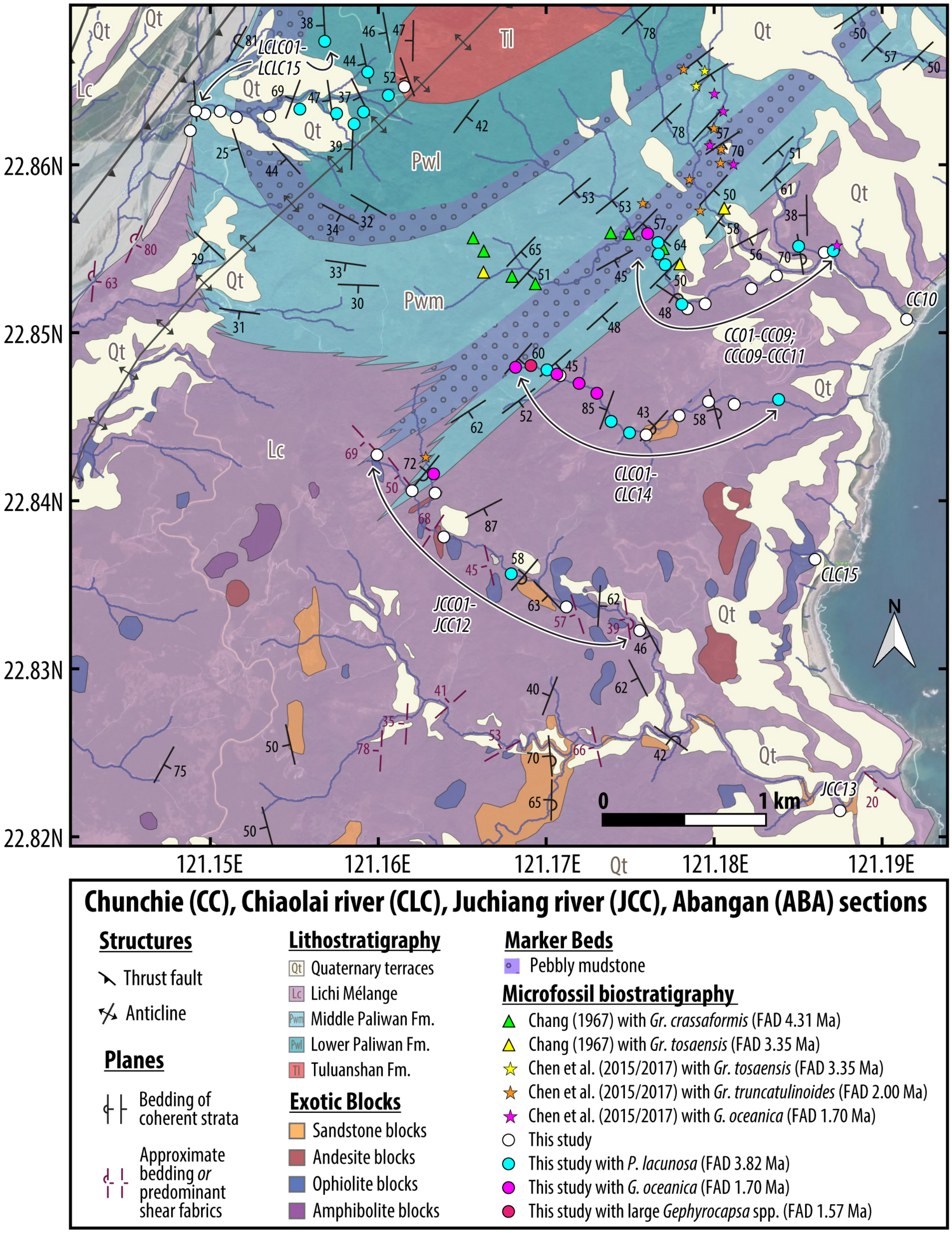

Figure S5. **Microfossil sample locations for CC, CLC, JCC, ABA sections.** See stratigraphic columns in Figure S12 and new raw data in Table S3.

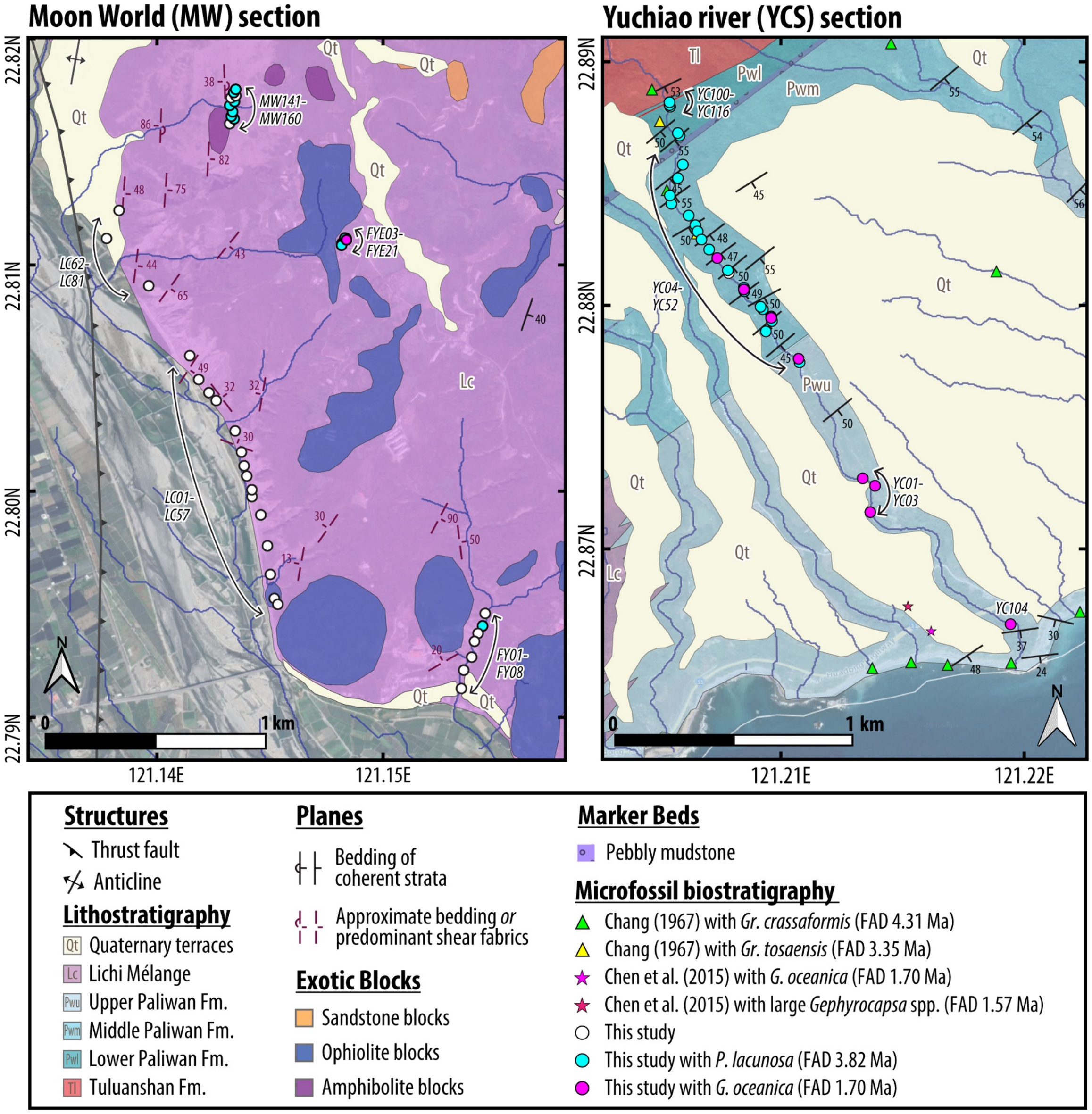

Figure S6. **Microfossil sample locations for MW and YCS sections.** See stratigraphic column for YCS in Figure S12 and new raw data in Table S3.

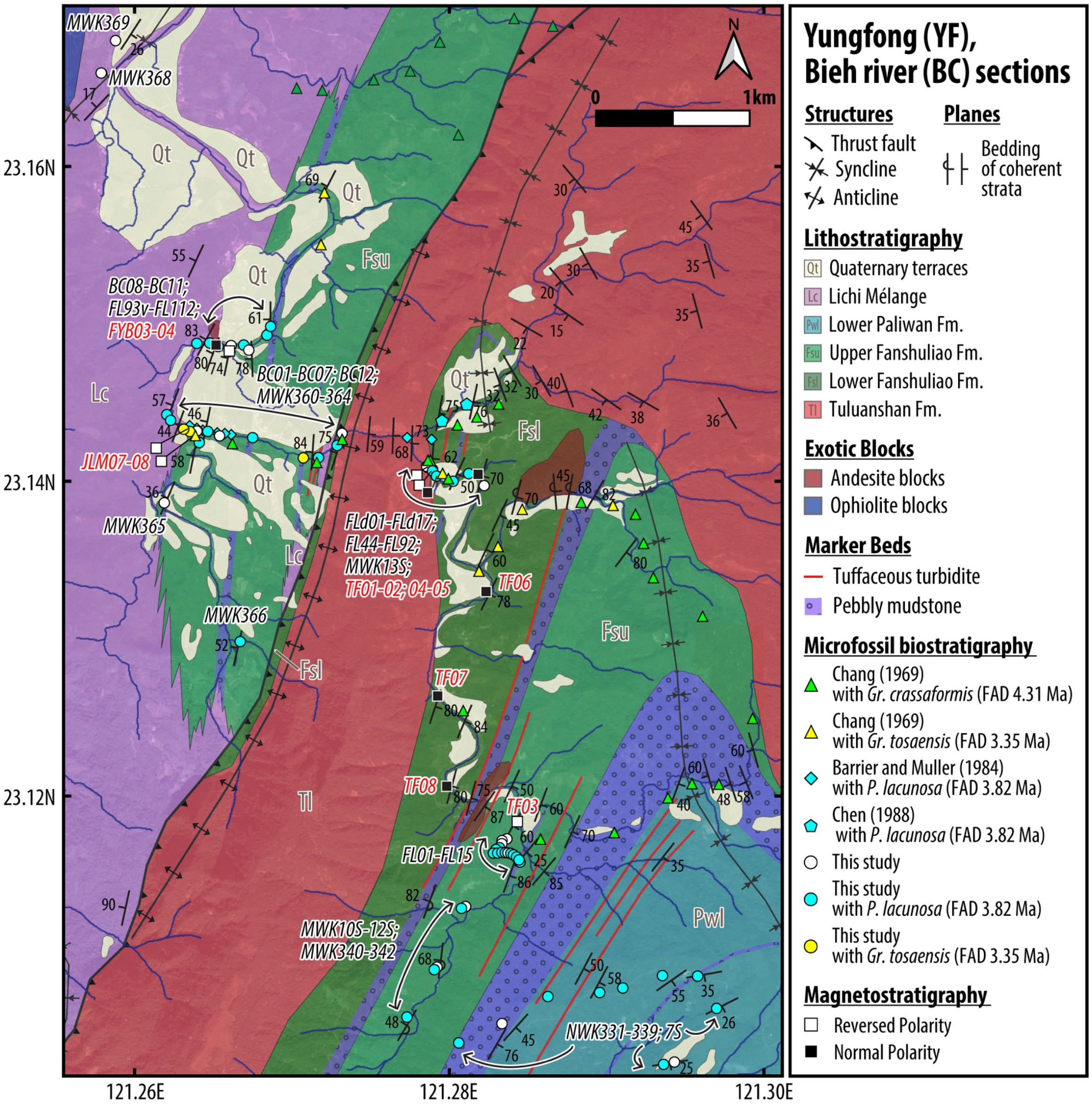

Figure S7. **Paleomagnetism (red labels) and microfossil sample (black labels) locations for YF and BC sections.** See stratigraphic columns in Figure S13 and new raw data in Tables S3-S5.

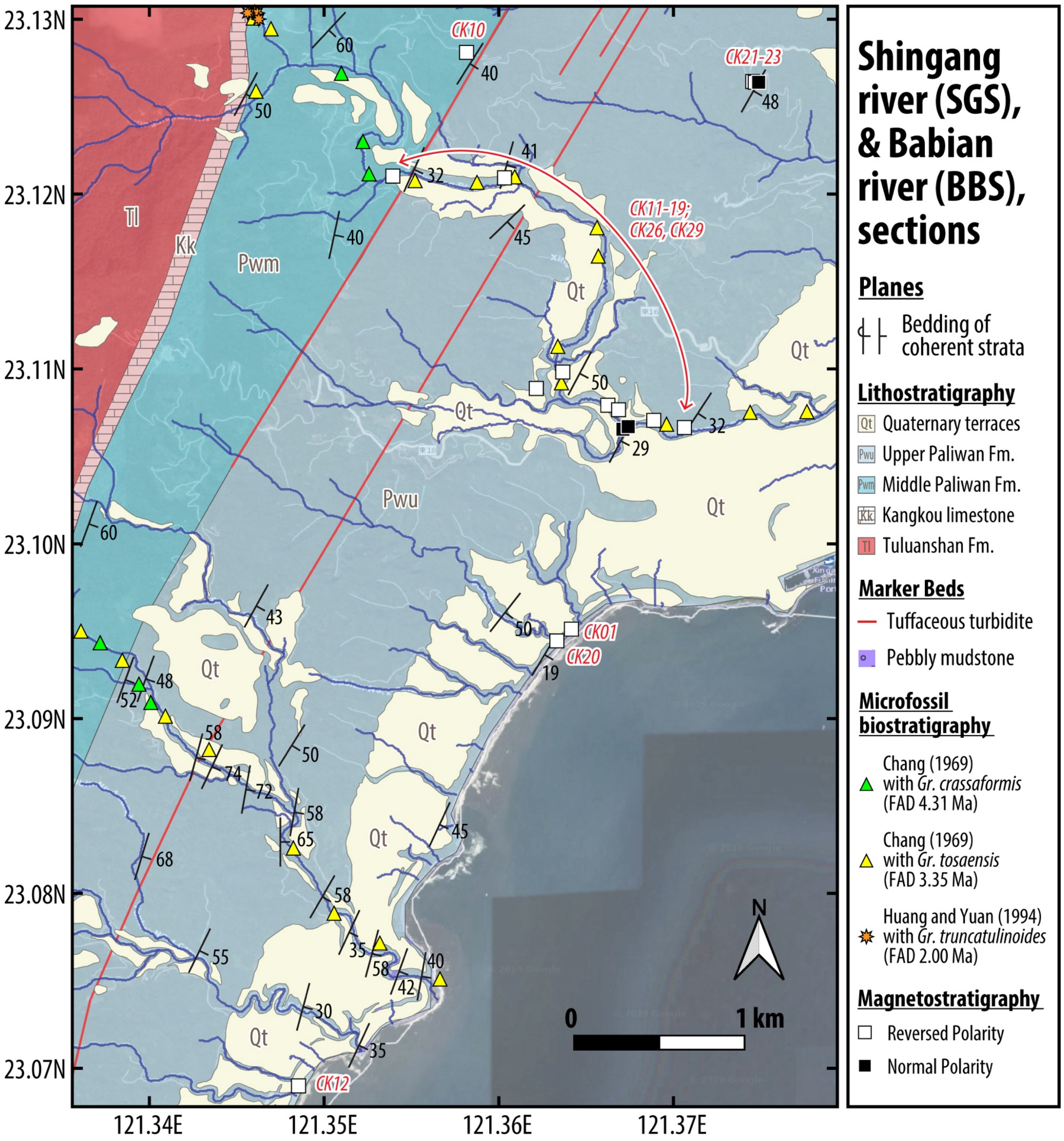

Figure S8. **Paleomagnetism (red labels) and microfossil sample (black labels) locations for SGS and BBS sections.** See their synthesized stratigraphic column in Figure S14 and new raw data in Tables S3, S5.

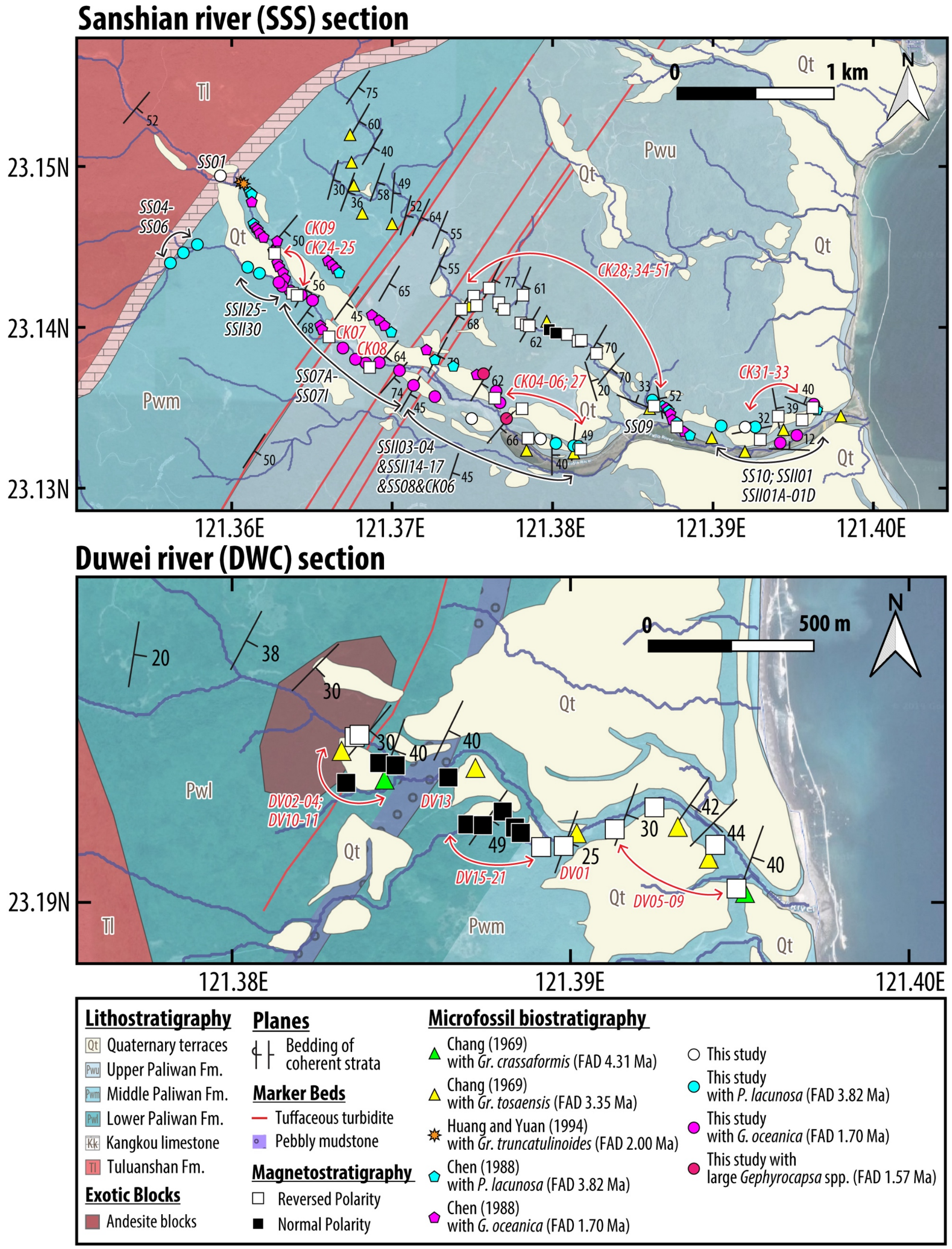

Figure S9. **Paleomagnetism (red labels) and microfossil sample (black labels) locations for SSS and DWC sections.** See stratigraphic columns in Figure S14 and new raw data in Tables S3, S5.

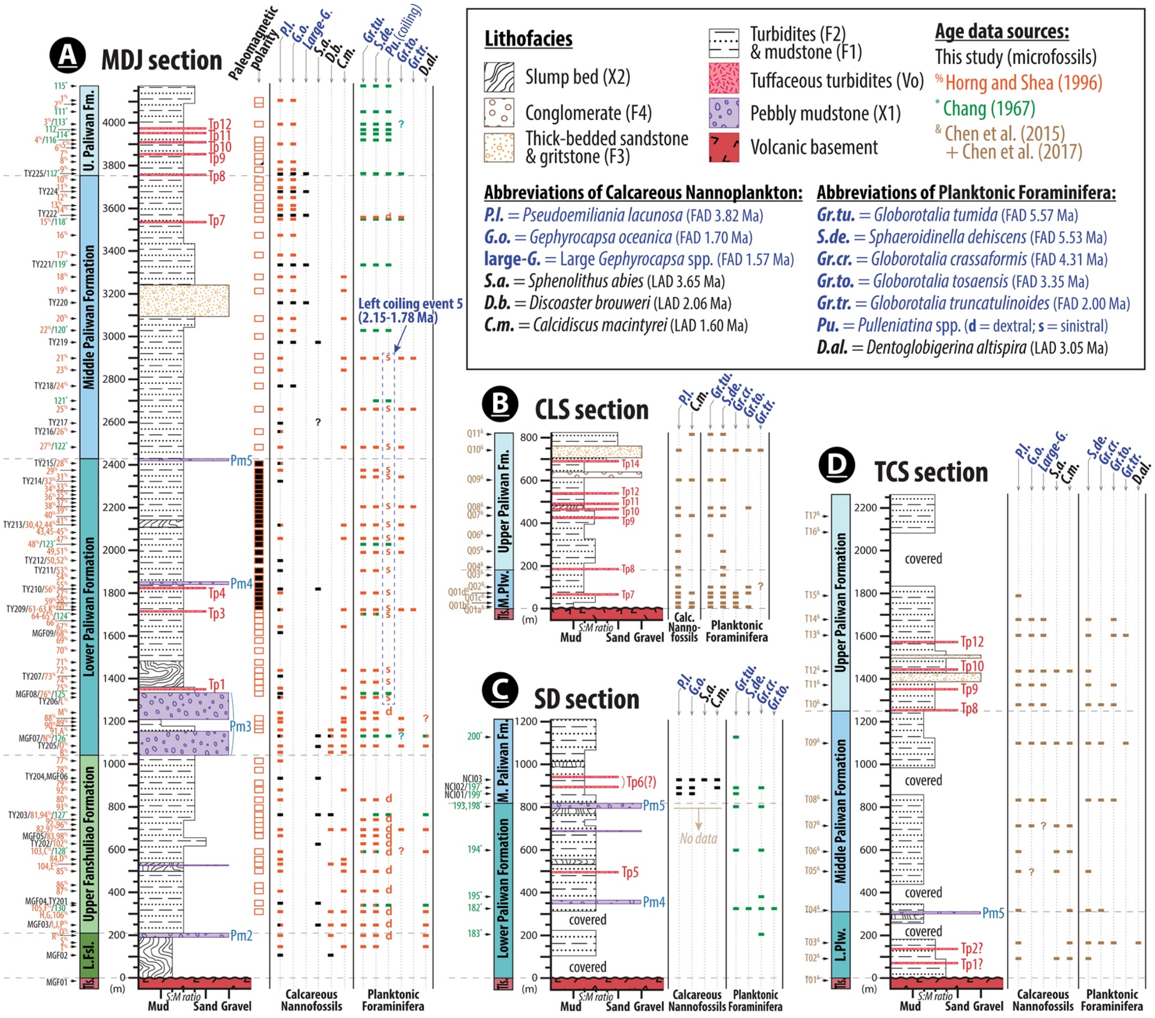

Figure S10. **Litho-, magneto-, biostratigraphy of (A) MDJ section; (B) CLS section; (C) SD section; (D) TCS section.** See locations in Figures 4, S1, S3. The "S:M ratio" in the grain-size axis show averaged fraction sand relative to mud in slump bed (X2), turbidites (F2), and mudstone (F1) facies. FAD and LAD are first and last appearance datum for index microfossils respectively. Black and white rectangles represent normal and inverse paleomagnetic polarities respectively. Sample numbers of paleomagnetism and microfossils are marked at the left of stratigraphic units, and their raw data are compiled in Tables S3, S5.

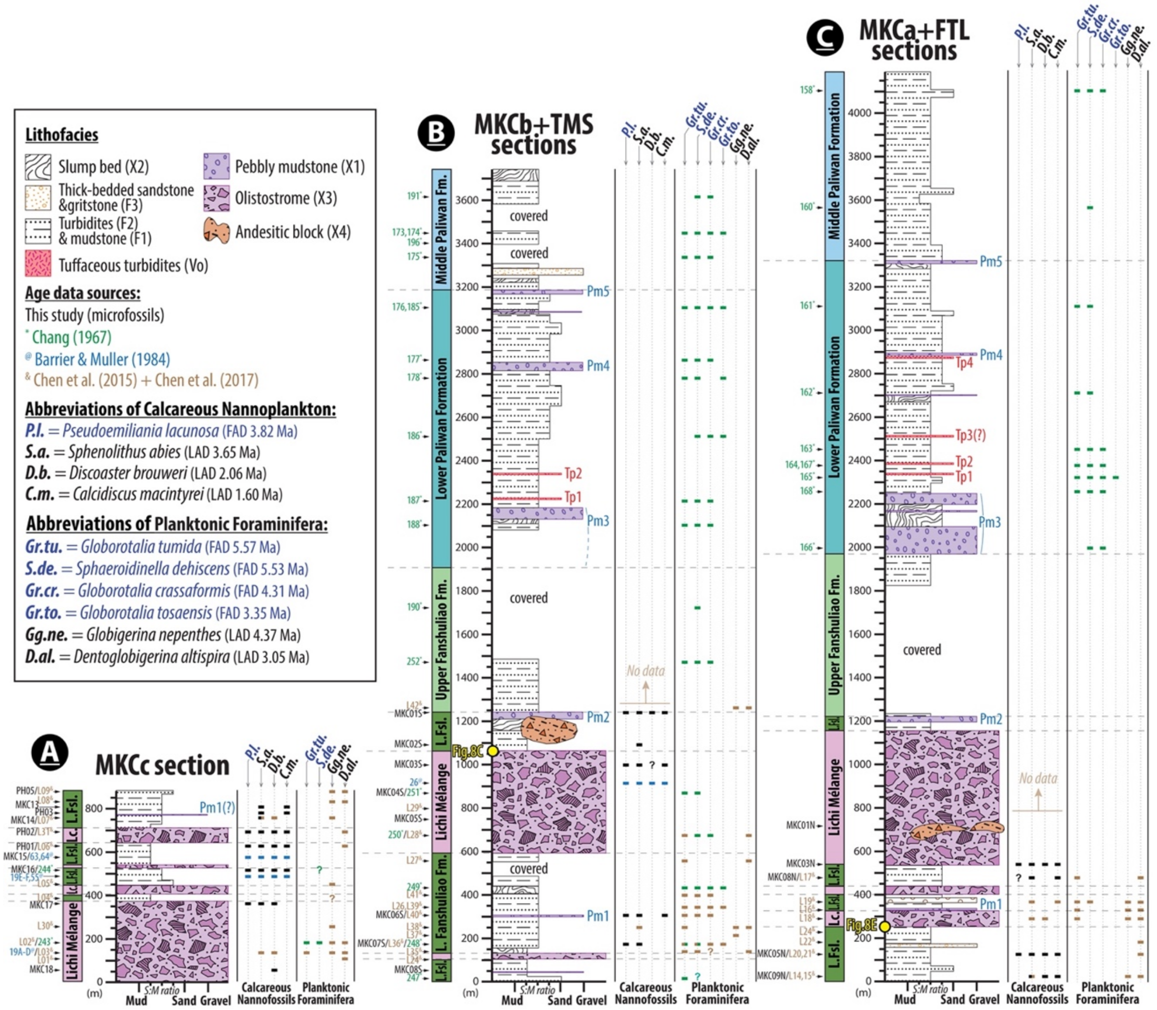

Figure S11. **Litho-, biostratigraphy of (A) MKCc section; (B) synthesis of the MKCb section and the TMS section; (C) synthesis of the MKCa section and the FTL section.** See locations in Figures 4, S2, S4. The "S:M ratio" in the grain-size axis show averaged fraction sand relative to mud in slump bed (X2), turbidites (F2), and mudstone (F1) facies. Yellow circles mark the depositional contact zone shown in Figure 8. FAD and LAD are first and last appearance datum for index microfossils respectively. Black and white rectangles represent normal and inverse paleomagnetic polarities respectively. Sample numbers of microfossils are marked at the left of stratigraphic units, and their raw data are compiled in Table S3.

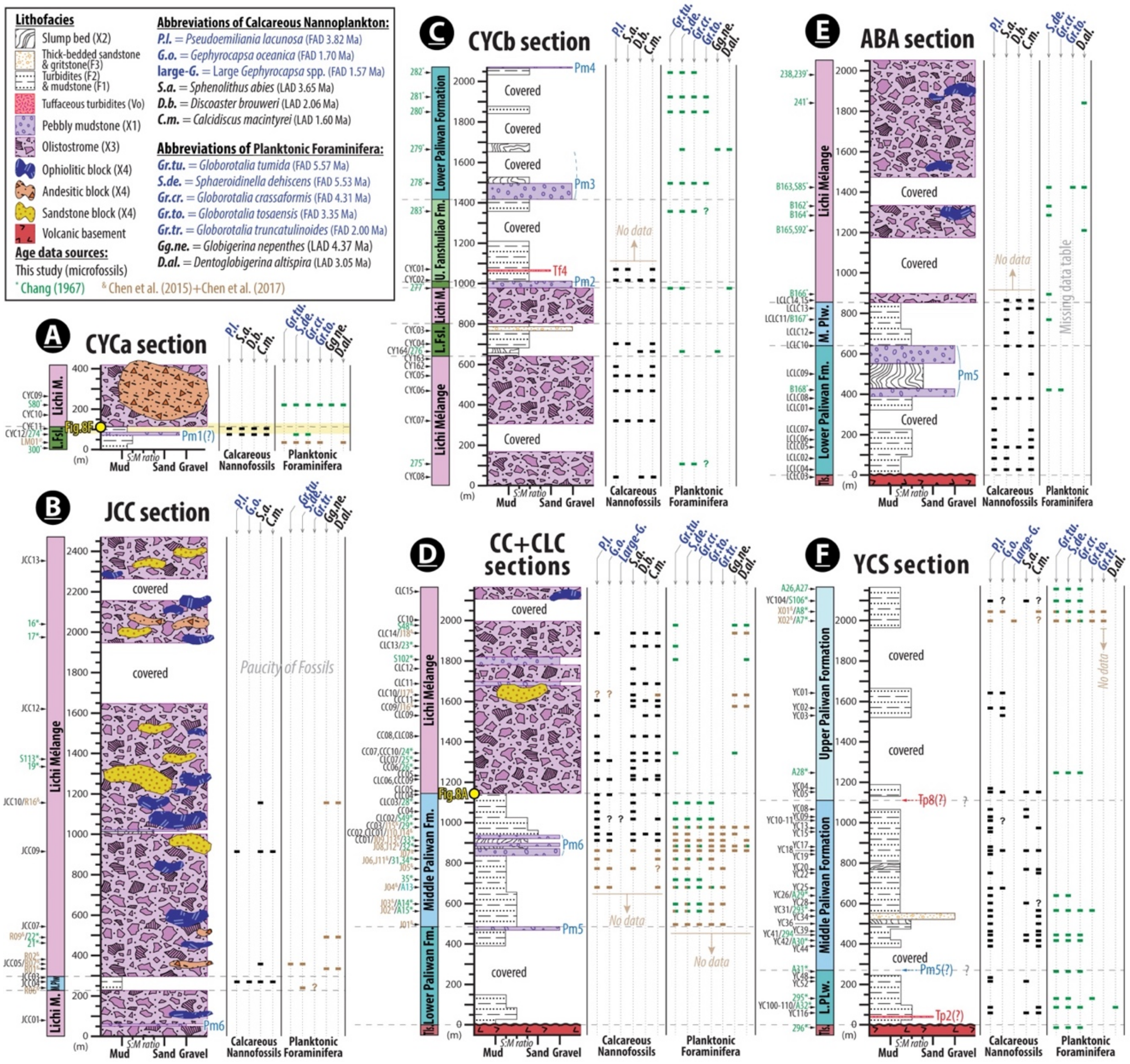

Figure S12. **Litho-, biostratigraphy of (A) CYCa section; (B) JCC section; (C) CYCb section; (D) synthesis of the CC section and CLC section; (E) ABA section; (F) YCS section.** See locations in Figure 4, S1, S3, S5, S6. The "S:M ratio" in the grain-size axis show averaged fraction sand relative to mud in slump bed (X2), turbidites (F2), and mudstone (F1) facies. The yellow circles and shade mark the depositional contact zone shown in Figures 8, S16. FAD and LAD are first and last appearance datum for index microfossils respectively. Black and white rectangles represent normal and inverse paleomagnetic polarities respectively. Sample numbers of microfossils are marked at the left of stratigraphic units, and their raw data are compiled in Table S3.

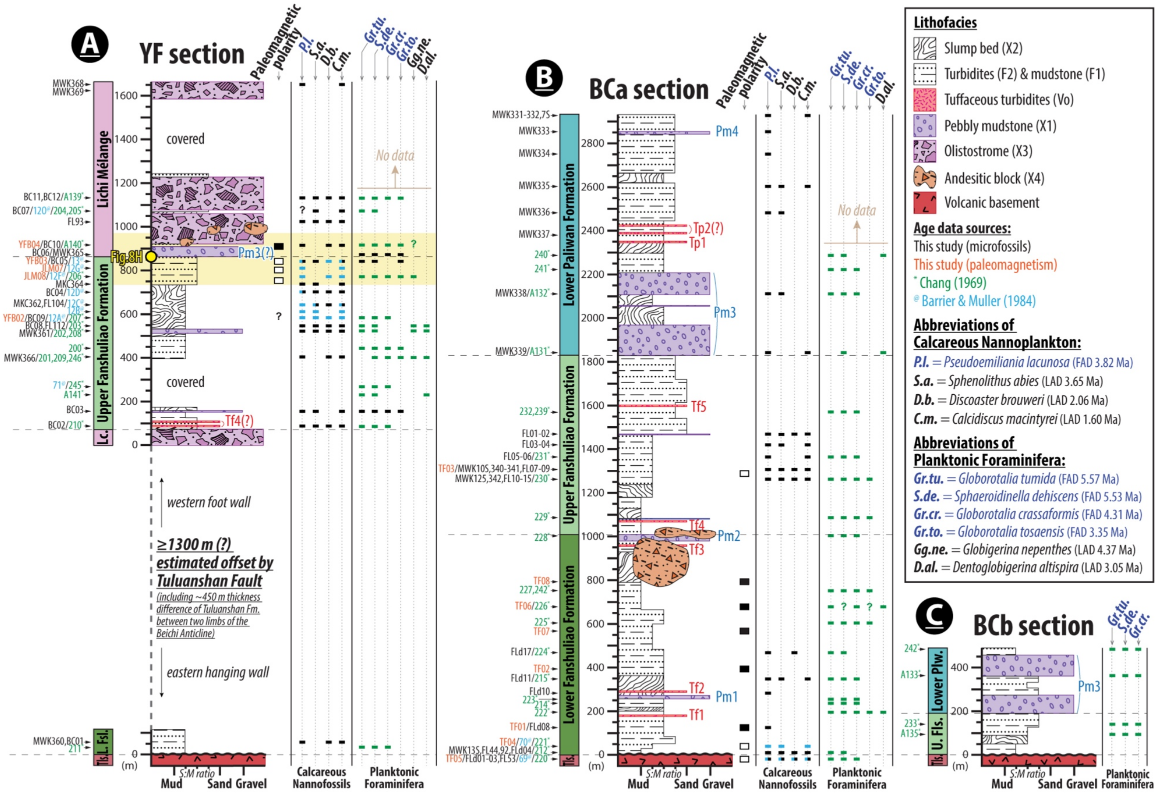

Figure S13. **Litho-, magneto-, biostratigraphy of (A) YF section; (B) BCa section; (C) BCb section.** See locations of in Figures S2, S7. The “S:M ratio” in the grain-size axis show averaged fraction sand relative to mud in slump bed (X2), turbidites (F2), and mudstone (F1) facies. The yellow circle and shade mark the depositional contact zone shown in Figures 8, S15, which is laterally equivalent to the contact in the southern exposure only 0.63 kilometers apart (Figure 8G). FAD and LAD are first and last appearance datum for index microfossils respectively. Black and white rectangles represent normal and inverse paleomagnetic polarities respectively. Sample numbers of paleomagnetism and microfossils are marked at the left of stratigraphic units, and their raw data are compiled in Tables S3-S5.

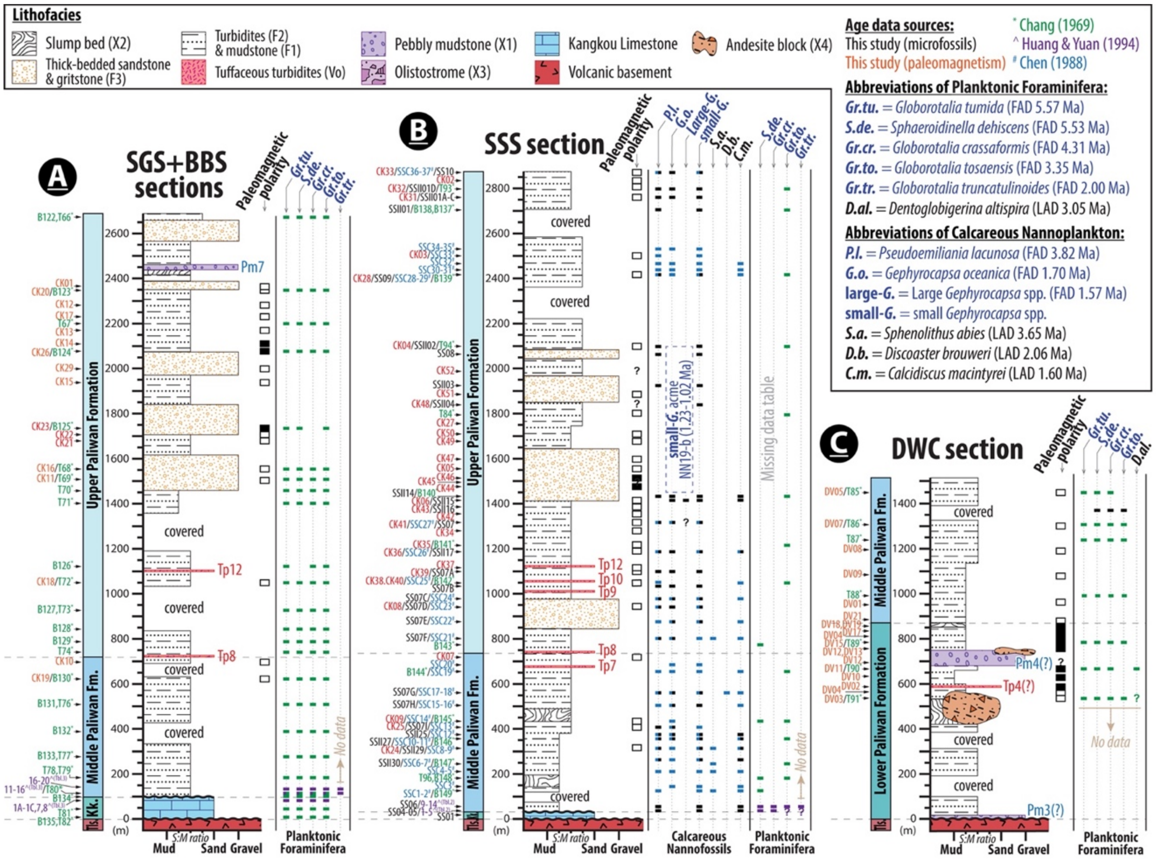

Figure S14. Litho-, magneto-, biostratigraphy of (A) synthesis of the SGS section and BBS section; (B) SSS section; (C) DWS section. See locations in Figures 4, S2, S8, S9. The "S:M ratio" in the grain-size axis show averaged fraction sand relative to mud in slump bed (X2), turbidites (F2), and mudstone (F1) facies. FAD and LAD are first and last appearance datum for index microfossils respectively. Black and white rectangles represent normal and inverse paleomagnetic polarities respectively. Sample numbers of paleomagnetism and microfossils are marked at the left of stratigraphic units, and their raw data are compiled in Tables S3, S5.

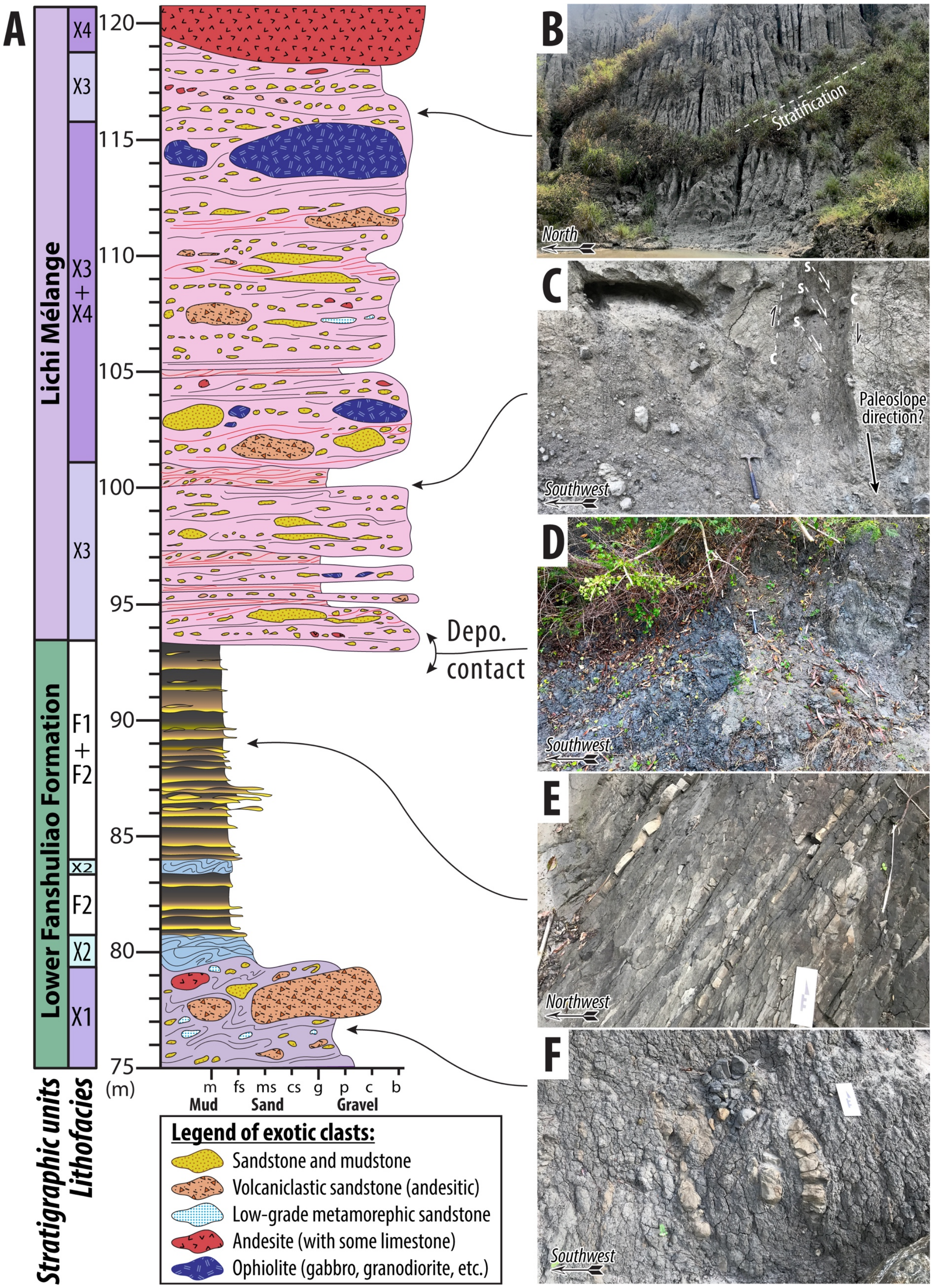

Figure S15. **Measured sections of depositional contact zone (equivalent to Figure 8F and ~75-121 m stratigraphic height of Figure S12A) between Lichi Mélange and lower Fanshuliao Formation in the CYCa section (See location in Figure S1).** Red lines in the stratigraphic column represent compacted shear fabrics. The "c" and "s" in photo C label the shear and foliation surfaces respectively (S-C fabrics) in a sheared horizon within the olistostrome (X3) facies.

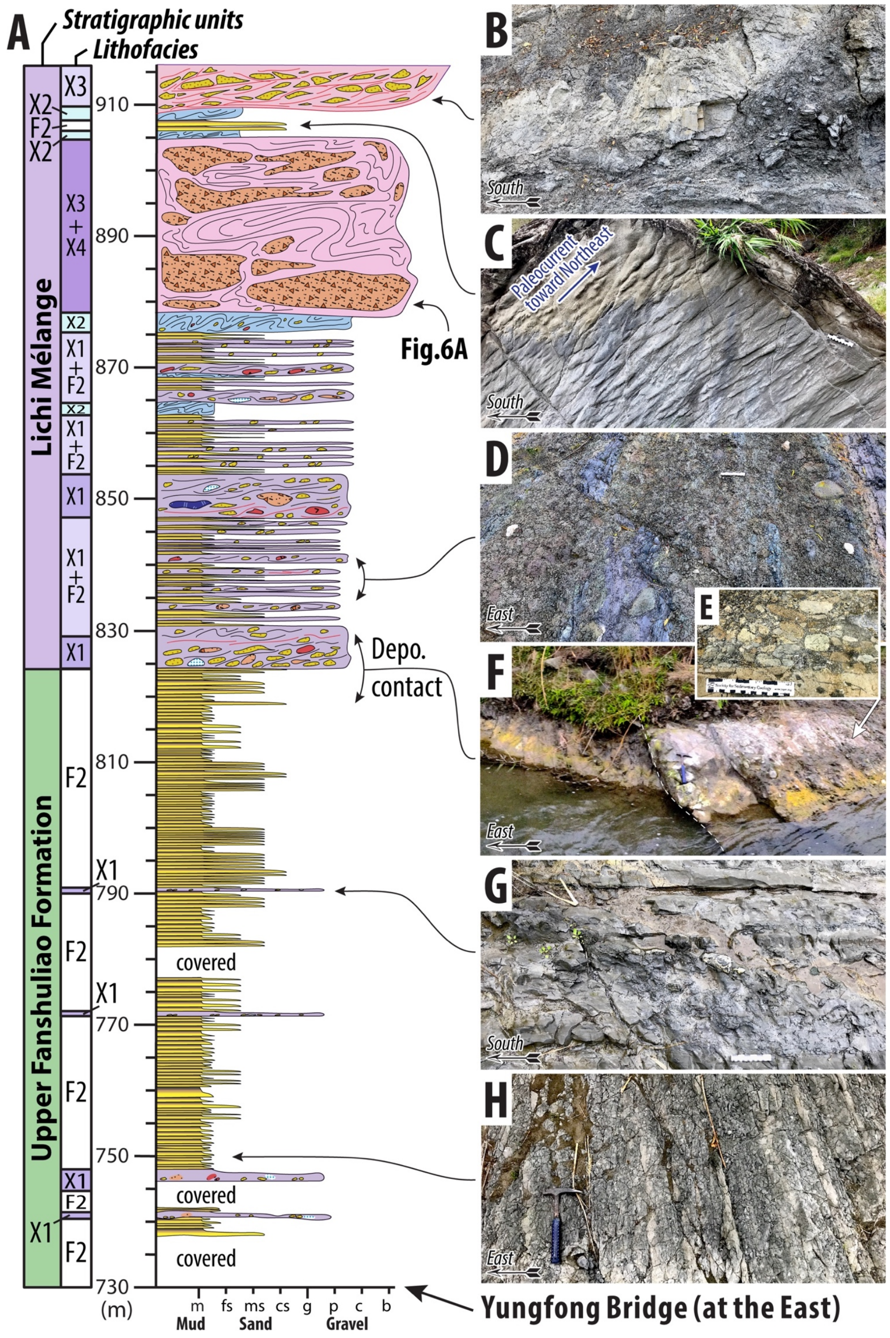

Figure S16. **Measured sections of depositional contact zone (equivalent to Figure 8H and ~730-915 m stratigraphic height of Figure S13A) between Lichi Mélange and upper Fanshuliao Formation in the YF section (See location in Figure S2).** It presents an up-section progressive change in lithofacies from coherent facies (F1, F2) to chaotic facies (X1-X4). The photo B shows a shear horizon with extensional structures. The photo C shows flute casts in the interbedded turbidites. The depositional contact (photo F) can be laterally correlated to the southern contact (Figure 8G), which was mapped as “Yungfong fault” in previous studies (Chang et al., 2000; Chen, 1997b). The photo E shows a cluster of rounded exotic clasts of sedimentary rocks (mudstone, sandstone) that present in the pebbly mudstone facies (X1). Other legends and captions follow Figure S15.

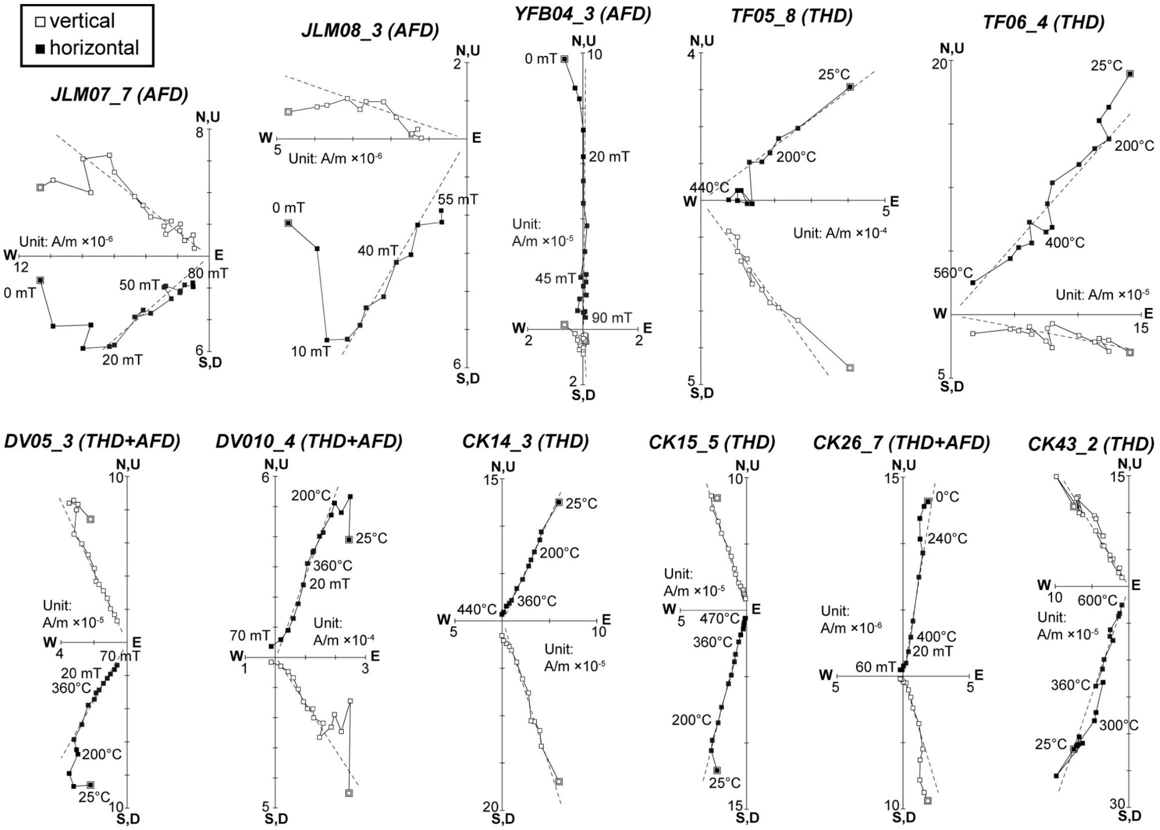

Figure S17. **Zijderveld-type diagrams of representative paleomagnetism samples.** Methods of demagnetization are described in parenthesis after sample names (THD = thermal demagnetization; AFD = alternating field demagnetization).

APPENDIX B

CHAPTER III SUPPORTING INFORMATION

***Supplementary Data 1–4 are included in supplemental files of this dissertation**

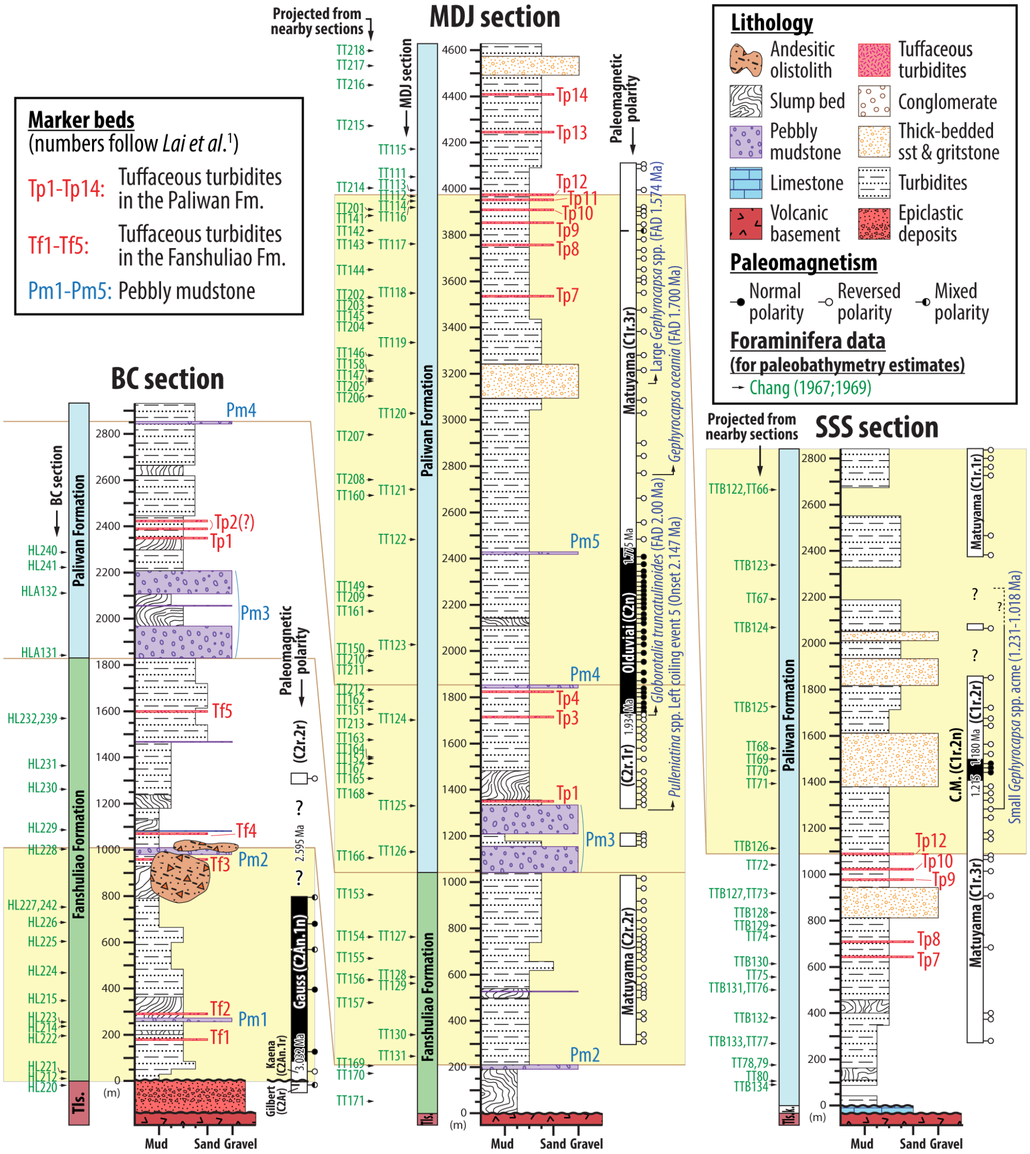

Supplementary Figure 1. Lithostratigraphy and age interpretations of the Bieh river (BC), Madagida river (MDJ), and Sanshian river (SSS) sections in southern Coastal Range, summarized from Lai, Dorsey, et al. (2021). Tick marks on the right side of paleomagnetic polarity columns show positions of paleomagnetic sample collecting sites. Projected positions of foraminifera data (Supplementary Data 3) used for paleobathymetry estimates are shown on the left. Grain size on the horizontal scale was used to determine sand:mud ratios used in the decompaction analysis (Supplementary Data 4). Portions of the synthesized section in the Figure 1 are shaded in yellow, with brown correlation lines.

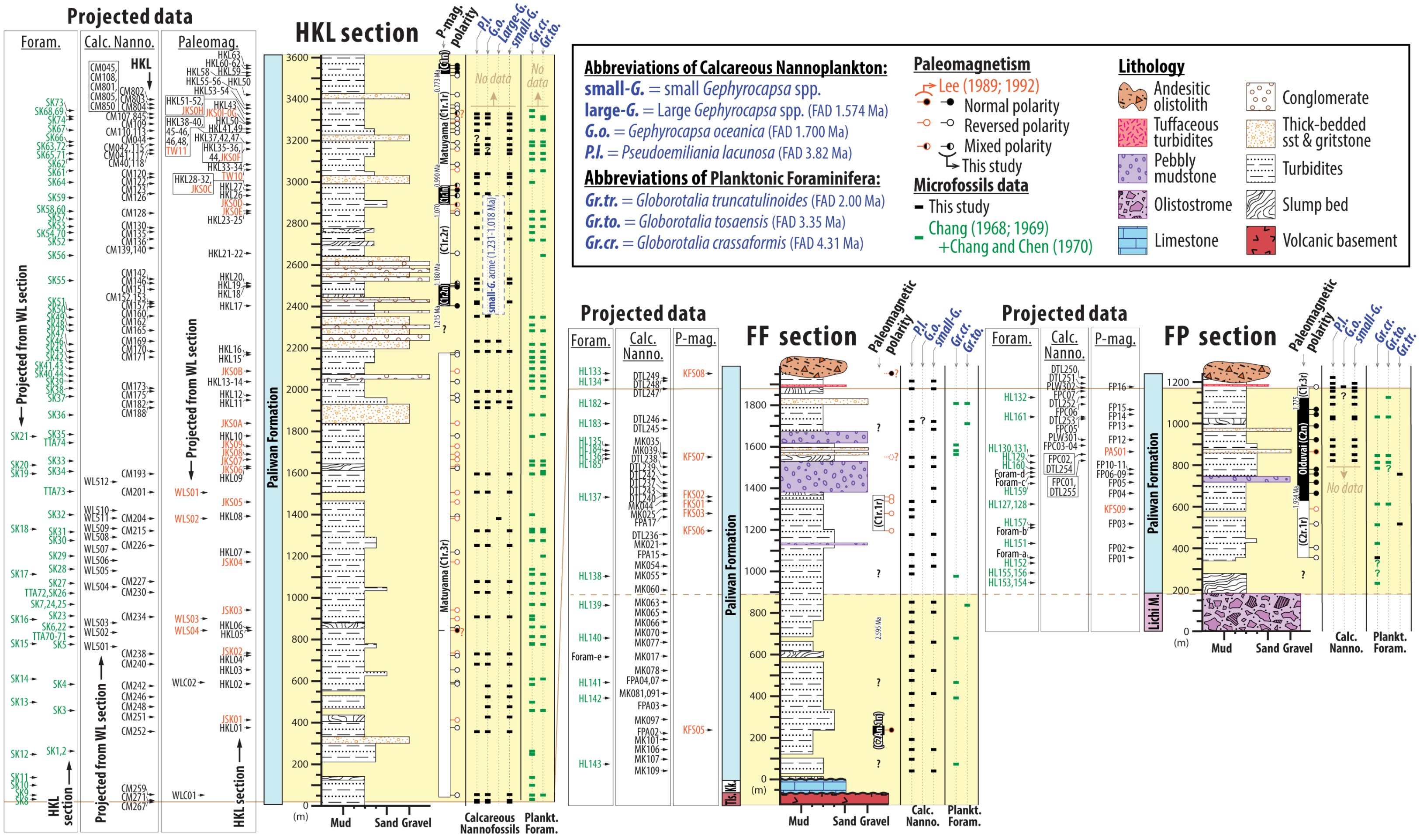

Supplementary Figure 2. Litho-, magneto-, biostratigraphy of Hsiukuluan river (HKL), Wulou river (WL), Fungfu (FF), and Fungpin (FP) sections in northern Coastal Range. See data locations in Supplementary Figures 3–4. Projected positions of new paleomagnetism and microfossils data (Supplementary Data 1–3) are marked at the left. Grain size on the horizontal scale was used to determine sand:mud ratios used in the decompaction analysis (Supplementary Data 4). Portions of the synthesized section in Figure 1 are shaded in yellow, with a brown correlation line.

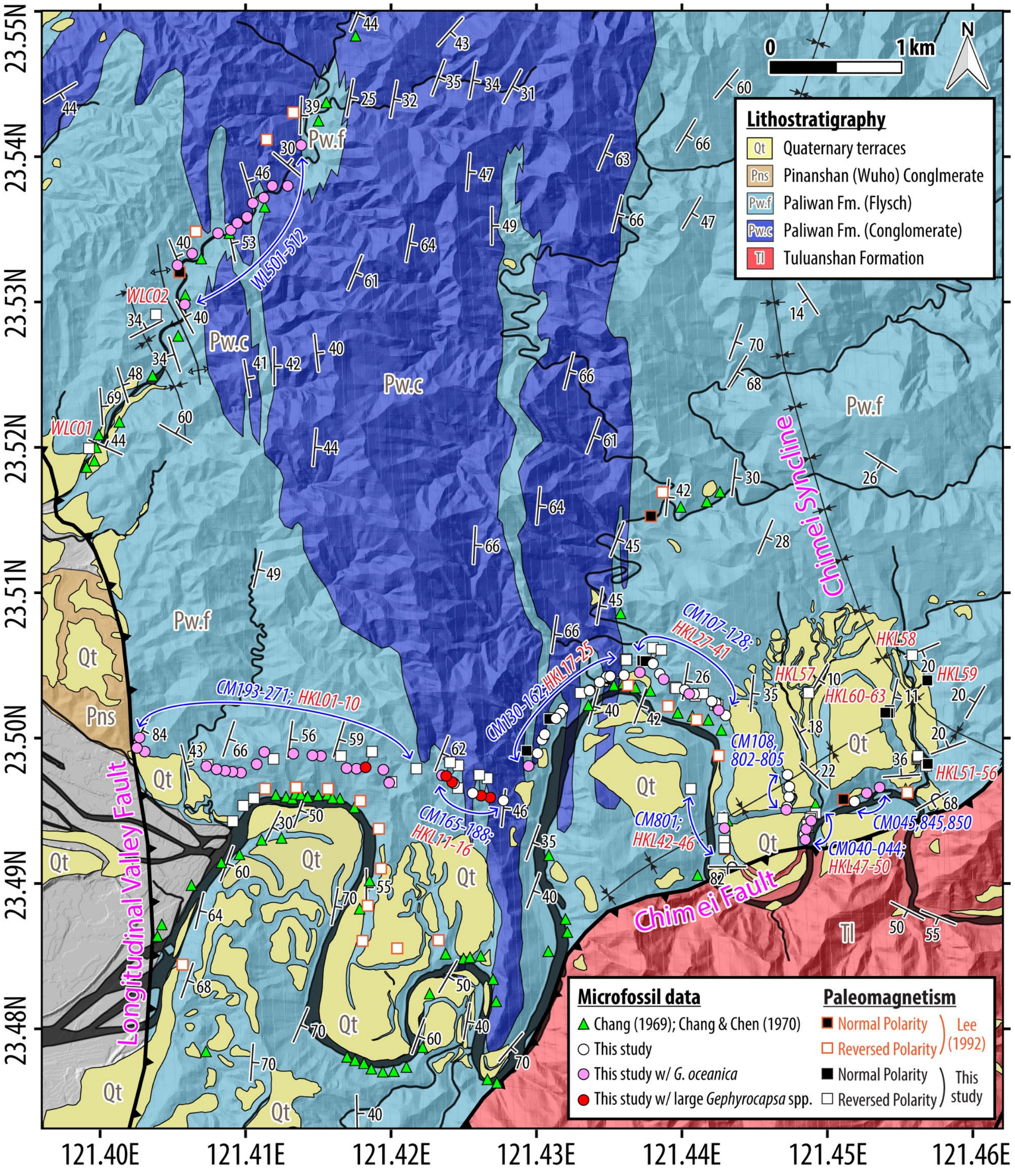

Supplementary Figure 3. Geologic map of the Hsiukuluan river (HKL) and Wulou river (WL) sections. Data are summarized from previously published works (Hsu et al., 2017; Teng et al., 2016; Wang & Chen, 1993; Yi et al., 2012) and this study. Paleomagnetic samples are marked in red labels (starting with HKL, WLC) and microfossil samples are marked in blue labels (starting with CM, WL). See details in Supplementary Figure 2 and Supplementary Data 1–2.

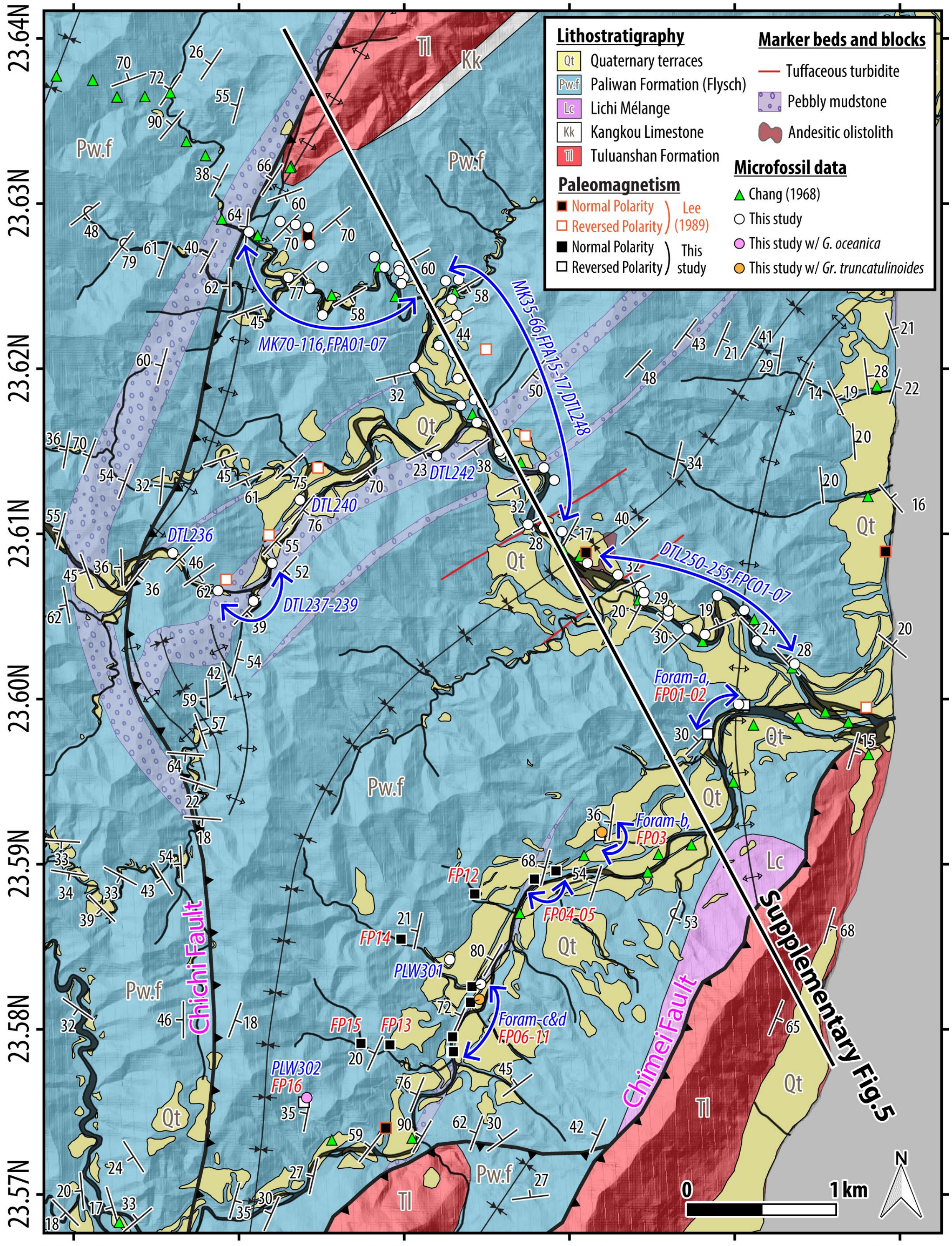

Supplementary Figure 4. Geologic map of the Fungfu (FF) and Fungpin (FP) sections. Data are summarized from previously published works (Chen & Wang, 1997; Hsu et al., 2017; Wang & Chen, 1993; Yi et al., 2012) and this study. Paleomagnetic samples are marked in red labels (starting with FP) and microfossil samples are marked in blue labels (DTL, PLW, MK, FPA, FPC, Foram). See details in Supplementary Figure 2 and Supplementary Data 1–2.

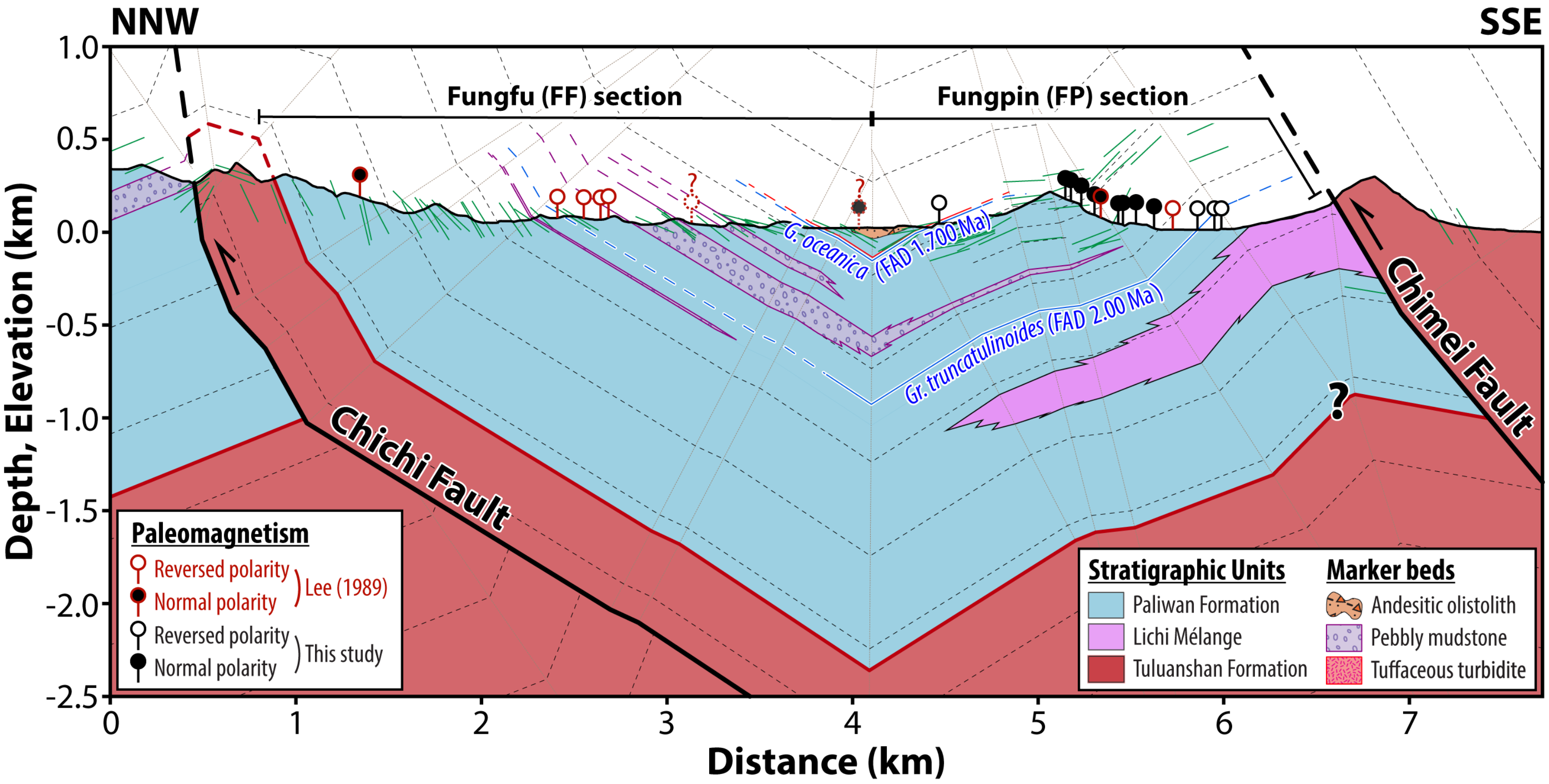

Supplementary Figure 5. Geologic cross section across Fungfu (FF) and Fungpin (FF) sections. Green short lines show projected (apparent) bedding dip. Paleomagnetic data collected in slump beds and olistoliths from Lee (1989) (in red dashed circles with question marks) are excluded in our analysis (Supplementary Figure 2; Supplementary Data 1). See location of the geological cross section in Supplementary Figure 4.

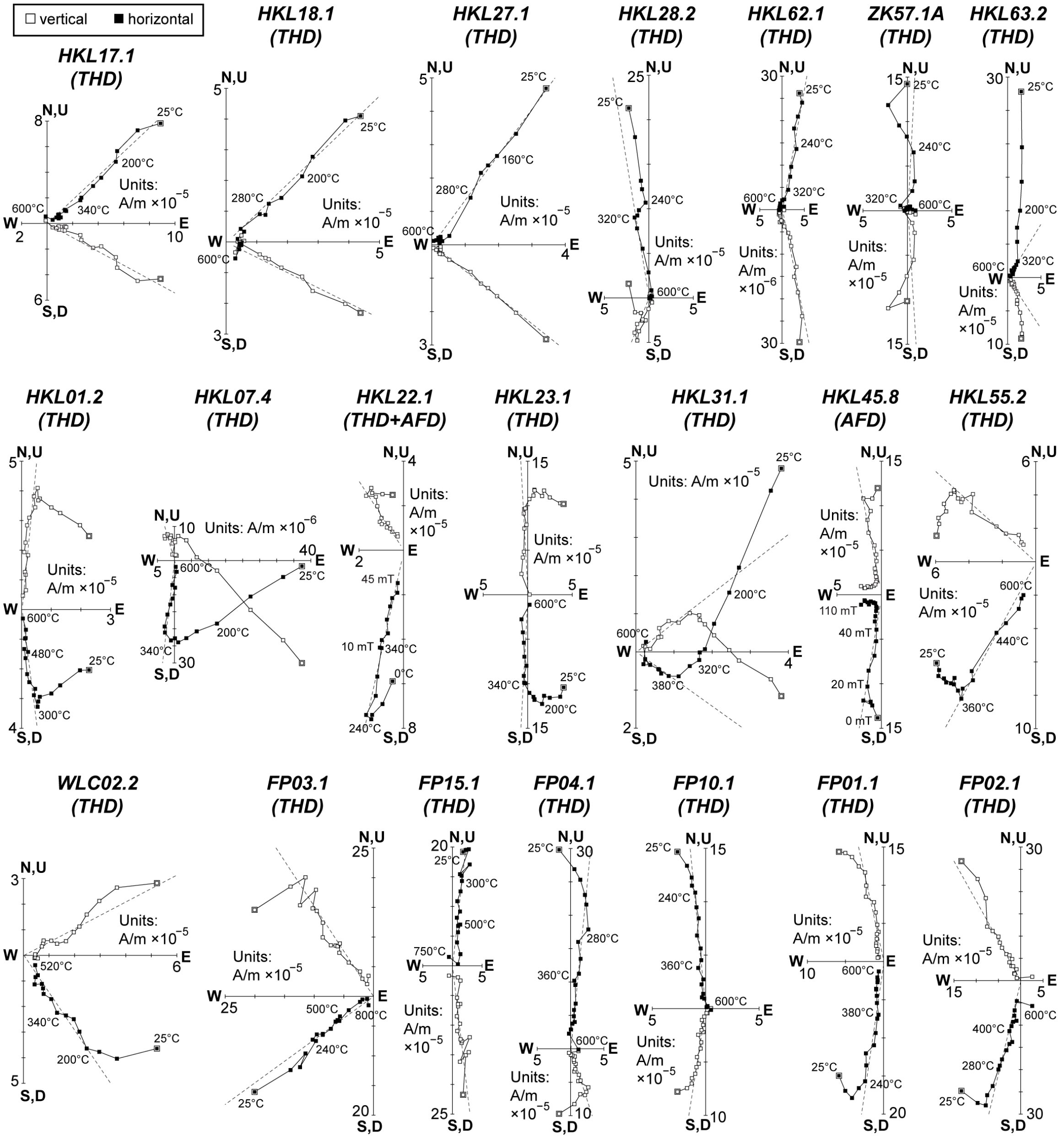

Supplementary Figure 6. Zijderveld-type diagrams showing representative results of demagnetization in paleomagnetic samples. Data are collected from Hsiukuluan river (HKL), Wulou river (WL), and Fungpin (FP) sections. Demagnetization methods are shown in parentheses after sample names (THD = thermal demagnetization; AFD = alternating field demagnetization). Sample locations are shown in Supplementary Figures 3–4. See details in Supplementary Data 1.

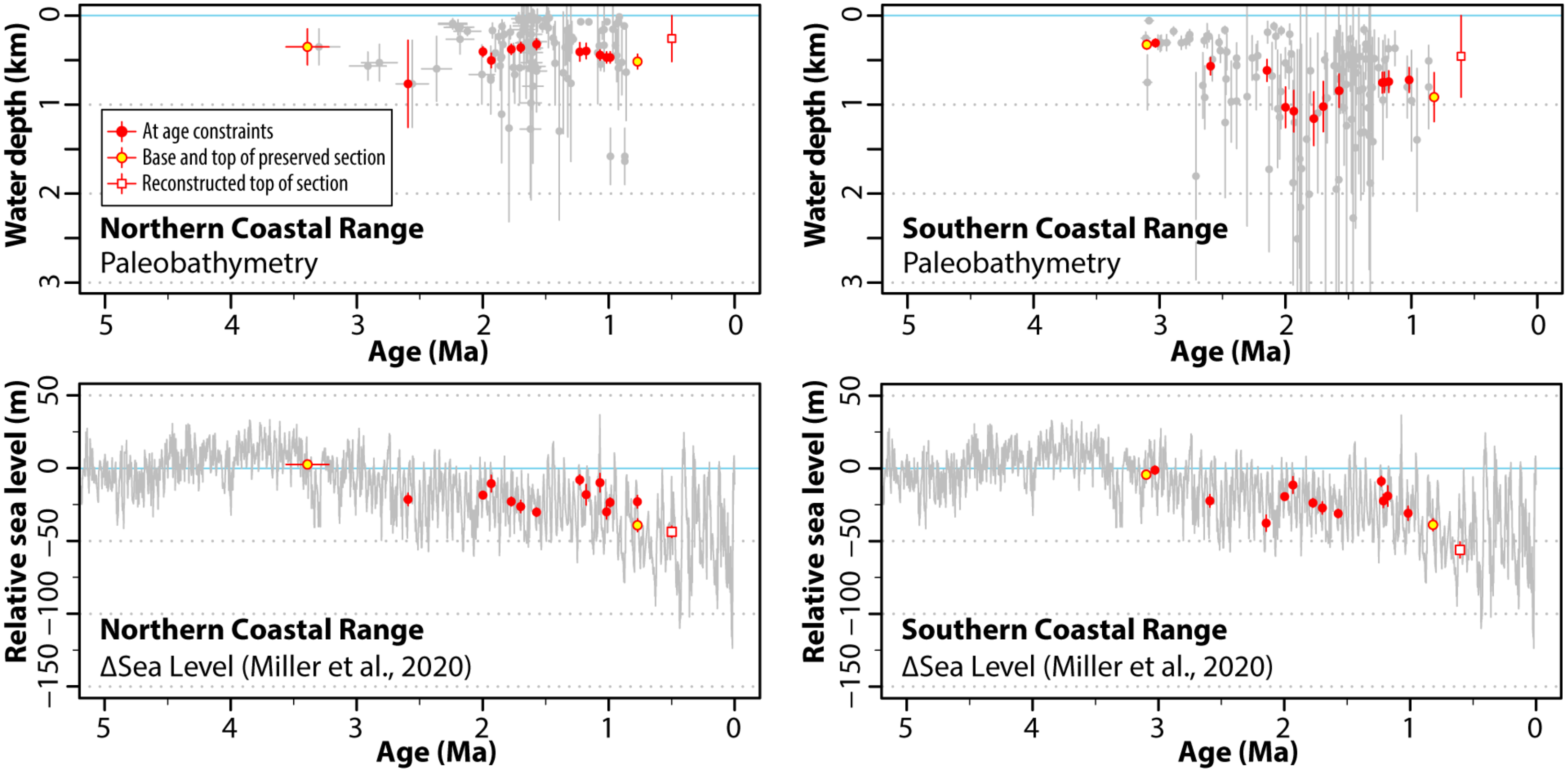

Supplementary Figure 7. Foraminifera-based paleobathymetry estimates and relative sea level (Miller et al., 2020). Blue lines are present-day sea level. Raw data are marked in gray in the background. Red points are means and standard errors of the nearest values around ages constraints (within the range of age uncertainty and extra ± 0.2 Myr for paleobathymetry and ± 0.01 Myr for relative sea level) that are used in the backstripping analysis. See details in Supplementary Data 3–4.

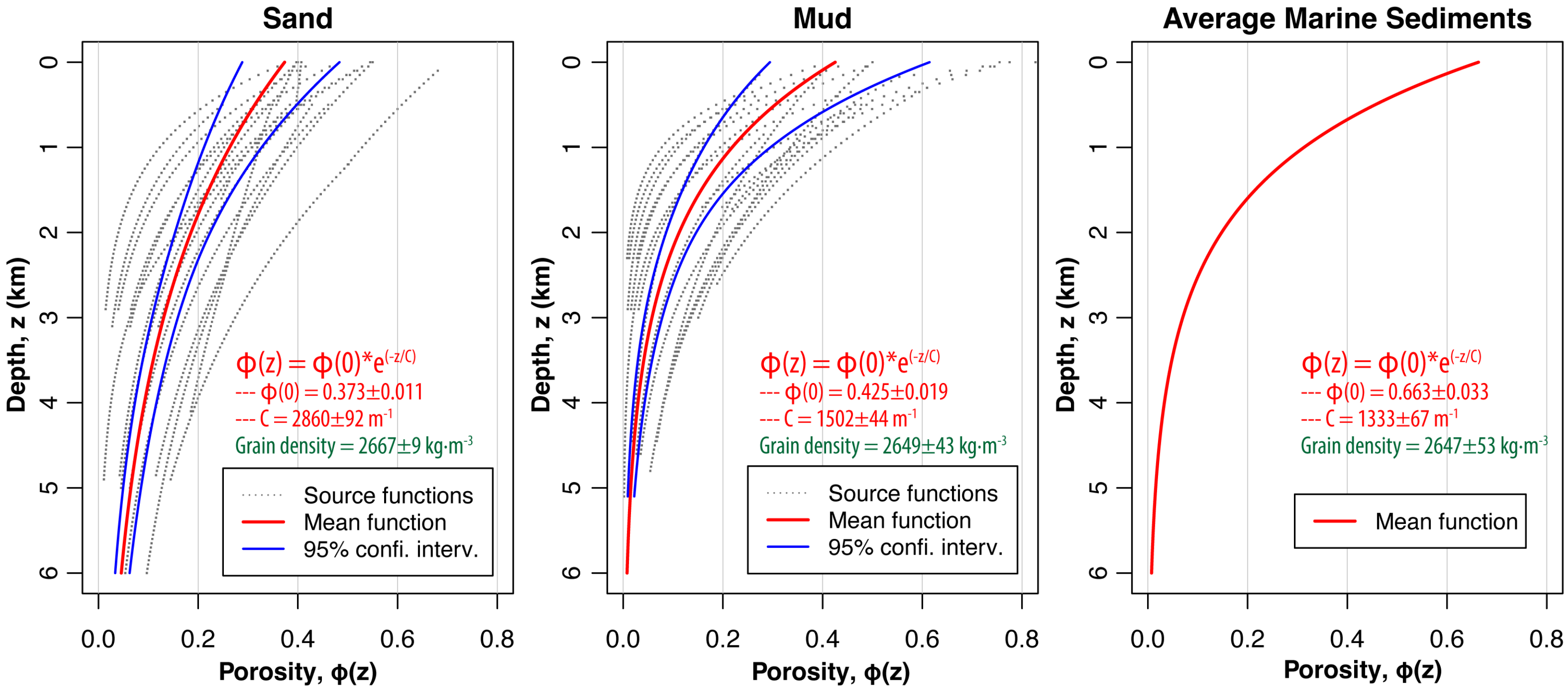

Supplementary Figure 8. Global average porosity-depth functions and grain density for sandy, muddy, and mean marine sediments (for pebbly mudstone). Source functions and averaged grain densities are compiled from previous publications (Gallagher & Lambeck, 1989; Hamilton & Bachman, 1982; Hansen, 1996; He et al., 2017; Kominz et al., 2011; Kominz & Pekar, 2001; Lee et al., 2019; Lee & Wagreich, 2016; Royden & Keen, 1980; Sclater & Christie, 1980; Van Sickel et al., 2004; Zhao et al., 2015). See details in Supplementary Data 4.

APPENDIX C

CHAPTER IV SUPPORTING INFORMATION

***Tables S1–S2 are included in supplemental files of this dissertation**

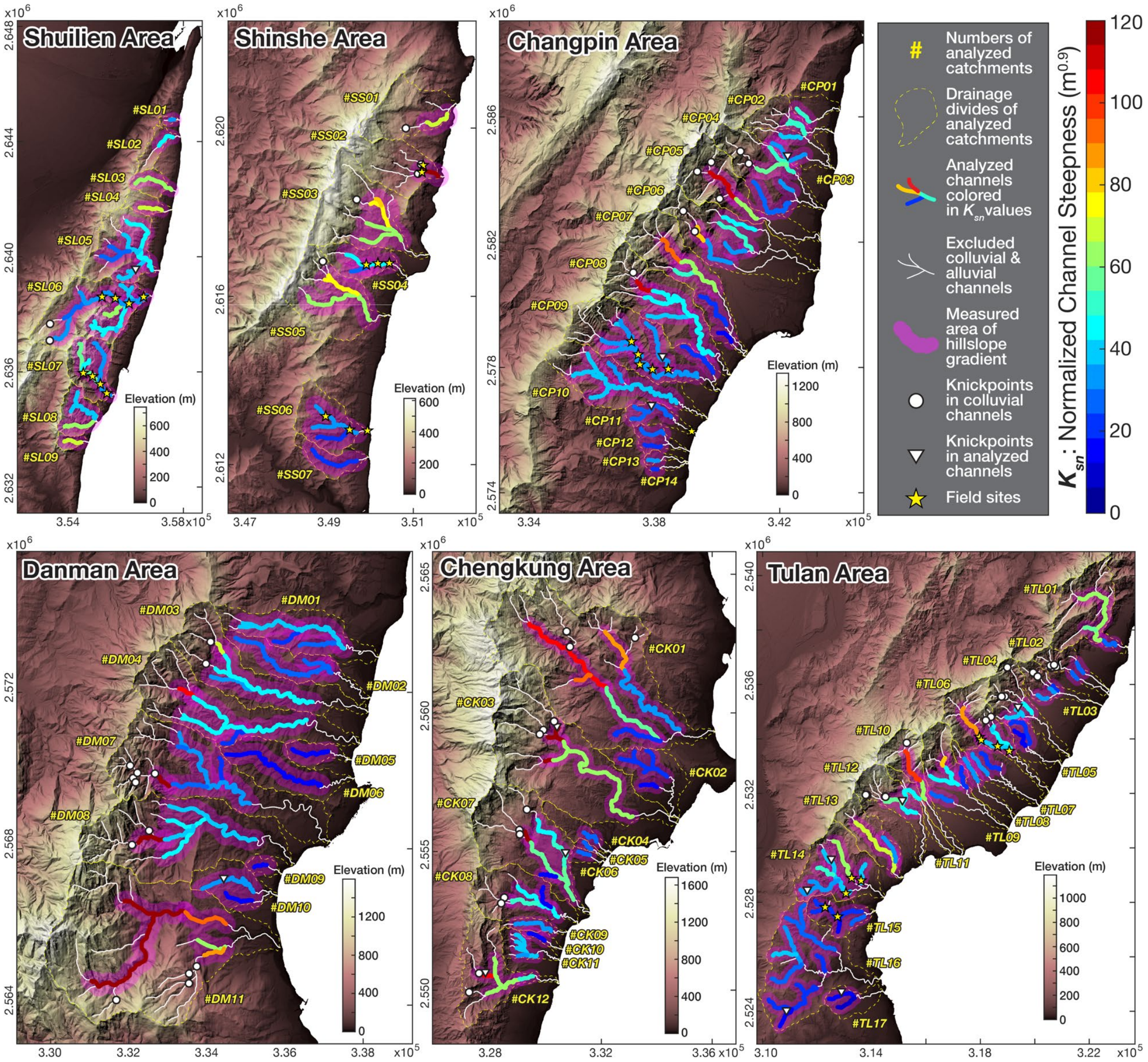

Figure S1. Topography (projected in UTM zone 15N coordinate system), analyzed reaches colored in normalized channel steepness (K_{sn}) based on θ_{ref} = 0.45, identified knickpoints, area for mean hillslope gradient, and locations of field sites in 6 study regions (Figure 1). See data in Table S1.

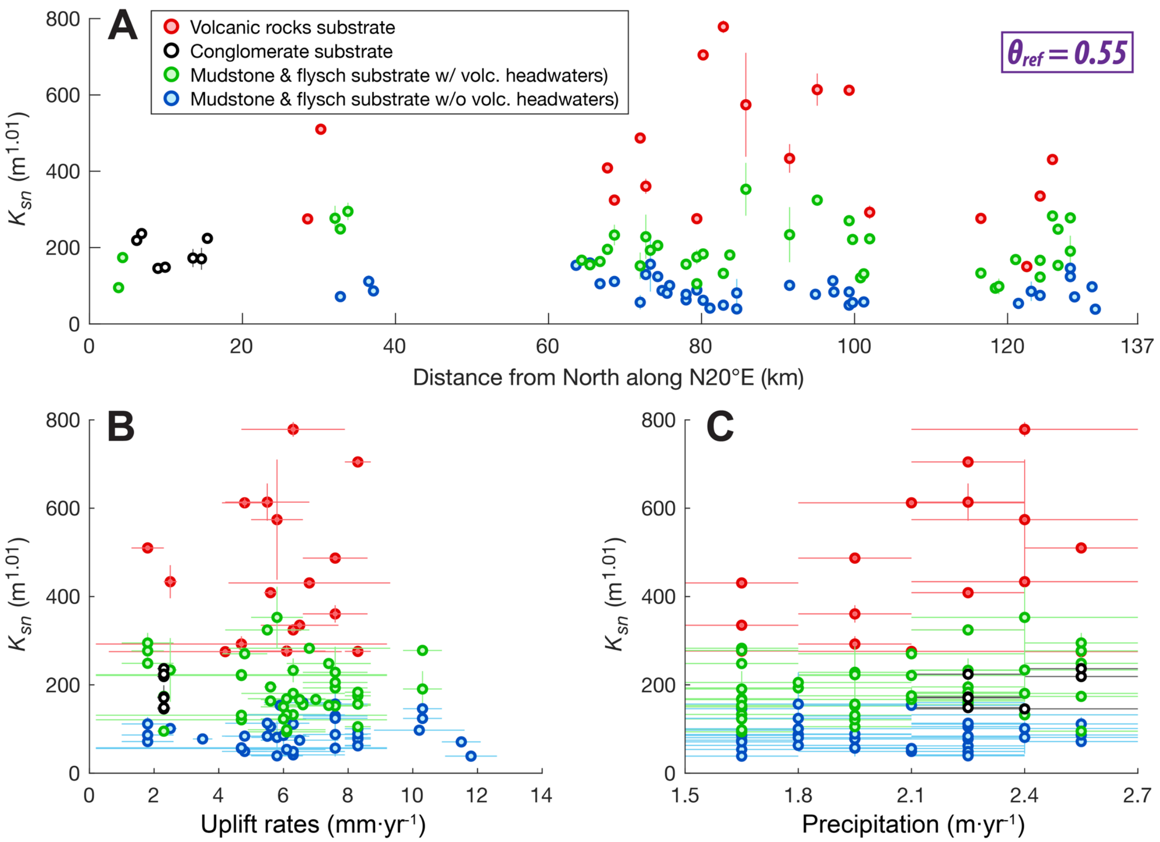

Figure S2. Normalized channel steepness (K_{sn}) calculated on the basis of reference concavity (θ_{ref}) 0.55, plotted against locations from the north end of the Coastal Range in (a), uplift rates in (b), and annual precipitation in (c). Uncertainties are the standard errors of the data or means. The results show the same patterns of K_{sn} calculated with $\theta_{\mathrm{ref}} = 0.45$ in Figures 1(c) and 5(a, b). See data in Table S1.

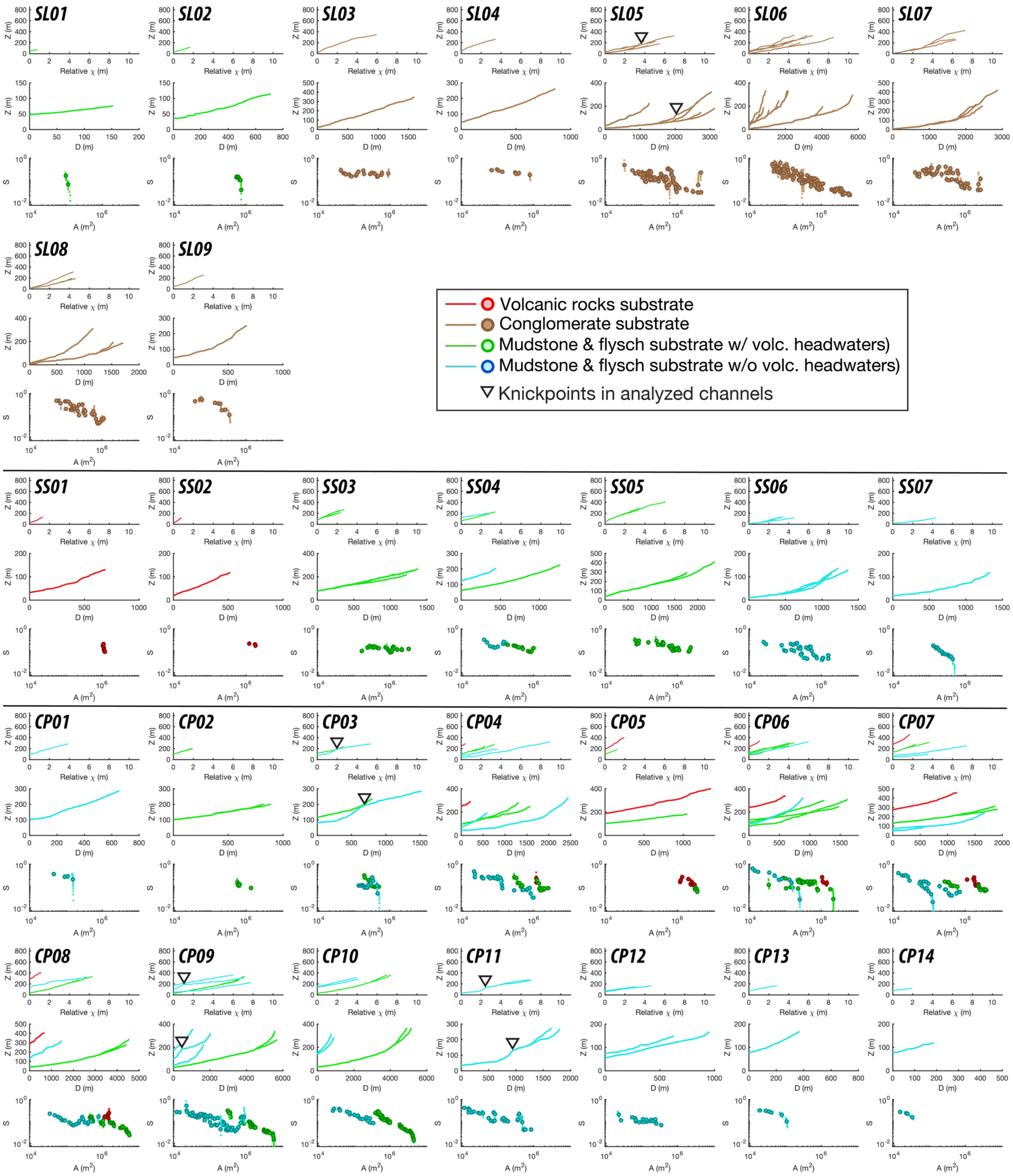

Figure S3. Profiles relative to outlets of analyzed channels, elevation (Z) versus χ plots (calculated based on $\theta_{\text{ref}} = 0.45$) with identified knickpoints, and channel slope (S) versus upstream drainage area (A) plots of analyzed reaches in each catchment. Notes the starting values of χ are shifted to the origin after calculation in order to visualize differences in channel steepness.

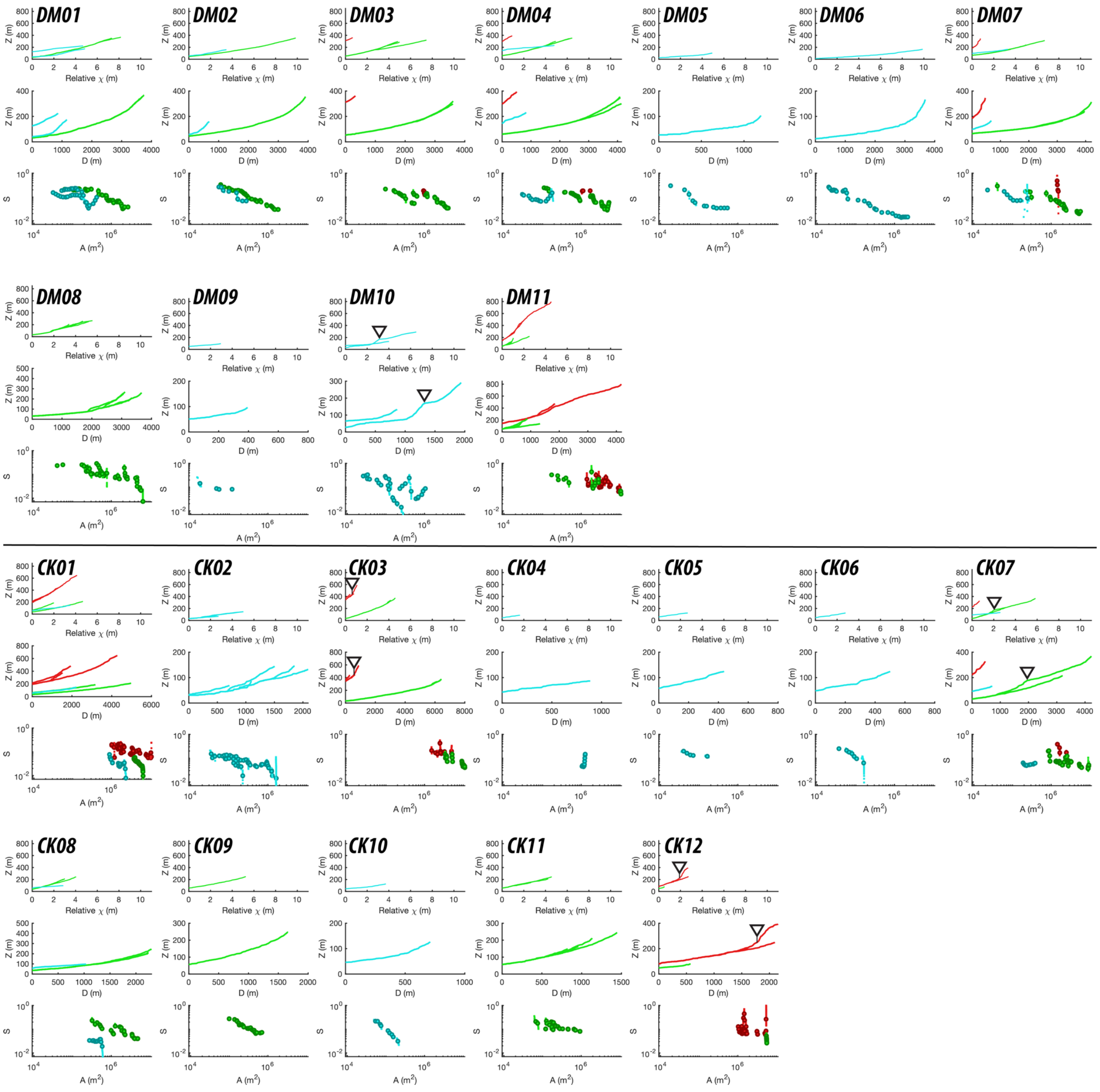

Figure S3 continued.

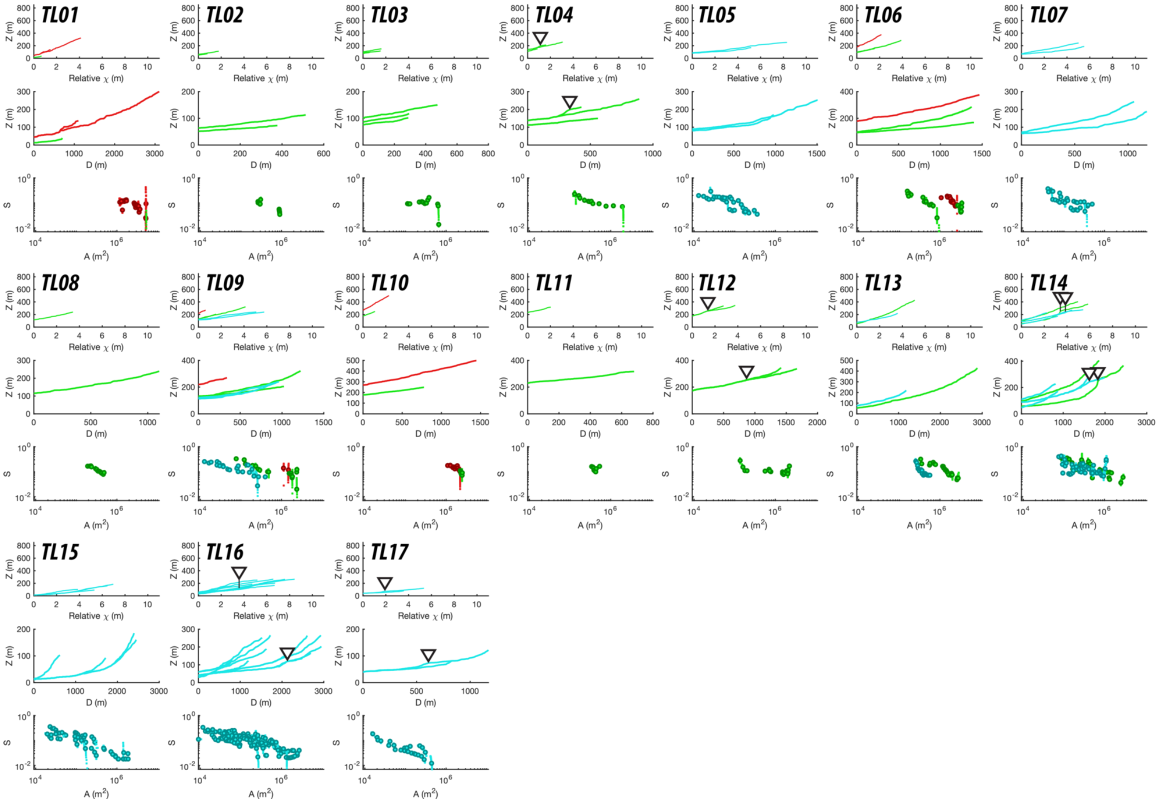

Figure S3 continued.

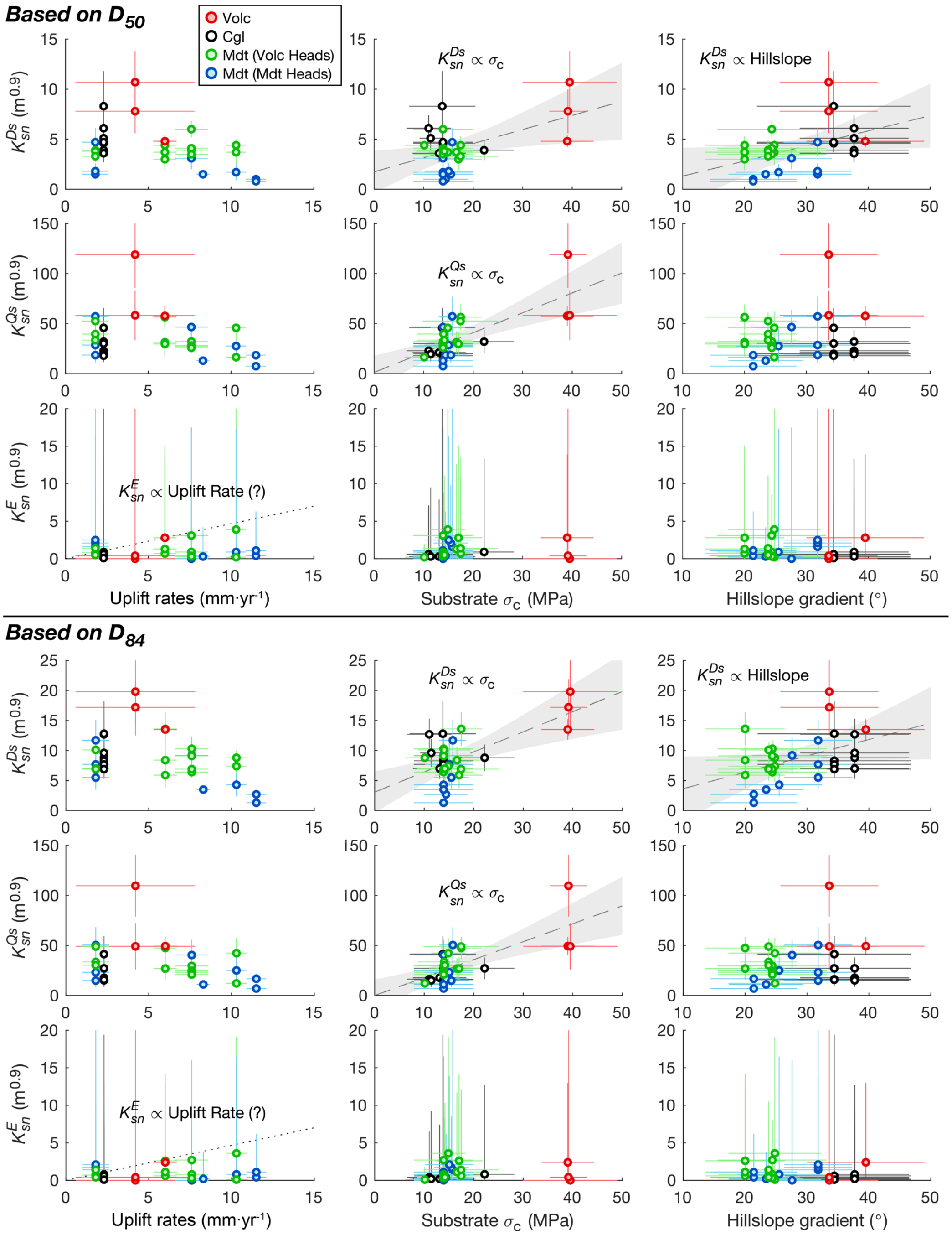

Figure S4. K_{sn} components (based on $\theta_{\text{ref}} = 0.45$) plotted against uplift rates, substrate uniaxial compressive strength (σ_c), and mean hillslope gradient. Uncertainties are the standard errors of the data. Broken lines and shades show linear regression and 95% confidence intervals. Thin dotted lines show hypothetic correlation between K_{sn}^{E} and uplift rate, but the uncertainties of K_{sn}^{E} in our sites are too large to distinctively display the correlation. The correlations for $K_{sn}^{D_s}$ and $K_{sn}^{Q_s}$ versus substrate strength (σ_c) suggest the signals of bedrock resistance in local K_{sn} (Figure 5d) are preserved in both $K_{sn}^{D_s}$ and $K_{sn}^{Q_s}$ through bed sediment size (D_{50} and D_{84}) (see Equations (5) to (7)). Abbreviations in legends: Volc = volcanic rock; Cgl = conglomerate; Mdt = mudstone and flysch. See data in Tables 1 and 2.

REFERENCES CITED

Abbott, L.D., Silver, E.A., Anderson, R.S., Smith, R., Ingle, J.C., Kling, S.A., Haig, D., Small, E., Galewsky, J., and Sliter, W.S. (1997) Measurement of tectonic surface uplift rate in a young collisional mountain belt. *Nature,* 385, 501-507.

Adams, B.A., Whipple, K.X., Forte, A.M., Heimsath, A.M., and Hodges, K.V. (2020) Climate controls on erosion in tectonically active landscapes. *Science Advances,* 6(42), eaaz3166.

Albarède, F. (1998) The growth of continental crust. *Tectonophysics,* 296(1), 1-14.

Allen, P.A. (2008) Time scales of tectonic landscapes and their sediment routing systems. *Geological Society, London, Special Publications,* 296(1), 7-28.

Allen, P.A., and Allen, J.R. (2013) *Basin Analysis: Principles and Application to Petroleum Play Assessment* (3 ed.). West Sussex, UK: John Wiley & Sons, Ltd.

Allen, P.A., Armitage, J.J., Carter, A., Duller, R.A., Michael, N.A., Sinclair, H.D., Whitchurch, A.L., and Whittaker, A.C. (2013) The Qs problem: Sediment volumetric balance of proximal foreland basin systems. *Sedimentology,* 60(1), 102-130.

Angelier, J., Chu, H.-T., Lee, J.-C., and Hu, J.-C. (2000) Active faulting and earthquake risk: the Chihshang Fault case, Taiwan. *Journal of Geodynamics,* 29, 151-185.

Anthonissen, D.E., and Ogg, J.G. (2012) Appendix 3 - Cenozoic and Cretaceous Biochronology of Planktonic Foraminifera and Calcareous Nannofossils. Gradstein, F.M., Ogg, J.G., Schmitz, M.D., and Ogg, G.M. (Eds.), *The Geologic Time Scale 2012* (p. 1083-1127). Boston: Elsevier.

Attal, M., Mudd, S.M., Hurst, M.D., Weinman, B., Yoo, K., and Naylor, M. (2015) Impact of change in erosion rate and landscape steepness on hillslope and fluvial sediments grain size in the Feather River basin (Sierra Nevada, California). *Earth Surface Dynamics,* 3(1), 201-222.

Backman, J., Raffi, I., Rio, D., Fornaciari, E., and Pälike, H. (2012) Biozonation and biochronology of Miocene through Pleistocene calcareous nannofossils from low and middle latitudes. *Newsletters on Stratigraphy,* 45, 221-244.

Baldwin, S.L., Monteleone, B.D., Webb, L.E., Fitzgerald, P.G., Grove, M., and June Hill, E. (2004) Pliocene eclogite exhumation at plate tectonic rates in eastern Papua New Guinea. *Nature,* 431(7006), 263-267.

Barbero, E., Festa, A., Saccani, E., Catanzariti, R., and D'Onofrio, R. (2020) Redefinition of the Ligurian Units at the Alps–Apennines junction (NW Italy) and their role in the evolution of the Ligurian accretionary wedge: constraints from mélanges and broken formations. *Journal of the Geological Society,* 177(3), 562-574.

Barletta, V.R., Bevis, M., Smith, B.E., Wilson, T., Brown, A., Bordoni, A., Willis, M., Khan, S.A., Rovira-Navarro, M., Dalziel, I., Smalley, R., Kendrick, E., Konfal, S., Caccamise, D.J., Aster, R.C., Nyblade, A., and Wiens, D.A. (2018) Observed rapid bedrock uplift in Amundsen Sea Embayment promotes ice-sheet stability. *Science,* 360(6395), 1335-1339.

Barrier, E., and Angelier, J. (1986) Active collision In eastern Taiwan: the Coastal Range. *Memoir of the Geological Society of China,* (7), 135-159.

Barrier, E., and Muller, C. (1984) New observations and discussion on the origin and age of the Lichi Mélange. *Memoir of the Geological Society of China,* (6), 303-325.

Berkland, J.O., Raymond, L.A., Kramer, J.C., Moores, E.M., and O'day, M. (1972) What is Franciscan? *AAPG Bulletin,* 56(12), 2295a-2302.

Beyssac, O., Negro, F., Simoes, M., Chan, Y.C., and Chen, Y.G. (2008) High-pressure metamorphism in Taiwan: from oceanic subduction to arc-continent collision? *Terra Nova,* 20(2), 118-125.

Biq, C.C. (1977) The Kenting Mélange and the Manila Trench. *Proceedings of the Geological Society of China,* (20), 119-122.

Bradley, D., and Hanson, L. (1998) Paleoslope analysis of slump folds in the devonian flysch of maine. *Journal of Geology,* 106(3), 305-318.

Bradley, D.C. (1987) Paleocurrent directions from two-dimensional exposures of cross laminae in the Devonian flysch of Maine. *Journal of Geology,* 95(2), 271-279.

Bradley, D.C., and Hanson, L.S. (2002) Paleocurrent analysis of a deformed Devonian foreland basin in the Northern Appalachians, Maine, USA. *Sedimentary Geology,* 148(3–4), 425-447.

Braun, J., van der Beek, P., and Batt, G. (2006) *Quantitative Thermochronology: Numerical Methods for the Interpretation of Thermochronological Data*. Cambridge: Cambridge University Press.

Brown, M. (2014) The contribution of metamorphic petrology to understanding lithosphere evolution and geodynamics. *Geoscience Frontiers,* 5(4), 553-569.

Buchovecky, E.J., and Lundberg, N. (1988) Clay mineralogy of mudstones from the southern Coastal Range, eastern Taiwan: Unroofing of the orogen versus in-situ diagenesis. *Acta Geologica Taiwanica: Science Reports of the National Taiwan University,* (26), 247-261.

Byrne, T.B., Chan, Y.-C., Rau, R.-J., Lu, C.-Y., Lee, Y.-H., and Wang, Y.-J. (2011) The arc-continent collision in Taiwan. Brown, D. and Ryan, P.D. (Eds.), *Arc-Continent Collision* (p. 213-245). Berlin, Heidelberg: Springer.

Champagnac, J.-D., Molnar, P., Sue, C., and Herman, F. (2012) Tectonics, climate, and mountain topography. *Journal of Geophysical Research: Solid Earth,* 117(B2).

Chang, C.-P., Angelier, J., and Huang, C.-Y. (2000) Origin and evolution of a melange: the active plate boundary and suture zone of the Longitudinal Valley, Taiwan. *Tectonophysics,* 325(1-2), 43-62.

Chang, C.-P., Angelier, J., Huang, C.-Y., and Liu, C.-S. (2001) Structural evolution and significance of a melange in a collision belt: the Lichi Melange and the Taiwan arc-continent collision. *Geological Magazine,* 138(6), 633-651.

Chang, L.-S. (1967) A biostratigraphic study of the Tertiary in the Coastal Range, eastern Taiwan, based on smaller foraminifera (I: southern part). *Proceedings of the Geological Society of China,* (10), 64-76.

Chang, L.-S. (1968) A biostratigraphic study of the Tertiary in the Coastal Range, eastern Taiwan, based on smaller foraminifera (Ⅱ: northern part). *Proceedings of the Geological Society of China,* (11), 19-33.

Chang, L.-S. (1969) A biostratigraphic study of the Tertiary in the Coastal Range, eastern Taiwan, based on smaller foraminifera (Ⅲ: middle part). *Proceedings of the Geological Society of China,* (12), 89-101.

Chang, L.-S., and Chen, T.H. (1970) A biostratigraphic study of the Tertiary along the Hsiukuluanchi in the Coastal Range, eastern Taiwan, based on smaller foraminifera. *Proceedings of the Geological Society of China,* (13), 115-128.

Chang, S.S.L., and Chi, W.-R. (1983) Neogene nannoplankton biostratigraphy in Taiwan and the tectonic implications. *Petroleum Geology of Taiwan,* (19), 93-147.

Channell, J.E.T., Singer, B.S., and Jicha, B.R. (2020) Timing of Quaternary geomagnetic reversals and excursions in volcanic and sedimentary archives. *Quaternary Science Reviews,* 228, 106114.

Chatanantavet, P., and Parker, G. (2008) Experimental study of bedrock channel alluviation under varied sediment supply and hydraulic conditions. *Water Resources Research,* 44(12), W12446.

Chatanantavet, P., and Parker, G. (2009) Physically based modeling of bedrock incision by abrasion, plucking, and macroabrasion. *Journal of Geophysical Research: Earth Surface,* 114(F4), F04018.

Chemenda, A.I., Yang, R.K., Stephan, J.F., Konstantinovskaya, E.A., and Ivanov, G.M. (2001) New results from physical modelling of arc–continent collision in Taiwan: evolutionary model. *Tectonophysics,* 333(1), 159-178.

Chen, C.-S., and Chen, Y.-L. (2003) The rainfall characteristics of Taiwan. *Monthly Weather Review,* 131(7), 1323-1341.

Chen, T.-W., Chung, S.-L., and Chen, W.-S. (2015) *Zircon U-Pb geochronology of the Plio-Pleistocene volcanogenic and orogenic sedimentary rocks from the Coastal Range, eastern Taiwan*. Paper presented at the EGU General Assembly 2015, Vienna, Austria.

Chen, W.-H., Huang, C.-Y., Lin, Y.-J., Zhao, Q., Yan, Y., Chen, D., Zhang, X., Lan, Q., and Yu, M. (2015) Depleted deep South China Sea δ13C paleoceanographic events in response to tectonic evolution in Taiwan–Luzon Strait since Middle Miocene. *Deep Sea Research Part II: Topical Studies in Oceanography,* 122, 195-225.

Chen, W.-H., Huang, C.-Y., Yan, Y., Dilek, Y., Chen, D., Wang, M.-H., Zhang, X., Lan, Q., and Yu, M. (2017) Stratigraphy and provenance of forearc sequences in the Lichi Mélange, Coastal Range: Geological records of the active Taiwan arc-continent collision. *Journal of Geophysical Research: Solid Earth,* 122(9), 7408-7436.

Chen, W.-S. (1988a) Development of deep-sea fan systems in Coastal Range basin, eastern Taiwan. *Acta Geologica Taiwanica: Science Reports of the National Taiwan University,* (26), 37-56.

Chen, W.-S. (1988b) *Tectonic evolution of sedimentary basins in Coastal Range, Taiwan.* (Doctoral dissertation), National Taiwan University, Taipei, Taiwan.

Chen, W.-S. (1991) Origin of the Lichi Melange in the Coastal Range, eastern Taiwan. *Special Publication of the Central Geological Survey, Ministry of Economic Affairs of Taiwan,* (5), 257-266.

Chen, W.-S. (1997a) Lithofacies analyses of the arc-related sequence in the Coastal Range, eastern Taiwan. *Journal of the Geological Society of China,* 40(2), 313-338.

Chen, W.-S. (1997b) Mesoscopic structures developed in the Lichi melange during arc-continent collision in Taiwan region. *Journal of the Geological Society of China,* 40(2), 415-434.

Chen, W.-S. (2009) Tectonostratigraphic framework and age of the volcanic-arc and collision basins in the Coastal Range, eastern Taiwan. *Western Pacific Earth Sciences,* 9, 67-98.

Chen, W.-S., Chung, S.-L., Chou, H.-Y., Zugeerbai, Z., Shao, W.-Y., and Lee, Y.-H. (2017) A reinterpretation of the metamorphic Yuli belt: Evidence for a middle-late Miocene accretionary prism in eastern Taiwan. *Tectonics,* 36(2), 188-206.

Chen, W.-S., Lin, I.-C., Yen, Y.-C., Yang, C.-C., Chi, C.-Y., Huang, N.-W., Lin, C.-W., Lin, W.-S., Hou, C.-S., Liu, Y.-C., Lin, Y.-H., Shih, T.-S., and Lu, S.-T. (2008) Fault segmentation of the Longitudinal Valley Fault in eastern Taiwan: Evidence from paleoseismic investigations and GPS observations. *Special Publication of the Central Geological Survey, Ministry of Economic Affairs of Taiwan,* (20), 165-191.

Chen, W.-S., and Wang, Y. (1997) *Geological map of Taiwan scale 1:50,000 - Fengpin sheet*. Central Geological Survey, Ministry of Economic Affairs of Taiwan, New Taipei, Taiwan.

Chen, W.-S., Yang, C.-Y., Chen, S.-T., and Huang, Y.-C. (2020) New insights into Holocene marine terrace development caused by seismic and aseismic faulting in the Coastal Range, eastern Taiwan. *Quaternary Science Reviews,* 240, 106369.

Chen, W.-S., Yeh, J.-J., and Syu, S.-J. (2019) Late Cenozoic exhumation and erosion of the Taiwan orogenic belt: New insights from petrographic analysis of foreland basin sediments and thermochronological dating on the metamorphic orogenic wedge. *Tectonophysics,* 750, 56-69.

Chi, W.-C., Chen, L., Liu, C.-S., and Brookfield, M. (2014) Development of arc–continent collision mélanges: Linking onshore geological and offshore geophysical observations of the Pliocene Lichi Mélange, southern Taiwan and northern Luzon arc, western Pacific. *Tectonophysics,* 636, 70-82.

Chi, W.-R., Namson, J., and Mei, W.W. (1980) Calcareous nannoplankton biostratigraphy of the late Neogene Sediments exposed along the Hsiukuluanchi In the Coastal Range, eastern Taiwan. *Petroleum Geology of Taiwan,* (17), 75-87.

Chi, W.-R., Namson, J., and Suppe, J. (1981) Stratigraphic record of plate interactions in the Coastal Range of eastern Taiwan. *Memoir of the Geological Society of China,* (4), 155-194.

Chim, L.K., Yen, J.-Y., Huang, S.-Y., Liou, Y.-S., and Tsai, L.L.-Y. (2018) Using Raman spectroscopy of carbonaceous materials to track exhumation of an active orogenic belt: An example from eastern Taiwan. *Journal of Asian Earth Sciences,* 164, 248-259.

Ching, K.-E., Hsieh, M.-L., Johnson, K.M., Chen, K.-H., Rau, R.-J., and Yang, M. (2011) Modern vertical deformation rates and mountain building in Taiwan from precise leveling and continuous GPS observations, 2000–2008. *Journal of Geophysical Research: Solid Earth,* 116(B8), B08406.

Chuang, C.-K., Lo, L., Zeeden, C., Chou, Y.-M., Wei, K.-Y., Shen, C.-C., Mii, H.-S., Chang, Y.-P., and Tung, Y.-H. (2018) Integrated stratigraphy of ODP Site 1115 (Solomon Sea, southwestern equatorial Pacific) over the past 3.2 Ma. *Marine Micropaleontology,* 144, 25-37.

Clift, P.D., Lin, A.T.S., Carter, A., Wu, F., Draut, A.E., Lai, T.H., Fei, L.Y., Schouten, H., and Teng, L. (2008) Post-collisional collapse in the wake of migrating arc-continent collision in the Ilan Basin, Taiwan. Draut, A.E., Clift, P.D., and Scholl, D.W. (Eds.), *Formation and Applications of the Sedimentary Record in Arc Collision Zones* (p. 257-278).

Clift, P.D., Schouten, H., and Draut, A.E. (2003) A general model of arc-continent collision and subduction polarity reversal from Taiwan and the Irish Caledonides. *Geological Society, London, Special Publications,* 219(1), 81-98.

Clift, P.D., and Vannucchi, P. (2004) Controls on tectonic accretion versus erosion in subduction zones: Implications for the origin and recycling of the continental crust. *Reviews of Geophysics,* 42(2), RG2001.

Codegone, G., Festa, A., Dilek, Y., and Pini, G.A. (2012) Small-scale polygenetic mélanges in the Ligurian accretionary complex, Northern Apennines, Italy, and the role of shale diapirism in superposed mélange evolution in orogenic belts. *Tectonophysics,* 568-569, 170-184.

Conand, C., Mouthereau, F., Ganne, J., Lin, A.T.-S., Lahfid, A., Daudet, M., Mesalles, L., Giletycz, S., and Bonzani, M. (2020) Strain partitioning and exhumation in oblique Taiwan collision: Role of rift architecture and plate kinematics. *Tectonics,* 39(4), e2019TC005798.

Cowan, D.S. (1985) Structural styles in Mesozoic and Cenozoic mélanges in the western Cordillera of North America. *Geological Society of America Bulletin,* 96(4), 451-462.

Cowie, P.A., Whittaker, A.C., Attal, M., Roberts, G., Tucker, G.E., and Ganas, A. (2008) New constraints on sediment-flux–dependent river incision: Implications for extracting tectonic signals from river profiles. *Geology,* 36(7), 535-538.

Dadson, S.J., Hovius, N., Chen, H., Dade, W.B., Hsieh, M.-L., Willett, S.D., Hu, J.-C., Horng, M.-J., Chen, M.-C., Stark, C.P., Lague, D., and Lin, J.-C. (2003) Links between erosion, runoff variability and seismicity in the Taiwan orogen. *Nature,* 426(6967), 648-651.

DeCelles, P.G. (2012) Foreland basin systems revisited: Variations in response to tectonic settings. Busby, C. and Azor, A. (Eds.), *Tectonics of Sedimentary Basins: Recent Advances* (p. 405-426). Oxford, UK: Blackwell Publishing Ltd.

DeCelles, P.G., and Giles, K.A. (1996) Foreland basin systems. *Basin Research,* 8(2), 105-123.

Di Martire, D., Ascione, A., Calcaterra, D., Pappalardo, G., and Mazzoli, S. (2015) Quaternary deformation in SE Sicily: Insights into the life and cycles of forebulge fault systems. *Lithosphere,* 7(5), 519-534.

DiBiase, R.A., Rossi, M.W., and Neely, A.B. (2018) Fracture density and grain size controls on the relief structure of bedrock landscapes. *Geology,* 46(5), 399-402.

DiBiase, R.A., and Whipple, K.X. (2011) The influence of erosion thresholds and runoff variability on the relationships among topography, climate, and erosion rate. *Journal of Geophysical Research: Earth Surface,* 116(F4), F04036.

DiBiase, R.A., Whipple, K.X., Heimsath, A.M., and Ouimet, W.B. (2010) Landscape form and millennial erosion rates in the San Gabriel Mountains, CA. *Earth and Planetary Science Letters,* 289(1), 134-144.

Dilek, Y., Festa, A., Ogawa, Y., and Pini, G.A. (2012) Chaos and geodynamics: Mélanges, mélange-forming processes and their significance in the geological record. *Tectonophysics,* 568-569, 1-6.

Doo, W.-B., Lo, C.-L., Hsu, S.-K., Tsai, C.-H., Huang, Y.-S., Wang, H.-F., Chiu, S.-D., Ma, Y.-F., and Liang, C.-W. (2018) New gravity anomaly map of Taiwan and its surrounding regions with some tectonic interpretations. *Journal of Asian Earth Sciences,* 154, 93-100.

Doo, W.-S., and Shyu, L.-M. (1966) *1:25,000 Geological Map of the Tuluanshan Anticline, Taitung*. Taiwan Petrolium Exploration Division, Chinese Petrolium Corporation,

Dorsey, R.J. (1985) Petrography of Neogene sandstones from the Coastal Range of eastern Taiwan: response to arc-continent collision. *Petroleum Geology of Taiwan,* (21), 187-215.

Dorsey, R.J. (1988) Provenance evolution and unroofing history of a modern arc-continent collision: Evidence from petrography of Plio-Pleistocene sandstones, eastern Taiwan. *Journal of Sedimentary Research,* 58(2), 208-218.

Dorsey, R.J. (1992) Collapse of the Luzon volcanic arc during onset of arc-continent collision: Evidence from a Miocene-Pliocene unconformity, eastern Taiwan. *Tectonics,* 11(2), 177-191.

Dorsey, R.J., Buchovecky, E.J., and Lundberg, N. (1988) Clay mineralogy of Pliocene-Pleistocene mudstones, eastern Taiwan: Combined effects of burial diagenesis and provenance unroofing. *Geology,* 16(10), 944-947.

Dorsey, R.J., Housen, B.A., Janecke, S.U., Fanning, C.M., and Spears, A.L.F. (2011) Stratigraphic record of basin development within the San Andreas fault system: Late Cenozoic Fish Creek–Vallecito basin, southern California. *Geological Society of America Bulletin,* 123(5-6), 771-793.

Dorsey, R.J., and Lundberg, N. (1988) Lithofacies analysis and basin reconstruction of the Plio-Pleistocene collisional basin, Coastal Range of eastern Taiwan. *Acta Geologica Taiwanica Science Reports of the National Taiwan University,* (26), 57-132.

Draut, A.E., and Clift, P.D. (2012) Basins in arc-continental collisions. Cathy, B. and Antonio, A. (Eds.), *Tectonics of Sedimentary Basins: Recent Advances* (p. 347-368). Oxford, UK: Blackwell Publishing Ltd.

Draut, A.E., and Clift, P.D. (2013) Differential preservation in the geologic record of intraoceanic arc sedimentary and tectonic processes. *Earth-Science Reviews,* 116, 57-84.

Dubille, M., and Lavé, J. (2015) Rapid grain size coarsening at sandstone/conglomerate transition: similar expression in Himalayan modern rivers and Pliocene molasse deposits. *Basin Research,* 27(1), 26-42.

Duvall, A., Kirby, E., and Burbank, D. (2004) Tectonic and lithologic controls on bedrock channel profiles and processes in coastal California. *Journal of Geophysical Research: Earth Surface,* 109(F3), F03002.

Egholm, D.L., Knudsen, M.F., and Sandiford, M. (2013) Lifespan of mountain ranges scaled by feedbacks between landsliding and erosion by rivers. *Nature,* 498, 475.

Ernst, W.G. (1977) Olistostromes and included ophiolitic debris from the Coastal Range of eastern Taiwan. *Memoir of the Geological Society of China,* (2), 97-114.

Fellin, M.G., Chen, C.-Y., Willett, S.D., Christl, M., and Chen, Y.-G. (2017) Erosion rates across space and timescales from a multi-proxy study of rivers of eastern Taiwan. *Global and Planetary Change,* 157, 174-193.

Festa, A., Dilek, Y., Pini, G.A., Codegone, G., and Ogata, K. (2012) Mechanisms and processes of stratal disruption and mixing in the development of mélanges and broken formations: Redefining and classifying mélanges. *Tectonophysics,* 568-569, 7-24.

Festa, A., Ogata, K., and Pini, G.A. (2020) Polygenetic mélanges: a glimpse on tectonic, sedimentary and diapiric recycling in convergent margins. *Journal of the Geological Society,* 177(3), 551-561.

Festa, A., Ogata, K., Pini, G.A., Dilek, Y., and Alonso, J.L. (2016) Origin and significance of olistostromes in the evolution of orogenic belts: A global synthesis. *Gondwana Research,* 39, 180-203.

Festa, A., Pini, G.A., Dilek, Y., and Codegone, G. (2010) Mélanges and mélange-forming processes: a historical overview and new concepts. *International Geology Review,* 52(10-12), 1040-1105.

Festa, A., Pini, G.A., Ogata, K., and Dilek, Y. (2019) Diagnostic features and field-criteria in recognition of tectonic, sedimentary and diapiric mélanges in orogenic belts and exhumed subduction-accretion complexes. *Gondwana Research,* 74, 7-30.

Finnegan, N.J., Klier, R.A., Johnstone, S., Pfeiffer, A.M., and Johnson, K. (2017) Field evidence for the control of grain size and sediment supply on steady-state bedrock river channel slopes in a tectonically active setting. *Earth Surface Processes and Landforms,* 42(14), 2338-2349.

Finnegan, N.J., Roe, G., Montgomery, D.R., and Hallet, B. (2005) Controls on the channel width of rivers: Implications for modeling fluvial incision of bedrock. *Geology,* 33(3), 229-232.

Finnegan, N.J., Schumer, R., and Finnegan, S. (2014) A signature of transience in bedrock river incision rates over timescales of 104–107 years. *Nature,* 505(7483), 391-394.

Finnegan, N.J., Sklar, L.S., and Fuller, T.K. (2007) Interplay of sediment supply, river incision, and channel morphology revealed by the transient evolution of an experimental bedrock channel. *Journal of Geophysical Research: Earth Surface,* 112(F3), F03S11.

Fisher, D.M., Willett, S., Yeh, E.-C., and Clark, M.B. (2007) Cleavage fronts and fans as reflections of orogen stress and kinematics in Taiwan. *Geology,* 35(1), 65-68.

Fisher, R.A. (1953) Dispersion on a sphere. *Proceedings of the Royal Society of London. Series A. Mathematical and Physical Sciences,* 217(1130), 295-305.

Flint, J.J. (1974) Stream gradient as a function of order, magnitude, and discharge. *Water Resources Research,* 10(5), 969-973.

Forte, A.M., and Whipple, K.X. (2019) Short communication: The Topographic Analysis Kit (TAK) for TopoToolbox. *Earth Surface Dynamics,* 7(1), 87-95.

Forte, A.M., Yanites, B.J., and Whipple, K.X. (2016) Complexities of landscape evolution during incision through layered stratigraphy with contrasts in rock strength. *Earth Surface Processes and Landforms,* 41(12), 1736-1757.

Froitzheim, N., Pleuger, J., and Nagel, T.J. (2006) Extraction faults. *Journal of Structural Geology,* 28(8), 1388-1395.

Gallagher, K., and Lambeck, K. (1989) Subsidence, sedimentation and sea-level changes in the Eromanga Basin, Australia. *Basin Research,* 2(2), 115-131.

Gasparini, N.M., Bras, R.L., and Whipple, K.X. (2006) Numerical modeling of non–steady-state river profile evolution using a sediment-flux-dependent incision model. Willett, S.D., Hovius, N., Brandon, M.T., and Fisher, D.M. (Eds.), *Tectonics, Climate, and Landscape Evolution* (Vol. 398, p. 127-141): Geological Society of America.

Gingerich, P.D. (2021) Rates of geological processes. *Earth-Science Reviews,* 220, 103723.

Greenly, E. (1919) *The Geology of Anglesey: London*. Richmond, UK: Geological Survey of Great Britain. Her Majesty's Stationery Office.

Hamilton, E.L., and Bachman, R.T. (1982) Sound velocity and related properties of marine sediments. *The Journal of the Acoustical Society of America,* 72(6), 1891-1904.

Hansen, S. (1996) A compaction trend for Cretaceous and Tertiary shales on the Norwegian shelf based on sonic transit times. *Petroleum Geoscience,* 2(2), 159-166.

Harris, R.A., and Audley-Charles, M.G. (1987) Taiwan and Timor neotectonics: A comparative review. *Memoir of the Geological Society of China,* (9), 45-61.

Harris, R.A., Sawyer, R.K., and Audley-Charles, M.G. (1998) Collisional melange development: Geologic associations of active melange-forming processes with exhumed melange facies in the western Banda orogen, Indonesia. *Tectonics,* 17(3), 458-479.

Hayward, B.W., and Triggs, C.M. (2016) Using multi-foraminiferal-proxies to resolve the paleogeographic history of a lower Miocene, subduction-related, sedimentary basin (Waitemata basin, New Zealand). *Journal of Foraminiferal Research,* 46(3), 285-313.

He, M., Zhong, G., Liu, X., Liu, L., Shen, X., Wu, Z., and Huang, K. (2017) Rapid post-rift tectonic subsidence events in the Pearl River Mouth Basin, northern South China Sea margin. *Journal of Asian Earth Sciences,* 147, 271-283.

Heller, P.L., Angevine, C.L., Winslow, N.S., and Paola, C. (1988) Two-phase stratigraphic model of foreland-basin sequences. *Geology,* 16(6), 501-504.

Hergarten, S., Robl, J., and Stüwe, K. (2016) Tectonic geomorphology at small catchment sizes – extensions of the stream-power approach and the χ method. *Earth Surface Dynamics,* 4(1), 1-9.

Hilley, G.E., Porder, S., Aron, F., Baden, C.W., Johnstone, S.A., Liu, F., Sare, R., Steelquist, A., and Young, H.H. (2019) Earth's topographic relief potentially limited by an upper bound on channel steepness. *Nature Geoscience,* 12, 828-832.

Hirtzel, J., Chi, W.C., Reed, D., Chen, L., Liu, C.S., and Lundberg, N. (2009) Destruction of Luzon forearc basin from subduction to Taiwan arc–continent collision. *Tectonophysics,* 479(1-2), 43-51.

Hohenegger, J. (2005) Estimation of environmental paleogradient values based on presence/absence data: a case study using benthic foraminifera for paleodepth estimation. *Palaeogeography, Palaeoclimatology, Palaeoecology,* 217(1), 115-130.

Hong, S.-M. (2020) *Using porosity-effective stress relationship curve to evaluate the erosion amount of the fore-arc basin in the southern part of Coastal Range.* (Master's thesis), National Central University, Taoyuan, Taiwan.

Horng, C.-S., and Shea, K.-S. (1996) Dating of the Plio-Pleistocene rapidly deposited sequence based on integrated magneto-biostratigraphy: a case study of the madagida-chi section, Coastal Range, eastern Taiwan. *Journal of the Geological Society of China,* 39(1), 31-58.

Howard, A.D., and Kerby, G. (1983) Channel changes in badlands. *Geological Society of America Bulletin,* 94(6), 739-752.

Hsieh, H.-H., Chen, C.-H., Lin, P.-Y., and Yen, H.-Y. (2014) Curie point depth from spectral analysis of magnetic data in Taiwan. *Journal of Asian Earth Sciences,* 90, 26-33.

Hsieh, M.-L., Hogg, A., Song, S.-R., Kang, S.-C., and Chou, C.-Y. (2017) A mass-wasting dominated Quaternary mountain range, the Coastal Range in eastern Taiwan. *Quaternary Science Reviews,* 177, 276-298.

Hsieh, M.-L., Liew, P.-M., and Chen, H.-W. (2011) Early Holocene catastrophic mass-wasting event and fan-delta development on the Hua-tung coast, eastern Taiwan. *Geomorphology,* 134(3), 378-393.

Hsieh, M.-L., and Rau, R.-J. (2009) Late Holocene coseismic uplift on the Hua-tung coast, eastern Taiwan: Evidence from mass mortality of intertidal organisms. *Tectonophysics,* 474, 595-609.

Hsieh, Y.-H., Liu, C.-S., Suppe, J., Byrne, T.B., and Lallemand, S. (2020) The Chimei submarine canyon and fan: A record of Taiwan arc-continent collision on the rapidly deforming over-riding plate. *Tectonics,* 39(11), e2020TC006148.

Hsu, C.-W., Liu, Y.-C., and Yen, Y.-C. (2017) A study on the fault trace and the recent drilling data of the Chimei Fault, eastern Taiwan. *Special Publication of the Central Geological Survey, Ministry of Economic Affairs of Taiwan,* (31), 91-116.

Hsü, K.J. (1968) Principles of mélanges and their bearing on the Franciscan-Knoxville paradox. *Geological Society of America Bulletin,* 79(8), 1063-1074.

Hsü, K.J. (1988) Melange and the mélange tectonics of Taiwan. *Proceedings of the Geological Society of China,* (31), 87-92.

Hsu, T.L. (1956) Geology of the Coastal Range, eastern Taiwan. *Bulletin of the Central Geological Survey of Taiwan,* (8), 39-63.

Hsu, W.-H., Byrne, T.B., Ouimet, W., Lee, Y.-H., Chen, Y.-G., van Soest, M., and Hodges, K. (2016) Pleistocene onset of rapid, punctuated exhumation in the eastern Central Range of the Taiwan orogenic belt. *Geology,* 44(9), 719-722.

Huang, C.-Y., Chen, W.-H., Wang, M.-H., Lin, C.-T., Yang, S., Li, X., Yu, M., Zhao, X., Yang, K.-M., Liu, C.-S., Hsieh, Y.-H., and Harris, R. (2018) Juxtaposed sequence stratigraphy, temporal-spatial variations of sedimentation and development of modern-forming forearc Lichi Mélange in North Luzon Trough forearc basin onshore and offshore eastern Taiwan: An overview. *Earth-Science Reviews,* 182, 102-140.

Huang, C.-Y., Chien, C.-W., Yao, B., and Chang, C.-P. (2008) The Lichi Mélange: A collision mélange formation along early arcward backthrusts during forearc basin closure, Taiwan arc-continent collision. Draut, A.E., Clift, P.D., and Scholl, D.W. (Eds.), *Formation and Applications of the Sedimentary Record in Arc Collision Zones* (p. 127-154).

Huang, C.-Y., Wu, W.Y., Chang, C.-P., Tsao, S., Yuan, P.B., Lin, C.W., and Xia, K.Y. (1997) Tectonic evolution of accretionary prism in the arc-continent collision terrane of Taiwan. *Tectonophysics,* 281(1-2), 31-51.

Huang, C.-Y., and Yuan, P.B. (1994) Stratigraphy of the Kangkou Limestone in the Coastal Range, eastern Taiwan. *Journal of Geological Society of China,* 37(4), 585-605.

Huang, C.-Y., Yuan, P.B., Lin, C.-W., Wang, T.K., and Chang, C.-P. (2000) Geodynamic processes of Taiwan arc–continent collision and comparison with analogs in Timor, Papua New Guinea, Urals and Corsica. *Tectonophysics,* 325(1), 1-21.

Huang, C.-Y., Yuan, P.B., Song, S.-R., Lin, C.W., Wang, C.S., Chen, M.T., Shyu, C.T., and Karp, B. (1995) Tectonics of short-lived intra-arc basins in the arc-continent collision terrane of the Coastal Range, eastern Taiwan. *Tectonics,* 14(1), 19-38.

Huang, C.-Y., Yuan, P.B., and Tsao, S.-J. (2006) Temporal and spatial records of active arc-continent collision in Taiwan: A synthesis. *Geological Society of America Bulletin,* 118(3-4), 274-288.

Huang, C.Y., Yuan, P.B., and Teng, L.S. (1988) Paleontology of the Kangkou Limestone in the middle Coastal Range, eastern Taiwan. *Acta Geologica Taiwanica: Science Reports of the National Taiwan University,* (26), 133-160.

Huang, W.-J., Johnson, K.M., Fukuda, J.i., and Yu, S.-B. (2010) Insights into active tectonics of eastern Taiwan from analyses of geodetic and geologic data. *Journal of Geophysical Research: Solid Earth,* 115(B3), B03413.

Ingle, J.C.J. (1975) Summary of late Paleogeneneogene insular stratigraphy, paleobathymetry, and correlations, Philippine Sea and Sea of Japan region. *Initial Reports of the Deep Sea Drilling Project,* 31, 837-855.

Jahn, B.M., and Liou, J.G. (1977) Age and geochemical constraints of glaucophane schists of taiwan. *Memoir of the Geological Society of China,* (2), 129-140.

Johnson, J.P.L., Whipple, K.X., Sklar, L.S., and Hanks, T.C. (2009) Transport slopes, sediment cover, and bedrock channel incision in the Henry Mountains, Utah. *Journal of Geophysical Research: Earth Surface,* 114(F2), F02014.

Keyser, W., Tsai, C.-H., Iizuka, Y., Oberhänsli, R., and Ernst, W.G. (2016) High-pressure metamorphism in the Chinshuichi area, Yuli belt, eastern Taiwan. *Tectonophysics,* 692, Part B, 191-202.

Kirby, E., and Whipple, K. (2001) Quantifying differential rock-uplift rates via stream profile analysis. *Geology,* 29(5), 415-418.

Kirby, E., and Whipple, K.X. (2012) Expression of active tectonics in erosional landscapes. *Journal of Structural Geology,* 44, 54-75.

Kirstein, L.A., Carter, A., and Chen, Y.-G. (2014) Impacts of arc collision on small orogens: new insights from the Coastal Range detrital record, Taiwan. *Journal of the Geological Society, London,* 171(1), 5-8.

Kirstein, L.A., Fellin, M.G., Willett, S.D., Carter, A., Chen, Y.G., Garver, J.I., and Lee, D.C. (2010) Pliocene onset of rapid exhumation in Taiwan during arc–continent collision: new insights from detrital thermochronometry. *Basin Research,* 22(3), 270-285.

Kominz, M.A., Patterson, K., and Odette, D. (2011) Lithology dependence of porosity In slope and deep marine sediments. *Journal of Sedimentary Research,* 81(10), 730-742.

Kominz, M.A., and Pekar, S.F. (2001) Oligocene eustasy from two-dimensional sequence stratigraphic backstripping. *Geological Society of America Bulletin,* 113(3), 291-304.

Kusky, T., Wang, J., Wang, L., Huang, B., Ning, W., Fu, D., Peng, H., Deng, H., Polat, A., Zhong, Y., and Shi, G. (2020) Mélanges through time: Life cycle of the world's largest Archean mélange compared with Mesozoic and Paleozoic subduction-accretion-collision mélanges. *Earth-Science Reviews,* 209, 103303.

Lague, D. (2010) Reduction of long-term bedrock incision efficiency by short-term alluvial cover intermittency. *Journal of Geophysical Research: Earth Surface,* 115(F2), F02011.

Lague, D. (2014) The stream power river incision model: evidence, theory and beyond. *Earth Surface Processes and Landforms,* 39(1), 38-61.

Lague, D., Hovius, N., and Davy, P. (2005) Discharge, discharge variability, and the bedrock channel profile. *Journal of Geophysical Research: Earth Surface,* 110(F4), F04006.

Lai, L.S.-H., Dorsey, R.J., Horng, C.-S., Chi, W.-R., Shea, K.-S., and Yen, J.-Y. (2021) Polygenetic mélange in the retrowedge foredeep of an active arc-continent collision, Coastal Range of eastern Taiwan. *Sedimentary Geology,* 418, 105901.

Lai, L.S.-H., Ng, T.-W., and Teng, L.S. (2018) Stratigraphic correlation of tuffaceous and psephitic strata in the Paliwan formation, southern Coastal Range of eastern Taiwan. *Bulletin of the Central Geological Survey, Ministry of Economic Affairs of Taiwan,* (31), 1-32.

Lai, L.S.-H., Roering, J.J., Finnegan, N.J., Dorsey, R.J., and Yen, J.-Y. (2021) Coarse sediment supply sets the slope of bedrock channels in rapidly uplifting terrain: Field and topographic evidence from eastern Taiwan. *Earth Surface Processes and Landforms,* 46(13), 2671-2689.

Lai, L.S.-H., and Teng, L.S. (2016) Stratigraphy and structure of the Tai-Yuan basin, southern Coastal Range, eastern Taiwan. *Bulletin of the Central Geological Survey, Ministry of Economic Affairs of Taiwan,* (29), 45-76.

Lai, Y.-M., Chu, M.-F., Chen, W.-S., Shao, W.-Y., Lee, H.-Y., and Chung, S.-L. (2018) Zircon U-Pb and Hf isotopic constraints on the magmatic evolution of the Northern Luzon Arc. *Terrestrial Atmospheric and Oceanic Sciences,* 29(1), 149-186.

Lai, Y.-M., and Song, S.-R. (2013) The volcanoes of an oceanic arc from origin to destruction: A case from the northern Luzon Arc. *Journal of Asian Earth Sciences,* 74(0), 97-112.

Lai, Y.-M., Song, S.-R., Lo, C.-H., Lin, T.-H., Chu, M.-F., and Chung, S.-L. (2017) Age, geochemical and isotopic variations in volcanic rocks from the Coastal Range of Taiwan: Implications for magma generation in the Northern Luzon Arc. *Lithos,* 272-273, 92-115.

Lamb, M.P., Dietrich, W.E., and Venditti, J.G. (2008) Is the critical Shields stress for incipient sediment motion dependent on channel-bed slope? *Journal of Geophysical Research: Earth Surface,* 113(F2), F02008.

Larsen, I.J., and Montgomery, D.R. (2012) Landslide erosion coupled to tectonics and river incision. *Nature Geoscience,* 5, 468.

Lavé, J., and Avouac, J.P. (2001) Fluvial incision and tectonic uplift across the Himalayas of central Nepal. *Journal of Geophysical Research: Solid Earth,* 106(B11), 26561-26591.

Lee, E.Y., Novotny, J., and Wagreich, M. (2019) *Subsidence Analysis and Visualization: For Sedimentary Basin Analysis and Modelling*. Cham: Springer International Publishing.

Lee, E.Y., and Wagreich, M. (2016) 3D visualization of the sedimentary fill and subsidence evolution in the northern and central Vienna Basin (Miocene). *Austrian Journal of Earth Sciences,* 109(2), 241-251.

Lee, J.-C., Chu, H.-T., Angelier, J., Hu, J.-C., Chen, H.-Y., and Yu, S.-B. (2006) Quantitative analysis of surface coseismic faulting and postseismic creep accompanying the 2003, Mw = 6.5, Chengkung earthquake in eastern Taiwan. *Journal of Geophysical Research: Solid Earth,* 111, B02405.

Lee, T.-Q. (1989) *Evolution tectonique et geodynamique neogene et quaternaire de la chaine cotiere de Taiwan: apport du paleomagnetisme.* (Doctoral dissertation), Universite Pierre et Marie Curie, Paris, France.

Lee, T.-Q. (1992) Study of the polarity transition record of the upper Olduvai event from Wulochi sedimentary sequence of the Coastal Range, eastern Taiwan. *Terrestrial Atmospheric and Oceanic Sciences,* 3(4), 503-518.

Lee, T.-Q., and Chi, W.-R. (1990) Paleomagnetic dating of the sedimentary formations in the Coastal Range. *Special Publication of the Central Geological Survey, Ministry of Economic Affairs of Taiwan,* (4), 271-294.

Lee, T.-Q., Kissel, C., Laj, C., Horng, C.-S., and Lue, Y.-T. (1990) Magnetic fabric analysis of the Plio-Pleistocene sedimentary formations of the Coastal Range of Taiwan. *Earth and Planetary Science Letters,* 98(1), 23-32.

Lee, Y.-H., Byrne, T., Wang, W.-H., Lo, W., Rau, R.-J., and Lu, H.-Y. (2015) Simultaneous mountain building in the Taiwan orogenic belt. *Geology,* 43(5), 451-454.

Li, M. (1984) *Geology of Ruiyuan area, southern Coastal Range, eastern Taiwan.* (Master's thesis), National Taiwan University, Taipei.

Lin, A.T., and Watts, A.B. (2002) Origin of the West Taiwan basin by orogenic loading and flexure of a rifted continental margin. *Journal of Geophysical Research: Solid Earth,* 107(B9), ETG 2-1-ETG 2-19.

Lin, A.T., Watts, A.B., and Hesselbo, S.P. (2003) Cenozoic stratigraphy and subsidence history of the South China Sea margin in the Taiwan region. *Basin Research,* 15(4), 453-478.

Lin, C.W., Liu, Y.C., Lai, W.C., and Cheng, W.H. (1999) Fault tectonics of the Coastal Range, eastern Taiwan. *Journal of the Geological Society of China,* 42(3), 429-446.

Lin, S.B., and Chen, G.T. (1986) Clay minerals from the Lichi Melange and its adjacent formations in the Coastal Range, eastern Taiwan. *Acta Geologica Taiwanica: Science Reports of the National Taiwan University,* (24), 319-356.

Lin, W.-H., Lin, C.-W., Liu, Y.C., and Chen, P.-T. (2008) *Geological map of Taiwan scale 1:50,000 - Taitung and Jhihben Sheet*. Central Geological Survey, Ministry of Economic Affairs of Taiwan, New Taipei.

Liou, J.G., Suppe, J., and Ernst, W.G. (1977) Conglomerates and pebbly mudstones in the Lichi Melange, eastern Taiwan. *Memoir of the Geological Society of China,* (2), 115-128.

Lister, G., and Forster, M. (2009) Tectonic mode switches and the nature of orogenesis. *Lithos,* 113(1), 274-291.

Lo, H.-J., Chen, W.-S., and Song, S.-R. (1993) *Geological map of Taiwan scale 1:50,000 - Chengkung and Tungho sheet*. Central Geological Survey, Ministry of Economic Affairs of Taiwan, New Taipei.

Lo, Y.-C., Chen, C.-T., Lo, C.-H., and Chung, S.-L. (2020) Ages of ophiolitic rocks along plate suture in Taiwan orogen: Fate of the South China Sea from subduction to collision. *Terrestrial Atmospheric and Oceanic Sciences,* 31(4), 383-402.

Lundberg, N., and Dorsey, R.J. (1988) Synorogenic sedimentation and subsidence in a Plio-Pleistocene collisional basin, eastern Taiwan. Kleinspehn, K. and Paola, C. (Eds.), *New Perspectives in Basin Analysis* (p. 265-280). New York: Springer.

Lundberg, N., and Dorsey, R.J. (1990) Rapid Quaternary emergence, uplift, and denudation of the Coastal Range, eastern Taiwan. *Geology,* 18(7), 638-641.

Lundberg, N., Reed, D.L., Liu, C.S., and Lieske, J. (1997) Forearc-basin closure and arc accretion in the submarine suture zone south of Taiwan. *Tectonophysics,* 274(1-3), 5-23.

Majka, J., Rosén, Å., Janák, M., Froitzheim, N., Klonowska, I., Manecki, M., Sasinková, V., and Yoshida, K. (2014) Microdiamond discovered in the Seve Nappe (Scandinavian Caledonides) and its exhumation by the “vacuum-cleaner” mechanism. *Geology,* 42(12), 1107-1110.

Malavieille, J., Dominguez, S., Lu, C.-Y., Chen, C.-T., and Konstantinovskaya, E. (2021) Deformation partitioning in mountain belts: insights from analogue modelling experiments and the Taiwan collisional orogen. *Geological Magazine,* 158(1), 84-103.

Malavieille, J., Lallemand, S.E., Dominguez, S., Deschamps, A., Lu, C.-Y., Liu, C.-S., Schnuerle, P., Angelier, J., Collot, J.Y., Deffontaines, B., Fournier, M., Hsu, S.K., Le Formal, J.P., Liu, S.Y., Sibuet, J.C., Thareau, N., Wang, F., Crew, t.A.S., Byrne, T.B., and Liu, C.-S. (2002) Arc-continent collision in Taiwan: New marine observations and tectonic evolution. *Geology and geophysics of an arc-continent collision, Taiwan* (Vol. 358, p. 187-211): Geological Society of America.

Malavieille, J., Molli, G., Genti, M., Dominguez, S., Beyssac, O., Taboada, A., Vitale-Brovarone, A., Lu, C.-Y., and Chen, C.-T. (2016) Formation of ophiolite-bearing tectono-sedimentary mélanges in accretionary wedges by gravity driven submarine erosion: Insights from analogue models and case studies. *Journal of Geodynamics,* 100, 87-103.

Marshall, J.A., and Sklar, L.S. (2012) Mining soil databases for landscape-scale patterns in the abundance and size distribution of hillslope rock fragments. *Earth Surface Processes and Landforms,* 37(3), 287-300.

Mesalles, L. (2014) *Mountain building at a subduction-collision transition zone, Taiwan - Insights from morphostructural analysis and thermochronological dating.* (Ph.D.), Université Pierre et Marie Curie, Paris, France.

Mesalles, L., Lee, Y.-H., Ma, T.-C., Tsai, W.-L., Tan, X.-B., and Lee, H.-Y. (2020) A Late-Miocene Yuli belt? New constraints on the eastern Central Range depositional ages. *Terrestrial Atmospheric and Oceanic Sciences,* 31(4), 403-414.

Mesalles, L., Mouthereau, F., Bernet, M., Chang, C.-P., Lin, A.T.-S., Fillon, C., and Sengelen, X. (2014) From submarine continental accretion to arc-continent orogenic evolution: The thermal record in southern Taiwan. *Geology,* 42(10), 907-910.

Michiguchi, Y., Ogawa, Y., Wakabayashi, J., and Dilek, Y. (2011) Implication of dark bands in Miocene–Pliocene accretionary prism, Boso Peninsula, central Japan. Wakabayashi, J. and Dilek, Y. (Eds.), *Mélanges: Processes of Formation and Societal Significance* (p. 247-260).

Migoń, P. (2020) Geomorphology of conglomerate terrains – Global overview. *Earth-Science Reviews,* 208, 103302.

Miller, K.G., Browning, J.V., Schmelz, W.J., Kopp, R.E., Mountain, G.S., and Wright, J.D. (2020) Cenozoic sea-level and cryospheric evolution from deep-sea geochemical and continental margin records. *Science Advances,* 6(20), eaaz1346.

Molnar, P. (2012) Isostasy can't be ignored. *Nature Geoscience,* 5(2), 83-83.

Montgomery, D.R., Abbe, T.B., Buffington, J.M., Peterson, N.P., Schmidt, K.M., and Stock, J.D. (1996) Distribution of bedrock and alluvial channels in forested mountain drainage basins. *Nature,* 381(6583), 587-589.

Montgomery, D.R., and Brandon, M.T. (2002) Topographic controls on erosion rates in tectonically active mountain ranges. *Earth and Planetary Science Letters,* 201(3), 481-489.

Montgomery, D.R., and Gran, K.B. (2001) Downstream variations in the width of bedrock channels. *Water Resources Research,* 37(6), 1841-1846.

Moore, G.F., Aung, L.T., Fukuchi, R., Sample, J.C., Hellebrand, E., Kopf, A., Naing, W., Than, W.M., and Tun, T.N. (2019) Tectonic, diapiric and sedimentary chaotic rocks of the Rakhine coast, western Myanmar. *Gondwana Research,* 74, 126-143.

Nagel, S., Castelltort, S., Garzanti, E., Lin, A.T., Willett, S.D., Mouthereau, F., Limonta, M., and Adatte, T. (2014) Provenance evolution during arc–continent collision: sedimentary petrography of Miocene to Pleistocene sediments in the western foreland basin of Taiwan. *Journal of Sedimentary Research,* 84(7), 513-528.

Neely, A.B., and DiBiase, R.A. (2020) Drainage area, bedrock fracture spacing, and weathering controls on landscape-scale patterns in surface sediment grain size. *Journal of Geophysical Research: Earth Surface,* 125(10), e2020JF005560.

Neely, A.B., DiBiase, R.A., Corbett, L.B., Bierman, P.R., and Caffee, M.W. (2019) Bedrock fracture density controls on hillslope erodibility in steep, rocky landscapes with patchy soil cover, southern California, USA. *Earth and Planetary Science Letters,* 522, 186-197.

Nemec, W. (1990) Aspects of sediment movement on steep delta slopes. Colella, A. and Prior, D.B. (Eds.), *Coarse-Grained Deltas* (p. 29-73).

Noda, A. (2016) Forearc basins: Types, geometries, and relationships to subduction zone dynamics. *Geological Society of America Bulletin,* 128(5-6), 879-875.

Noda, A. (2018) Forearc basin stratigraphy and interactions with accretionary wedge growth according to the critical taper concept. *Tectonics,* 37(3), 965-988.

Ogata, K., Festa, A., Pini, G.A., and Alonso, J.L. (2019) Submarine landslide deposits in orogenic belts. Ogata, K., Festa, A., and Pini, G.A. (Eds.), *Submarine Landslides: Subaqueous Mass Transport Deposits from Outcrops to Seismic Profiles* (p. 1-26): John Wiley & Sons, Inc., Hoboken, NJ and American Geophysical Union, Washington, D.C., USA.

Ogata, K., Festa, A., Pini, G.A., Pogačnik, Ž., and Lucente, C.C. (2019) Substrate deformation and incorporation in sedimentary mélanges (olistostromes): Examples from the northern Apennines (Italy) and northwestern Dinarides (Slovenia). *Gondwana Research,* 74, 101-125.

Ogata, K., Mountjoy, J.J., Pini, G.A., Festa, A., and Tinterri, R. (2014) Shear zone liquefaction in mass transport deposit emplacement: A multi-scale integration of seismic reflection and outcrop data. *Marine Geology,* 356, 50-64.

Ogata, K., Mutti, E., Pini, G.A., and Tinterri, R. (2012) Mass transport-related stratal disruption within sedimentary mélanges: Examples from the northern Apennines (Italy) and south-central Pyrenees (Spain). *Tectonophysics,* 568-569, 185-199.

Ogg, J.G. (2012) Geomagnetic polarity time scale. Gradstein, F.M., Ogg, J.G., Schmitz, M.D., and Ogg, G.M. (Eds.), *The Geologic Time Scale 2012* (p. 85-113). Boston: Elsevier.

Ogg, J.G. (2020) Chapter 5 - Geomagnetic Polarity Time Scale. Gradstein, F.M., Ogg, J.G., Schmitz, M.D., and Ogg, G.M. (Eds.), *Geologic Time Scale 2020* (p. 159-192): Elsevier.

Öğretmen, N., Cipollari, P., Frezza, V., Faranda, C., Karanika, K., Gliozzi, E., Radeff, G., and Cosentino, D. (2018) Evidence for 1.5 km of uplift of the central Anatolian plateau's southern margin in the last 450 kyr and Implications for Its multiphased uplift history. *Tectonics,* 37(1), 359-390.

Ooe, G. (1939) Geologic map of Taiwan, Taito sheet. *Goverment General of Taiwan,* (861), 1-26.

Ouimet, W.B., Whipple, K.X., and Granger, D.E. (2009) Beyond threshold hillslopes: Channel adjustment to base-level fall in tectonically active mountain ranges. *Geology,* 37(7), 579-582.

Page, B.M., and Suppe, J. (1981) The Pliocene Lichi Mélange of Taiwan: its plate-tectonic and olistostromal origin. *American Journal of Science,* 281(3), 193-227.

Penserini, B.D., Roering, J.J., and Streig, A. (2017) A morphologic proxy for debris flow erosion with application to the earthquake deformation cycle, Cascadia Subduction Zone, USA. *Geomorphology,* 282, 150-161.

Perron, J.T., and Royden, L. (2013) An integral approach to bedrock river profile analysis. *Earth Surface Processes and Landforms,* 38(6), 570-576.

Raffi, I., Wade, B.S., Pälike, H., Beu, A.G., Cooper, R., Crundwell, M.P., Krijgsman, W., Moore, T., Raine, I., Sardella, R., and Vernyhorova, Y.V. (2020) Chapter 29 - The Neogene Period. Gradstein, F.M., Ogg, J.G., Schmitz, M.D., and Ogg, G.M. (Eds.), *Geologic Time Scale 2020* (1 ed., p. 1141-1215): Elsevier.

Ragan, D.M. (2009) *Structural Geology: An Introduction to Geometrical Techniques*. Cambridge, UK: Cambridge University Press.

Ramsay, J.G. (1961) The effects of folding upon the orientation of sedimentation structures. *The Journal of Geology,* 69(1), 84-100.

Raymond, L.A. (1984) Classification of melanges. Raymond, L.A. (Ed.), *Melanges: Their Nature, Origin, and Significance* (p. 7-20).

Raymond, L.A. (2019) Perspectives on the roles of melanges in subduction accretionary complexes: A review. *Gondwana Research,* 74, 68-89.

Reed, D.L., Lundberg, N., Liu, C.-S., and Kuo, B.Y. (1992) Structural relations along the margins of the offshore Taiwan accretionary wedge: implications for accretion and crustal kinematics. *Acta Geologica Taiwanica: Science Reports of the National Taiwan University,* (30), 105-122.

Reiners, P.W., and Brandon, M.T. (2006) Using thermochronology to understand orogenic erosion. *Annual Review of Earth and Planetary Sciences,* 34(1), 419-466.

Rickenmann, D., and Recking, A. (2011) Evaluation of flow resistance in gravel-bed rivers through a large field data set. *Water Resources Research,* 47(7), W07538.

Roda-Boluda, D.C., D'Arcy, M., McDonald, J., and Whittaker, A.C. (2018) Lithological controls on hillslope sediment supply: insights from landslide activity and grain size distributions. *Earth Surface Processes and Landforms,* 43(5), 956-977.

Roering, J.J. (2012) Landslides limit mountain relief. *Nature Geoscience,* 5, 446-447.

Romans, B.W., Castelltort, S., Covault, J.A., Fildani, A., and Walsh, J.P. (2016) Environmental signal propagation in sedimentary systems across timescales. *Earth-Science Reviews,* 153, 7-29.

Royden, L., and Keen, C.E. (1980) Rifting process and thermal evolution of the continental margin of Eastern Canada determined from subsidence curves. *Earth and Planetary Science Letters,* 51(2), 343-361.

Sandmann, S., Nagel, T.J., Froitzheim, N., Ustaszewski, K., and Münker, C. (2015) Late Miocene to Early Pliocene blueschist from Taiwan and its exhumation via forearc extraction. *Terra Nova,* 27(4), 285-291.

Schmidt, K.M., and Montgomery, D.R. (1995) Limits to Relief. *Science,* 270(5236), 617-620.

Schwanghart, W., and Scherler, D. (2014) Short Communication: TopoToolbox 2 – MATLAB-based software for topographic analysis and modeling in Earth surface sciences. *Earth Surface Dynamics,* 2(1), 1-7.

Sclater, J.G., and Christie, P.A.F. (1980) Continental stretching: An explanation of the Post-Mid-Cretaceous subsidence of the central North Sea Basin. *Journal of Geophysical Research: Solid Earth,* 85(B7), 3711-3739.

Shobe, C.M., Braun, J., Yuan, X., Campforts, B., Gailleton, B., Baby, G., Guillocheau, F., and Robin, C. (2022) Inverting passive margin stratigraphy for marine sediment transport dynamics over geologic time. *Basin Research.*

Shobe, C.M., Hancock, G.S., Eppes, M.C., and Small, E.E. (2017) Field evidence for the influence of weathering on rock erodibility and channel form in bedrock rivers. *Earth Surface Processes and Landforms,* 42(13), 1997-2012.

Shobe, C.M., Tucker, G.E., and Anderson, R.S. (2016) Hillslope-derived blocks retard river incision. *Geophysical Research Letters,* 43(10), 5070-5078.

Shobe, C.M., Turowski, J.M., Nativ, R., Glade, R.C., Bennett, G.L., and Dini, B. (2021) The role of infrequently mobile boulders in modulating landscape evolution and geomorphic hazards. *Earth-Science Reviews,* 220, 103717.

Shyu, C.-T., Chih, M.-C., Hsu, S.-K., Wang, C., and Karp, B. (1996) Northern Luzon Arc: Location and tectonic features from magnetic data off eastern Taiwan. *Terrestrial Atmospheric and Oceanic Sciences,* 7(4), 535-548.

Shyu, J.B.H., Chen, C.-F., and Wu, Y.-M. (2016) Seismotectonic characteristics of the northernmost Longitudinal Valley, eastern Taiwan: Structural development of a vanishing suture. *Tectonophysics,* 692(Part B), 295-308.

Shyu, J.B.H., Sieh, K., Avouac, J.-P., Chen, W.-S., and Chen, Y.-G. (2006) Millennial slip rate of the Longitudinal Valley fault from river terraces: Implications for convergence across the active suture of eastern Taiwan. *Journal of Geophysical Research,* 111(B8), B08403.

Shyu, J.B.H., Sieh, K., Chen, Y.-G., Chuang, R.Y., Wang, Y., and Chung, L.-H. (2008) Geomorphology of the southernmost Longitudinal Valley fault: Implications for evolution of the active suture of eastern Taiwan. *Tectonics,* 27(1), TC1019.

Shyu, J.B.H., Wu, Y.-M., Chang, C.-H., and Huang, H.-H. (2011) Tectonic erosion and the removal of forearc lithosphere during arc-continent collision: Evidence from recent earthquake sequences and tomography results in eastern Taiwan. *Journal of Asian Earth Sciences,* 42(3), 415-422.

Sibuet, J.-C., Zhao, M., Wu, J., and Lee, C.-S. (2021) Geodynamic and plate kinematic context of South China Sea subduction during Okinawa trough opening and Taiwan orogeny. *Tectonophysics,* 817, 229050.

Silver, E.A., and Beutner, E.C. (1980) Melanges. *Geology,* 8(1), 32-34.

Sinclair, H.D. (2012) Thrust wedge/foreland basin systems. Busby, C. and Azor, A. (Eds.), *Tectonics of Sedimentary Basins: Recent Advances* (p. 522-537). Chichester, UK: John Wiley & Sons, Ltd.

Sinotech Engineering Consultants Inc. (2006) *Final Report of the Integrated Environmental-Geological Database for Urban and Hillslope - Investigation on Hillslope Rock Properties (5/5) - Eastern Area*. 177 pp. Retrieved from 95-21A, Central Geological Survey, M.o.E.A., Taiwan, New Taipei.

Sklar, L.S., and Dietrich, W.E. (1998) River longitudinal profiles and bedrock incision models: stream power and the influence of sediment supply. Tinkler, K.J. and Wohl, E.E. (Eds.), *Rivers Over Rock: Fluvial Processes in Bedrock Channels* (p. 237-260). Washington, D.C., USA: American Geophysical Union.

Sklar, L.S., and Dietrich, W.E. (2001) Sediment and rock strength controls on river incision into bedrock. *Geology,* 29(12), 1087-1090.

Sklar, L.S., and Dietrich, W.E. (2004) A mechanistic model for river incision into bedrock by saltating bed load. *Water Resources Research,* 40(6), W06301.

Sklar, L.S., and Dietrich, W.E. (2006) The role of sediment in controlling steady-state bedrock channel slope: Implications of the saltation–abrasion incision model. *Geomorphology,* 82(1), 58-83.

Sklar, L.S., and Dietrich, W.E. (2008) Implications of the saltation–abrasion bedrock incision model for steady-state river longitudinal profile relief and concavity. *Earth Surface Processes and Landforms,* 33(7), 1129-1151.

Sklar, L.S., Riebe, C.S., Marshall, J.A., Genetti, J., Leclere, S., Lukens, C.L., and Merces, V. (2017) The problem of predicting the size distribution of sediment supplied by hillslopes to rivers. *Geomorphology,* 277, 31-49.

Snyder, N.P., Whipple, K.X., Tucker, G.E., and Merritts, D.J. (2003) Channel response to tectonic forcing: field analysis of stream morphology and hydrology in the Mendocino triple junction region, northern California. *Geomorphology,* 53(1), 97-127.

Song, S.-R., and Lo, H.-J. (2002) Lithofacies of volcanic rocks in the central Coastal Range, eastern Taiwan: implications for island arc evolution. *Journal of Asian Earth Sciences,* 21(1), 23-38.

Song, S.-R., Lo, H.-J., and Chen, W.-S. (1994) Origin of clastic dikes In the Coastal Range, eastern Taiwan with implications for sedimentary processes during the arc-continent collision. *Journal of the Geological Society of China,* 37(3), 407-424.

Song, S.-R., and Tang, H.-Y. (2019) *Tuff layers in the fore-arc basin of south Coastal Range, eastern Taiwan: Implications for volcanic activity and evolution after the arc-continent collision*. Paper presented at the American Geophysical Union, Fall Meeting 2019, San Francisco, California, USA.

Song, T.-R.A., Ma, K.-F., Byrne, T.B., and Liu, C.-S. (2002) Estimation of the thermal structure of a young orogenic belt according to a model of whole-crust thickening. *Geology and geophysics of an arc-continent collision, Taiwan* (Vol. 358, p. 0): Geological Society of America.

Spotila, J.A., Farley, K.A., Yule, J.D., and Reiners, P.W. (2001) Near-field transpressive deformation along the San Andreas fault zone in southern California, based on exhumation constrained by (U-Th)/He dating. *Journal of Geophysical Research: Solid Earth,* 106(B12), 30909-30922.

Stanley, R.S., Hill, L.B., Chang, H.C., and Hu, H.-N. (1981) A transect through the metamorphic core of the central mountains, southern Taiwan. *Memoir of the Geological Society of China,* (4), 443-473.

Sternberg, H. (1875) Untersuchungen iiber langen-und Querprofil geschiebefiihrende Flusse. *Zeitschrift Bauwesen,* 25, 483-506.

Stock, J., and Dietrich, W.E. (2003) Valley incision by debris flows: Evidence of a topographic signature. *Water Resources Research,* 39(4), 1089.

Stock, J.D., Montgomery, D.R., Collins, B.D., Dietrich, W.E., and Sklar, L. (2005) Field measurements of incision rates following bedrock exposure: Implications for process controls on the long profiles of valleys cut by rivers and debris flows. *Geological Society of America Bulletin,* 117(1-2), 174-194.

Stow, D.A.V., and Mayall, M. (2000) Deep-water sedimentary systems: New models for the 21st century. *Marine and Petroleum Geology,* 17(2), 125-135.

Strachan, L.J., and Alsop, G.I. (2006) Slump folds as estimators of palaeoslope: a case study from the Fisherstreet Slump of County Clare, Ireland. *Basin Research,* 18(4), 451-470.

Straub, K.M., Duller, R.A., Foreman, B.Z., and Hajek, E.A. (2020) Buffered, Incomplete, and Shredded: The Challenges of Reading an Imperfect Stratigraphic Record. *Journal of Geophysical Research: Earth Surface,* 125(3), e2019JF005079.

Sun, C.-H., Smith, A.D., and Chen, C.-H. (1998) Nd-Sr isotopic and geochemical evidence on the protoliths of exotic blocks in the Juisui Area, Yuli Belt, Taiwan. *International Geology Review,* 40(12), 1076-1087.

Sung, Q. (1991) Some characteristics of sedimentary blocks in the Lichi Mélange, Coastal Range, Taiwan. *Special Publication of the Central Geological Survey, Ministry of Economic Affairs of Taiwan,* (5), 231-256.

Suppe, J. (1981) Mechanics of mountain building and metamorphism in Taiwan. *Memoir of the Geological Society of China,* (4), 67-89.

Suppe, J. (1984) Kinematics of arc-continent collision, flipping of subduction, and back-arc spreading near Taiwan. *Memoir of the Geological Society of China,* (6), 21-33.

Suppe, J., and Liou, J.G. (1979) Tectonics of the Lichi Mélange and East Taiwan Ophiolite. *Memoir of the Geological Society of China,* (3), 147-153.

Sweeney, K.E., and Roering, J.J. (2017) Rapid fluvial incision of a late Holocene lava flow: Insights from LiDAR, alluvial stratigraphy, and numerical modeling. *Geological Society of America Bulletin,* 129(3-4), 500-512.

Tate, G.W., McQuarrie, N., van Hinsbergen, D.J.J., Bakker, R.R., Harris, R., and Jiang, H. (2015) Australia going down under: Quantifying continental subduction during arc-continent accretion in Timor-Leste. *Geosphere,* 11(6), 1860-1883.

Taylor, M., Forte, A.M., Laskowski, A., and Ding, L. (2021) Active uplift of southern Tibet revealed. *GSA TODAY,* 31(8), 4-10.

Teng, L.S. (1979) Petrographical study of the Neogene sandstones of the Coastal Range, eastern Taiwan (I. northern part). *Acta Geologica Taiwanica: Science Reports of the National Taiwan University,* (20), 129-156.

Teng, L.S. (1980) Lithology and provenance of the Fanshuliao formation, northern Coastal Range, eastern Taiwan. *Proceedings of the Geological Society of China,* (23), 118-129.

Teng, L.S. (1981) On the origin and tectonic significance of the Lichi Formation, Coastal Range, eastern Taiwan. *Ti-Chih,* 3, 51-61.

Teng, L.S. (1982) Stratigraphy and sedimentation of the Suilien conglomerate, northern Coastal Range, eastern Taiwan. *Acta Geologica Taiwanica: Science Reports of the National Taiwan University,* (21), 201-220.

Teng, L.S. (1987) Tectostratigraphic facies and geologic evolution of the Coastal Range, eastern Taiwan. *Memoir of the Geological Society of China,* (8), 229-250.

Teng, L.S. (1990) Geotectonic evolution of late Cenozoic arc-continent collision in Taiwan. *Tectonophysics,* 183(1-4), 57-76.

Teng, L.S., Chen, W.-S., Wang, Y., Song, S.-R., and Lo, H.-J. (1988) Toward a comprehensive stratigraphic system of the Coastal Range, eastern Taiwan. *Acta Geologica Taiwanica: Science Reports of the National Taiwan University,* (26), 19-35.

Teng, L.S., Lee, C.T., Tsai, Y.B., and Hsiao, L.Y. (2000) Slab breakoff as a mechanism for flipping of subduction polarity in Taiwan. *Geology,* 28, 155-158.

Teng, L.S., Lee, J.C., and Hsu, C.B. (2002) Soft-sediment deformation in the Fanshuliao formation of the Coastal Range, eastern Taiwan. *Bulletin of the Central Geological Survey, Ministry of Economic Affairs of Taiwan,* (15), 103-137.

Teng, L.S., Tsai, Y.-l., and Kuo, S.-T. (2016) On the Chimei Fault zone of the Coastal Range, eastern Taiwan. *Bulletin of the Central Geological Survey, Ministry of Economic Affairs of Taiwan,* (29), 1-44.

Tensi, J., Mouthereau, F., and Lacombe, O. (2006) Lithospheric bulge in the West Taiwan Basin. *Basin Research,* 18(3), 277-299.

Thomas, M.Y., Avouac, J.-P., Gratier, J.-P., and Lee, J.-C. (2014) Lithological control on the deformation mechanism and the mode of fault slip on the Longitudinal Valley Fault, Taiwan. *Tectonophysics,* 632, 48-63.

Tomkin, J.H., Brandon, M.T., Pazzaglia, F.J., Barbour, J.R., and Willett, S.D. (2003) Quantitative testing of bedrock incision models for the Clearwater River, NW Washington State. *Journal of Geophysical Research: Solid Earth,* 108(B6), 2308.

Tripsanas, E.K., Piper, D.J.W., Jenner, K.A., and Bryant, W.R. (2008) Submarine mass-transport facies: new perspectives on flow processes from cores on the eastern North American margin. *Sedimentology,* 55(1), 97-136.

Tsai, M.-C., Yu, S.-B., Shin, T.-C., Kuo, K.-W., Leu, P.-L., Chang, C.-H., and Ho, M.-Y. (2015) Velocity field derived from Taiwan continuous GPS array (2007 - 2013). *Terrestrial Atmospheric and Oceanic Sciences,* 26(5), 527-556.

Turner, J.P., and Williams, G.A. (2004) Sedimentary basin inversion and intra-plate shortening. *Earth-Science Reviews,* 65(3), 277-304.

van der Beek, P., and Bishop, P. (2003) Cenozoic river profile development in the Upper Lachlan catchment (SE Australia) as a test of quantitative fluvial incision models. *Journal of Geophysical Research: Solid Earth,* 108(B6), 2309.

van Hinsbergen, D.J.J., Kouwenhoven, T.J., and van der Zwaan, G.J. (2005) Paleobathymetry in the backstripping procedure: Correction for oxygenation effects on depth estimates. *Palaeogeography, Palaeoclimatology, Palaeoecology,* 221(3), 245-265.

Van Sickel, W.A., Kominz, M.A., Miller, K.G., and Browning, J.V. (2004) Late Cretaceous and Cenozoic sea-level estimates: backstripping analysis of borehole data, onshore New Jersey. *Basin Research,* 16(4), 451-465.

Vázquez-Tarrío, D., Piégay, H., and Menéndez-Duarte, R. (2020) Textural signatures of sediment supply in gravel-bed rivers: Revisiting the armour ratio. *Earth-Science Reviews,* 207, 103211.

Venditti, J.G., Li, T., Deal, E., Dingle, E., and Church, M. (2020) Struggles with stream power: Connecting theory across scales. *Geomorphology,* 366, 106817.

Wakabayashi, J. (2019) Sedimentary compared to tectonically-deformed serpentinites and tectonic serpentinite mélanges at outcrop to petrographic scales: Unambiguous and disputed examples from California. *Gondwana Research,* 74, 51-67.

Wang, C.S. (1976) The Lichi Formation of the Coastal Range and arc-continent collision In eastern Taiwan. *Bulletin of the Geological Survey of Taiwan,* (25), 73-86.

Wang, J., Li, X., Ning, W., Kusky, T., Wang, L., Polat, A., and Deng, H. (2019) Geology of a Neoarchean suture: Evidence from the Zunhua ophiolitic mélange of the Eastern Hebei Province, North China Craton. *Geological Society of America Bulletin,* 131(11-12), 1943-1964.

Wang, W.-H., and Lee, Y.-H. (2011) 3-D plate interactions in central Taiwan: Insight from flexure and sandbox modeling. *Earth and Planetary Science Letters,* 308(1), 1-10.

Wang, Y., and Chen, W.-S. (1993) *Geological map of eastern Coastal Range*. Central Geological Survey, Ministry of Economic Affairs of Taiwan, New Taipei, Taiwan.

Water Resources Agency. (2019) *Hydrological Year Book of Taiwan Repulic of China 2018 Part I — Rainfall*. 296 pp. Retrieved from 00-H-30-49, Water Resources Agency Ministry of Economic Affairs of Taiwan, Taipei.

Watts, A.B. (2001) *Isostasy and Flexure of the Lithosphere*: Cambridge University Press.

Watts, A.B., and Cochran, J.R. (1974) Gravity anomalies and flexure of the lithosphere along the Hawaiian-Emperor seamount chain. *Geophysical Journal International,* 38(1), 119-141.

Whipple, K.X. (2004) Bedrock Rivers and the Geomorphology of Active Orogens. *Annual Review of Earth and Planetary Sciences,* 32(1), 151-185.

Whipple, K.X., DiBiase, R.A., and Crosby, B.T. (2013) Bedrock Rivers. Shroder, J.F. (Ed.), *Fluvial Geomorphology* (p. 550-573): Elsevier Inc.

Whipple, K.X., and Tucker, G.E. (1999) Dynamics of the stream-power river incision model: Implications for height limits of mountain ranges, landscape response timescales, and research needs. *Journal of Geophysical Research: Solid Earth,* 104(B8), 17661-17674.

Whipple, K.X., and Tucker, G.E. (2002) Implications of sediment-flux-dependent river incision models for landscape evolution. *Journal of Geophysical Research: Solid Earth,* 107(B2), 2039.

Whittaker, A.C., Attal, M., and Allen, P.A. (2010) Characterising the origin, nature and fate of sediment exported from catchments perturbed by active tectonics. *Basin Research,* 22(6), 809-828.

Willett, S.D. (1999) Orogeny and orography: The effects of erosion on the structure of mountain belts. *Journal of Geophysical Research: Solid Earth,* 104(B12), 28957-28981.

Wobus, C., Whipple, K.X., Kirby, E., Snyder, N., Johnson, J., Spyropolou, K., Crosby, B., and Sheehan, D. (2006) Tectonics from topography: Procedures, promise, and pitfalls. Willett, S.D., Hovius, N., Brandon, M.T., and Fisher, D.M. (Eds.), *Tectonics, Climate, and Landscape Evolution* (Vol. 398, p. 55-74): Geological Society of America.

Wolman, M.G. (1954) A method of sampling coarse river-bed material. *Eos, Transactions American Geophysical Union,* 35(6), 951-956.

Wu, J., Suppe, J., Lu, R., and Kanda, R. (2016) Philippine Sea and East Asian plate tectonics since 52 Ma constrained by new subducted slab reconstruction methods. *Journal of Geophysical Research: Solid Earth,* 121(6), 4670-4741.

Yang, T.F., Lee, T., Chen, C.-H., Cheng, S.-N., Knittel, U., Punongbayan, R.S., and Rasdas, A.R. (1996) A double island arc between Taiwan and Luzon: consequence of ridge subduction. *Tectonophysics,* 258(1–4), 85-101.

Yang, T.F., Tien, J.-l., Chen, C.-H., Lee, T., and Punongbayan, R.S. (1995) Fission-track dating of volcanics in the northern part of the Taiwan-Luzon Arc: eruption ages and evidence for crustal contamination. *Journal of Southeast Asian Earth Sciences,* 11(2), 81-93.

Yanites, B.J., Mitchell, N.A., Bregy, J.C., Carlson, G.A., Cataldo, K., Holahan, M., Johnston, G.H., Nelson, A., Valenza, J., and Wanker, M. (2018) Landslides control the spatial and temporal variation of channel width in southern Taiwan: Implications for landscape evolution and cascading hazards in steep, tectonically active landscapes. *Earth Surface Processes and Landforms,* 43(9), 1782-1797.

Yanites, B.J., and Tucker, G.E. (2010) Controls and limits on bedrock channel geometry. *Journal of Geophysical Research: Earth Surface,* 115(F4), F04019.

Yao, T.M., Tien, P.L., and Wang Lee, C.-M. (1988) Clay mineralogical studies on the Neogene formations, Taiyuan Basin, southern Coastal Range of Taiwan. *Acta Geologica Taiwanica: Science Reports of the National Taiwan University,* (26), 263-277.

Yen, J.Y., Lu, C.H., Dorsey, R.J., Kuo-Chen, H., Chang, C.P., Wang, C.C., Chuang, R.Y., Kuo, Y.T., Chiu, C.Y., Chang, Y.H., Bovenga, F., and Chang, W.Y. (2018) Insights into seismogenic deformation during the 2018 Hualien, Taiwan, earthquake sequence from InSAR, GPS, and modeling. *Seismological Research Letters,* 90(1), 78-87.

Yi, D.-C., Chen, C.-Y., and Lin, C.-W. (2012) *Geological map of Taiwan - Guangfu sheet*. Central Geological Survey, Ministry of Economic Affairs of Taiwan, New Taipei, Taiwan.

Yu, P.-S., Yang, T.-C., and Kuo, C.-C. (2006) Evaluating long-term trends in annual and seasonal precipitation in Taiwan. *Water Resources Management,* 20(6), 1007-1023.

Yu, S.-B., Chen, H.-Y., and Kuo, L.-C. (1997) Velocity field of GPS stations in the Taiwan area. *Tectonophysics,* 274(1), 41-59.

Yui, T.-F., Usuki, T., Chen, C.-Y., Ishida, A., Sano, Y., Suga, K., Iizuka, Y., and Chen, C.-T. (2014) Dating thin zircon rims by NanoSIMS: the Fengtien nephrite (Taiwan) is the youngest jade on Earth. *International Geology Review,* 56(16), 1932-1944.

Zhang, Y., Tsai, C.-H., Froitzheim, N., and Ustaszewski, K. (2020) The Yuli Belt in Taiwan: Part of the suture zone separating Eurasian and Philippine Sea plates. *Terrestrial Atmospheric and Oceanic Sciences,* 31(4), 415-435.

Zhao, Z., Sun, Z., Wang, Z., Sun, Z., Liu, J., and Zhang, C. (2015) The high resolution sedimentary filling in Qiongdongnan Basin, Northern South China Sea. *Marine Geology,* 361, 11-24.